EVALUATION OF HUMAN THERMAL RESPONSE AND BUILDING RESILIENCE TO EXTREME HEAT EVENTS

Lili Ji

A Thesis

In the Department

of

Building, Civil, and Environmental Engineering

Presented in Partial Fulfilment of the Requirements

For the Degree of

Doctor of Philosophy (Building Engineering) at

Concordia University

Montreal, Quebec, Canada

October 2022

CONCORDIA UNIVERSITY

SCHOOL OF GRADUATE STUDIES

This is to certify that the thesis prepared

By: Lili Ji

Entitled: Evaluation of human thermal response and building resilience to extreme heat events

and submitted in partial fulfillment of the requirements for the degree of

Doctor Of Philosophy (Building Engineering)

complies with the regulations of the University and meets the accepted standards with respect to originality and quality.

Signed by the final Examining Committee:

_____ Chair
Dr. Andrea Schiffauerova

_____ External Examiner
Dr. James Voogt

_____ External to Program
Dr. Yong Zeng

_____ Examiner
Dr. Radu Zmeureanu

_____ Examiner
Dr. Hua Ge

_____ Thesis Supervisor
Dr. Liangzhu (Leon) Wang

_____ Thesis Supervisor
Dr. Abdelaziz Laouadi

Approved by _____
Dr. Mazdak Nik-Bakht, Graduate Program Director

January/17/2023

_____
Dr. Mourad Debbabi, Dean of Faculty

Abstract

Evaluation of human thermal response and building resilience to extreme heat events

Lili Ji, Ph.D.

Concordia University, 2022

Under the current and potential impact of climate change, there is a growing concern about extreme heat events and their challenges to human health and building resilience. The indoor heat-stress situation relates to the interaction of outdoor extreme heat events, building characteristics, and occupants' vulnerability. The high heat-related mortality rate of older people (aged 65+) and the trend of the population aging worldwide indicate the significant importance of evaluating and predicting heat-stress conditions for older people. Building thermal resilience determines the ability to tolerate extreme heat events and maintain or recover indoor comfort. Models of the relation between outdoor extreme weather data, indoor environment parameters, and human physiological responses are still needed to predict the consequences of global warming. Therefore, this research aims to evaluate building occupants' thermal response and quantify building thermal resilience against extreme heat events. The Bioheat models applicable to calculating young and older adults' physiological responses under hot exposure were developed. The validation study shows that the simulation results of the proposed models agree well with the published experimental data. The heat-stress index Standard Effective Temperature (SET) can be calculated based on the proposed Bioheat models and used in the selection of extreme hot years (EHY) and quantification of building thermal resilience. The EHY was selected by quantifying the degree of synchronization between outdoor heatwave events and building indoor overheating conditions based on the concept of POS (Percentage of Synchronization). It has been proved that in building

overheating-centric studies, the EHYs should be selected according to the severity and intensity of heatwaves defined by SET. A new quantification framework for building thermal resilience against extreme heat events was developed. The framework includes the conceptual resilience trapezoid curve, Thermal Resilience Index (TRI), and resilience labelling system for zone level and building level resilience. The proposed framework has been implemented in a calibrated building model to quantify the building thermal resilience with different retrofit strategies. With this method, the effect of retrofit strategies and their combinations on the building and zonal thermal resilience can be quantified, labelled, and compared, thereby, a detailed design of resilience enhancement strategies to be achieved. The contributions of the thesis include validated new models and methods to quantify human thermal responses and building resilience to extreme heat events. These new methods and models contribute potentially significant impacts to the research under different climate zones and future climates covering from a single building to large scales to quantify community or city scale resilience to heat.

Acknowledgments

I would like to express my sincere gratitude to my co-supervisor, Dr. Liangzhu (Leon) Wang, for his continuous support of my Ph.D. study and related research and his patience, motivation, and immense knowledge. The same acknowledgements to my co-supervisor, Dr. Abdelaziz Laouadi, whose detailed guidance and inspiring suggestions have been precious for the Ph.D. study. This thesis would not have been possible without their guidance and persistent assistance.

I would like to thank the members of the examining committee, Dr. Radu Zmeureanu, Dr. James Voogt, Dr. Yong Zeng, Dr. Hua Ge, and Dr. Andrea Schiffauerova, for their precious and inspiring comments on my thesis work.

Besides, I would thank my friend and colleague, Dr. Chang Shu, who inspired me with new ideas and provided valuable suggestions for my research. I wish to extend my special thanks to Dr. Michael Lacasse, for his support and encouragement throughout my Ph.D. process. In addition, I would like to extend my regards to all the colleagues in Dr. Wang's lab at Concordia University and FSP group at National Research Council, for the fun times we had working and socializing together.

Finally, my deepest gratitude goes to my mother, Xiuying Han, and my father, Jing Ji, for their unconditional love, respect for my choices and support in realizing my dreams.

Contribution of authors

This thesis includes four published journal papers. The contribution of each co-author is explained as below.

Chapter 3: Lili Ji conceived and designed the analysis, collected the data, performed the analysis and wrote the paper. Laouadi Abdelaziz contributed to the conceptualization, methodology, review and editing. Chang Shu contributed to the methodology, review and editing. Liangzhu (Leon) Wang and Michael Lacasse contributed to review and editing.

Chapter 4: Lili Ji conceived and designed the analysis, collected the data, performed the analysis and wrote the paper. Laouadi Abdelaziz contributed to the conceptualization, methodology, review and editing. Liangzhu (Leon) Wang and Michael Lacasse contributed to review and editing.

Chapter 5: Lili Ji proposed the concept and method, conceived and designed the analysis, collected the data, performed the analysis and wrote the paper. Laouadi Abdelaziz provided the archetype building models, contributed to the methodology, review and editing. Chang Shu contributed to the conceptualization, methodology, review and editing. Abhishek Gaur provided the climate data. Michael Lacasse contributed to review and editing. Liangzhu (Leon) Wang contributed to the conceptualization, methodology, review and editing.

Chapter 6: Lili Ji proposed the concept and method, conceived and designed the analysis, collected the data, performed the analysis and wrote the paper. Chang Shu contributed to the conceptualization, methodology, data collection, review and editing. Abdelaziz Laouadi and Michael Lacasse contributed to the review and editing. Liangzhu (Leon) Wang contributed to the conceptualization, methodology, review and editing.

Preface

This is a manuscript-based thesis, a collection of four published journal papers. The four papers compose Chapter 3 ~ Chapter 6, and each manuscript is an independent chapter. Details of the journal paper are provided at the start of each chapter.

For easy reading, these four manuscripts are modified from the original ones. The numbering of equations, tables, and figures includes the numbers of the chapters, and the references of different chapters are combined at the end of the thesis.

Table of Contents

List of Figures

List of Tables

Nomenclature

A_b	Dubois body surface area (m^2)
A_{cof}	Sweating model coefficient
A_j	Floor area of each zone (m^2)
BF	Body fat percentage (%)
CCE	Attenuation coefficients of vasoconstriction for older people
c_{cr}	Specific thermal capacity of the core node (W/kg·℃)
CDE	Attenuation coefficient of vasodilation for older people
$CDIL$	Coefficient of vasodilation (L/m^2·hr·℃)
Clo	Clothing insulation (clo)
$Cof_{scs}, Cof_{sc}, Cof_{ss}$	Shivering model coefficients
$cRMSE$	Combined RMSE
c_{sk}	Specific thermal capacity of the skin node (W/kg·℃)
$CSTR$	Coefficient of vasoconstriction (L/m^2·hr·℃)
CSW	Sweating model constant
$CSWE$	Sweating attenuation coefficient for older people
$CSHE$	Shivering attenuation coefficient for older people
Dry	Skin sensible heat exchange (W/m^2)
$d\tau$	Time step
EHY	Extreme hot year
E_{max}	Maximum evaporative heat (W/m^2)

E_{rsw}	Sweating per body surface area (W/m^2)
$Evap$	Skin evaporative heat exchange (W/m^2)
h_c	Convective heat transfer coefficient W/(m^2·°C)
h_r	Radiative heat transfer coefficient W/(m^2·°C)
h_{sk}	Thermal conductance of skin accounting for blood flow perfusion (W/m^2·°C)
i	the index of the time step
M	Metabolic rate of activity (W/m^2)
m_{cr}	Mass of the core node (kg)
Met	Metabolic rate (met)
m_{sk}	Mass of the skin node (kg)
N	Duration (in days) of a heat event; the total number of thermal zones in the studied building
POS	Percentage of Synchronization
PTS	Predicted thermal sensation
Q_{res}	Respiration heat loss (W/m^2)
$R_{d,air}$	Air layer thermal resistances (m^2·°C/W)
$R_{d,clo}$	Clothing layer thermal resistances (m^2·°C/W)
RH	Relative humidity (%)
RT	Radiant temperature (°C)
$RMSE$	Root Mean Square Error
$RMSE_{cr}$	RMSE values for the core temperature

$RMSE_{sk}$	RMSE values for the skin temperature
SBF	Skin blood flow rate (L/m^2/hr)
SBF_{basal}	Basal skin blood flow rate (L/m^2/hr)
SET	Standard Effective Temperature (℃)
SET_{comf}	SET threshold of habitable level (℃)
SET_{alert}	SET threshold of alert level (℃)
SET_{emer}	SET threshold of emergency level (℃)
SET_{max}	Maximum SET (℃)
$SETH_d$	Severity of the event during the daytime (℃·h)
$SETH_n$	Severity of a heat event at preceding nighttime (℃·h)
$SHIV$	Shivering metabolic rate (W/m^2)
SWR	Sweating rate (g/m^2·h)
t_0, t_1, t_2	Time points of resilience process
T_a	Ambient air temperature (℃)
T_{cr}, T_{sk}, T_b	Core temperature, mean skin temperature, and body temperature (℃)
T_{cr0}, T_{sk0}, T_{b0}	Core temperature threshold, mean skin temperature threshold, and body temperature threshold (℃)
$T_{b0,sw}, T_{cr0,sw}$	Body and core temperature thresholds for sweating (℃)
$T_{cr0,dil}, T_{sk0,cons}$	Core temperature threshold for vasodilation and skin temperature threshold for vasoconstriction (℃)
$T_{cr0,sh}, T_{sk0,sh}$	Core and skin temperature thresholds for shivering (℃)
T_{cu}	Adaptive threshold temperature for the location under consideration (℃)

T_{op}	Operative temperature (℃)
TRI_b	Building level thermal resilience index
TRI_z	Zone level thermal resilience index
T_{rm}	Running mean temperature (℃)
T_{upp}	Limiting maximum acceptable temperature (℃)
$t\text{-}SET$	Transient SET (℃)
$t\text{-}SET_d$	t-SET threshold values during the daytime (℃)
$t\text{-}SET_n$	t-SET threshold values during the nighttime (℃)
V_a	Air velocity (m/s)
W	Body mechanical work (W/m^2); Penalty coefficient
w	Skin wettedness
w'	Ratio of sweat secretion to the maximum evaporative heat
$WCDH$	Weighted Cooling Degree Hour (℃^{2}·h)
W_{cr}	Weighted coefficient of core temperature signal of sweating
W_{sk}	Weighted coefficient of skin temperature signal of sweating
$WSETH$	Absolute resilience performance (℃·h)

Greek and math symbols

α, β	Coefficients of the average sweating rate (g/(min·℃))
η_{evap}	Sweat evaporation efficiency
ΔT_c	Cold signal (℃)
$\Delta T_{cr,dil}$	Core temperature control signal for vasodilation (℃)
$\Delta T_{sk,cons}$	Skin temperature control signal for vasoconstriction (℃)

$\Delta T_{cr,sh}$	Core temperature control signal for shivering (℃)
$\Delta T_{b,sw}$	Body temperature control signal for sweating (℃)
$\Delta T_{sk,sw}$	Skin temperature control signals for sweating (℃)
ΔT_{w}	Warm signal (℃)

Subscripts

a	Ambient air
air	Air layer
b	Human body; Building
basal	Basic value
b0	Body temperature threshold
c	Combined equation; Convection
clo	Cloth layer
cof	Coefficient
cr	Core node
cr0	Core temperature threshold
i	Segment number
j	Zone number
sc	Core temperature signal
sk	Skin node
ss	Skin temperature signal
max	Maximum value
n	Nighttime

τ	Time
o	Operative; Original
r	Radiation; Retrofit
res	Respiration
sw	Sweating
sk0	Skin temperature threshold
sh	Shivering
z	Zone

Chapter 1 Introduction

1.1. Statement of the problem

Overheating in buildings has led to adverse impacts, including heat-related health concerns and mortality (Lomas and Porritt, 2017; Vellei et al., 2017). Currently, about 30% of the world's population is exposed to deadly heat for over 20 days annually (Mora et al., 2017). Heat-related mortality cases have been reported from 164 cities across 36 countries; among them, the well-known heatwaves in mid-latitudes are those in Chicago in 1995 (~ 740 deaths) (Whitman et al., 1997), Paris in 2003 (~4870 deaths) (Dousset et al., 2011) and Moscow in 2010 (~10860 deaths) (Shaposhnikov et al., 2014). Even in cold climate zones (ASHRAE, 2013a) in Canada, five heatwaves in 1987, 1994, 2010, 2018, and 2021 resulted in mortality, for example, 106 deaths in 2010 (Bustinza et al., 2013), 66 deaths in 2018 (Lamothe et al. 2019), and 676 deaths in 2021 (Egilson, 2022). Meanwhile, climate change is expected to exacerbate heatwaves worldwide. By 2100, mid-latitudes will be exposed to about 60 days of lethal heatwaves annually, and 48%~74% of the world's population is projected to experience deadly heatwaves (Mora et al., 2017). Consequently, building overheating risk is expected to follow suit: the building overheating discomfort rate in Paraguay will reach 30% to 50% in 2070, considering a high greenhouse gas emission scenario (RCP 8.5) (Silvero et al., 2019). The summer indoor air temperatures are estimated to increase by up to 7℃ in Dutch cities in a future scenario by 2100 (Hamdy et al., 2017). Under the current and potential impact of climate change, research on human health risks and building resilience to extreme heat events are significantly important.

Human vulnerability to heat varies among different age groups. Most heat wave deaths occur in buildings, including residential buildings, nursing homes, and hospitals (Liu *et al.*, 2017; Macintyre *et al.*, 2018). The highest levels of excess mortality were found in areas with larger elderly populations (Taylor et al., 2015). There is epidemiological evidence that older people are more vulnerable to high ambient temperatures because of the weakening of thermoregulatory activities and sensory delays in triggering the thermoregulatory system (Soebarto et al., 2019). The world population aging process has been escalating: the number of people aged 60 years and over was tripled in the last 50 years and is expected to reach over 2.1 billion in the next thirty years (Issahaku and Neysmith, 2013; Mba, 2010). Western Europe and Northern America are continuously at the highest population aging rate, and developing countries have the most significant increases in absolute numbers of older populations (Wang, 2020). Attention and care should be on older people, especially their physiological responses under heat-stress conditions they become more vulnerable than younger populations.

Extreme hot weather is the primary exterior forcing for building overheating. Proper usage of extreme weather data is essential to evaluate building overheating problems under current and future climates. The selection of extreme hot years (EHYs) for providing outdoor weather data for building simulation is typically based on outdoor temperature data (Guo et al., 2019; Liu et al., 2021). Direct indices such as dry bulb temperature or empirical indices such as operative temperature (OT) have been commonly used as the dominant factor in assessing the indoor overheating situation (Gustin et al., 2020; Jentsch et al., 2015). However, there is still only limited and indirect epidemiological evidence concerning indoor temperature exposure during overheating that gives rise to adverse health effects (Hamdy et al., 2017).

Building thermal resilience determines the ability to tolerate extreme heat events and maintain or recover to an indoor comfortable environment. No consistent index has been proposed to evaluate the building resilience to heat and compare different resilient cooling strategies. Most related studies have used overheating metrics to indicate building thermal resilience (Flores-Larsen et al., 2022; Flores-Larsen and Filippín, 2021; Hess et al., 2018; Katal et al., 2019; Loughnan et al., 2015; Nicol et al., 2020). However, resilience is related to the whole process of disruption, absorption, and recovery (Homaei and Hamdy, 2021), and building thermal resilience further involves building characteristics and occupants' thermal responses. Therefore, a comprehensive framework is needed to assess and quantify building resilience to heat concerning the whole resilience procedure and impact factors about building features, occupants' response, and resilient cooling strategies.

1.2. Objectives of this thesis

To solve the problems mentioned above, this thesis aims to evaluate building occupants' thermal response and building thermal resilience against extreme heat events. The bioheat models that are applicable to calculate young and older adults' physiological responses under hot exposure will be developed to provide useful tools to predict thermal responses and calculate the physiological-based heat-stress index for occupants with different heat vulnerability levels. To ensure the indoor overheating patterns can be sufficiently captured during the studied weather situation, a new method of selecting EHYs based on the synchronization of indoor and outdoor heat events will be proposed. Under extreme heat events, the quantification framework for building thermal resilience will be developed. The framework considered the resilience profile, quantification index, and resilience level labeling. The outcomes of the thesis provide tools to quantify human thermal

responses and building resilience to extreme heat events. The tools can then be applied to research under different climate zones and future climates, as well as be extended from a single building to quantify community or city scale resilience to heat.

1.3. Summary and thesis layout

This chapter introduces the research gaps in the study of evaluating human thermal response and building resilience to extreme heat events. It points out the important need to develop quantification tools to assess occupants' vulnerability and building thermal resilience with a proper selection of extreme hot years. To solve the problems mentioned above:

Chapter 2 reviewed the research in recent years about indoor heat-stress evaluation, extreme weather year selection and building thermal resilience assessment and enhancement. The human physiological modelling, heat-stress indices and mortality risk analysis for young and older adults are summarized. The selection methods of extreme weather years for overheating studies are reviewed along with the typical year selections. The assessment methods of building resilience to heat events and resilience mitigation strategies are summarized.

Chapter 3 improves the two-node bioheat model for young adults to make it applicable to the hot environment. By collecting relevant thermoregulatory models and testing their performance in the two-node model structure based on published experimental data, the thermoregulatory system of the bioheat model for young adults was improved and validated under heat and cold exposure conditions. Higher accuracy than previous models was achieved when predicting the core and skin temperatures in hot environments.

Chapter 4 develops a two-node bioheat model for older people. The model was developed based on the two-node model for young adults by accounting for the age-related attenuation of

thermoregulation and sensory delays in triggering thermoregulatory actions. The model was validated with published experimental data and achieved good agreement with the measured skin temperature and core temperature. This model can predict older people's thermal response in heat-stress environments.

Chapter 5 develops a new method for selecting EHYs. A new approach to select EHYs based on the synchronization of outdoor and indoor-based extreme years was proposed. This approach allows a comparison between the temperature-based and thermal-based indices and among the duration, intensity, and severity-based extreme years. On top of that, a representative extreme year for each city could be identified with the proposed method.

Chapter 6 develops a new framework to quantify building thermal resilience. Building thermal resilience can be quantified based on the resilience trapezoid concept. An index was proposed to label the building resilience classes with respect to the relative improvement from original indoor thermal conditions. Except for the whole building resilience, the zone-level resilience was also evaluated. The proposed framework can be used to quantify the overall and zonal thermal resilience of a building against extreme heat events.

This thesis contributes to bioheat models applicable to hot exposure of young and older adults, a new method to select EHY for building overheating studies, and a new framework for quantifying building thermal resilience to extreme heat events. Different from previous studies, this work provides a clear definition of building thermal resilience and quantification tools for heat-vulnerable people's physiological responses and building resilience to heat. The models and methods have evident potential to be used in extended spatial and temporal scales.

Chapter 2 Literature Review

2.1. Introduction

This section summarizes research in recent years about indoor heat-stress evaluation, extreme weather year selection, and building thermal resilience assessment and enhancement. The three main methods used to evaluate human heat-related health risks are physiological modelling, heat-stress indices, and mortality risk analysis. As extreme events have had a substantial impact on older people's mortality and mobility, the studies on heat-stress evaluation of older people are summarized in a separate subsection to understand the research direction better to protect the heat-vulnerable population. The selection methods of extreme weather years for overheating studies are also reviewed along with the typical year selections, as the extreme year selection methods are often derived from existing typical year selection methods. Finally, the assessment of building resilience to heat events, including building thermal modelling, overheating, and resilience evaluation and mitigation strategies, are summarized. The research gaps are analyzed based on the reviewed studies in each section.

2.2. Indoor heat-stress evaluation

It is important to have models and indices to evaluate human heat stress to avoid health risks and reduce mortalities during extreme heat events. Human physiological models, which can predict thermal risks by calculating core temperature, skin temperature, and water loss of the human body, are helpful tools in heat-stress evaluation. Besides, heat-stress indices are also widely used to assess and predict human thermal risks. There are more than 100 heat-stress indices over the last 70 years of development (Havenith and Fiala, 2016), which include direct indices that can be

measured by instruments, empirical indices that are derived from experimental and survey data, and rational indices developed based on physiological models. Older people aged 65+ account for a large percentage of heat-related mortality. Due to the heat vulnerability of older people, physiological models and heat-stress indices need to be adjusted for application to the aging population.

2.2.1 Heat-stress modelling and indices

Physiological models consist of the passive system indicating the heat balance of the human body and the active system taking into account thermoregulatory activities such as sweating, skin blood flow, and shivering. Under hot exposure, the thermoregulatory actions would be triggered to increase the heat transfer from the body core to the skin and, after that, from the skin surface to the environment, thus releasing heat to the environment and protecting the human body from heat injuries by accumulative heat. Because the thermoregulatory activity is essential when people are exposed to a heat-stress environment, the active system enables physiological models to be used as thermal strain assessment tools.

Although initially developed for thermal comfort research, the two-node physiological model (Gagge et al., 1986) has been successfully used in the assessment of heat strain (Havenith and Fiala, 2016). The multi-node models, which can calculate local physiological responses of different body parts, are also widely used in heat stress evaluation. Physiological models have been developed and improved in the past 70 years and are still being investigated, compared, and modified for various research purposes. For example, Unnikrishnan et al. (2021) developed a thermoregulatory model to predict the whole body and organ- and tissue-level heat-stress responses under different environments, activity, and clothing levels and found the activity level

is the primary driver of rectal temperature increase. Under the current situation of COVID-19, the thermal stress caused by wearing facial masks is also investigated with modified physiological models (Shi et al., 2021).

Table 2-1 Heat-stress index

Heat-stress index	Environmental and occupants' variables						Reference
	T_a	RH	RT	V_a	Met	Clo	
Direct							
Dry bulb temperature	√						
Wet bulb temperature	√	√					
Empirical							
Effective temperature (ET)	√	√		√			Holmes et al. (2016)
Equivalent Temperature (EqT)	√		√	√			Kownacki *et al.* (2019)
Discomfort Index (DI)	√	√					Holmes et al. (2016)
Heat Index (HI)	√	√					Loenhout *et al.* (2016)
Apparent Temperature (AT)	√	√		√			Pioppi *et al.* (2020)
Environmental stress index (ESI)	√	√	√				Liang *et al.* (2011)
Operative Temperature (OT)	√		√	√		√	Holmes et al. (2016)
Wet Bulb Globe Temperature (WBGT)	√	√	√	√	√	√	Holmes et al. (2016)
Rational							
Heat Stress Index (HSI)	√	√	√	√	√		Holmes et al. (2016)
Index of Thermal sensation (TS)	√	√	√	√	√	√	Kownacki *et al.* (2019)
Predicted Heat strain (PHS)	√	√	√	√	√	√	Holmes et al. (2016)
Predictive Mean Vote (PMV)	√	√	√	√	√	√	Kownacki *et al.* (2019)
Standard Effective Temperature (SET)	√	√	√	√	√	√	Holmes et al. (2016)
Universal Thermal Climate Index (UTCI)	√	√	√	√	√	√	Langner et al. (2013)
Thermal Work Limit (TWL)	√	√	√	√	√	√	Kownacki *et al.* (2019)
Physiologically Equivalent Temperature (PET)	√	√	√	√	√	√	Pioppi *et al.* (2020)

As mentioned earlier, heat-stress indices have been developed to evaluate thermal risks. Many direct, empirical, and rational heat-stress indices are used in existing literature (Holmes et al.,

2016). The direct index can be measured, such as dry and wet bulb temperatures. Empirical indices are developed from field experiments and generally expressed in terms of some environmental parameter, not a physiological parameter (Brake and Bates, 2002). Examples of empirical indices include the Effective Temperature (ET), Wet Bulb Globe Temperature (WBGT), and others. Rational indices include physiological parameters such as sweat rate, core temperature, or heart rate and parameters calculated based on the physiological models, such as Predicted Heat strain (PHS), Standard Effective Temperature (SET), and others.

Table 1 lists 16 heat-stress indices widely used in existing studies and indicates the factors they include. The environmental variables, including air temperature, relative humidity, radiation, air speed, and occupants' characteristics, such as activity level and clothing level, can be considered in a heat-stress index.

2.2.2 Heat-related mortality risk

Heat-related mortality burdens have increased due to extreme heat events and urban heat islands along with climate change. The number of summer-season heat-related deaths was found to grow on every continent (Vicedo-Cabrera et al., 2021). Studies were conducted to relate daily mortality with thermal parameters like air temperature, PET and UTCI and found that hot conditions are risk factors for daily mortality (Nastos and Matzarakis, 2012). Predicting the mortality risk is also a topic many researchers focus on to assess the consequence of global warming and evaluate potential mitigation strategies. Peng et al. (2011) estimated the relationship between heatwaves and mortality with Poisson regression models. The widely used quantitative method to assess the impacts of heat on mortality was developed by Honda et al. (2014). They calculated the relative mortality risk (RMR) based on the deviation of air temperature from an optimum temperature, at

which the heat-related excessive mortality has the lowest value. Mitchell et al. (2016) estimated the number of heat-related deaths (M) by relating the change in apparent temperature (AT) with the difference in the baseline mortality rate. The above-mentioned methods have been used to estimate the heat-related mortality risk in the US (Shindell et al., 2020), Middle East and North Africa (MENA) (Ahmadalipour and Moradkhani, 2018), Greece (Nastos and Matzarakis, 2012), and other areas of the world.

Studies have found that an increase in heat-related deaths was related to the increased number of older adults, who are more vulnerable to heat due to psycho-physical impairment and/or lack of socio-economic resources (Liotta et al., 2018). Studies have shown that a 1°C temperature rise would increase cardiovascular (3.44%, 95% CI 3.10–3.78), respiratory (3.60%, 3.18–4.02), and cerebrovascular (1.40%, 0.06–2.75) mortality of elderly by 3.44%, 3.60%, and 1.4%, respectively, at the confidence interval of 95% (Bunker et al., 2016). Extreme heat led to a significant risk for mortality and morbidity in the US elderly (Chien et al., 2016). A review study about heat-related mortality risk in Europe suggested that older women are at higher risk than men (van Steen et al., 2019). Heat-related elderly deaths in August have been predicted to increase by 12-15 times in the 2050s than 2010s in a megacity in Indonesia (Varquez et al., 2020). It was also suggested that the heat-related mortality rate of the older population in Korea would be increased by social isolation indicators (Kim et al., 2020). The high heat-related mortality rate of older people and the population aging problem happening worldwide indicate the significant importance of evaluating and predicting the heat-stress conditions specifically for older people to establish a more reliable heat-alert system.

2.2.3 Heat-stress evaluation of older people

To develop physiological models applicable to predict older peoples' physiological responses under hot exposure, studies have been conducted to adjust the existing models for average-aged people based on age-related changes and hot exposure thermoregulation. Studies were conducted to explore the impact of indoor overheating on heat-related symptoms of older people and found that high air temperatures were related to rising risks of dry mouth, fatigue, thirst, less frequent urination, and trouble sleeping (Teyton et al., 2022). Experimental studies have also shown that older people store more heat than young people during short exposure to dry and humid hot environments, meaning they experience more significant thermal strain during heat events (Stapleton et al., 2014). Based on the multi-node thermal comfort model for average-aged people of Karaki et al. (2013), Rida et al. (2014) developed a model for older people by modifying basic metabolic rate, skin fat, skin blood flow, and thermoregulatory factors, and Itani et al., (2020b) adjusted the model for fat thickness, threshold of sweating, metabolic rate, heart rate, and cardiac output to make it applicable to the hot environment. However, a widely used heat-stress index considering the age-related difference and physiological responses of older people under hot exposure is still lacking. The understanding of the mechanistic links between heatwaves and health is still insufficient (Meade et al., 2020). More studies are required to integrate physiological research with climate-health models to help protect vulnerable heat populations.

2.3. Reference weather year selection

Indoor thermal condition is often studied using thermal simulation with historical, current, and future climate data. Due to computational complications and time consumption of climate modelling and building simulation, long-term multidecadal assessment is challenging. The

reference weather years are therefore generated to decrease the number of simulations for assessing the impact of climate on indoor thermal and energy performance. The reference years should keep the quality and main characteristics of the interest of long-term climate datasets. Two categories of reference weather years are often generated: Typical reference weather years and extreme reference weather years.

2.3.1 Typical reference weather year

Typical reference weather years represent the typical weather conditions, excluding extremes within multi-years. The widely used typical meteorological year (TMY) is an artificial year that is derived from multi-year weather datasets through mathematical methods (Yuan et al., 2022). By the Sandia method, a TMY is created by selecting each typical meteorological month (TMM) that consider the minimum difference between the cumulative distribution function (CDF) of the month and the long-term, while the Danish method is to compare the difference of standard deviation between selected months and the long-term (Li et al., 2020; Yaqubi et al., 2022). Researchers also improved these methods to generate typical reference weather years that are applicable to different locations. Arima et al. (2017) proposed Typical and Design Weather Year (TDWY) to estimate both annual and maximum cooling/heating loads by including monthly and yearly averages and minimum/maximum hourly values of multi-year data in the TDWY. Murphy (2017) modified TMY with Regional Climate Models to get more accurate solar radiation data for the simulation of the photovoltaic system.

2.3.2 Extreme reference weather year

Including extreme weather conditions in the reference weather years are essential to assess indoor overheating risks or maximum cooling/heating load under the impact of climatic uncertainties. To

do this, the Design Summer Year (DSY) was developed to assess natural ventilation in summer, which considers the near-extreme weather conditions by selecting the year with the third hottest summer within 20 years (Levermore and Parkinson, 2006). In addition to DSY, the design reference year (DRY) was a year formed from individual extreme weather months in respect of not only air temperature but also humidity and solar radiation (Watkins et al., 2013). Summer Reference Year (SRY) was produced by adjusting the months of Typical Reference Year (TRY) to represent near-extreme air temperatures, cloud cover and wind speed (Jentsch et al., 2015), which overcame the shortcomings of DSY and DRY that the discomfort evaluation results were inconsistent with the corresponding TRY. Similarly, Extreme Meteorological Year (XMY) was produced based on the typical weather year TMY and adjusted the months with the highest and lowest daily or hourly average dry-bulb temperature (Crawley and Lawrie, 2015). Based on the quantile regression method, the quantile regression ensemble summer year (QRESY) that contains heatwaves was produced using a weighted average ensemble (Herrera et al., 2018). Typical Hot Years (THYs) were produced accounting for both outdoor and indoor thermal conditions (Guo et al., 2019), which focused more on the impact of outdoor climate on the indoor heat events intensity and therefore more suitable to conduct the indoor overheating assessment.

To explore the impact of climate change on building thermal and energy performance, future years consisting of both typical and extreme conditions were generated. Nik (2016) selected one typical year Typical Downscaled Year (TDY), and two extreme years Extreme Cold Year (ECY) and Extreme Warm Year (EWY), through a similar procedure of selecting TMY. The difference is that the three years were selected based only on dry-bulb temperature instead of four variables. The extreme years were selected by the maximum (EWY) and minimum (ECY) absolute difference. Machard et al. (2020) conducted building thermal simulations with Future Typical Year (TWY)

composing the 12 most statistically common months and Future Heatwave Event (HWE) weather files selected based on percentile thresholds calculated by mortality data from historical heatwaves. The above-mentioned extreme reference weather years SRY, XMY, THY-I, and THY-E were compared in the study of Liu et al. (2021) who found that those years could capture different patterns of overheating events, for example, the THY-I (THY-Intensity) could capture the severest daytime overheating and the THY-E (THY-Event) could examine the longest duration of daytime overheating, while in XMY one could find the severest and longest nighttime overheating. Therefore, the current extreme reference weather years still lead to inconsistent results about indoor overheating problems, and there is no conclusion on which year is more representative. The investigation of which pattern of the overheating problem has the most significant impact on occupants might be a way to inversely explain which extreme year is appropriate for overheating analysis.

2.4. Building thermal resilience quantification

2.4.1 Building thermal modelling

Building thermal models can be developed based on building energy simulation models that include the heat transfer processes or based on heat, air and moisture transfer (HAMT) analysis of the building envelope and indoor environment. With the boundary condition obtained from building thermal models, the detailed indoor airflow and temperature distribution can be simulated with computational fluid dynamics (CFD) analysis or other alternative ways. Data-driven methods are also used to predict indoor thermal environments in recent years.

By calibrating and validating the models based on monitored indoor climate data or thermal comfort surveys, building energy models developed by software such as EnergyPlus (DOE, 2020), ESP-r (Energy Systems Research Unit, 2020), TRNSYS (Thermal Energy System Specialists, 2019) and Pleiades-Comfie (Tsoka, 2015) can be used to study the indoor thermal condition due to their consideration of heat transfer processes (Baba et al., 2022; Benchekroun et al., 2019; Elsharkawy and Zahiri, 2020). Because ventilation and infiltration produce heat transfer related to airflow currents, airflow network models are often integrated with the building energy models to develop combined thermal and airflow calculations (Firląg and Murray, 2013; Martínez-Ibernón et al., 2016; Martínez-Mariño et al., 2021). In such models, the thermal condition in a zone is considered uniform. Thus, a thermal zone should be divided into smaller cells to capture the spatial variations of indoor temperature in a room (Vidhyashankar et al., 2022). IDA Indoor Climate and Energy (ICE) is another tool widely used to simulate indoor climate, which can model indoor air flows, thermal conditions and energy performance (Kistelegdi and Baranyai, 2013; Paliouras et al., 2015; Rohdin et al., 2014; Sana et al., 2021). It is able to model buildings with multiple zones and variable time steps (Ahmed et al., 2022).

The hygrothermal analysis considers the HAMT of building envelope and indoor spaces and, therefore, can precisely model the indoor thermal conditions under the effect of the outdoor climate. Whole building hygrothermal models such as WUFI+ (Künzel et al., 2005) and DETECt (Buonomano et al., 2015) were developed by integrating HAMT through building envelope with indoor heat and moisture balances (Tariku et al., 2010). Simplified indoor climate models were also designed to predict the dynamic indoor situation in response to outdoor climate and building operation. A building indoor model can be developed based on the analytic solution of Fourier's equation to consider the heat transfer, but this approach ignores moisture (Pfafferott et al., 2021;

Ryzhov et al., 2019). The benefit of the simplified building physics models is that they could be continuously recalibrated with the operation of buildings to capture the time-dependent change of building characteristics for more efficient indoor climate control (Yang et al., 2019).

The surface temperatures output from building thermal models can be used as boundary conditions for the CFD to simulate air movements and temperature distribution (Rohdin et al., 2014; Ţurcanu et al., 2020), and the results can then be validated with measured indoor thermal data (Zhao et al., 2022). This way, indoor climate distribution in different usage conditions such as seasons, occupancy densities and air diffusers can be predicted and evaluated (Zhao et al., 2022). Considering the computationally time-consuming requirements of CFD, an alternative simplified way to simulate indoor air temperature distribution is based on the contribution ratio of indoor climate (CRI), which indicates the personal impact of all heat factors, and can achieve similar accuracy with CFD but with much shorter simulation time (Huang et al., 2012; Zhang et al., 2013). Modelica-based room thermal modelling is another way to simulate the detailed indoor climate, which can consider the view factors for arbitrary polygon for radiation calculation, vertical temperature gradient and airflow under the effect of other room features (Eriksson et al., 2012)(Christoph Nytsch-Geusen et al., 2021).

Data-driven methods like Artificial neural networks (ANNs) were also used to simulate the indoor climate (Aliberti et al., 2019; Ganguly et al., 2020; Mba et al., 2016; Sözer and Aldin, 2019). The parameters of Linear Time Invariant (LTI) models can be determined with physical data, which was suitable to predict building indoor climate insensitive to short-term disturbances (Kramer et al., 2013).

2.4.2 Building overheating evaluation

After defining a heat-stress index, a threshold is needed to identify whether the environment is in a heat-stress situation. Besides, different types of heat events might result in various health effects. For example, a continuous heat event might bring cumulative heat injury inside a person, and a rapid temperature increase might lead to intense heat injury, so a method is needed to identify the pattern of a heat event. Many heat-stress indices have associated heat-stress thresholds. However, a limited number of them have been related to the patterns of heat stress situations applied to building overheating analysis.

The Chartered Institution of Building Services Engineers (CIBSE) proposed the most popular overheating criteria based on the indoor operative temperature. One way to define overheating is to identify a particular temperature above which a given proportion of people in a building vote +2 or +3 on the PMV scale (Irving et al. 2005). For bedrooms in residential buildings, the temperature should not exceed 26°C for 1% of the annual occupied hours. The temperature should not exceed 28°C for 1% of the yearly occupied hours for living rooms. Space temperature should not exceed 28°C for 1% of the annual occupied hours for school and office buildings. The other overheating criteria are based on the adaptive thermal comfort model, which gives a temperature threshold that changes with mean ambient temperature and the occupants' sensitivity. The operative temperature thresholds per building category are shown in Table 2. The T_{rm} in Table 2 means the exponentially weighted running mean of the daily mean outdoor air temperature. In Technical Memorandum 52 (TM52) (CIBSE, 2013), there are three criteria considering the deviation between the actual operative temperature in the room T_{op} and the limiting maximum acceptable temperature T_{max}, namely Hours of exceedance (H_e), Daily weighted exceedance (W_e) and Upper limit temperature (T_{upp}). A similar logic is adopted by ASHRAE 55 (ASHRAE, 2013)

to define the acceptability comfort ranges. The standard first measures comfort temperature and the acceptability ranges for three categories of people are then defined based on the comfort temperatures, as listed in Table 2-2. The T_{ref} is the monthly mean outdoor air temperature.

Table 2-2 Operative temperature benchmark thresholds

Category	Building category	Limiting maximum acceptable temperature T_{max}	
		CIBSE	ASHRAE
I	Spaces to be occupied by very sensitive and fragile persons with special requirements, such as the handicapped, sick, the very young and the elderly	$0.33T_{rm}+18.8+2$	$0.31\times T_{ref}+17.8+2$ (90% acceptability)
II	New buildings and renovations	$0.33T_{rm}+18.8+3$	$0.31\times T_{ref}+17.8+3$ (80% acceptability)
III	Existing buildings	$0.33T_{rm}+18.8+4$	$0.31\times T_{ref}+17.8+4$ (60% acceptability)

Besides the overheating criteria based on operative temperature, U.S. Green Building Council uses Standard Effective Temperature (SET) to define overheating for residential or non-residential buildings. It evaluates overheating with the resolution of one week instead of considering annual occupied hours. It requires simulation to demonstrate that a building's interior environment will maintain "livable temperatures" during a power outage that lasts seven days during the peak summertime of a typical year. Laouadi et al. (2020b) evaluated overheating in buildings with SET and defined different patterns of the heat event: duration, intensity and severity. The overheating criteria to limit the intensity and severity were developed based on the heat-related health outcomes related to maximum body dehydration and core temperature of occupants. Adaptive thermal comfort is not included in the method.

There are studies exploring further overheating event patterns. Lee (Lee and Shaman, 2017) introduced continuously overheated intervals (COIs), which account for continuous exposure duration. The interval approach will render several COIs, or stretches of time within each T_{op} remains continuously above T_{limit}. The overheating risk of a modelled building was evaluated with

COI under current and future climates. Potential overheating issues for space under evaluation can be quickly discerned in this way. Hamdy (Hamdy et al., 2017) proposed Indoor overheating degree (IOD) and Overheating escalation rate (OER) to precisely assess the thermal response of dwellings to an increase in thermal stress due to, for example, global warming and the urban heat island effect. IOD considers both the intensity and the frequency. OER represents the sensitivity of indoor overheating to climate change (caused by global warming).

The indoor climate and overheating problems under the impact of climate change were evaluated in previous research, and consistent conclusions about the increased indoor heat stress were made. Hosseini et al. (Hosseini et al., 2022) simulated the indoor climate of residential buildings in Sweden under the effects of both climate change and microclimate. A 17% rise in cooling degree-day (CDD) and a 25% increase of daily peak cooling load on an extremely warm day were found when considering microclimate. The overheating hours would increase by 140% in the future climate. Lei et al. (Lei et al., 2022) studied the current and future indoor overheating situations in bedrooms of heritage apartments in China. At least a 41% increase in overheating hours was found in 2050 compared to the current climate. Fiorito et al. (Fiorito et al., 2022) evaluated the thermal comfort in naturally ventilated historic buildings in Italy under current and future climates and found the discomfort levels would not be acceptable in the 2050 and 2080 scenarios. Escandón et al. (Escandón et al. 2022) studied the overheating situation of social housing stock in Spain. It was found that by 2050, according to the Chartered Institution of Building Services Engineers (CIBSE) criteria, 100% of social housing would be overheated due to global warming. Rahif et al. (Rahif et al., 2022) assessed the discomfort in a nearly zero-energy dwelling in Brussels and found that overheating risk would increase up to 528% by the end of this century. Dodoo (2020) studied the overheating risk and indoor thermal comfort of a modern multi-story residential building in

Sweden and found the overheating hours and Predicted Percentage of Dissatisfied (PPD) increased significantly under future climate scenarios.

2.4.3 Building thermal resilience evaluation and enhancement

Extreme heat events challenge the ability of buildings to maintain and recover to thermal comfort conditions. The evaluation and enhancement of building resilience have been important topics in recent years. To assess building resilience to heat, there is no consistent index. Many studies used the overheating evaluation metrics to indicate resilience, such as indoor temperature (Katal et al., 2019; Nicol et al., 2020), Heat Index (Flores-Larsen and Filippín, 2021), Indoor Overheating Degree (IOD) (Flores-Larsen et al., 2022), the mortality rate (Hess et al., 2018), and thermal sensation of occupants (Loughnan et al., 2015). Hatvani-Kovacs et al. (2016) proposed a more comprehensive framework to assess population heat stress resilience, involving heat stress resistance, vulnerability, and adaptation ability. Therefore, building resilience to heat is related to the whole process of disruption, absorption, and recovery, thus needs to be assessed and quantified with a more comprehensive index involving the resilience procedure and impact factors. The influential factors of building resilience were also investigated. The building design characteristics are the main impactor of building resilience to heat, including solar heat gains through the glazed balconies and low potential of natural ventilation (Schünemann et al., 2022), the social location of buildings, and occupants' access to mitigation sources (Eady et al., 2020), the age of the house, the number of air-conditioning units, the pitch of the roof, home insulation and the number of heat-mitigation modifications (Loughnan et al., 2015), building orientation, thermal mass and shading (Iddon et al., 2015).

The failure to build a tolerance to extreme heat events indicated the significant importance of applying strategies to enhance resilience. Studies have shown that the performance of resilience enhancement strategies varies with building characteristics and surrounding environments (Sun et al., 2021). Zeng et al. (2022) proposed a strategy of pre-cooling the house during off-peak hours during heatwaves, which improved the overheating problems of most of the 814 residential buildings in California, US. López-García et al. (2022) tested reducing solar heat gains and increasing ventilative cooling for residential buildings in Spain to mitigate the overheating situation assessed with real monitored data. Heracleous et al. (2021) suggested that natural ventilation and roof insulation could minimize the cooling degree hours by 96.8% of their studied school building in Cyprus. Schünemann et al. (2021) explored the impact of individual window ventilation behaviour of residents on overheating risk by comparing six window ventilation profiles applied to a multi-residential building in Germany and found that fully opened windows and room doors could reduce overheating risk significantly. The application of green roofs on buildings in Italy has been proven to have the ability to save cooling energy, improve indoor comfort and attenuate ceiling temperatures of top floors (Cirrincione et al., 2021). Sun et al. (2021) compared eleven passive cooling strategies applied to vulnerable communities in California and the US. They proved that installing solar-control window films and adding roof insulation were the two most effective measures. A review study about natural ventilation in warm climate suggested that cross ventilation performed better than single-sided ventilation, while windcatchers and solar chimneys displayed a better performance by creating higher ventilation rates (Ahmed et al., 2021). The study also recommended combining solar chimneys or windcatchers with water evaporation cooling to achieve indoor comfort as well as cooling energy saving. Mohaibesh et al. (2021) suggested to learn from the design of traditional typologies to enhance resilience by

comparing the thermal performance of traditional house and modern buildings and found the vernacular architecture and the use of thermal insulation made the traditional building more resilience to extreme weather. Therefore, quantification methods of building resilience to heat are still needed to evaluate various enhancement strategies when applying to different buildings and climates.

Chapter 3 Evaluation and Improvement of the Thermoregulatory System for the Two-node Bioheat Model

The contents of this chapter are published in "Ji, L., Laouadi, A., Shu, C., Wang, L., & Lacasse, M. A. (2021). Evaluation and improvement of the thermoregulatory system for the two-node bioheat model. Energy and Buildings, 249, 111235. https://doi.org/10.1016/j.enbuild.2021.111235 ". The contents are slightly modified.

Abstract

The two-node bioheat model is widely used in thermal comfort standards and design tools. In recent years, there have been many new experimental studies and thermoregulatory models developed under stressful heat or cold conditions, but those have not been tested under the two-node model structure. Furthermore, limited validation studies of the two-node model revealed significant discrepancies in the prediction of skin temperature. This study collects relevant thermoregulatory models (six for sweating, three for skin blood flow and shivering, and four for sweat evaporation efficiency) and devises a methodology to compare the accuracy of various model combinations against experimental data. An improved model is developed and validated under heat and cold exposure conditions. The RMSE method is used to compare the accuracy of various model combinations and to optimize the proposed thermoregulatory model constants.

3.1. Introduction

Bioheat modeling is an important approach in thermal comfort and heat stress standards in built environments to protect the health of people and maximize their performance and productivity in workplaces. Bioheat modeling predicts the dynamic physiological response of the human body

when subjected to stressful thermal conditions. A bioheat model consists of two systems: passive and thermoregulatory (active). The passive system deals with the different mechanisms of heat exchange between the human body and the environment. The thermoregulatory system deals with the physiological control mechanisms for sweating, vasodilation, vasoconstriction, and shivering. Bioheat modeling was extensively addressed in the past decades, and various one to multi-segment body models have been proposed (Havenith and Fiala, 2016). The simplest two-node model (Gagge et al., 1986) in which the human body is represented by one segment with two nodes, one for the core and one for skin layers has gained widespread popularity in engineering applications due to its simplicity, easy implementation in computer tools, and faster calculation time (Enescu, 2019). The model has been implemented in thermal comfort standards and building energy design tools (ASHRAE-55, 2017; Tartarini et al., 2020). The two-node model provides the physiological parameters required for the calculation of the standard effective temperature (SET*) index (Wang et al., 2020; Zhang and Lin, 2020). The SET* index is both a thermal comfort and heat stress index, and its thermal sensation scale was established based on the skin temperature and wettedness (Blazejczyk et al., 2012). ASHRAE (2017) uses the SET* index to compute the cooling effect of high airspeed, which is not covered in the predicted mean vote (PMV) index (developed for still air). The two-node model has as well been used and adapted to cover outdoor thermal comfort (Ooka et al., 2010). Due to its simplicity and quick calculation time, the most popular building simulation software such as EnergyPlus (DOE, 2020), ESP-r (Rida and Kelly, 2017), and TRNSYS (TEES, 2021) have implemented the two-node model and SET* index for indoor thermal comfort analysis. Furthermore, the predictions of the two-node model were consolidated by several experimental studies in the past (Doherty and Arens, 1988; Takada et al., 2011). Recently, laboratory thermal comfort and calorimetry studies on human subjects have received a renewed

interest to explore the physiological response of people under stressful heat or cold exposure (Stapleton et al., 2014; Kenny et al., 2017, 2019; Notley et al., 2020). Newer thermoregulatory models have also been developed for other bioheat models (Katić et al., 2016). It is, therefore, worthwhile to investigate the accuracy of the two-node model with various thermoregulatory models against recent experimental data and explore any further model improvements.

Gagge et al. (1971, 1986) developed the foundation of the two-node model of the whole body. The passive system of the model is based on a straightforward one-dimensional transient heat transfer from the core to the skin layer and then to the environment. However, the thermoregulatory system for sweating, skin blood flow, and shivering are based on empirical relationships developed for average (male and females) young adults. The accuracy of the empirical models, particularly the model constants, is tied to the experimental conditions, measurement quality, parameter ranges, and subject physiological differences (Havenith, 2001; Takada et al., 2011). Limited experimental validation studies of the Gagge et al. (1986) model showed indeed conflicting results. Doherty and Arens (1988) found that the model under-predicts the core temperature by 0.31°C and skin wettedness by 0.16, but overestimates the skin temperature by 0.48 °C. Similarly, Ooka et al. (2010) found the model under predicts the core temperature by up to 0.32 °C and overestimates the skin temperature by up to 0.75 °C. Furthermore, Takada et al. (2009) found the two-node model underestimates the core temperature by up to 0.5 °C and skin temperature by up to 1.8 °C under cool exposure conditions. In addition, Li et al. (2017) found that the Gagge et al. (1986) model under or over-predicts the skin temperature by 0.49 °C or 0.09 °C, respectively, for male subjects and 0.52 °C or 0.19 °C, respectively, for female subjects. However, Takada et al. (2011) found that the model provides a good estimate of the steady-state skin temperature under low-activity

(metabolic) conditions. Further improvements of the thermoregulatory system of the two-node model and validation studies of the model covering wider ranges of model inputs are therefore needed.

Several studies have addressed the improvement of the thermoregulatory system of the two-node model. Takada et al. (2009) considered personal differences of subjects in their thermoregulatory responses by adjusting six coefficients related to the regulation of sweating and skin blood flow. The six coefficients were obtained using limited sets of experimental data for young male subjects seated and wearing trunks. Ooka et al. (2010) included the effect of the metabolic rate on sweating secretion at high activity levels. Their model was validated with experimental data conducted on university-age subjects. Dongmei et al. (2012) extended the two-node model for sleeping subjects by modifying the vasomotor and sweating functions. Recent thermoregulatory models have also been developed for segmented and multi-node bioheat models (Havenith and Fiala, 2016). The thermoregulatory system is controlled either by a unified controller or by an individual controller for each effector. The unified controller uses common thresholds (thermo-neutral) for all effectors involving sweating, skin blood flow, and shivering. This was adopted by Hirata et al. (2015) and Li et al. (2017). The individual controller treats each effector as having its own threshold, which was adopted by Fiala et al. (2012), Karaki et al. (2013), Rida and Kelly (2017), and Coccarelli et al. (2018). However, the performances of these thermoregulatory models applied to the two-node structure have not been evaluated and compared yet.

The goal of this paper is to compare and improve the prediction accuracy of relevant thermoregulatory models for implementation in the two-node model structure of the whole body. The paper is structured as follows: Section 2 presents the methodology to compare the prediction accuracy of thermoregulatory models collected from literature with selected public experimental

data, and development of improved thermoregulatory models; and Section 3 presents the results of inter-mode comparison and validation of the proposed two-node model for the whole body.

3.2. Methodology

The methodology includes first a brief description of the two-node model with relevant thermoregulatory models for sweating, skin blood flow, and shivering as collected from the literature. Second, criteria to select the benchmark experiments are presented, followed by the proposed method to compare the prediction accuracy of models. Finally, an improved thermoregulatory model is proposed.

3.2.1 Description of the two-node model

The two-node model treats the human body as two concentric cylinders for the core and skin layers. The core and skin layers are represented by one node each (Figure 3-1). A uniform layer of clothing covers the skin layer throughout the body. Metabolic heat is generated at the core layer. A small portion of that heat is dissipated from respiration through convection and evaporation, and the remainder is transported by conduction and skin blood flow to the skin surface. The heat loss from the skin surface to the environment is divided into two parts: 1) the sensible heat by conduction, radiation, and convection from the skin surface to the clothing layer and then to the environment; 2) the insensible heat by the evaporation of sweat and water diffusion from the skin surface.

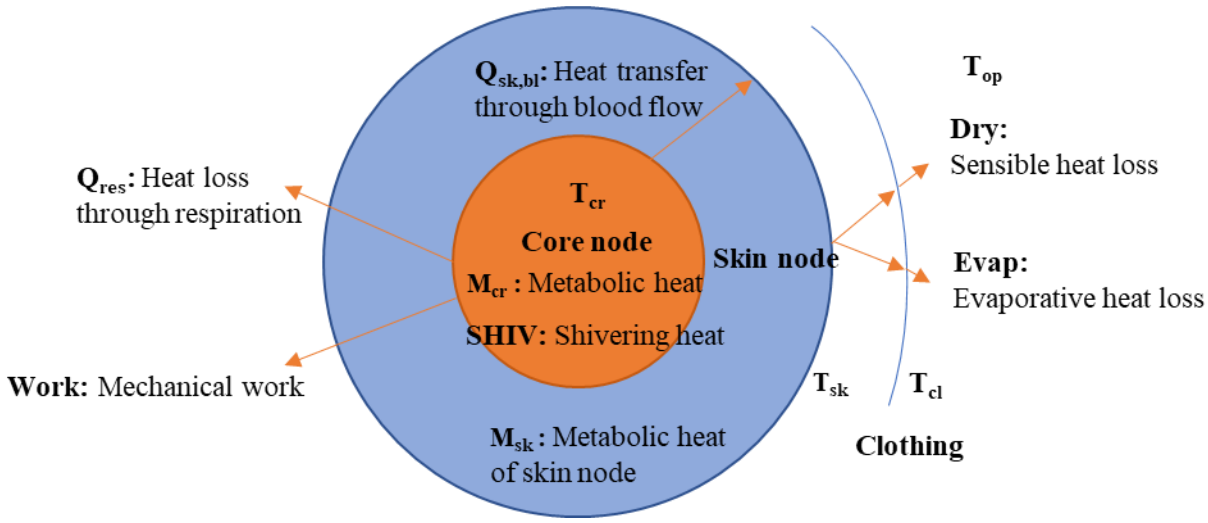

Figure 3-1 Schematic of the two-node model representation of the human body

The heat balance at the core and skin nodes is expressed as follows:

$$m_{cr}c_{cr}\frac{dT_{cr}}{d\tau}/A_b = M + SHIV - W - Q_{res} - h_{sk}(T_{cr} - T_{sk}) \quad (3\text{-}1)$$

$$m_{sk}c_{sk}\frac{dT_{sk}}{d\tau}/A_b = h_{sk}(T_{cr} - T_{sk}) - Dry - Evap \quad (3\text{-}2)$$

where m_{cr} and c_{sk} are the mass (kg) of the core and skin nodes, respectively; c_{cr} and c_{sk} are the specific thermal capacity (W/kg·°C) of the core and skin nodes, respectively; T_{cr} and T_{sk} are the core and skin node temperatures (°C), respectively; $d\tau$ is the time step (1 min); A_b is the Dubois body surface area (m^2); M is the metabolic rate (W/m^2); SHIV is the shivering metabolic rate (W/m^2); W is the mechanical work done by the body (W/m^2); Q_{res} is the heat loss through respiration (W/m^2); h_{sk} is the skin thermal conductance that accounts for the blood flow (W/m^2·°C); Dry and Evap are the sensible and evaporative heat exchanges of the skin node (W/m^2), respectively.

The sensible heat balance of the clothing layer is given by Equation 3-3,

$$\frac{1}{R_{d,air}+R_{d,clo}}(T_{sk} - T_{op}) = (h_c + h_r)(T_{cl} - T_{op}) \quad (3\text{-}3)$$

where $R_{d,air}$ and $R_{d,clo}$ are the dry thermal resistances of the air and clothing layers (m^2·°C/W), respectively, T_{op} is the operative temperature (°C), h_c is the convective heat transfer coefficient of ambient air (W/(m^2·°C)), and h_r is the radiative heat transfer coefficient (W/(m^2·°C)).

The skin evaporative heat loss (Esk) consists of the heat loss due to the regulatory sweating (SWR) and moisture diffusion (Edif) from the skin surface. The Esk is given by Equation 3-4,

$$E_{sk} = \eta_{evap} \times (0.68 \times \mathrm{SWR} + \mathrm{E_{dif}}) = w \times E_{max} \quad (3\text{-}4)$$

Where SWR is the sweating rate (g/m^2·h), w is the skin wettedness defined as the ratio of the evaporative heat flux (E_{sk}) to the maximum evaporative heat flux (E_{max}), and η_{evap} is the sweat evaporation efficiency.

3.2.2 Thermoregulatory controls

Under heat or cold conditions, the deviation of T_{cr}, T_{sk} or T_b (body temperature) from their threshold values (T_{cr0}, T_{sk0} or T_{b0}) are set as the thermoregulatory control signals. The warm signal is given by $\Delta T_w = (T - T_0)^+$ while the cold signal is given by $\Delta T_c = (T_0 - T)^+$, where '+' means the only positive value will be taken. These signals would trigger the regulatory sweating, vasodilation, vasoconstriction, and shivering. In the following section, various thermoregulatory models are selected from public literature to investigate their prediction accuracy under the two-node model structure.

a. Sweating models

Under hot exposure or high activity levels, the human body relies on sweat secretion and evaporation from the skin surface to cool and maintain its core temperature. Sweating is triggered when the core and skin temperatures exceed their threshold values.

Gagge et al. (1986) proposed a model in which the sweating rate is a function of the body and skin temperature control signals as given by Equation 3-5,

$$SWR = \text{CSW} \times \Delta T_{b,sw} \times \exp(\frac{\Delta T_{sk,sw}}{10.7}) \quad (3\text{-}5)$$

where SWR is the sweating rate (g/m^{2}h), CSW is a model constant, $\Delta T_{b,sw}$ is the body temperature control signal for sweating (°C), $\Delta T_{sk,sw}$ is the skin temperature control signal for sweating (°C). The threshold temperatures for sweating are set equal to the neutral values of $T_{b0,\text{sw}} = 36.49$°C, $T_{sk0,\text{sw}} = 33.7$°C, $T_{cr0,\text{sw}} = 36.8$°C.

Based on evidence from their own and third-party experiments that sweating rate increases with activity level at the constant core and skin temperatures, Ooka et al. (2010) modified Equation 3-5 by accounting for the effect of the metabolic rate on the sweat secretion as given by Equation 3-6,

$$SWR = \left\{\text{CSW} \times \Delta T_{b,sw} \times \exp(\frac{\Delta T_{sk,sw}}{10.7})\right\} \times [\{1 + 3 \times exp(-0.5(Met - 1))\} \times \{1 - exp(-(Met - 1))\}^2] \quad (3\text{-}6)$$

where Met is the metabolic rate in met units.

Rida and Kelly (2017) adopted the model in which the sweating threshold of the core temperature ($T_{cr0,sw}$) is not a fixed value, but calculated through a piecewise function of the skin temperature using Equation 3-7. This model stipulates that sweat secretion is delayed under cold exposure conditions when the skin temperature is lower than 33°C,

$$T_{cr0,sw} = \begin{cases} 42.084 - 0.15833 \times T_{sk};\ for\ T_{sk} < 33℃ \\ 36.85;\ for\ T_{sk} \geq 33℃ \end{cases} \quad (3\text{-}7)$$

The sweat rate is then given as a linear function of the core temperature control signal ($\Delta T_{cr,sw}$) by Equation 3-8,

$$SWR = 45.8 + 739.4 \times \Delta T_{cr,sw} \quad (3\text{-}8).$$

Hirata et al. (2015) adopted the Fiala et al. (2001) model by assuming that the sweating rate depends on the temperature elevation in the skin and core layers, as given by Equations 3-9 to 3-11,

$$SWR = \left(W_{sk} \times \Delta T_{sk,sw} + W_{cr} \times \Delta T_{cr,sw}\right) \times 2^{\frac{\Delta T_{b,sw}}{10}} \quad (3\text{-}9)$$

$$W_{sk} = \alpha_{11}\tanh\left(\beta_{11}\Delta T_{sk,sw} - \beta_{10}\right) + \alpha_{10} \quad (3\text{-}10)$$

$$W_{cr} = \alpha_{21}\tanh\left(\beta_{21}\Delta T_{cr,sw} - \beta_{20}\right) + \alpha_{20} \quad (3\text{-}11)$$

where the coefficients α (g/(min·°C)) and β (g/(min·°C)) are determined for the average sweating rate based on measurements. For people with standard sweating, the coefficients are defined as α_{10}=1.20 g/(min·°C), α_{11}=0.80 g/(min·°C), β_{10}=0.19, β_{11}=0.59 [°C -1], α_{20}=6.30 g/(min·°C), α_{21}=5.70 g/(min·°C), β_{20}=1.03, β_{21}=1.98 [°C $^{-1}$].

Li et al. (2017) proposed a model in which the gender difference is considered. The sweating threshold temperatures for the core and skin nodes are: $T_{cr0,\mathrm{sw}}$ = 36.94°C and 36.67°C for males and females, respectively; and $T_{sk0,\mathrm{sw}}$ = 34.16°C and 33.8 °C for males and females, respectively. The heat loss by regulatory sweating per body surface area (E_{rsw}) is calculated for males and females by Equations 3-12 to 3-13. In this paper, the average values for males and females are used,

$$E_{rsw}(males) = \left(223 \cdot \Delta T_{cr,sw} + 20 \times \Delta T_{sk,sw}\right)2^{\frac{\Delta T_{sk,sw}}{10}}/1.89 \quad (3\text{-}12)$$

$$E_{rsw}(\mathrm{females}) = \left(111 \cdot \Delta T_{cr,sw} + 10 \times \Delta T_{sk,sw}\right)2^{\frac{\Delta T_{sk,sw}}{10}}/1.89 \quad (3\text{-}13)$$

b. Sweat evaporation efficiency models

Sweat evaporation efficiency is also an important parameter to account for. Sweat evaporation efficiency is defined as the ratio of the evaporated sweat heat to the total secreted sweat heat (including the one by skin diffusion). In humid conditions, the sweat secreted by the human body would accumulate on the skin surface, thus raising the skin wettedness and causing sweat to start dripping off instead of evaporating. This leads to a decrease in sweat evaporation efficiency (Candas, et al. 1979). The sweating formulation of Gagge et al. (1986) assumes that all sweat is evaporated ($\eta_{evap} = 1$) before the skin wettedness reaches a critical value. However, ISO (2018) proposed a quadratic expression as a function of the skin wettedness as given by Equation 3-14,

$$\eta_{evap} = 1 - \frac{w^2}{2} \tag{3-14}$$

where η_{evap} is the sweat efficiency, and the w is the skin wittedness.

Similarly, Candas et al. (1979) experimentally found that the sweat evaporation efficiency is a function of the skin wettedness, and proposed a relationship by fitting the experimental data, as given by Equation 3-15,

$$\eta_{evap} = \begin{cases} -4.8076 \times w^3 + 8.3638 \times w^2 - 5.0536 \times w + 2; \ if \ 0.4143 \leq w \leq 1 \\ 1; \quad if \ w < 0.4143 \end{cases} \tag{3-15}.$$

Kubota et al. (2014) applied a piecewise function to calculate the sweat evaporation efficiency as given by Equation 3-16,

$$\eta_{evap} = \begin{cases} 0.37 + 0.31/w'; \ if \ 0.49 \leq w' \leq 1 \\ 1; \quad if \ w' < 0.49 \end{cases} \tag{3-16}$$

where w' is equal to the skin wettedness (w) when the evaporative efficiency is unity.

c. Skin blood flow models

The skin blood flow (SBF) is controlled by vasoconstriction and vasodilation. Vasoconstriction constricts blood vessels to decrease the SBF under cold exposure, whereas vasodilation opens them to increase the SBF under hot exposure. Vasoconstriction is triggered when the mean skin temperature is below the neutral value to decrease heat loss. Vasodilation is, however, triggered when the core temperature is above the neutral value to increase heat loss (Rida et al., 2014). During vasoconstriction or vasodilation, the SBF varies between the minimum and maximum values. The maximum vasoconstriction occurs when the mean skin temperature reaches 27.8 °C (Smith, 1991), and the maximum vasodilation occurs when the core temperature reaches 37.2 °C (Karaki et al., 2013). In the Gagge et al. (1986) model, the SBF is given by Equation 3-17:

$$\text{SBF} = (SBF_{basal} + CDIL \times \Delta T_{cr,dil})/(1 + CSTR \times \Delta T_{sk,cons}) \quad (3\text{-}17)$$

where SBF_{basal} is about 6.3 litre/m^2/hr, and CDIL and CSTR are model constants. The SBF of the human body is also limited by the maximum and minimum values, namely $SBF_{max} = 90$ litre/m^2/hr and $SBF_{min} = 0.5$ litre/m^2/hr.

Vanggaard et al. (2011) reported that arterio-venous anastomoses (AVA) play a major role in the blood circulation in the peripheral body parts. The blood circulation in the arteries and veins and blood perfusion to the skin can be modeled using the nonlinear formulation of the Avolio multi-branched model of the human arterial system (Karaki et al., 2013). According to this theory, the SBF rate is calculated by Equations 3-18 to 3-20,

$$SBF = \frac{SBF_{dil} \times SBF_{cons}}{SBF_{basal}} \quad (3\text{-}18)$$

$$SBF_{dil} = \begin{cases} SBF_{basal}; & for\ T_{cr} \leq 36.8℃ \\ \frac{T_{cr}-36.8}{37.2-36.8}(SBF_{max} - SBF_{basal}) + SBF_{basal}; & for\ 36.8℃ \leq T_{cr} \leq 37.2℃ \\ SBF_{max}; & for\ T_{cr} \geq 37.2℃ \end{cases} \quad (3\text{-}19)$$

$$SBF_{cons} = \begin{cases} SBF_{min}; \quad for\ T_{sk} \leq 10.7℃ \\ \frac{T_{sk}-10.7}{33.7-10.7}(SBF_{basal} - SBF_{min}) + SBF_{min} \quad for\ 10.7℃ \leq T_{sk} \leq 33.7℃ \\ SBF_{basal}; \quad for\ T_{sk} \geq 33.7℃ \end{cases}$$

(3-20).

Li et al. (2017) abstracted the human body as four concentric cylinders: core, muscle, fat, and skin. A central pool of blood delivers the arterial blood to the capillaries and tissues in each layer, and the blood flows back to the central pool through the veins. For the skin layer, the blood flow rate is calculated using Equations 3-21 to 3-23,

$$SBF = \frac{11.89+DL}{1+ST} \times 2^{\Delta T_{sk,dil}/10} \times \frac{A_b}{1.89} \quad (3\text{-}21)$$

$$DL = 117 \times \Delta T_{cr,dil} + 7.5 \times \Delta T_{sk,dil}; \quad \text{DL} = 0 \text{ if DL} < 0 \quad (3\text{-}22)$$

$$ST = -0.63 \times \Delta T_{cr,cons} - 0.63 \times \Delta T_{sk,cons}; \quad \text{ST} = 0 \text{ if ST} > 0 \quad (3\text{-}23).$$

d. Shivering models

When vasoconstriction is triggered under cool exposure conditions, the non-shivering thermogenesis increases metabolic heat generation. When a further decrease occurs in the core temperature under cold exposure conditions, shivering (muscle movement) is triggered as a second line of defense against cold to generate metabolic heat. Shivering occurs when the core temperature is between 35.8 °C and 37.1 °C (Smith, 1993). A resting person can increase his or her metabolic heat production by shivering about three- to fourfold (Kenney, 2012).

In the Gagge et al. (1986) model, the shivering rate is controlled by multiplicative changes of the skin and core temperature control signals as given by Equation 3-24,

$$SHIV = 19.4 \times \Delta T_{sk,cons} \times \Delta T_{cr,sh} \quad (3\text{-}24).$$

Tikuisis and Giesbrecht (1999) added body fat percentage as an attenuation factor and fitted their experimental data as in Equation 3-25,

$$SHIV = \frac{1}{\sqrt{BF}}\{155.5 \times (37 - T_{cr}) \ + \ 47.0 \times (33 - T_{sk}) \ - \ 1.57 \times (33 - T_{sk})^2\} \quad (3\text{-}25)$$

where BF is the body fat percentage (%), which varies with the subject's age.

Coccarelli et al. (2018) adopted a piecewise function to calculate the shivering rate based on a variable shivering threshold temperature as given by Equation 3-26,

$$T_{sk0,sh} = \begin{cases} 35.5; & if\ T_{cr} \leq 35.8℃ \\ -10222 + 570.9 \times T_{cr} - 7.9455 \times T_{cr}^2; & if\ 35.8℃ \leq T_{cr} \leq 37.1℃ \end{cases} \quad (3\text{-}26).$$

The shivering metabolic heat $SHIV$ is given by Equation 3-27,

$$SHIV = \begin{cases} 0; & if\ T_{sk} \leq 40 - T_{sk0,sh} \\ SHIV_{max}\left[1 - (\frac{T_{sk}-20}{T_{sk0,sh}-20})^2\right] & if\ (40 - T_{sk0,sh}) \leq T_{sk} \leq T_{sk0,sh} \end{cases} \quad (3\text{-}27)$$

where the maximum shivering rate $SHIV_{max}$ of the whole body is calculated by Equation 3-28,

$$SHIV_{max} = \frac{1}{3600}(-1.1861 \times 10^9 + 6.552 \cdot 10^7 \times T_{cr} - 9.0418 \cdot 10^5 \times T_{cr}^2) \quad (3\text{-}28).$$

3.2.3 Numerical solution procedure

The time-explicit scheme is used to solve Equations 3-1 and 3-2, where the future values of the nodal temperatures are calculated based on the present thermal state of the human body. Equations 3-1 and 3-2 are thus numerically converted as follows:

$$T_{cr,i} = T_{cr,i-1} + \left[M_{\,i-1} + SHIV_{\,i-1} - W_{i-1} - Q_{res,i-1} - h_{sk}\left(T_{cr,i-1} - T_{sk,i-1}\right)\right] \times A_b \times \Delta\tau / m_{cr}c_{cr} \quad (3\text{-}29)$$

$$T_{sk,i} = T_{sk,i-1} + \left[h_{sk}\left(T_{cr,i-1} - T_{sk,i-1}\right) - Dry_{i-1} - E_{sk,i-1}\right] \times A_b \times \Delta\tau / m_{sk}c_{sk} \quad (3\text{-}30)$$

where (i) is the index of the time step.

Figure 3-2 shows the flow chart to solve for T_{cr} and T_{sk}. The environmental parameters, physiological values, and temperature threshold values are defined in the initial step (i = 0). The

clothing surface temperature T_{cl} can be calculated iteratively at each time step as shown in the chart.

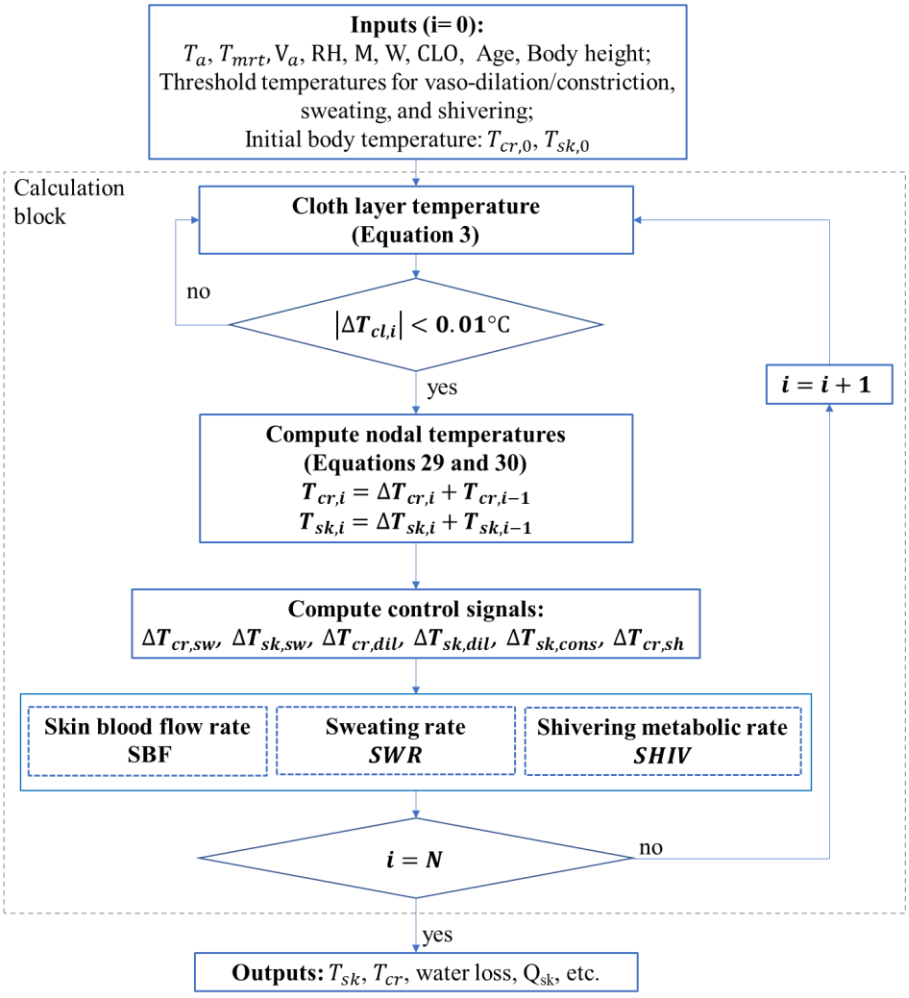

Figure 3-2 Numerical solution procedure

3.2.4 Selection of benchmark experiments

To compare the accuracy of the two-node model with the above-mentioned thermoregulatory models, benchmark experimental cases have to be collected and selected from public literature. The following screening criteria are used to select such cases:

- The experiments should be conducted in controlled climate chambers

- The experiments should cover hot and cold conditions with at least 60 min exposure time.
- Experiments should be performed on large representative numbers of young (average age) adult subjects with known characteristics (weight, height, age, clothing)
- Subjects should be un-acclimatized to warm or cold temperatures
- Measurement should include core and skin temperatures and metabolic rate with adequate accuracy

Based on the literature search, the selected experiments include: Stapleton et al. (2014) for hot exposure, Tsuzuki and Iwata (2002) for mild cold (cool) exposure, and Inoue et al. (1992) for cold exposure. For testing the sweat evaporation efficiency models, the Ooka et al. (2010) experiment with the intense sweating condition is selected. Brief descriptions of these experiments follow:

Stapleton et al. (2014) conducted laboratory experiments in a calorimeter chamber on 12 young subjects (males and females) aged below 24 years while wearing light athletic shorts and sandals. While seated, the subjects were exposed to 36.5°C and 20% relative humidity (RH) (hot-dry condition) or 36.5°C and 60% RH (hot-humid condition) for 120 min. The core temperature and skin temperature at four body locations were measured every 10 min and 30 min, respectively. The metabolic rate of subjects was continuously measured during the exposure time. Tsuzuki and Iwata (2002) conducted experiments on 100 young adults (males and females) averaged 23.5 years old while wearing cotton sweatshirts, sweat pants, and calf-length socks. The subjects were sedentary, sitting quietly, talking, and reading magazines in an environment of 23°C and 60% RH for 150 min. The core temperature and skin temperature at eight body locations were measured at an interval of 30 min and 10 min, respectively. The metabolic rate of subjects was continuously measured during the exposure time. Inoue et al. (1992) conducted experiments on nine young

adults (males) averaged 21.7 years old while wearing only swimming trunks. The subjects were sedentary, sitting quietly in an environment of 12°C and 45% RH for 60 min. The core temperature and skin temperature at nine body locations were measured at an interval of 5 min. The metabolic rate of subjects was measured three times at 10 to 20, 30 to 40, and 50 to 60 min during the exposure time. The average value was used for the simulation. Ooka et al. (2010) conducted experiments on 39 young adults (males and females) of university age (averaged 20 years old) while wearing T-shirts and short pants. The subjects were seated silently in an environment of 35°C and 70% RH for 60 min. The core temperature and skin temperature at eight body locations were obtained at an interval of 5 min. The authors did not measure the metabolic rate of subjects but estimated it according to the activity level of subjects. Table 3-1 summarizes the conditions of the five benchmark experimental scenarios.

Table 3-1 Benchmark experiment settings

Scenarios	$Ta=T_{mrt}$ (℃)	V_a (m/s)	RH (%)	M (met)	CLO	Age (year)	Height (m)	Duration (min)	Reference
1	36.5	0.25	20	0.93	0.1	24	1.7	120	Stapleton et al. (2014)
2	36.5	0.25	60	0.94	0.1	24	1.7	120	Stapleton et al. (2014)
3	23	0.2	60	1	0.63	23.5	1.652	150	Tsuzuki et al. (2002)
4	12	0.05	45	1	0.06	21.7	1.728	60	Inoue et al. (1992)
5	35	0.1	70	1	0.3	20	1.619	60	Ooka et al. (2010)

3.2.5 Model evaluation method

The two-node model combined with the selected thermoregulatory models is evaluated in terms of their prediction accuracy for the core and skin temperatures under steady-state conditions or in the last 30 min of exposure time to avoid the effects of the initial conditions, which were usually not known in most cases before experiments. The root mean square error (RMSE) method is used according to Yang et al. (2015). The RMSE is calculated for each set of node temperatures under

hot or cold exposure based on the deviation between the experimental data and model predictions. The RMSE is calculated as follows:

$$cRMSE = \sqrt{RMSE_{cr}^2 + RMSE_{sk}^2} \quad (3\text{-}31)$$

where $cRMSE$ is the combined RMSE, $RMSE_{cr}$ and $RMSE_{sk}$ are RMSE values calculated for the core and skin temperatures, respectively, of each experimental scenario.

3.2.6 Improvements of the two-node model

Given the limited accuracy of the popular Gagge et al. (1986) model as discussed in Section 3.1, the proposed model improvements deal with fine-tuning the thermoregulation model constants of the Gagge et al. (1986) model and including the influence of other control signal terms under both warm and cold exposure conditions. For sweating, the Gagge et al. (1986) model assumes the sweat secretion is controlled by the body temperature control signal with a modifying factor based on the skin temperature control signal. Other formulations assume that the sweat secretion is triggered by both the core and skin temperature control signals. A possible improvement of the Gagge et al. (1986) model would therefore include the skin control signal as the main influencer. The following model is proposed:

$$SWR = \mathrm{CSW} \times (\Delta T_{b,sw} + A_{cof} \times \Delta T_{sk,sw}) \times \exp(\frac{\Delta T_{sk,sw}}{10.7}) \quad (3\text{-}32)$$

where the added A_{cof} constant may take values between 0 and 0.5 (calculated from the Fiala et al. (2001) formulation for sweat secretion).

For the skin blood flow, the Gagge et al. (1986) model assumes a range of values for the model constants for vasodilation and constriction. However, optimizing these constants to cover a wide range of hot and cold exposure conditions has not been attempted before. The proposed model, therefore, deals with fine-tuning the values of these constants CDIL and CSTR in Equation 3-17.

(Note that we also tried to include the influence of the skin temperature control signal but found it has no influence on the skin blood flow). According to ASHRAE (2013), CDIL takes values between 50 and 225 litre/(m^2·hr·°C) and CSTR takes values between 0.25 and 0.75.

For shivering, the Gagge et al. (1986) model assumes that shivering is triggered by multiplicative control signals of core and skin nodes. In the shivering models of Tikuisis and Giesbrecht (1999), Li et al. (2017), and Coccarelli et al. (2018), shivering is triggered by additive control signals. Possible improvement of the Gagge et al. (1986) shivering model would therefore include the combination of the additive and duplicative control signals of the core and skin temperatures. The proposed model for shivering is expressed as follows:

$$SHIV = 19.4 \times \Delta T_{sh,sk} \times \Delta T_{sh,cr} + Cof_{sc} \times \Delta T_{sh,cr} + Cof_{ss} \times \Delta T_{sh,sk} \quad (3\text{-}33).$$

The added coefficients Cof_{sc} and Cof_{ss} are to be determined using the evaluation method as explained below.

The constants of the proposed models in Equations 3-17, 3-32, and 3-33 are determined by conducting a series of numerical experiments under hot and cold exposures with known experimental data. The evaluation method of Section 3.2.5 is applied to select the optimized values of the constants leading to the minimum combined $cRMSE$. Table 3-2 lists the ranges of each constant and the sampling interval for the numerical experiments. A total number of 165 possible combinations of A_{cof} and $CDIL$ are created and tested under hot exposure, and 1331 possible combinations of $CSTR$, Cof_{sc}, and Cof_{ss} are created and tested under cold exposure. The optimized values are presented in the results section.

Table 3-2 Ranges and sampling of possible constants values

Constants	Ranges	Reference	Sampling interval	Number of possible values
A_{cof}	[0, 0.5]	Fiala et al., 2001	0.05	11
$CDIL$	[50, 225]	ASHRAE, 2013	12.5	15
$CSTR$	[0.25, 0.75]		0.05	11
Cof_{sc}	[0, 50]	Tikuisis and	5	11
Cof_{ss}	[0, 5]	Giesbrecht, 1999	0.5	11

Another improvement of the Gagge et al. (1986) model is to account for the sweat evaporation efficiency. To this end, the sweat evaporation efficiency models, as presented before, are integrated into the Gagge et al. (1986) model and tested in terms of the deviation of the skin and core temperatures from the benchmark experimental data of scenario 5 (Ooka et al., 2010). The model with the lowest combined cRMSE is selected and implemented in the inter-comparison of the next section.

3.2.7 Model inter-comparison

The selected thermoregulatory models are tested under the two-node model structure. Table 3-3 lists the selected models to be evaluated.

Table 3-3. List of selected thermoregulatory models for testing

Sweating model						
S1	**S2**	**S3**	**S4**	**S5**	**S6**	**S7**
Gagge et al (1986)	Ooka et al, (2010)	Rida et al, (2017)	Hirata et al, (2015)	Li et al, (2017)	Yang et al, (2015)	Proposed
Skin blood flow model						
B1		**B2**		**B3**		**B4**
Gagge et al, (1986)		Karaki et al, (2013)		Li et al, (2017)		Proposed
Shivering model						
SHIV1		**SHIV2**		**SHIV3**		**SHIV4**
Gagge et al, (1986)		Tikuisis, (1998)		Coccarelli et al. (2018)		Proposed

The model evaluation method of Section 3.2.5 is applied to rank and select the best performing model combinations based on the minimum value of the combined RMSE (Equation 3-31). The procedure to conduct the model inter-comparison is composed of three steps, as shown in Figure 3-3. In the first step, the benchmark experimental input data are collected and divided into two categories: hot and cold exposure. The input data include: environmental conditions (air temperature, mean radiant temperature, relative humidity, airspeed, and exposure times) and subjects' data (age, weight, height, metabolic rate of activity, clothing insulation level). In the second step, all the selected thermoregulatory models are implemented in the two-node model structure. Under hot exposure, the sweating and skin blood flow models are combined to produce a total of 28 model combinations. Under cold exposure, the skin blood flow and shivering models are combined to produce a total of 16 model combinations. In the third step, simulations are run and then compared with the experimental data to calculate RMSEs. In addition to the core and skin temperatures, other outputs including skin evaporative heat loss and body water loss percentage and relative change in the skin blood flow from the neutral (basal) condition are also compared with the experimental data but are not presented in this chapter.

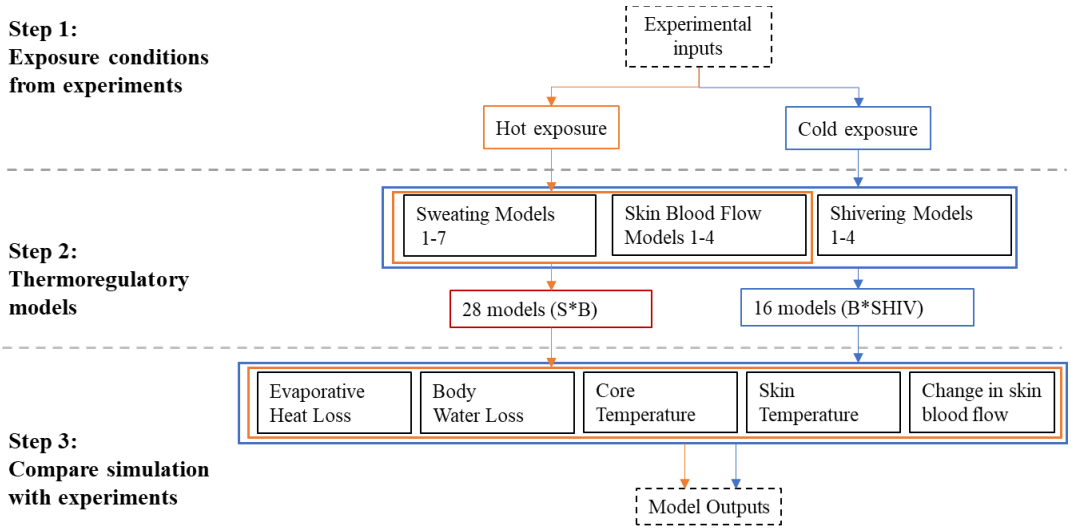

Figure 3-3 Procedure of inter-model comparison

3.3. Results

3.3.1 Sweat evaporation efficiency

Figure 3-4 shows the effect of the sweat evaporation efficiency models on the transient core and skin temperatures. The tested models are: E1-efficiency =1, E2-Equation 3-14, E3-Equation 3-15 and E4-Equation 3-16. At steady-state conditions (end of exposure time), the E4 model results in cRMSE = 0.14°C, followed by E2 (cRMSE = 0.18°C), E3 (cRMSE = 0.31°C) and E1 (cRMSE = 0.42°C). E4 and E2 are therefore regarded as the most applicable to the two-node model under intense sweating conditions.

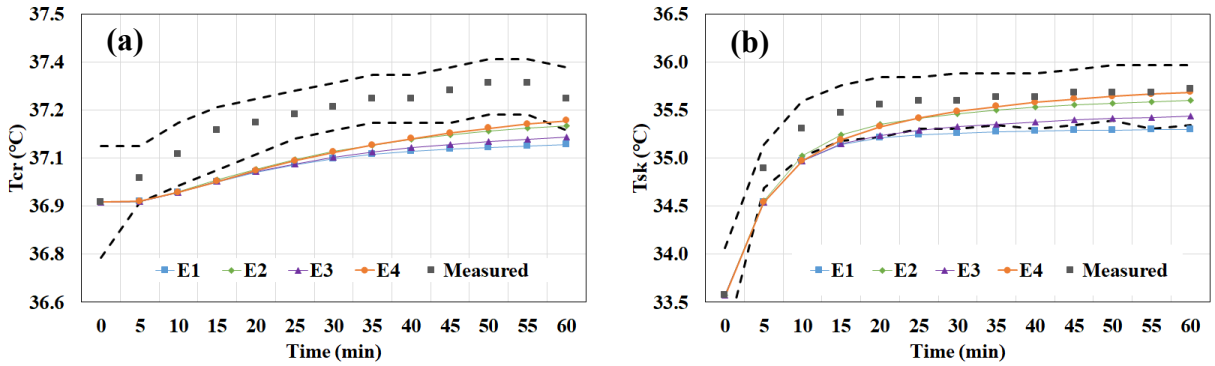

Figure 3-4 Comparison of the sweat evaporation efficiency models for the prediction of the core (a) and skin (b) temperatures using Gagge et al. (1986) model against the experimental data of Ooka et al. (2010) (dashed lines are the margins of the experimental error)

3.3.2 Proposed two-node model

The experimental data of Stapleton et al. (2014), Tsuzuki and Iwata (2002), and Inoue et al. (1992) are used for hot and cold exposure to fine-tune the model constants. The detailed settings of the experiments are shown in Table 3-1. Scenario 1 (hot-dry) and scenario 2 (hot-humid) are for hot exposure, while scenario 3 (cool) and scenario 4 (cold) are for cold exposure. The model constants

Acof and CDIL are tested under hot exposure, while CSTR, $Cof_{sc,}$ and Cof_{ss} are tested under cold exposure. Figure 3-5(a) shows the RMSE for the core and skin temperatures of the hot exposure scenarios 1 and 2 to fine-tune Acof and CDIL. With the increase of CDIL, both $RMSE_{sk}$ and $RMSE_{cr}$ increase; with the increase of Acof, the $RMSE_{sk}$ decreases whereas $RMSE_{cr}$ increases. The point (red dot in the dashed circle), which has the smallest distance to the origin point (minimum cRSME), corresponds to the optimized values of Acof and CDIL. Figure 3-5(b) shows the RMSE for the core and skin temperatures of the cold exposure of scenarios 3 and 4. With the increase of CSTR, both $RMSE_{cr}$ and $RMSE_{sk}$ decreases; with the increase of Cof_{ss}, or Cof_{sc} the $RMSE_{cr}$ decreases whereas and $RMSE_{sk}$ increases. The point (red dot in the dashed circle), which has the smallest distance to the origin point, corresponds to the optimized values of CSTR, $Cof_{sc,}$ and Cof_{ss}. Table 3-4 compares the optimized values of the proposed model constants with the original values of Gagge et al. (1986) and ASHRAE-55 (2017).

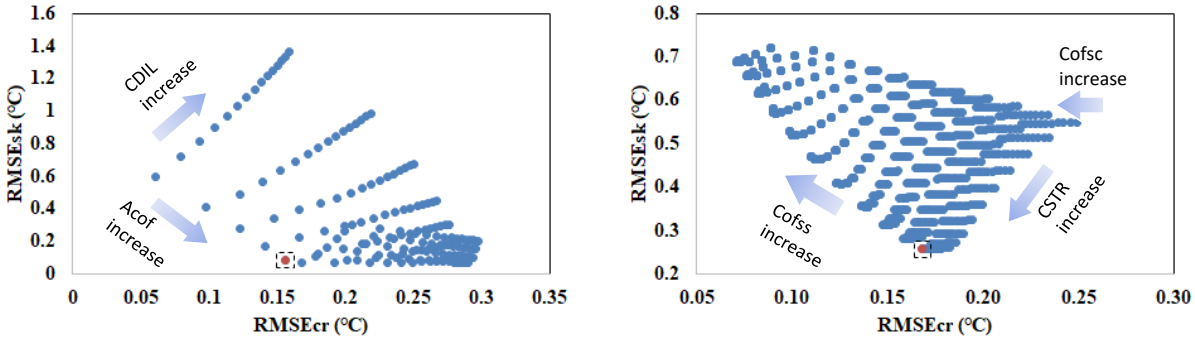

Figure 3-5 RMSE between simulations and experiments of (a) hot exposure (scenarios 1 and 2) and (b) cold exposure (scenarios 3 and 4)

Table 3-4 Comparison of model constants

Model constants	**Gagge et al. (1986) / ASHRAE(2017)**	**Proposed model**
CSW [g/(m^2·h)]	170	170
A_{cof}	0	0.2
$CDIL$ [litre/(m^2·hr·°C)]	200/120	50
$CSTR$	0.1/0.5	0.75
Cof_{sc}	0	50
Cof_{ss}	0	0.5
η_{evap}	1	Equation (3-16)

Figures 3-6 and 3-7 show a comparison between the proposed and Gagge et al. (1986) models for the predictions of the core and skin temperatures under hot and cold exposures, respectively. Under hot exposure (Figures 3-6 (a) and (b)), the Gagge et al. (1986) model overestimates the skin temperature by up to 1.25 °C, but slightly underestimates the core temperature by a maximum discrepancy of 0.18 °C. The proposed model predicts the core temperature with similar accuracy as the Gagge et al. (1986) model. However, for the skin temperature, the predictions of the proposed model are in good agreement with the experimental data with a maximum discrepancy of 0.11 °C. Under cold exposure (Figures 3-7 (a) and (b)), the Gagge et al. (1986) model again overestimates the skin temperature by up to 1.06 °C, and underestimates the core temperature by up to 0.43 °C. The predictions of the proposed model are, however, in good agreement with the experimental data with a maximum discrepancy of 0.31 °C for the skin temperature and 0.19 °C for the core temperature.

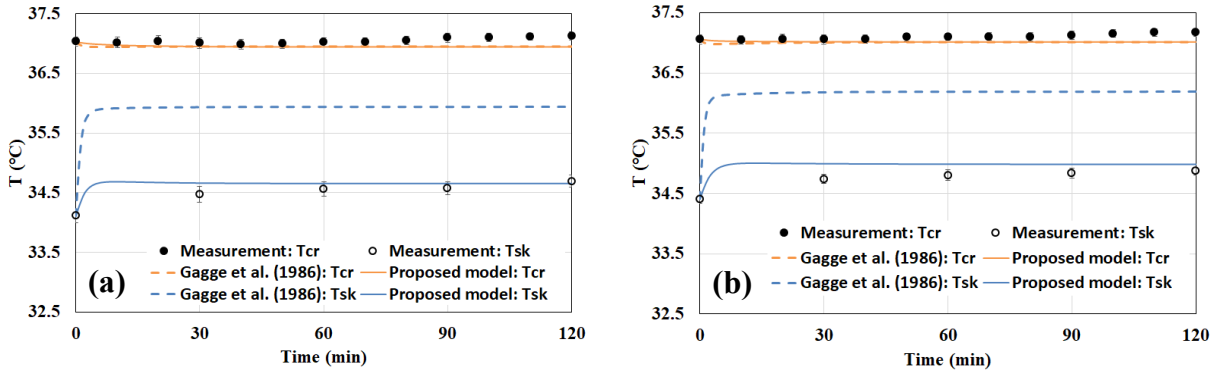

Figure 3-6 Comparison of the Gagge et al. (1986) and proposed models with experimental data for the prediction of the core and skin temperatures under (a) hot-dry scenario 1 and (b) hot-humid scenario 2.

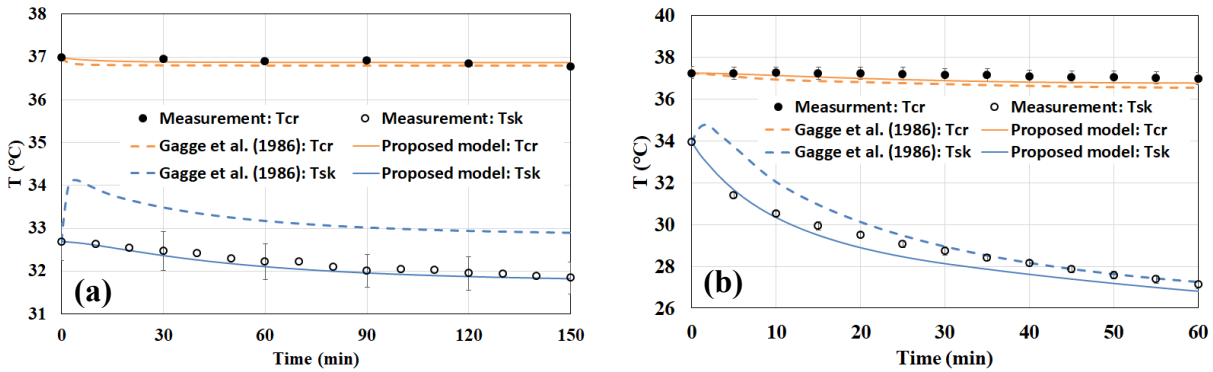

Figure 3-7 Comparison of the Gagge et al. (1986) and proposed models with experimental data for the prediction of the core and skin temperatures under (a) cool scenario 3 and (b) cold scenario 4.

3.3.3 Inter-model comparison

The model combinations as shown in Figure 3-3 are simulated for the experimental scenarios of Table 3-1 (Scenarios 1-4). The sweat evaporation efficiency model E4 is included in all model combinations, except for the Gagge et al. (1986) model (S1B1).

Figure 3-8 shows the cRMSE of each model combination under hot exposure conditions (scenarios 1 and 2) ranked in ascending order. The proposed model (S7B4) has the smallest cRMSE of 0.18

°C, followed by S4B4 and S3B4 (0.22 °C). If the model accuracy is cut off by cRMSE < 0.4 °C (corresponding to 0.1°C and 0.39 °C uncertainties in the core and skin temperatures, respectively), six model combinations (S7B4, S4B4, S3B4, S7B3, S4B3, S7B1) will qualify for the accurate predictions of both the core and skin temperatures. However, the model combinations with higher cRSME can be regarded as accurate for the prediction of either the skin temperature or the core temperature, or not accurate at all for both temperatures. An example of a model that predicts the core temperature with better accuracy than skin temperature is the Gagge et al. (1986) model (S1B1), which produces a cRMSE of 1.32 °C (RMSEcr = 0.15 °C, RMSEsk = 1.31°C). Besides yielding the best model combinations for the accurate prediction of the core and skin temperatures, the cRMSE comparison method is as well useful to indicate which best skin blood flow model can be combined with each sweating model or vice versa to produce the best results. In this regard, all the sweating models produce the best results if they are combined with the proposed skin blood flow model (B4). Similarly, all the skin blood flow models produce the best results if they are combined with the proposed sweating model S7.

Given these results, the proposed sweating model S7 is, therefore, the most accurate model, followed by S4 and S3 (cRMSE < 0.4°C). The accuracy of the sweating models S1, S2, and S6 depends on the combined skin blood flow model, resulting in intermediate accuracy levels (0.4°C < cRMSE < 0.8 °C) if combined with B4, or significantly lower accuracy levels (cRMSE > 0.8°C) if combined with other skin blood flow models. Sweating model S5 produces higher uncertainty (cRMSE > 0.8°C) with any skin blood flow model, and therefore it is not recommended for integration in the two-node model. The four skin blood flow models B1-4 may produce high accuracy levels, particularly if they are combined with the proposed sweating model S7.

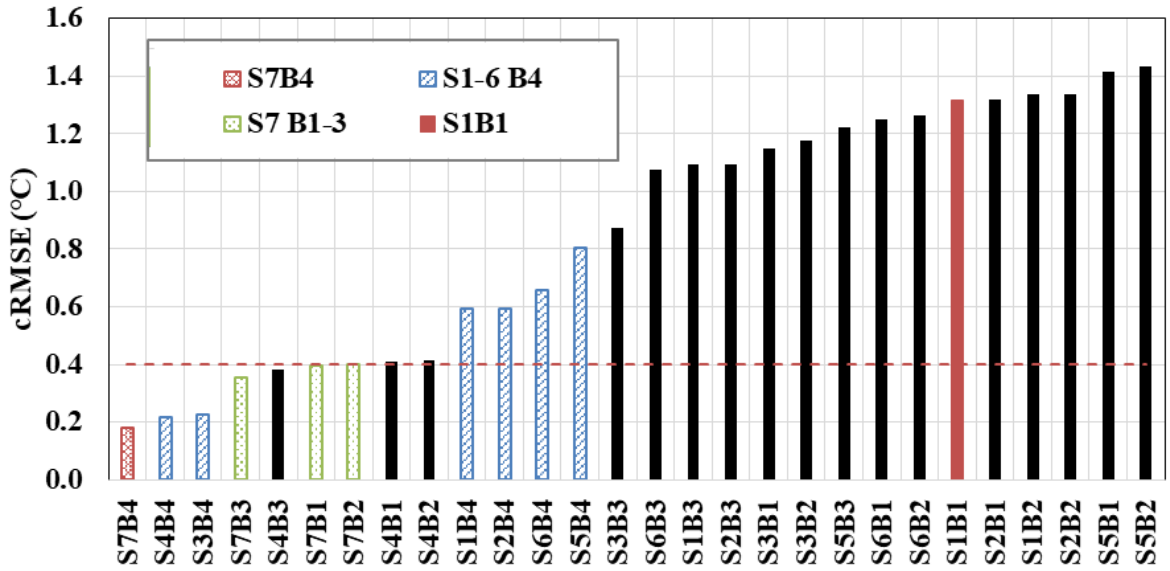

Figure 3-8 cRMSE of combinations of sweating models (S1-7) with skin blood flow models (B1-4) under hot exposure conditions (scenarios 1 and 2) for the prediction of the core and skin temperatures

Figure 3-9 compares all the sweating models combined with the best skin blood flow model (S1-7B4) for the predictions of the core and skin temperatures under hot-humid exposure conditions (scenario 2). The core temperature predictions of the model S5B4 are the closest to the measurement data, with a discrepancy of $\Delta T = 0.007$ °C at the end of exposure time, followed by S6B4 (0.05°C) and S2B4 (0.06°C). However, their predictions for the skin temperature have higher discrepancies of 0.79°C (S5B4), 0.63°C (S6B4), and 0.58 °C (S2B4). The skin temperature predictions of the proposed model S7B4 are the closest to the measurement data, with a discrepancy of 0.12 °C at the end of exposure time while the maximum discrepancy for the core temperature is 0.15 °C.

Figure 3-10 compares all the skin blood flow models combined with the best sweating model (S7B1-4) to predict the core and skin temperatures under hot-humid exposure (scenario 2). The

predictions of the proposed model S7B4 are the closest to the measurement data, followed by S7B3 and S7B2 (or S7B1). The predictions of S7B2 and S7B1 models have discrepancies of 0.36°C and 0.34°C for the core and skin temperatures, respectively.

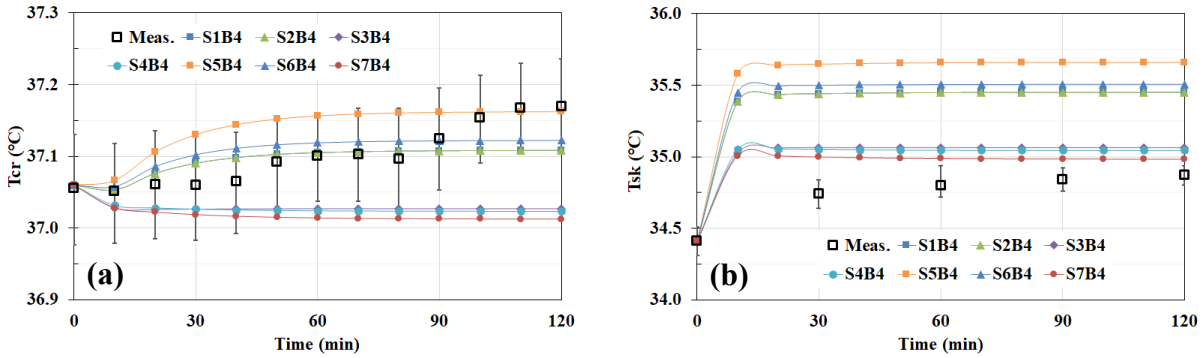

Figure 3-9 Comparison of sweating models (S1-7) combined with the best skin blood flow model (B4) for the predictions of the (a) core and (b) skin temperatures under scenario 2.

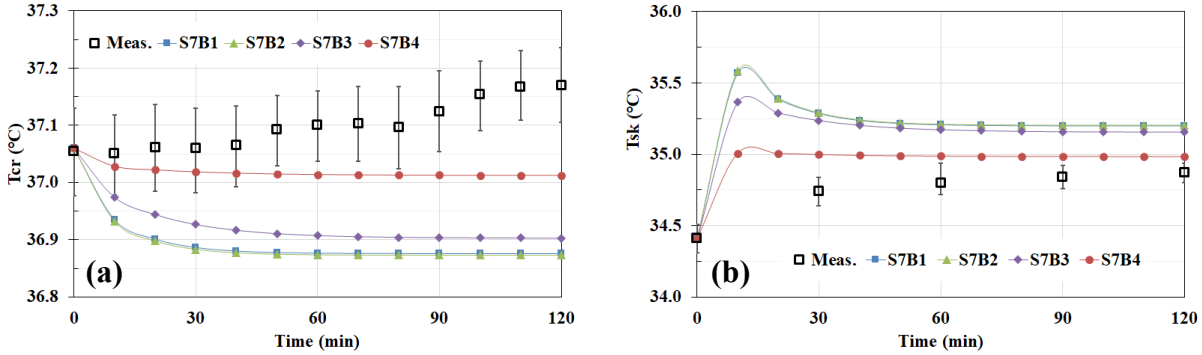

Figure 3-10 Comparison of the skin blood flow models (B1-4) combined with the best sweating model (S7) for the predictions of the (a) core and (b) skin temperatures under scenario 2.

Figure 3-11 shows the cRMSE of each combination of shivering models (SHIV1-4) with the skin blood flow models (B1-4) for the prediction of the core and skin temperatures under cold exposure conditions (scenarios 3 and 4) ranked in ascending order. The proposed model B4SHIV4 has the smallest cRMSE of 0.30°C, followed by B3SHIV4 (cRMSE = 0.31°C), and B3SHIV1 (cRMSE =

0.32°C). If the model accuracy is cut-off by cRMSE < 0.5°C, only a few model combinations (B4SHIV4, B4SHIV3, and B4SHIV1) will qualify to accurately predict both the core and skin temperatures. Gagge et al (1986) (S1B1) produces an intermediate accuracy with a cRMSE of 0.78 °C. The proposed skin blood flow model B4 produces the best results when it is combined with each shivering model. Similarly, the proposed shivering model SHIV4 produces the best results if it is combined with each skin blood flow model.

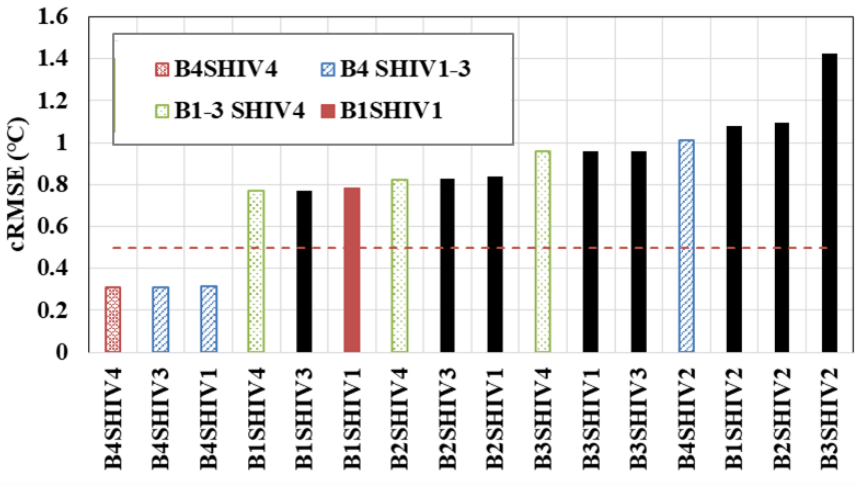

Figure 3-11 cRMSE of combinations of shivering models (SHIV1-4) with skin blood flow models (B1-4) under cold exposure conditions (scenarios 3 and 4) for the prediction of the core and skin temperatures.

In view of these results, the proposed skin blood flow model B4 is therefore the most accurate model (cRMSE < 0.4 °C), followed by B1 and B2 (intermediate accuracy; 0.4 °C < cRMSE < 0.8 °C), and B3 (low accuracy; cRMSE > 0.8 °C). Likewise, the shivering models SHIV1, SHIV3, and SHIV4 are considered as accurate models for the prediction of the core and skin temperatures, particularly when they are combined with the proposed skin blood flow model B4. However, the shivering model SHIV2 (which is adopted in ASHRAE, 2013) is in the last ranks when it is

combined with all the skin blood flow models with cRMSE > 1°C, and it is therefore not considered as an accurate model.

Figure 3-12 compares all skin blood models combined with the best shivering model (B1-4SHIV4) and all shivering models combined with the best skin blood flow models (B4SHIV1-4) for the predictions of the core and skin temperatures under cool exposure conditions (scenarios 3). The core temperature predictions of the models B1-2SHIV4 are the closest to the measurement data, with a discrepancy of $\Delta T = 0.03$ °C at the end of exposure time, followed by B4SHIV4, B4SHIV1, and B4SHIV3 with approximately the same uncertainty level (~0.09 °C). However, B4SHIV4, B4SHIV1, and B4SHIV3 perform the best for the skin temperature prediction, with a discrepancy of 0.01 °C at the end of the exposure time. Models B1-2SHIV4 produce higher discrepancies of 1.06 °C. The models of B4SHIV4, B4SHIV1, and B4SHIV3 are therefore considered as the best models for the predictions of the core and skin temperatures under cool exposure scenario 3.

Figure 3-13 compares the models B1-4SHIV4 and B4SHIV1-4 for the predictions of the core and skin temperatures under cold exposure conditions (scenarios 4). The models that produce the best predictions with a discrepancy $\Delta T < 0.2$ °C for the core temperature at the end of the exposure time are in order B3SHIV4, B4SHIV4, B4SHIV1, and B4SHIV3. The models that produce the best predictions with a discrepancy < 0.3 °C for the skin temperature at the end of exposure time are in order B3SHIV4, B1SHIV4, B4SHIV4, and B4SHIV3. The proposed model B4SHIV4 is, therefore, among the first ranked models under this cold exposure scenario 4. Considering both exposure scenarios 3 and 4, the proposed model B4SHIV4 produces the best and reliable results for predicting the core and skin temperatures.

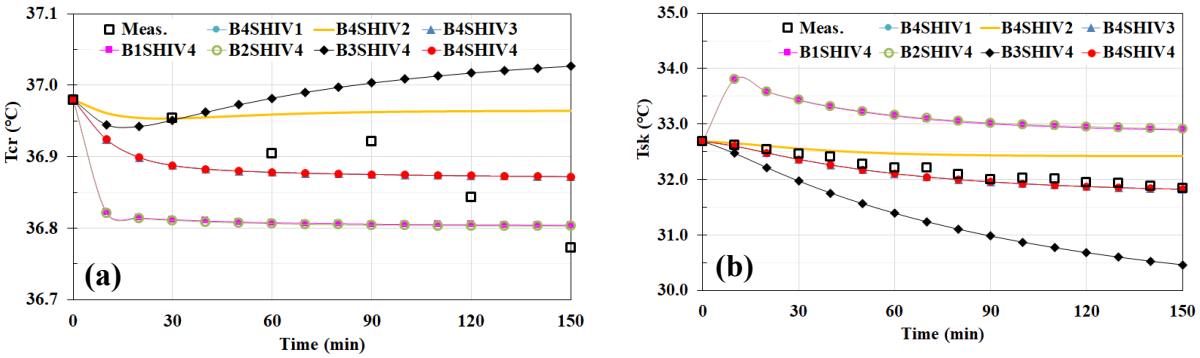

Figure 3-12 Comparison of model combinations (B1-4SHIV4, B4SHIV1-4) for the predictions of the (a) core and (b) skin temperatures under cool exposure conditions of scenario 3.

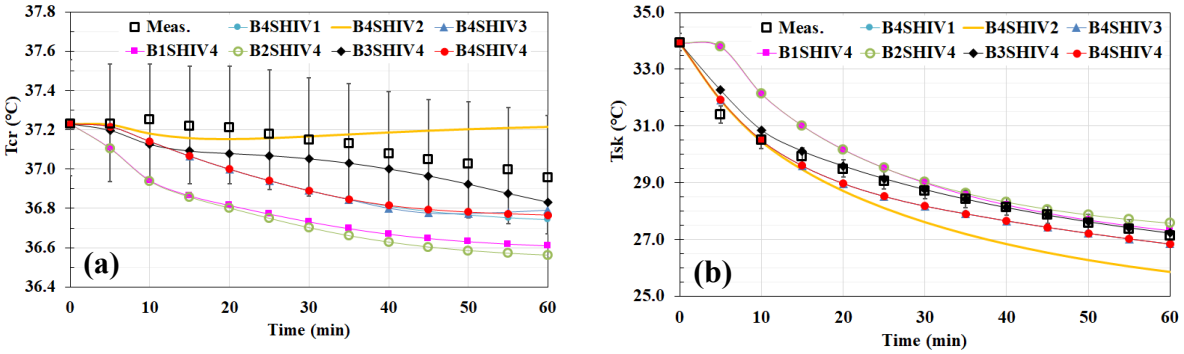

Figure 3-13 Comparison of model combinations (B1-4SHIV4, B4SHIV1-4) for the predictions of the (a) core and (b) skin temperatures under cold exposure conditions of scenario 4.

Based on the results of Figures 3-8 to 3-13 for hot and cold exposures, the common skin blood flow model for the accurate prediction of the core and skin temperatures under hot and cold exposures is the proposed model B4. Furthermore, these models can be ordered by the prediction accuracy (cRMSE < 0.4 °C): S7B4SHIV4, S4B4SHIV4, S3B4HSIV4, S7B4SHIV3, S4B4SHIV3, S3B4HSIV3, S7B4SHIV1, S4B4SHIV1, S3B4HSIV1. The less accurate models (0.4 °C < cRMSE < 0.8 °C) should be used with caution since they may under or over-estimate either the core or skin temperature. The rest of the models should be avoided due to their lower accuracy (cRMSE > 0.8 °C).

3.3.4 Additional validation of the proposed model

The proposed model is further validated using other experimental studies with wider ranges of the input parameters. Based on the screening criteria of Section 2.4, additional experiments of Ooka et al. (2010) under hot exposure conditions and Inoue et al. (1992) under cold exposure conditions are used for the validation. Four experimental scenarios (6-9) are therefore added for the validation study, as shown in Table 3-5.

Table 3-5 Experimental conditions of scenarios 6-9

Scenarios	Ta=T_{mrt} (°C)	V_a (m/s)	RH (%)	M (met)	CLO	Age (year)	Height (m)	Duration (min)	Reference
6	35	0.1	50	1	0.3	20	1.619	60	Ooka et al. (2010)
7	35	0.1	50	2	0.3	20	1.619	45	Ooka et al. (2010)
8	40	0.1	50	1	0.3	20	1.619	60	Ooka et al. (2010)
9	17	0.05	45	1	0.06	21.7	1.728	60	Inoue et al. (1992)

Figures 3-14 and 3-15 show a comparison between the proposed model predictions and experimental data for the transient mean skin and core temperatures under the hot exposure scenarios 5-8. The model predictions are within the experimental error ranges and are in good agreement with the experimental data with maximum discrepancies of 0.19 °C and 0.52 °C for the core and mean skin temperatures, respectively.

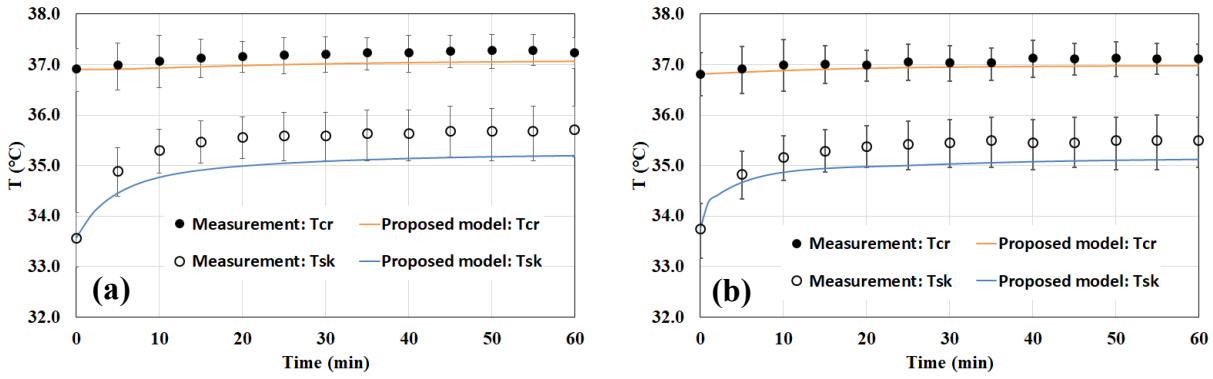

Figure 3-14 Comparison of the proposed model predictions with the experimental data for the core and skin temperatures under hot exposure of (a) scenario 5 and (b) scenario 6.

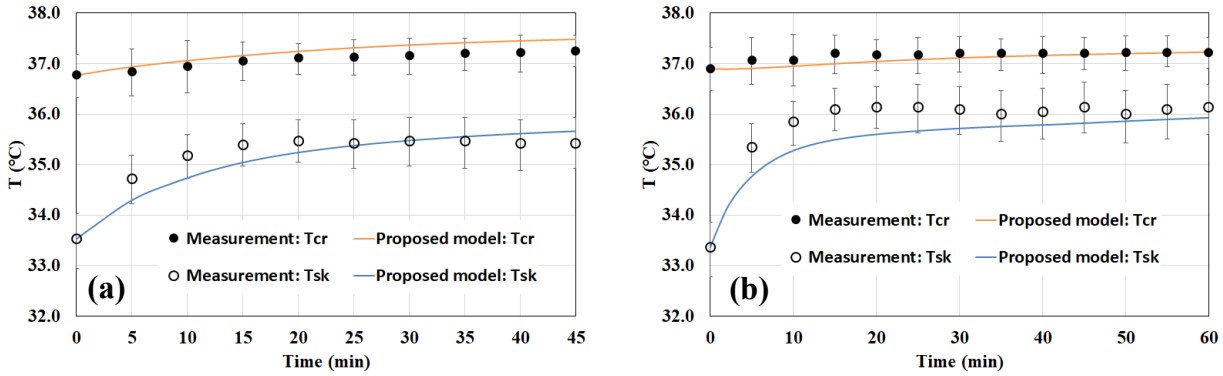

Figure 3-15 Comparison of the proposed model predictions with experimental data for the core and skin temperatures under hot exposure of (a) scenario 7 and (b) scenario 8.

Figure 3-16 shows a comparison between the proposed model predictions and the experimental data for the transient mean skin and core temperatures under the cold exposure scenario 9. The model predictions are again in good agreement with the experimental data with maximum discrepancies of 0.11 °C and 0.54 °C in the core and mean skin temperatures, respectively.

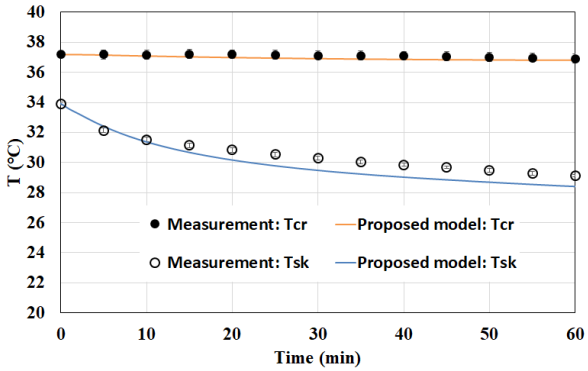

Figure 3-16 Comparison of the proposed model predictions with the experimental data for the core and skin temperatures under cold exposure of scenario 9.

3.4. Discussion

The results of Figure 3-4 reveal that the sweat evaporation efficiency should be accounted for in heat stress standards (e.g., ISO 7933, 2018) that are based on bioheat models, particularly under intense sweating conditions (wettedness close to the critical value of 0.85 resulting from high activity levels with metabolic rate > 1 met) or hot and humid conditions. The effect of the sweat evaporation efficiency is more perceptible for the skin temperature than the core temperature. If not accounted for, the skin temperature will be under-predicted (by at least 0.5°C), and consequently the heat transfer from the skin surface to the environment and body dehydration (water loss) will be under-predicted. For situations where the sweating is not intense (slightly warm or warm sensation with wettedness lower than 0.5), the effect of the sweat evaporation efficiency is not significant.

The results of the inter-model comparison showed that combinations of various thermoregulatory models for sweating, skin blood flow, and shivering may lead to different accuracy levels. A few or several model combinations may result in acceptable accuracies for the prediction of the core and skin temperatures, but many of them produce high uncertainties, and therefore they should be avoided in bioheat modeling. This substantiates the need to further improve such thermoregulatory models for better accuracy. The proposed approach to improve such models under the two-node model structure proved to be effective and lead to the best two-node model that can predict the core and skin temperatures with high accuracy under heat and cold exposures with wide ranges of input parameters. This improved and experimentally validated model is recommended for use in thermal comfort and heat stress metrics that are based on simple (two-node) bioheat modeling, namely:

- Update the Gagge et al. (1986) model for the calculation of the standard effective temperature (SET) of ASHRAE-55 (2017) with its online tool (Tartarini et al., 2020).
- Update the predicted heat strain (PHS) model of ISO 7933 (2018). The PHS model is not based on bioheat modeling and is valid only under constant environmental conditions (not accurate under alternating cool and warm conditions (Havenith and Fiala, 2016; Laouadi et al., 2020b; Lundgren-Kownacki et al., 2017; Ooka et al., 2010).
- Update the thermoregulatory models of future editions of the Handbook of Fundamentals of ASHRAE (2017).
- Implement the improved model in building simulation software to perform thermal comfort and overheating analysis in built environments.

3.5. Conclusion

In this study, recently published thermoregulatory models for sweating (six models), skin blood flow (three models), shivering (three models), and sweat evaporation efficiency (four models) were collected and an approach was developed to evaluate their accuracy under the two-node bioheat model structure against benchmark experimental data. A new two-node model with an improved thermoregulatory system was developed and extensively validated using experimental data covering hot and cold exposure conditions. The benchmark experimental data were selected from public literature through a list of screening criteria to ensure the measurement data were of high quality and suitable for use in the two-node model.

The root mean square error (RMSE) method of two variables was used to compare various model combinations for the prediction of the core and skin temperatures under scenarios of hot and cold exposure conditions. The proposed model improved the thermoregulatory system of the two-node

model of Gagge et al. (1986) by including additional temperature control signals and optimizing the values of the model constants against the selected experimental data for hot and cold exposure conditions. The RMSE method was used to carry out the optimization in which the values of the model constants were sampled from reasonable ranges to cover all possible cases. The values of the model constants that resulted in the lowest combined RMSE values for the prediction of the core and skin temperatures were chosen. The model was further validated by comparing its predictions for the core and skin temperatures with additional experimental data covering wider ranges of input data.

The comparison of the sweat evaporation efficiency models against experimental data revealed that the efficiency affects to a greater extent the skin temperature (by more than 0.5 °C) than the core temperature under intense sweating conditions. The models of Kubota et al. (2014) and ISO 7933 (2018) produced the best results.

The inter-model comparison, including the proposed thermoregulatory models, showed that only several model combinations can be considered as accurate for the prediction of the core and skin temperatures under hot and cold exposure conditions. These models include, in order of accuracy: S7B4SHIV4, S4B4SHIV4, S3B4HSIV4, S7B4SHIV3, S4B4SHIV3, S3B4HSIV3, S7B4SHIV1, S4B4SHIV1, and S3B4HSIV1, from which the proposed models (S7, B4, and SHIV4) were found to be the most accurate in predicting the core and skin temperatures. Other model combinations may be considered as accurate for the prediction of the core temperature or the skin temperature or not accurate at all for both temperatures.

The extensive validation study of the proposed model under a wide range of input data of hot and cold exposure conditions supports the belief that the proposed model should be integrated into thermal comfort and thermal (heat and cold) stress standards and design tools, including the

ASHRAE thermal comfort online tool (Tartarini et al., 2020), ISO 7933 (2018) standard, and building energy simulation software to permit carrying out thermal comfort calculations and overheating analysis in built environments.

Chapter 4 Development of a Bioheat Model for Older People under Hot and Cold Exposures

The contents of this chapter are published in "Ji, L., Laouadi, A., Wang, L., & Lacasse, M. A. (2022). Development of a bioheat model for older people under hot and cold exposures. Building Simulation. https://doi.org/https://doi.org/10.1007/s12273-022-0890-3 ". The contents are slightly modified.

Abstract

Physiological modeling is important to evaluate the effects of heat and cold conditions on people's thermal comfort and health. Experimental studies have found that older people (above 65-year-old) undergo age-related weakening changes in their physiology and thermoregulatory activities, which makes them more vulnerable to heat or cold exposure than average aged young adults. However, addressing the age-related changes by modeling has been challenging due the wide variability in seniors' physiology and thermoregulatory characteristics. This study develops a two-node physiological model to predict the thermal response of older people. The model is built on a newly developed two-node model for average-age young adults by accounting for the age-related attenuation of thermoregulation and sensory delays in triggering thermoregulatory actions. A numerical optimization method is developed to compute the model parameter values based on selected benchmark data from the literature. The proposed model is further validated with published measurement data covering large input ranges. The model predictions are in good agreement with the measurements in hot and cold exposure conditions with a discrepancy 0.60 ℃ for the mean skin temperature and of 0.30 ℃ for the core temperature. The proposed model can

be integrated into building simulation tools to predict heat and cold stress levels and the associated thermal comfort for older people in built environments.

4.1. Introduction

Physiological models for the human body are essential to studying heat and cold effects on people's thermal comfort and health in built environments. Under heat or cold exposure, occupants can adapt to the imposed conditions through thermoregulatory controls of sweating, vasodilation, vasoconstriction, and shivering. However, thermoregulation efficiency declines with age (Van Hoof et al., 2017; Balmain et al., 2018). Older people (above 65 years old) may experience delayed and weakened vasodilation/constriction, sweating, shivering, and lower metabolism and cardiac output (blood volume), making them more vulnerable to succumb to heat or cold events. (Rida et al., 2014; Hirata et al., 2015). Meanwhile, the world population aging process has been escalating: the number of people aged 60 years and over was tripled in the last 50 years and is expected to reach over 2.1 billion in the next thirty years; the aged population currently reaches the highest level in human history (Issahaku and Neysmith, 2013; Mba, 2010). In Canada, the senior population reached over 6 million in 2014, 15.6% of Canada's population, and is expected to surpass 9.5 million, making up 23% of Canadians (Government of Canada, 2014). Therefore, the senior population should receive great attention and adequate care, especially for their physiological responses under stressful hot and cold conditions. Unfortunately, current heat/cold stress and thermal comfort standards in built environments for older people are limited (Zhao et al., 2020), and therefore more research efforts are needed. Experimental studies on older people showed that they were less sensitive than young people to changes in the operative temperature (between 21°C and 31°C). This was explained by the increased thermal detection thresholds caused

by reduced skin innervation and vascular supply (Guergova and Dufour, 2011; Xiong et al., 2019). In both moderate temperature drift (17℃ to 25℃) and steady-state (21.5℃) conditions, older people felt cooler than young people and showed more distal vasoconstriction (Schellen et al., 2010). Another experimental study showed that older and young people have similar thermal sensation, comfort, and acceptability in near-neutral environments (20℃ and 25℃) (Soebarto et al., 2019). The above studies indicate that older people's thermal sensations are related to their thermoregulation to different environments (Tejedor et al., 2020).

Table 4-1 Experimental studies on age-related weakening of thermoregulatory activities

Physiological parameter	References	Exposure Condition	No. of subjects	Age	Activity	Age-related Changes
Metabolic rate	Tsuzuki and Ohfuku (2002)	Cool to hot	109	72.4±5.3	Sedentary	**-30%**
	Van Pelt *et al.* (2002)	Room temperature	166	66±4	Sedentary Exercise	**-12.5% to -16.4%**
	Frisard *et al.* (2007)	Room temperature	49	60-74	Sedentary	**-8% (±5%)**
			74	>90	Sedentary	**-27% (±5%)**
	Stapleton *et al*. (2014)	Hot	12	65±5	Sedentary	**no changes**
Vasodilation	Kenney and Havenith (1993)	Hot	34	49-74	Sedentary Exercise	**-24 to -41%**
	Pierzga *et al*. (2003)	Hot	12	64-75	Sedentary	**-33%**
Maximum SBF	Holowatz and Kenney (2010)	Hot	/	65-85	Sedentary	**-50%**
	Kenney and Havenith (1993)				Sedentary	
Vasoconstriction	DeGroot and Kenney (2007)	Mild cold	36	65-89	Sedentary	**+25% to +50%**
Minimum SBF	Fox *et al.* (1977)	Cold	47	65-90	Sedentary	**50%**
	Waller and Maibach (2005)				Sedentary	
Whole-body sweating rate	Sagawa *et al.* (1988)	Hot	6	61-73	Sedentary	**-22(±6%)**
	Inoue (1996)	Hot	8	65-70	Sedentary	**-17% (±10%)**
	Andersen (1996)	Hot	9	73.9±4.8	Sedentary	**-24% (±6%)**
	Inbar *et al.* (2004)	Hot	8	71±1.0	Sedentary	**-25% (±2.7%)**
	Inoue *et al.* (1999)	Hot	5	67±3	Exercise	**-25% (±1.5%)**
	Larose *et al.* (2013)	Hot	16	56-70	Exercise	**-12% (±0.4%)**
Shivering rate	Kenney and Buskirk (1995)	Cold	40	70	Sedentary	**-20%**
	Andersen (1996)	Cold	9	73.9±4.8	Sedentary	**-23%**
	Sessler (2008)	/	8	89±7	Sedentary	**-10%**
	Haman *et al.* (2010)	/	/	/	Sedentary	**decrease**

To further explore the mechanisms of thermoregulation changes with age, more experimental studies in climatic chambers are reviewed to provide supportive evidence to the modeling work. Public studies on age-related physiological changes of a human body are divided into two categories: (1) weakening of thermoregulatory activities; and (2) sensory delays in triggering thermoregulatory actions. The weakened thermoregulatory activities include basal metabolism, skin blood flow, sweating, and shivering. Many experimental studies have found that older adults' metabolic rate is lower than young adults but with considerable variability amongst older people. Changes in metabolism are attributed to decreased lean body mass (muscles) and water content and increased body fat (Elmadfa and Meyer, 2008). The experiment study of Tsuzuki and Ohfuku (2002) showed that the metabolic rate of older people could be as low as 30% compared to young people in a sedentary position. The ability to adjust the skin blood flow is also attenuated during vasodilation and vasoconstriction. This is due to two mechanisms: First, the redistribution of the cardiac blood output from body organs to the skin layer to dissipate internal heat or reduce internal heat loss is impaired in older people; and Second, the sensitivity and responses of the vasodilator and vasoconstrictor system are attenuated compared to young adults (Balmain et al., 2018). As a consequence, during vasodilation, the skin blood flow is reduced in older people by up to 30%, as reported in Holowatz and Kenney (2010). During vasoconstriction, older people experience, however, higher skin blood flows (Kenney & Munce, 2003). DeGroot and Kenney (2007) conducted experiments on more than 36 older subjects under mild cold stress conditions and found that the skin blood flow was higher by 25 to 50% than young subjects. Older people also experience a decrease in sweating due to the impairment of the eccrine sweat gland receptors and sweat gland outputs (Akbari Rad et al., 2016; Balmain et al., 2018). The experiment of Larose et al. (2013) on 85 people aged between 20 and70 years old during exercise found that the whole body sweat rate

of older people (56-70 years old) was reduced by about 12% compared to young adults. Likewise, the shivering metabolic rate is diminished for older people due to decreased lean body mass (muscles) (Frank et al., 2000). The experiments of Anderson et al. (1996) under cold conditions showed that the shivering metabolic rate was about 23% lower in the older group than the young group. More experimental studies addressing age-related weakening in metabolism, vasodilation, vasoconstriction, sweating, and shivering are summarized in Table 4-1.

For the second category, published studies on sensory delay signals of older people show considerable variability. The human body includes temperature sensors distributed in the skin layer and hypothalamus and built-in temperature threshold values to trigger thermoregulation actions. With aging, the sensitivities of these sensors are significantly reduced, putting older people at potential health risk of hyper or hypothermia. For the skin blood flow control of older people, vasodilation and vasoconstriction are triggered using signals from the skin and core (hypothalamus) temperature sensors. The experiment of Greaney et al. (2020) on 26 older and young people under passive heating showed that the core temperature threshold for vasodilation was increased by 0.5℃. The experiment of Ozaki et al. (1997) showed that the threshold skin temperature for vasoconstriction of older people was delayed by up to 1.6°C. Similarly, older people show a large variability of temperature threshold values to trigger sweating. Sweating regulation is triggered by both the skin and hypothalamus sensors. Dufour and Candas (2007) found up to a 2 ℃ increase in the threshold skin temperature for the sweating of older people. Experimental studies found that the null zone (the difference between sweating and shivering temperature thresholds) of older people is larger than young adults. For older people, the null zone is 1.12 °C, whereas the one for young adults is 0.43°C (Appenzeller et al., 1999). Non-shivering thermogenesis for both older and young people starts with vasoconstriction (Sessler, 2008).

However, the shivering thermogenesis of older people starts at lower skin and core temperatures than young adults. Table 4-2 summarizes the experimental studies reporting changes in temperature threshold values for vasodilation, vasoconstriction, sweating, and shivering.

Table 4-2 Experimental studies on age-related sensory delays

Physiological parameter	References	Exposure condition	No. of subjects	Age	Activity	Age-related Changes (°C)
Core temperature threshold for vasodilation	Tankersley *et al.* (1991)	Warm	13	65±1.2	Exercise	**+0.09(±0.03)**
	Holowatz *et al.* (2003)	Hot	7	71±6	Sedentary	**+0.1 (±0.1)**
	Greaney *et al.* (2020)	Hot	13	67±7	Sedentary	**+0.5(±0.1)**
	(Tochihara *et al.* 1993)	Hot	9	62-72	Sedentary	**0.05**
Skin temperature threshold for vasoconstriction	(Tochihara *et al.* 1993)	Cold	10	66-79	Sedentary	**-0.5**
	Ozaki *et al.* (1997)	/	14	60–80	Sedentary	**-1.6 (±0.3)**
Core temperature threshold for vasoconstriction	Plattner *et al.* (1993)	/	24	/	/	**-1.2**
	Frank *et al.* (2000)	Cold	8	55-71	Sedentary	**-0.7 (±0.1)**
	El-Gamal *et al.* (2000)	Room temperature	20	60-75	Sedentary	**-0.3 (±0.1)**
Core temperature threshold for sweating	Sagawa *et al.* (1988)	Hot	6	61-73	Sedentary	**+0.28 (±0.01)**
	Andersen (1996)	Hot	9	73.9±4.8	Sedentary	**+0.27 (±0.12)**
	Tankersley *et al.* (1991)	Warm	13	65±1.2	Exercise	**no significant changes**
Skin temperature threshold for sweating	Dufour and Candas (2007)	Hot	15	67.8±3.7	Sedentary	**+2.0 (±0.1)**
Body temperature threshold for sweating	Armstrong and Kenney (1993)	Hot	6	61± 1	Sedentary	**no significant changes**
	Stapleton *et al*. (2014)	Room temperature	8	65± 3	Exercise	**+0.35 (±0.25)**
Core temperature threshold for shivering	Vassilieff (1994)	/	18	76± 4.8	Sedentary	**-0.3 to -1.3**
	Andersen (1996)	Cold	9	73.9±4.8	Sedentary	**-0.27**
	Sessler (2008)	/	8	89±7	Sedentary	**-0.9 (±0.2)**
Skin temperature threshold for shivering	Sessler (2008)	/	14	60–80	Sedentary	**-1.6**

It is evident from the reviewed studies (Tables 4-1 and 4-2) that the reported weakenings in thermoregulatory activities include as well the effects of sensory signal delays to trigger thermoregulatory actions, thus making it difficult to isolate the weakening factors. Furthermore,

activity levels may interfere with the weakening factors. In addition, the large variability of temperature threshold values to trigger thermoregulation actions amongst older people makes it difficult to assume average values for modeling purposes. To address these challenges, several attempts have been conducted to model the physiological changes in older people, primarily through multi-node segmental models. Novieto (2013) developed an older people multi-node model by modifying the Fiala model for young adults (Fiala et al., 2012) and accounting for personal parameters (weight, height, and metabolic rate) and thermoregulatory changes of older people. The thermoregulation changes were established by fitting published experimental data. The model accuracy was good for the core temperature (< 0.1℃.) but had a large deviation (1.2℃) for the skin temperature. Rida et al. (2014) developed a multi-node model for older people based on the Karaki et al. (2013) model for young adults. The model accounts for the age-related changes in metabolism, skin blood flow, sweating, shivering, and body fat thickness. The temperature threshold values were assumed based on literature data. The model was validated with public measurement data under cold and hot conditions (air temperature: 10℃ to 35℃). Hirata et al. (2015) developed a multi-node model under hot exposure conditions by accounting for older people's sensory delays for the skin blood flow and sweating. The temperature threshold values were determined by sensitivity analysis. The model was validated with experiments in hot and humid exposure environments. The predicted core temperature agreed well with the measurement data, but the model accuracy for the skin temperature was within 20% uncertainty. Ma et al. (2017) developed an individualized multi-node segmental model for Chinese older people based on an existing model for young adults. The model accounts for the age-related changes for metabolism, cardiac output, body fat, and skin surface area but does not consider the changes in temperature threshold values. The model was validated only for the skin temperature prediction under hot and

cold exposure conditions with an uncertainty of 14%. Wang et al.(2018) developed a data-driven model to predict the thermal sensation and skin temperature of older people. The model training data were taken from field studies in China and may not be applied to other locations. Coccarelli et al. (2018) developed a multi-node model for older people by accounting for the age-related changes of tissue distribution in each body segment and sensory delays in thermoregulation. This model was validated under hot exposure conditions and showed good agreement with the measured core and skin temperatures. Itani et al. (2020) developed a multi-node model for older people based on the Karaki et al. (2013) model for average-aged people. The thermoregulation threshold temperatures were determined by a sensitivity analysis using public experimental data. The model predictions agreed well with the selected experiments under heat-stressful conditions.

In summary, the previously mentioned modeling work has been based on multi-node segmental body models of older people**.** No attempts have been tried to develop simplified models for the whole body of older people for possible integration in comfort and heat stress standards and design tools for built environments. Compared to the multi-node segmental models, the two-node model represents a human body by the core node and skin node. The two-node model is popular in thermal comfort studies (Enescu, 2019). The mean skin temperature calculated from the two-node model has been correlated with whole-body thermal sensation by multiple studies under steady-state conditions (Takada et al., 2013). Similarly, the core temperature obtained from the two-node model is a criterion to evaluate thermal-related health safety (ISO 7933, 2017). In building thermal design standards and tools (ASHRAE-55, 2017; Tartarini et al., 2020), and building simulation software such as ESP-r (Rida and Kelly, 2017), EnergyPlus (DOE, 2020), and TRNSYS (Klein et al., 2004), the two-node model has been implemented to evaluate the occupants' thermal comfort. Rational heat-stress indices such as the standard effective temperature (SET*) are calculated based on the

physiological parameters provided by the two-node model (Wang et al., 2020a; Zhang and Lin, 2021). It is, therefore, worthwhile and important to extend the two-node model for young adults to cover the heat vulnerable older adults by considering the aging effects on their thermal responses.

This study aims to develop a two-node model for older people by accounting for the age-related physiological changes under stressful hot and cold exposure conditions. The paper is structured into five sections. After the introduction, the second section presents the methodology to build the two-node model for older people and the optimization method to determine the key model parameter values. The third section presents the model optimization results and the model validation studies, followed by the sections on discussion and conclusion.

4.2. Methodology

The development of the bioheat model for older people is built on a newly developed two-node model for young adults (Ji et al., 2021). The age-related physiological changes of older people are accounted for in the thermoregulatory actions and threshold values triggering these actions. The details of the model development follow.

4.2.1 Heat balance of human body

The heat balance of the human body accounts for the internal heat generation by metabolism and heat exchange with the surrounding environment. In the two-node model, the metabolic heat is produced at the core node. Part of this internal heat is dissipated to the environment through respiration and to the skin node through conduction, convection, and skin blood flow perfusion. The skin node exchanges dry and evaporative heat with the environment. The heat balance equations for the skin and core nodes are given below,

$$\frac{m_{cr}c_{cr}}{A_b}\frac{dT_{cr}}{d\tau} = M + SHIV - W - Q_{res} - h_{sk}(T_{cr} - T_{sk}) \quad (4\text{-}1)$$

$$\frac{m_{sk}c_{sk}}{A_b}\frac{dT_{sk}}{d\tau} = h_{sk}(T_{cr} - T_{sk}) - Dry - Evap \quad (4\text{-}2).$$

The skin sensible heat loss (Dry) and evaporative heat loss (Evap) are given by Equation 4-3 and Equation 4-4, respectively,

$$Dry = \frac{1}{R_{d,air}+R_{d,clo}}(T_{sk} - T_a) = (h_c + h_r)(T_{cl} - T_a) \quad (4\text{-}3)$$

$$Evap = \eta_{evap} \times (0.68 \times SWR + Edif) = w \times Emax \quad (4\text{-}4).$$

4.2.2 Thermoregulatory system

The thermoregulatory activities, including sweating, vasodilation, vasoconstriction, and shivering, are triggered by warm or cold temperature signals. The signals are the deviation of the body temperature, core temperature, and mean skin temperature from their threshold values. The thermoregulatory system of the proposed model for older people is built around that for young adults by introducing new thermoregulatory attenuation coefficients and directly using the threshold temperature values for older people. The description of each thermoregulatory system follows:

a. Skin blood flow

The skin blood flow rate (SBF) depends on the body's thermal state and varies between the upper and lower limits. Under heat-stressful conditions, the skin blood flow is increased by vasodilatation, while under cold conditions, skin blood flow is controlled by vasoconstriction. The skin blood flow rate is expressed by the following equation:

$$SBF = [SBF_{basal} + CDE \cdot CDIL \times \Delta T_{cr,dil}]/[1 + CCE \cdot CSTR \times \Delta T_{sk,cons}] \quad (4\text{-}5)$$

where CDE and CCE are attenuation coefficients of vasodilation and vasoconstriction of older people, respectively. The attenuation coefficients account for age-related weakening in vasodilation and vasoconstriction activities, which makes the skin blood flow regulation vary from

young adults. The ranges of these coefficients will be discussed in Section 2.2, and the final values will be determined. CDIL and CSTR are constants equal to 50 and 0.75 Litre/(m^2·hr·°C), respectively. $\Delta T_{cr,dil}$ is the warm control signal of the core temperature for vasodilation, and $\Delta T_{sk,cons}$ is the cold control signal of the skin temperature for vasoconstriction. These are given by $\Delta T_{cr,dil} = (T_{cr} - T_{cr0,dil})^+$, and $\Delta T_{sk,cons} = (T_{sk0,cons} - T_{sk})^+$, where $T_{cr0,dil}$ is the core temperature threshold for vasodilation and $T_{sk0,cons}$ is the skin temperature threshold for vasoconstriction. '+' means only positive values will be taken. For young people, the values of $T_{cr0,dil}$ and $T_{sk0,cons}$ are 36.8°C and 33.7°C, respectively (Ji et al., 2021). For older people, $T_{cr0,dil}$ is higher and $T_{sk0,cons}$ is lower, resulting in delays in triggering vasodilation and vasoconstriction. The ranges and values of these threshold values will be analyzed and determined in the following sections.

b. Sweating regulation

Under hot and/or humid exposure or with a high activity level, the human body releases heat from the skin surface to the environment through sweat evaporation. The sweating rate is calculated with Equation 4-6,

$$SWR = CSWE \times CSW \times \left(\Delta T_{b,sw} + Acof \times \Delta T_{sk,sw}\right) \times exp\left(\frac{\Delta T_{sk,sw}}{10.7}\right) \quad (4\text{-}6)$$

where CSWE is a sweat attenuation coefficient for older people with respect to the age-related weakening in sweating rate, and CSW and $Acof$ are model constants for young adults, equal to 170 g/m^2h and 0.2, respectively. $\Delta T_{b,sw}$ and $\Delta T_{sk,sw}$ are the body and mean skin temperature control signals for sweating, expressed by $\Delta T_{b,sw} = (T_b - T_{b0,sw})^+$, and $\Delta T_{sk,sw} = (T_{sk} - T_{sk0,sw})^+$.

The average body temperature (T_b) can be calculated by the weighted average of the mean skin and core temperatures:

$$T_b = \alpha T_{sk} + (1-\alpha)T_{cr} \quad (4\text{-}7)$$

where α is the ratio of the thermal mass of the skin layer to the total body mass, given by Equation 4-8 as a function of the skin blood flow rate:

$$\alpha = 0.0417737 + 0.7451832/(SBF + 0.5854417) \quad (4\text{-}8).$$

Similarly, the body temperature threshold $T_{b0,sw}$ is calculated as the weighted average of the core temperature threshold $T_{cr0,sw}$ and skin temperature threshold $T_{sk0,sw}$ using Equation 4-7. For young people, $T_{cr0,sw}$ and $T_{sk0,sw}$ are 36.8°C and 33.7°C, respectively (Ji et al., 2021), whereas, for older people, the values are higher, resulting in delays in sweating activity.

Under hot and humid exposure conditions, sweating evaporation is restricted, resulting in a decrease in sweat evaporation efficiency (Itani et al., 2020). The model of Kubota et al. (2014) for the sweat evaporation efficiency was found to produce better results than other formulations (Ji et al., 2021), and therefore, it is adopted in this study. The sweat evaporative efficiency is given by Equation 4-9,

$$\eta_{evap} = \begin{cases} 0.37 + 0.31/w'; \ if \ 0.49 \le w' \le 1 \\ 1; \quad if \ w' < 0.49 \end{cases} \quad (4\text{-}9)$$

where w' is the skin wettedness when sweating is fully converted to evaporative heat loss.

c. Shivering

Under cold exposure conditions, when the non-shivering thermogenesis during vasoconstriction is not sufficient to maintain the body core temperature at the neutral value, shivering activity will be triggered. Shivering can increase heat production by superficial muscle fibers contraction. In this study, the shivering rate is expressed by Equation 4-10,

$$SHIV = CSHE \times (Cof_{scs} \times \Delta T_{cr,sh} \times \Delta T_{sk,cons} + Cof_{sc} \times \Delta T_{cr,sh} + Cof_{ss} \times \Delta T_{sk,cons}) \quad (4\text{-}10)$$

where CSHE is an attenuation coefficient for shivering rate of older people, which is added due to the age-related weakening of shivering action. $\Delta T_{cr,sh}$ is the core temperature control signal for shivering given by $\Delta T_{cr,sh} = (T_{cr0,sh} - T_{cr})^+$. For young people, the core temperature threshold value for shivering $T_{cr0,sh}$ is 36.8℃, while the value is lower for older people, leading to a delay in triggering the shivering activity. Cof_{scs}, Cof_{sc}, and Cof_{ss} are model constants equal to 19.4, 50, 0.5, respectively.

4.2.3 Extents of age-related attenuation factors

The model parameters that need to be determined for older people include the attenuation coefficients (CDE, CCE, CSWE, CSHE), and temperature threshold values for vasodilation and constriction, sweating and shivering. The value ranges for those parameters are collected from public literature data as presented in Section 4.1. Figure 4-1 presents the ranges of the attenuation percentage for metabolism and thermoregulatory activities for vasodilation and constriction, sweating, and shivering based on the literature review of Table 4-1. The theoretical parameter ranges vary from 0% (no age-related change) to the measured maximum change percentage. Figure 4-2 shows the ranges of the difference between older and young people in the thresholds of the core and mean skin temperatures for vasodilation, vasoconstriction, sweating, and shivering based on the literature review of Table 4-2.

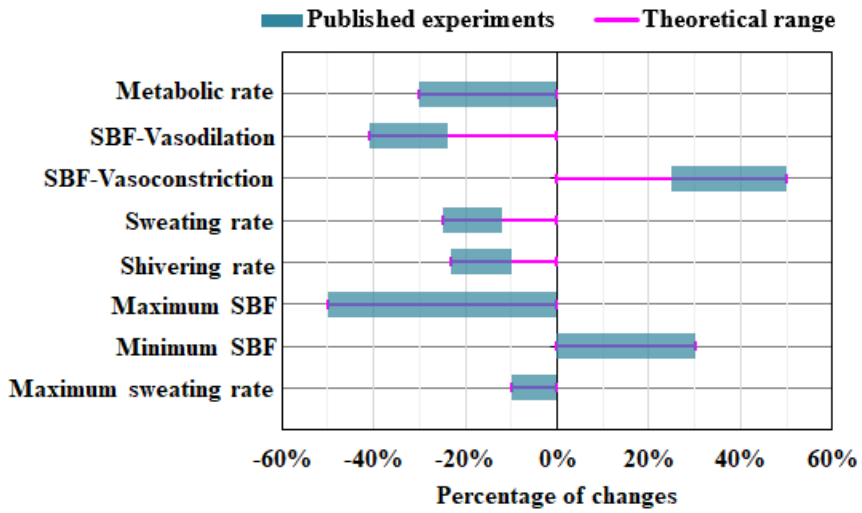

Figure 4-1 Experimental ranges of age-related changes in thermoregulation relative to young people

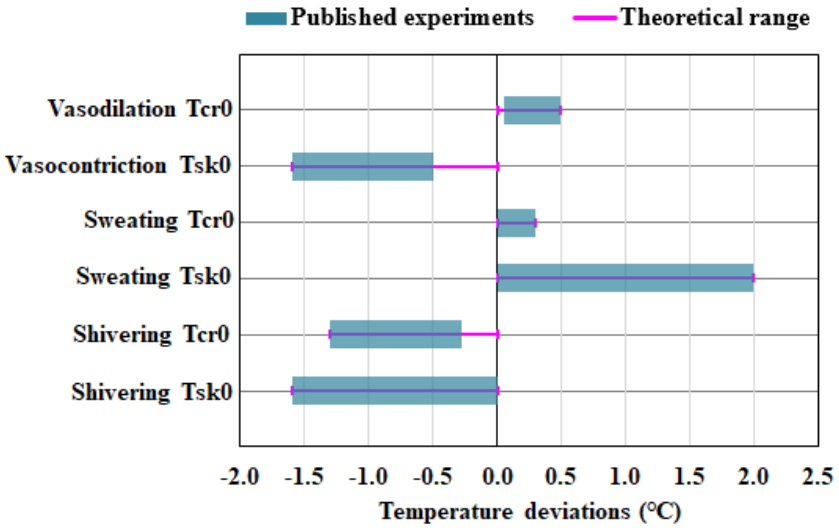

Figure 4-2 Experimental ranges of age-related deviations in regulatory temperature threshold values relative to young people

4.2.4 Optimization of model parameters

The values of the model parameters for the thermoregulatory system of older people are optimized by minimizing the error between the model predictions and the selected experimental benchmark data. The parameters that need to be optimized include the attenuation coefficients of vasodilation,

vasoconstriction, sweating, and shivering, and the temperature threshold values for triggering these thermoregulatory activities. However, the attenuation coefficient of the metabolic rate of older people is considered variable, and its value is directly taken from the measured experimental data. The proposed optimization process consists of a series of numerical experiments in which the parameter values are sampled from the experimental ranges to cover a sufficiently high number of points to locate the optimum values. Table 4-3 summarizes the parameter ranges from Figures 4-1 and 4-2. 16200 possible combinations of model coefficients and temperature threshold values are evaluated in hot exposure scenarios, and 7488 possible combinations are tested under cold exposure conditions.

Table 4-3 Sampling of model coefficients and threshold temperature values

Exposure	Parameters	Range	Sampling interval	Number of possible values
Hot	Vasodilation attenuation coefficient CDE	[0.6,1]	0.05	9
	Sweating attenuation coefficient CSWE	[0.75,1]	0.05	6
	Deviation of vasodilation threshold $T_{cr0,dil}$ (℃)	(0, 0.5]	0.1	5
	Deviation of sweating threshold $T_{cr0,sw}$ (℃)	(0, 0.3]	0.05	6
	Deviation of sweating threshold $T_{sk0,sw}$ (℃)	(0, 2]	0.2	10
Cold	Vasoconstriction attenuation coefficient CCE	[0.5,1]	0.1	6
	Shivering attenuation coefficient CSHE	[0.77,1]	0.046	6
	Deviation of vasoconstriction threshold $T_{sk0,cons}$ (℃)	[-1.6,0)	0.1	16
	Deviation of shivering threshold $T_{cr0,sh}$ (℃)	[-1.3,0)	0.1	13

4.2.5 Benchmark cases

Seven benchmark experimental cases are selected to cover the scenarios from cold, mild cold to hot exposure conditions. Older people's core and skin temperatures are measured for at least 60 min in climate chambers. At least ten older people subjects were measured in each experimental case. More details on the screening criteria and measurement process of the selected experimental cases can be found in the previous work by the authors (Ji et al., 2021). In total, 2346 core

temperature data and 5154 mean skin temperature data were obtained. The data at each time point were then averaged by the number of subjects in each scenario. Finally, 68 core temperature data and 79 mean skin temperature data were used to compare with the simulation results. The detailed experimental settings of the benchmark cases are shown in Table 4-4.

Table 4-4 Detailed settings of the benchmark experiments

Scenario	Number of Subjects	Ta=T_{mrt} (°C)	V_a (m/s)	RH (%)	MET	CLO	Age (year)	Height (m)	Weight (kg)	Duration (min)	Reference
1	12	36.5	0.25	20	0.95	0.1	65	1.8	80.1	120	Stapleton et al. (2014)
2	12	36.5	0.25	60	0.96	0.1	65	1.8	80.1	120	Stapleton et al. (2014)
3	109	31	0.2	60	0.7	0.67	72.4	1.525	55.7	150	Tsuzuki and Ohfuku (2002)
4	109	27	0.2	60	0.7	0.67	72.4	1.525	55.7	150	Tsuzuki and Ohfuku (2002)
5	109	23	0.2	60	0.7	0.67	72.4	1.525	55.7	150	Tsuzuki and Ohfuku (2002)
6	10	17	0.2	45	0.9	0.06	63.7	1.602	53.8	60	Inoue *et al.* (1992)
7	10	12	0.2	45	0.9	0.06	63.7	1.602	53.8	60	Inoue *et al.* (1992)

4.2.6 Optimization function

The proposed two-node model with each possible combination of parameters is evaluated according to its accuracy in predicting the core and mean skin temperatures. To obtain a model that performs well for the prediction of both the core temperature and mean skin temperature, the function to be minimized uses the combined root mean square error (cRMSE) method (Ji et al., 2021). The cRMSE is calculated based on the difference between the experiments and predictions. The cRMSE is calculated in the last 30 minutes of the exposure time to capture the steady-state conditions. Moreover, to get equal weighting for each experimental scenario of a given exposure type, a fixed number of data points is applied to each scenario. The combined RMSE is thus obtained as follows:

$$cRMSE = \sqrt{RMSE_{cr}{}^2 + RMSE_{sk}{}^2} \quad (4\text{-}13)$$

where the RMSE of each nodal temperature is calculated for all scenarios of each exposure type as follows:

$$RMSE = \sqrt{\sum_{i=1}^{m} RMSE_i{}^2 / m} \quad (4\text{-}14)$$

where (m) is the number of scenarios.

It should be noted that the minimization function (Equation 4-13) theoretically leads to the same optimum parameter values as by maximizing the coefficient of determination (R^2) when the latter is calculated for both the core and mean skin temperatures for all scenarios of a given exposure type.

4.3. Results

4.3.1 Optimized values of model parameters

Figure 4-3 shows the distribution of RMSEcr and RMSEsk for each combination of the parameter values under hot exposure (a- Scenarios 1 to 4) and cold exposure (b- Scenarios 5 to 7). The distance of the points to the axis origin is the cRMSE, amongst which the smallest distance (the distance of the framed colored point to the axes origin; note as well the different scales of the horizontal and vertical axes) corresponds to the optimum value. Table 4-5 lists the optimum values of the attenuation coefficients and temperature thresholds for older adults and their deviations from those for young adults (taken from Gagge et al, 1986).

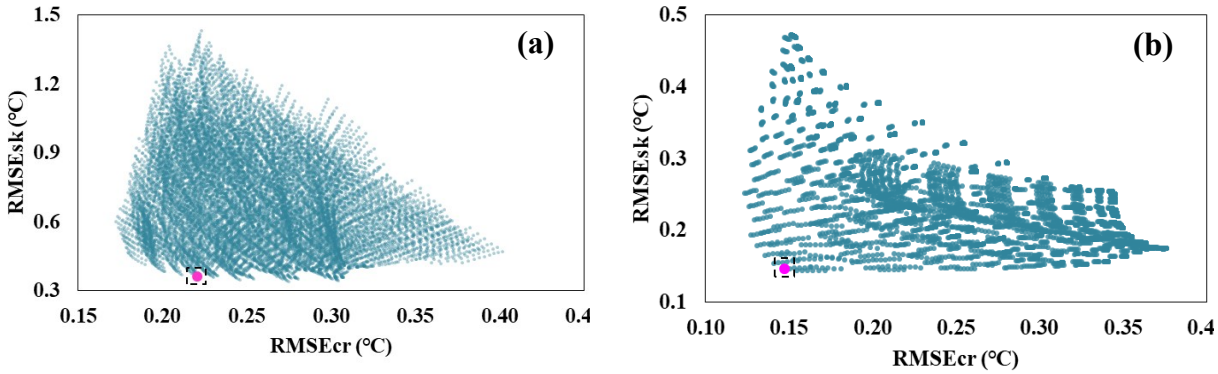

Figure 4-3 The RMSE values of the mean skin and core temperature predictions under (a) hot exposure conditions (Scenarios 1 to 4), and (b) cold exposure conditions (Scenarios 5 to 7) Note: the colored point in each figure has the smallest distance to the axes origin.

Table 4-5 Optimized values of model parameters

Parameters	Young	Deviation	Older
Vasodilation threshold $T_{cr0,dil}$ (°C)	36.80	+0.50 (±0.05)	37.30
Vasoconstriction threshold $T_{sk0,cons}$ (°C)	33.70	-0.45 (±0.05)	33.25
Sweating threshold $T_{cr0,sw}$ (°C)	36.80	+0.20 (±0.05)	37.00
Sweating threshold $T_{sk0,sw}$ (°C)	33.70	+0.60 (±0.05)	34.30
Shivering threshold $T_{cr0,sh}$ (°C)	36.80	-0.10 (±0.02)	36.70
Vasodilation attenuation coefficient CDE	1	-0.40 (±0.05)	0.60
Vasoconstriction attenuation coefficient CCE	1	-0.50 (±0.05)	0.50
Sweating attenuation coefficient CSWE	1	0 (±0.02)	1.00
Shivering attenuation coefficient CSHE	1	0 (±0.02)	1.00
Min SBF rate (L/h/m^2) (fixed)	0.5	+50%	0.75
Max SBF rate (L/h/m^2) (fixed)	90	-30%	63
Max sweating rate factor (fixed)	1	-0.1	0.9

It would also be helpful to find a representative value of the metabolic rate reduction factor for an average older population for thermal comfort calculation purposes. To do so, the optimization method was run using the optimized parameter values in Table 4-5. The attenuation factor of the metabolic rate covers the range 0.7 to 1 (Figure 4-1). The corresponding minimum cRMSE value

for the core and mean skin temperatures for all scenarios in Table 4-4 (m = 6; excluding Scenario 3 due to its RMSE dominance) yields an optimized attenuation factor for the metabolic rate of 0.8.

4.3.2 Core and mean skin temperature predictions

Figure 4-4 shows the core and mean skin temperature predictions of the proposed model under the hot scenarios (Scenarios 1-2). To eliminate the impacts of occupants' initial conditions and capture the prediction accuracy during the steady-state, the deviations between experiments and predictions of each scenario are evaluated during the last 0.5 hours of exposure. Under the hot-dry exposure (a), the maximum deviations between the proposed model predictions and experimental data are 0.13℃ in Tcr, and 0.6 ℃ in Tsk. Similar results are obtained under the hot-humid exposure (b). The maximum discrepancy between the predictions and experiments is 0.1℃ for Tcr, and 0.29 ℃ for Tsk.

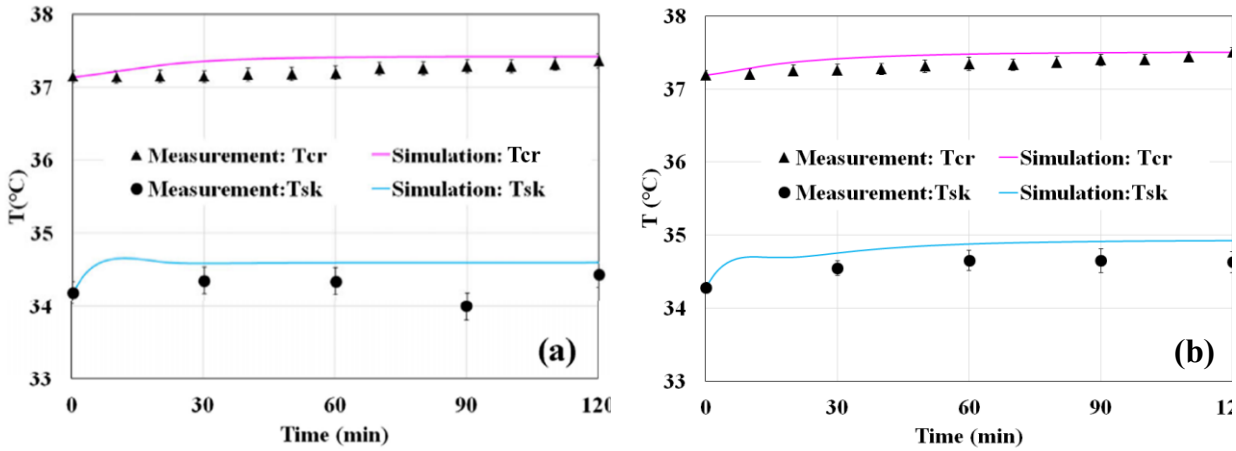

Figure 4-4 Comparison of the results between the model and experiments of hot (a) Scenario 1, and (b) Scenario 2

Figure 4-5 shows the results of the proposed model and the benchmark data under warm scenarios (Scenarios 3-4). Under Scenario 3, the maximum discrepancies between the predictions and experiments are 0.30℃ in T_{cr}, and 0.59 ℃ in T_{sk}. Similar results are obtained under the warm scenario 4 (b) with maximum discrepancies of 0.30℃ in T_{cr} and 0.20 ℃ in T_{sk}.

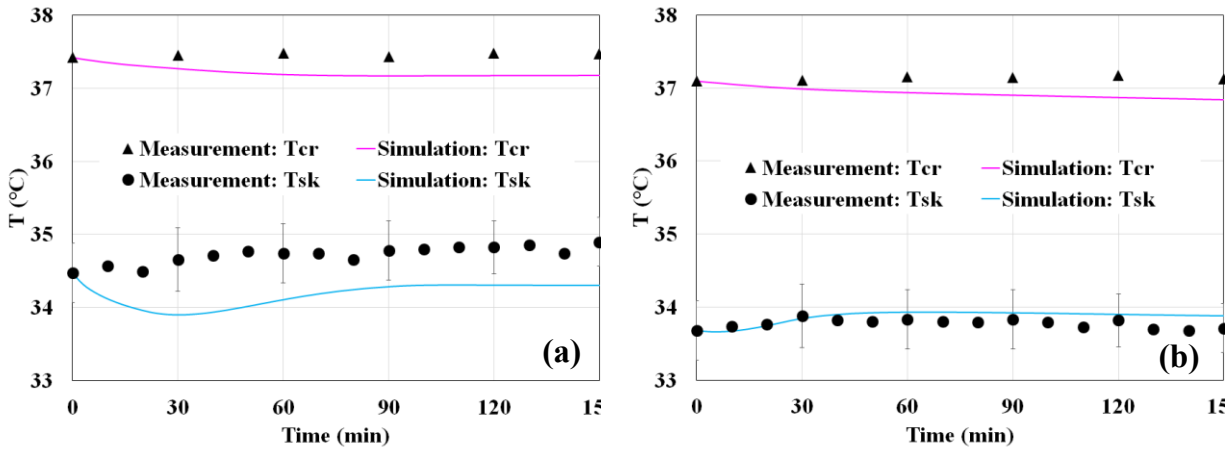

Figure 4-5 Comparison of the results between the model and experiments of warm (a) Scenario 3, and (b) Scenario 4

Figure 4-6 shows the results of the proposed model and the experimental data of mild cold to cold scenarios (Scenarios 5-7). Under mild cold exposure (a), the maximum discrepancies between predictions and the experiments are 0.29℃ in T_{cr}, and 0.14 ℃ in T_{sk}. Similar results are obtained for the cold scenarios (b) and (c) with maximum discrepancies of 0.11℃ in T_{cr}, and 0.35 ℃ in T_{sk}.

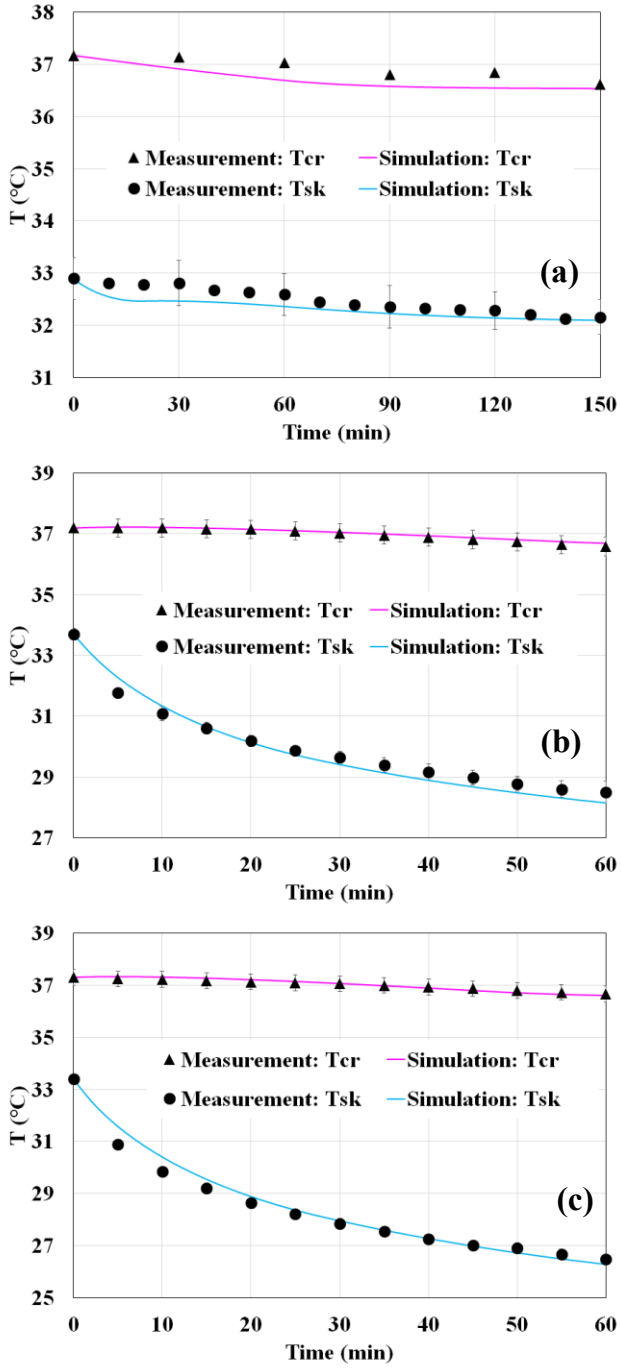

Figure 4-6. Comparison of the results between the model and experiments of the cold (a) Scenario 5, (b) Scenario 6, and (c) Scenario 7

4.3.3 Further model validation

To validate the proposed model with new datasets which have not been used in the optimization process, five extra experimental cases are obtained from literature according to the previously mentioned screening criteria. Table 4-6 shows the detailed settings of the selected experiment cases.

Table 4-6 Validation experiment settings

Scenario	Number of Subjects	Ta= T_{mrt} (℃)	V_a (m/s)	RH (%)	MET	CLO	Age (year)	Height (m)	Weight (kg)	Duration (min)	Reference
8	16	21	0.1	50	0.8	0.55	70	1.603	59.0	60	
9	16	25	0.1	30	0.8	0.55	70	1.603	59.0	60	Xiong *et al.* (2019)
10	16	28	0.1	50	0.8	0.55	70	1.603	59.0	60	
11	16	31	0.1	70	0.8	0.55	70	1.603	59.0	60	
12	46	26.5 to 19	0.2	60	0.65	0.05	71	1.69	69.2	120	DeGroot and Kenney (2007)

Scenarios 8 to 11 are taken from the experiments of Xiong et al. (2019), in which 16 older people (males and females) aged 70 years old were tested during hot and humid summer of a subtropical climate location in China. The subjects would therefore be fully acclimatized to warm and humid conditions. During the experiments, the subjects were exposed to four constant warm and cool environmental conditions for 60 min. The subjects wore short-sleeved T-shirts, long trousers, and slippers and were seated and relaxed. The skin temperatures at ten body locations were measured per minute, and the mean skin temperature was calculated. However, the core temperature and metabolic rate of the subjects were not measured. An average value of the metabolic rate for the older people was therefore assumed 80% of sedentary young adults (1 met).

Scenario 12 is taken from the experiments of DeGroot and Kenney (2007), in which an initial number of 46 (the number was significantly decreased with the exposure time) older people (males

and females) aged about 71 years old were exposed to mild cold environmental conditions with a variable temperature from 26.5℃ to 19℃ for 120 min. The temperature was initially kept constant at 26.5℃ for 20 min and then was steadily reduced with two rates at 0.25°C/min for 20 min followed by 0.05°C/min for the remainder time. During the experiments, the subjects were clothed with shorts (for men) or shorts and sports bras (for women). With a time interval of 5 min, the skin temperature at eight body locations and the core temperature was measured. The metabolic rate was indirectly measured by continuously measuring the volume of oxygen consumption and carbon dioxide production during the exposure time. The net (excluding respiration heat loss) metabolic heat, therefore, includes the portion due to shivering under such cold exposure. The net average (overexposure time) metabolic rate was calculated as 37.7 W/m^2 (0.65 met) and used in the simulation.

Figure 4-7 shows the validation results of Scenarios 8-11. The maximum discrepancy between model predictions and experimental data is 0.32 ℃ in T_{sk} during the last 0.5h in the hot Scenario 11.

Figure 4-8 shows a comparison of the model predictions for the core and mean skin temperatures with the experimental data of Scenario 12. The maximum discrepancy between core temperature predictions and experimental data is 0.27 ℃ during the last 0.5h. The mean skin temperature during the last 0.5h of exposure time was, however, over-predicted by 1.2℃. In Scenario 12, the air temperature decreased from 26.5℃ to 19℃. The overestimation of skin temperature might be due to the shivering rate added to the heat generation with the process of air temperature decrease.

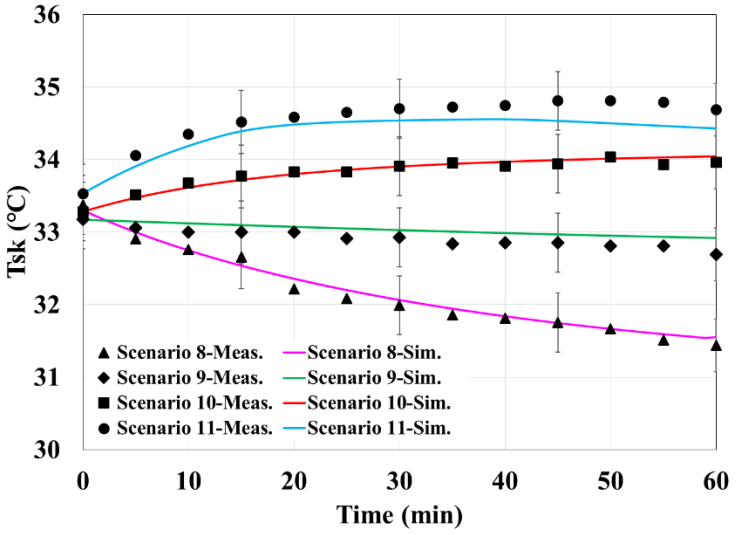

Figure 4-7 Validation results of Scenarios 8 to 11

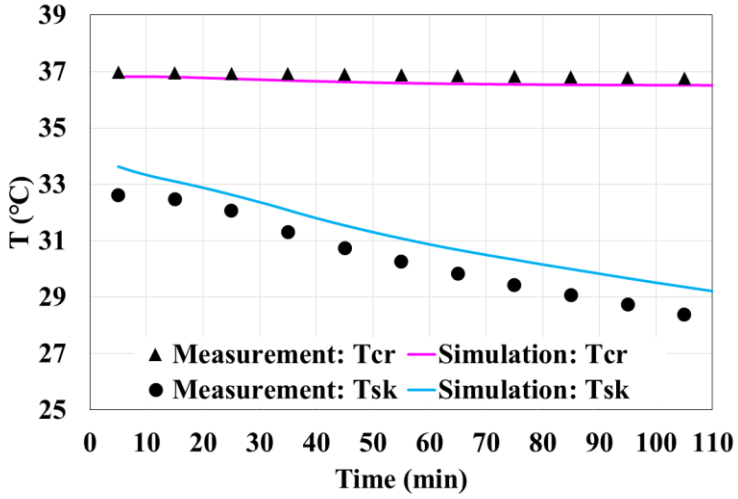

Figure 4-8 Validation results of Scenario 12

4.4. Discussion

A couple of things are noted for the model development for older people. To obtain average representative values of the model parameters, the prediction error is minimized for the core temperature and mean skin temperature in multiple experimental conditions (with various

environmental settings as listed in Table 4-4). If the cRMSE for each experiment is minimized independently of the other experimental settings, the corresponding optimum parameter values would not be representative of older people as a large group. Similarly, to get the model that performs well for both the mean skin temperature and core temperature, the metric cRMSE is used to integrate the error of the core temperature (RMSEcr) and mean skin temperature (RMSEsk). Moreover, the obtained optimized values of the model parameters are numerical values and not necessarily equal to the actual average values of a large pool of older people under wide ranges of exposure conditions and activity levels. If such parameter values are measured and available, they should be directly used in the model, but the model accuracy would differ from those with the general optimized values.

The model predictions for the experimental Scenarios 1 to 12 show overall good trend and accuracy levels with the measured core and mean skin temperatures. For well controlled steady experimental conditions (measured environmental conditions and subject data) such as the benchmark cases (Scenarios 1 to 11), the accuracy of the model for both the core temperature and mean skin temperature are good and within the experimental errors (maximum deviations are 0.30 °C for T_{cr} and 0.60 °C for T_{sk}), whereas in previously published multi-node models, the maximum prediction deviations were 0.35°C in the core temperature and 1.2°C in the mean skin temperature (Novieto, 2013; Rida et al., 2014). For transient exposure cases where the subject data (particularly the metabolic rate under cold exposure conditions where the shivering metabolic rate cannot be separated from the net measured metabolic rate; Scenario 12) are estimated, the model prediction accuracy is expected to be lower, particularly for the most sensitive mean skin temperature.

To further evaluate the accuracy of the proposed model, a comparison of the simulation results is conducted with average-aged young people's model. Figure 4-9 shows the simulated core

temperature and mean skin temperature by the proposed model and the new two-node model of young people by (Ji et al., 2021) under the hot to cold exposure conditions (Scenarios 1, 2, 5, 7; Table 4). The measurement data of older and young subjects in each scenario are also plotted. From the measurements in hot scenarios (Scenarios 1-2), older people's core temperature is higher than young people by a maximum of 0.5℃, and mean skin temperature is lower than young people by a maximum of 0.5℃. In the mild cold scenario (Scenario 5), the core temperature of older people is higher than young people at the beginning of exposure and slightly lower at the end of exposure by 0.2℃. The mean skin temperature of older people is higher than young people by a maximum of 0.4℃. In the cold scenario (Scenario 7), the core temperature of older people is close to young people and slightly lower at the end of exposure by 0.3℃, and the mean skin temperature of older people is also lower than young people by a maximum of 0.9℃. From Figure 4-9, the simulation results can capture the relative difference between older and young people in each scenario. The simulated core temperature of older people is higher than young people by a maximum of 0.5℃ in hot scenarios, which is consistent with public measurement data (Stapleton et al., 2014). However, in hot scenarios, the difference between the simulated mean skin temperatures of older and young people is smaller than the measurements. In the mild cold scenario, the simulated core temperature difference and mean skin temperature difference between older and young people are within 0.2℃ and 0.3℃, respectively, which are consistent with the measurement data. In the cold scenario, the simulated core temperature difference between older and young people is 0.3℃ at the end of exposure time, similar to the measurements, while the simulated mean skin temperature difference reaches a maximum error of 0.8℃, which is smaller than measurements. Overall, the simulations can capture the relative difference between older and young people in hot to cold scenarios. The simulated core temperature difference between the two

age groups is consistent with the measurements, while the accuracy of the simulated mean skin temperature difference is relatively limited (note as well the measured mean skin temperature may carry significant inaccuracies depending on the number of measurement points on the skin surface; Liu et al., 2011).

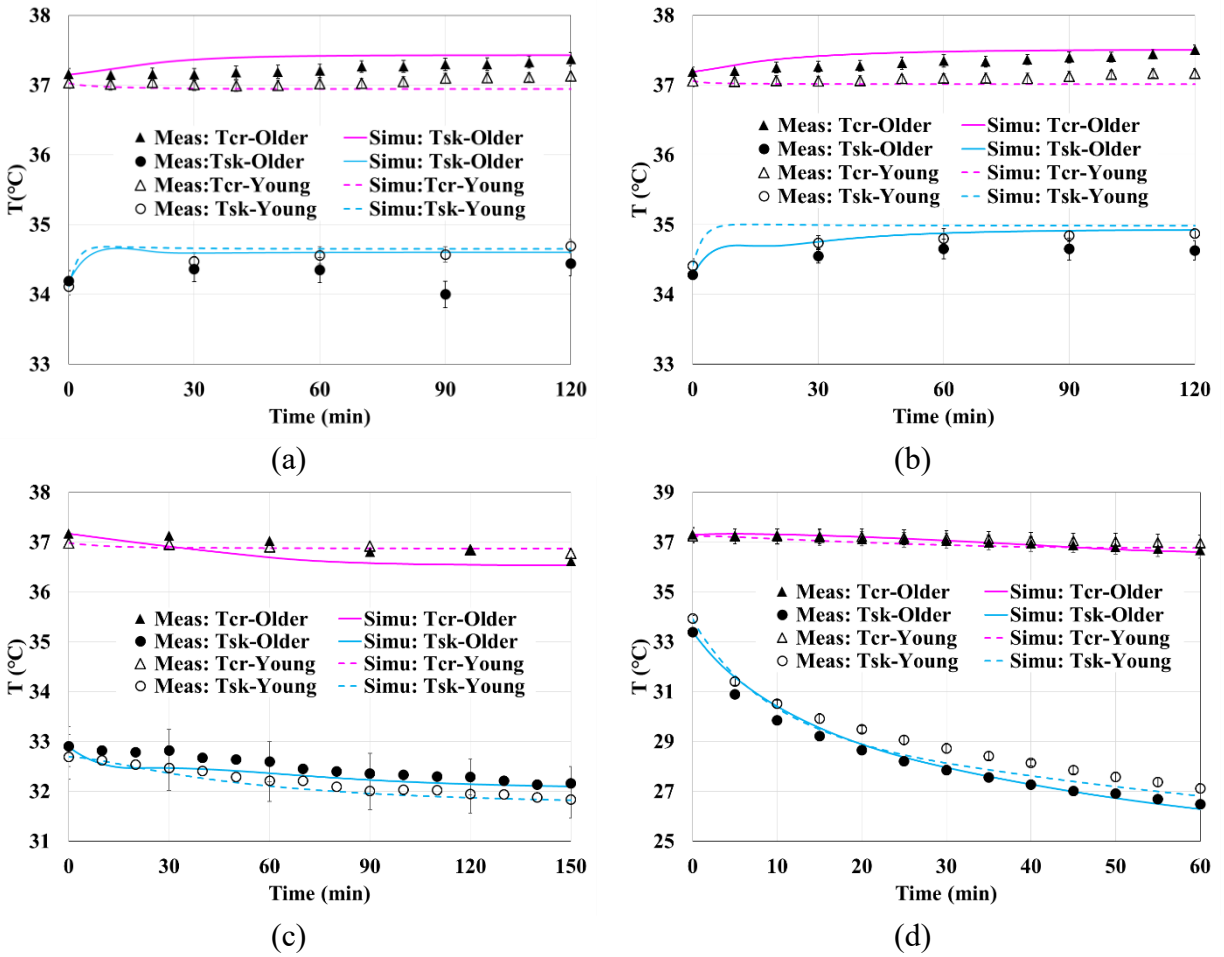

Figure 4-9 Comparison of older people and young people's simulations in (a) Scenario 1, (b) Scenario 2, (c) Scenario 5, and (d) Scenario 7

The proposed model of older people can replicate thermal responses with acceptable accuracy levels under both hot and cold exposures, particularly the core temperature, which is the most important thermal safety index used in existing building thermal design standards (ISO 7933, 2017) to limit heat-related health issues of people in workplaces. In this regard, the proposed

model can be applied to analyze the thermal stress of older people and should be included in existing relevant standards for built environments (e.g., ASHRAE-55, 2017 and ISO 7933, 2018) to cover older people.

4.5. Conclusion

This paper developed a two-node physiological model for older people under both hot and cold exposures. The model was built around a newly developed model for young adults by accounting for the age-related weakening changes in physiology and thermoregulatory activities for sweating, vasomotor, and shivering. Two types of age-related physiological changes were considered: the weakening of thermoregulatory activities and sensory delays in triggering thermoregulatory actions. The age-related changes were collected from public literature. A new optimization method was developed to obtain the optimized values of the model parameters. The method consisted of selecting high-quality experimental benchmark cases from published literature and conducting numerical experiments, in which the proposed model was run for each benchmark case using large combinations of model parameter values pooled from possible ranges. The combined RMSE (cRMSE) between predictions and experiments were calculated to evaluate the performance of reproducing the core temperature and mean skin temperature of the different scenarios. Its minimum value corresponded to the optimized parameter values.

The model was extensively validated using published experimental studies. In constant environmental conditions, the proposed model predictions agreed well with the experiments: the maximum deviation was 0.30℃ in the core temperature and 0.60℃ in the mean skin temperature under steady hot and cold exposures. In transient environmental conditions, the model prediction accuracy is limited particularly for the mean skin temperature. The proposed model can capture

the relative difference between older and young people in hot to cold scenarios. The simulated core temperature difference between the two age groups is consistent with the selected public measurement data, whereas the accuracy of the simulated mean skin temperature difference is limited. Future work should be conducted to improve the model prediction accuracy for the mean skin temperature under transient conditions.

Overall, given the model's simplicity and accuracy in predicting thermal responses of older people, it is recommended to integrate the proposed model in building simulation design tools to predict heat and cold stress levels and the associated thermal comfort for older people in built environments.

Chapter 5 Evaluating Approaches of Selecting Extreme Hot Years for Assessing Building Overheating Conditions during Heatwaves

The contents of this chapter are published in "Ji, L., Laouadi, A., Shu, C., Gaur, A., Lacasse, M., & Wang, L. (Leon). (2022). Evaluating approaches of selecting extreme hot years for assessing building overheating conditions during heatwaves. Energy and Buildings, 254, 111610. https://doi.org/10.1016/j.enbuild.2021.111610 ". The contents are slightly modified.

Abstract

When assessing a buildings' performance under overheating conditions there is a need to identify extreme hot years (EHYs) for a given climate location. Different types of EHYs can be selected depending on the criteria used for their selection, such as long, intense, or severe heatwaves defined based on dry-bulb temperature and other thermal comfort indices. However, the effect of the EHY type on the extent of indoor overheating has not been quantitively evaluated. The selection of multi EHYs also complicates the overheating assessment process. Therefore, an investigation was undertaken to explore the suitability of different EHY when assessing the extent of indoor overheating in buildings. In this study, the "Percentage of Synchronization" (POS) of outdoor and indoor-based extreme years was proposed as an approach to the selection of EHYs. A higher value of POS for a given EHY implied that there was a more significant risk for indoor overheating to occur. Thus, when evaluating different EHYs, the most suitable choice in EHY would then be selected as the one with the highest POS value. The proposed method was demonstrated for residential archetype building models for five different climate zones. In the selection of EHYs for building overheating analysis, the thermal-based index was confirmed to be more suitable than the

temperature-based index in the selection process; in the same context, the heatwave intensity and severity are more important than the duration of the event. Representative EHYs for each of the cities studied were identified; these include: 2010 (Ottawa and Montreal), 2013 (Toronto), 2006 (Baltimore), 1992 (Phoenix), and 2005 (Houston).

5.1. Introduction

Overheating in buildings has created serious health concerns, particularly about heat-vulnerable populations such as elders, children, and sick people during summertime heatwaves (Lomas and Porritt, 2017; Vellei et al., 2017). Heat-related mortality cases have been reported in 164 cities across 36 countries (Mora et al., 2017), of which, the most well-known heatwaves as having caused significant mortality in the mid-latitudes are those of Chicago in 1995 (~ 740 deaths) (Whitman et al., 1997), Paris in 2003 (~4870 deaths) (Dousset et al., 2011) and Moscow in 2010 (~10860 deaths) (Shaposhnikov et al., 2014). Currently, about 30% of the world's population is annually exposed to extreme heat events of over 20 days duration (Mora et al., 2017). Even in a cold climate zone (ASHRAE, 2013a) such as in Canada, four heatwaves with mortality occurred in 1987, 1994, 2010, and 2018 for which 106 deaths happened in 2010 and 66 deaths in 2018 (Lamothe et al. 2019). Understandably climate change is expected to exacerbate the occurrence of heatwaves worldwide. For example, by 2100, 48% to ~74% of the world's population is projected to experience deadly heatwaves and the mid-latitudes will be exposed to about 60 days of lethal heatwave events annually (Mora et al., 2017). As a consequence, the risk of building interiors overheating is expected to follow suit. For instance, if considering a high greenhouse gas emission scenario (RCP 8.5) the building overheating discomfort rate in Paraguay is expected to reach 30% to 50% by 2070 (Silvero et al., 2019). Due to the effect of global warming, the summer indoor air

temperatures are estimated to increase on average by up to 7℃ in the Netherlands by 2100 compared to the current climate, even when maximum ventilation rates are applied. Indeed, traditional mitigation strategies such as natural ventilation are expected to become less efficient as global warming increases (Hamdy et al., 2017). The building overheating problem has already seriously affected the health of building occupants and it will become even unhealthier in the future.

Therefore, it is essential to quantify the risks to building overheating during extreme heat events to permit mitigation measures to be developed. Such information would be useful in responding to these overheating challenges as they can be applied to improving standards and building codes. A highly valuable approach in the development of overheating mitigation measures is conducting building thermal response simulations from which one can determine the response of buildings to local historical and future climate loads. Building overheating assessments for different climate scenarios necessarily need to be realized using building simulation with local climate data. The evaluation of different mitigation strategies to decrease overheating also relies on building simulation models. When conducting a building overheating assessment using simulation, one first needs to identify extreme weather scenarios, i.e., a so-called "extreme hot year" (EHY). Unlike a typical meteorological year (TMY), which represents the typical (average) climate trends (Hall et al., 1978; Bilbao, 2003), an EHY is selected by evaluating the occurrence and intensity of outdoor heatwave events that span one or more months (such as warm/hot climates) amongst several years of weather data; the World Meteorological Organization recommends the use of at least 31 years of climate data (WMO, 2017). The selection of an EHY (or occurrences when multiple years need to be selected) is the first step when undertaking a building overheating simulation analysis. An improper selection could underestimate and thus exaggerate the effects on building overheating

from outdoor heat events with conservative and overambitious mitigation and code recommendations. As such, this study focuses on the selection of EHYs to be used in simulations of the thermal response of buildings, a prerequisite for building overheating analysis.

The selection of EHYs requires first addressing a few key issues. The first is the selection criteria. There are often two types of indices to evaluate heatwaves: temperature-based indices and those that are thermal-based. The former is more often applied with the majority based on dry bulb temperatures. A few examples include, but are not limited to, the: Design Summer Year (DSY) (CIBSE, 2002); probabilistic Design Summer Year (pDSY) (Eames, 2016); near extreme Summer Reference Year (SRY) (Jentsch et al., 2015); future probabilistic Hot Summer Year-1 (pHSY-1), and; Typical Hot Year (THY) (Guo et al., 2019). On the other hand, there are a limited number of studies that have been conducted based on thermal indices. The future probabilistic Hot Summer Year-2 (pHSY-2) is based on the Physiological Equivalent Temperature (PET) heat stress index (Liu et al., 2016). Laouadi et al.(2020a) proposed the Reference Summer Weather Year (RSWY) based on the transient Standard Effective Temperature (t-SET), taking into account temperature, relative humidity, wind speed, and a person's level of activity and extent of clothing.

Because of the different indices used, the selected EHYs often vary. For example, the temperature-based EHY for Ottawa, Canada, is 2012, whereas it is 2010 when a thermal-based index is employed (Laouadi et al. 2020a). A thermal-based index considers temperature and other parameters, including relative humidity, wind speed, and a person's thermal response characteristics. Although they seem intuitively more reasonable than temperature-based indices, thermal-based methods require more inputs (indoor conditions and occupant parameters) and are therefore more complicated to calculate, as a result many previous studies have chosen to use temperature-based indices for convenience. Although the temperature is commonly regarded as an

important factor in building overheating analysis, other thermal-related parameters such as relative humidity (related to sweating rate) and airspeed (related to evaporative heat release) have not been proven to be essential parameters to include in overheating studies. So the difference between using a temperature-based index and a thermal-based index needs to be evaluated quantitatively, to permit selecting the more reliable index. Currently, there is no consensus on the standard practices for the selection of EHY or indices. It may be possible to select both temperature and thermal indices in an actual situation, which, however, could overcomplicate the analysis. Therefore, it is still preferable to rely on one criterion to identify a unique EHY for a given city, which should not vary amongst different studies. As such, one of the objectives of this study is to evaluate the temperature-based and thermal-based indices in the selection of an EHY.

The second issue that needs to be resolved is related to the various types of heatwave events (i.e., as may result from different durations, severity, and intensity), and those also resulting in multiple EHYs. Hamdy et al. (2017) quantify the severity of outdoor heatwaves, the so-called outdoor ambient warmness degree, by the time-averaged deviation between the outdoor air temperature and the threshold temperature of 18 ℃. Guo et al. (2019) took into consideration the intensity, duration, and total intensity of heatwave events. The intensity of a heatwave event is determined based on the difference in outdoor air temperature to that of the threshold temperature (35 ℃), whereas the duration is the number of days or hours when the air temperature is higher than the same threshold, and finally, the total intensity is defined as the integration in time of the difference between the air temperature and threshold temperature. Guo et al. (2019) selected three THYs, including THY-I based on the total heatwave intensity, THY-E based on the maximum heatwave intensity and duration, and THY-N by the number of hot nights. Machard et al. (2020) characterized heatwaves in terms of maximal temperature, duration, and intensity, based on three

percentile thresholds calculated from mortality data based on historical heatwaves. In the study of Machard et al. (2020), the duration of a heatwave was the period when the air temperature exceeded the 97.5 percentile threshold, and the intensity was the ratio between the global intensity and the difference between the 99.5 percentile threshold and the 97.5 percentile threshold. The global intensity was the sum, for each day of a heatwave event, of the positive difference between daily mean temperature and the 97.5 percentile threshold.

Laouadi et al. (2020a) selected the duration, severity, and intensity of outdoor heatwave events. The severity was determined as the time integration of the difference between the outdoor standard effective temperature (SET) and its threshold (30 ℃). The duration was the number of days when the daily severity exceeded the threshold value, and the intensity was the ratio of the severity to the duration. Laouadi et al. (2020a) also selected three types of Reference Summer Weather Year (RSWY) having the maximum heatwave event duration, severity and intensity as criteria for selection. Practically speaking, having multiple EHYs complicates the selection and analysis process, especially when using long-term historical weather data for building simulations. For example, separate building overheating analyses could be required for up to six different EHYs (2 selection indices × 3 heatwave types). In contrast, such an overheating analysis often targets the same objective which is to evaluate and reduce an occupants' thermal risk. The process becomes quite challenging when multiple city locations are considered each having long-term weather data files required to complete the analysis (e.g., 31 years). Therefore, another objective of this study was to evaluate the types of heatwave events (long, severe, intense) used for EHY selection and then explore the possibility of selecting one representative EHY instead of having to complete an anlysis with several EHYs.

In summary, because of the nature of outdoor heatwave events and existing practices in respect to different selection criteria, multiple EHYs could be selected. The question that is posed is whether it is possible to develop a method to evaluate the EHYs using different selection criteria and from which the preferred approach to selection can be proposed, following which a unique EHY may be identified for a given city. The proposed method would be expected to address and quantify the significance of different indices and permit selecting the most important EHY. No existing study has been completed where multiple EHYs were compared for which the selection was based on temperature and thermal indices according to the duration, severity, and intensity of heatwave events. There is also a lack of information on selecting the most important EHY as compared to the use of multiple EHYs.

In this study, a method to identify a unique EHY is proposed and compared using different indices and types of heatwaves based on the concept of "synchronization" of the outdoor heatwave and the indoor overheating. Unlike meteorological or climate studies focusing on outdoor heatwave events, a building overheating analysis is "indoor-overheating centric" and is intended for evaluating the indoor thermal response of building occupants. The impact of heatwave events on the indoor thermal environment is based on outdoor weather conditions and building characteristics that cannot be simplified by being purely driven by outdoor weather parameters. As such, it is important that the EHYs are also those years when indoor overheating is most likely to occur. Building overheating analysis focuses on the concept of the synchronization between the outdoor heatwave event and indoor overheating so that an EHY can be selected based on the increased likelihood of occurrence of this synchronization. In other words, although outdoor heatwave events could manifest different behaviour, the indoor thermal response could nonetheless be similar or these different heatwave events: an extreme year could be selected for

the highest (higher) probability of building thermal response. For example, a year should be selected with a higher chance of creating the longest, most severe, or most intense, indoor overheating. A similar idea to the "indoor-overheating-centric" approach to selecting extreme weather data has been mentioned in previous studies. Guo et al. (2019) proposed choosing the extreme weather data based on a long-term indoor thermal scenario for a typical residential building. The concept of indoor extreme year is therefore adopted in this study. Laouadi et al. (2020a) validated the selection of outdoor EHYs by their consistency with indoor-based extreme years. However, a quantifiable approach has still not yet been developed or extended to broader applications.

In this study, EHY selections are evaluated concerning the suitability of different heatwave indices, or definitions, based on the indoor-overheating centric concept. Unlike previous studies where multi EHYs were selected based only on outdoor weather data, the innovation in this study is consideration of both outdoor extreme weather and building thermal response simultaneously. Hence the objectives in this study are to:

- Explore the possibility of selecting a representative EHY based on the idea of "synchronization" of the outdoor and indoor extreme years.
- Evaluate the temperature-based and thermal-based indices in the selection of EHY for an indoor-overheating centric analysis and illustrate the importance of using the thermal-based index.
- Compare the three types of heatwave parameters (duration, severity and intensity) in the selection of EHY for an indoor-overheating centric analysis and determine the most important parameter affecting the selection of EHY.

As well, given that the building thermal response is being evaluated, buildings with representative configurations and operating conditions should be considered, as has been previously recommended in the studies of Guo et al. (2019) and Laouadi et al. (2020a). Therefore, in this study, archetype building models were employed to represent typical old and current construction practices and building operations, including shading systems, natural ventilation, and intermittent cooling systems. In the subsequent sections, the method of obtaining the percentage of synchronization (POS) is first introduced, and thereafter an in-depth discussion is provided on the definition of an extreme year, long-term climate data, building simulation, and analysis of results.

5.2. Methodology

The proposed methodology is illustrated in Figure 5-1 for the percentage of synchronization (POS) of the outdoor extreme years (left column) and indoor extreme years (right column) (Guo et al., 2019), which are defined following an existing method for three different types of heatwave events (Laouadi, et al. 2020a, 2020b). The procedure is as follows: With the long-term climate data of air temperature, relative humidity, atmospheric pressure, and wind speed, the heatwave events are evaluated either by using the temperature-based index or thermal-based index (SET). The calculation method of SET is shown in the Appendices A.1.The duration, severity, and intensity for each heatwave event are calculated. The EHYs are then selected based on yearly heatwave events to obtain the longest, most severe, and most intensive weather year. The indoor thermal situation is identified by building simulations using long-term climate data. The indoor overheating conditions are then evaluated to determine the extreme years indoors following a similar method for identifying outdoor EHYs. The synchronization of outdoor and indoor weather years is quantified using the percentage of synchronization (POS) for a given city. The suitability of a

selected weather year, the selection criteria, and the type of heatwave event can then be indicated by the values calculated for their POS. A higher value for POS implies that the selection approach, or the weather year, is more suitable for conducting an indoor-overheating centric study. It should be noted that the method uses long-term weather data to select the EHY, but does not generate any new weather data. In this paper, the use of this method is illustrated using historical weather data although it can also be applied to future scenarios should future weather data be available. Also note that according to the information provided in previous studies (Laouadi et al., 2020a) and that given in this study, the synchronization-based weather year selection could depend on building types. Therefore, it may be possible to identify a universal weather year when multiple archetype buildings are evaluated so that the year with the highest POS score for different building types can then be selected following the proposed method. This signifies that for most of the buildings evaluated, the selected year covers most of the cases having a higher chance of occurrence of indoor and outdoor heatwave events. Although the proposed method could initially be cumbersome to use, the resultant weather year will be unique, and this will simplify the complex analysis of other building simulations once it is determined.

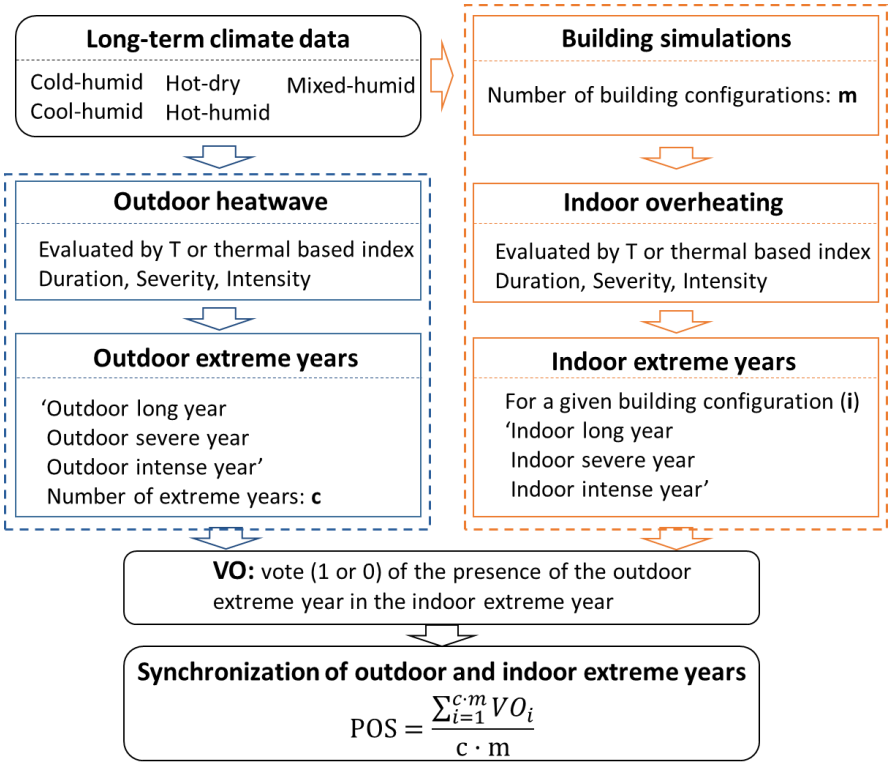

Figure 5-1 Schematic of the proposed methodology to select extreme years and evaluate synchronization

The POS value for outdoor and indoor extreme years is defined as the percentage of occurrence of any of the outdoor EHYs for the indoor extreme years in respect to a given building type under local climate loads; the POS is quantified according to that given in Equation 5-1:

$$\mathrm{POS} = \frac{\sum_{i=1}^{c \cdot m} VO_i}{\mathrm{c \cdot m}} \tag{5-1}$$

where VO is the vote (1 or 0) in respect to the presence of an indoor extreme year for a given building configuration, m is the number of archetype building configurations, and c is the number of types of extreme years taken into consideration. The criterion of VO=1 indicates that the indoor extreme year is the same as any of the outdoor extreme years. For example, the indoor extreme long duration event heatwave year is the same as any outdoor extreme long duration/severe/intense year. When comparing the POS of different extreme year types (long/severe/intense), the POS of

each type needs to be calculated, and as such, c=1; when evaluating the value of POS for a type of building or a city, the POS value of three types of extreme years all need to be considered, hence in this instance, c=3. A calculation example of POS and details about the vote criteria are provided in Section 5.3.2.

5.2.1 Outdoor and indoor extreme years

In this study, both the thermal-based and temperature-based indexes were used to determine outdoor and indoor extreme years. Most of the traditional methods to select extreme weather data use temperature-based indices. In this study, when the temperature-based index is used, the heatwave duration is measured in terms of the number of days of a continuous heat event. The severity ($°C^2 \cdot h$) is given in Equation 5-2, which is the weighted number of cooling degree hours, as adopted by CIBSE TM49 (2014), to select EHYs. The intensity ($°C^2$) of a heatwave event is calculated as the ratio of severity to the duration of the event, expressed in hours.

$$\text{WCDH} = \sum_{i=1}^{N} \sum_{t=1}^{24} (T_o - T_{cu})^2 \quad (5\text{-}2)$$

Where T_o is the hourly daily operative temperature and Tcu is the adaptive threshold temperature for the location under consideration, calculated using the running mean of the outside dry-bulb temperature (CIBSE, 2014); weather variables other than temperature are not considered.

In comparison, the thermal-based index uses the comfort index for the transient Standard Effective Temperature (t-SET) (Laouadi et al. 2020a) and considers the effect of other weather variables including dry bulb temperature, relative humidity, airspeed, and a reference person's posture and clothing level, which is used to evaluate the effect of heat events on building occupants from a thermal comfort perspective. With t-SET as an index, the severity ($°C \cdot h$) of a heat event is given

by Equation 5-3 (Laouadi et al. 2020a, 2020b). The duration (d) and intensity (°C) are defined using the same method as above.

$$\mathbf{SETH} = \sum_{N} \mathrm{SETH_d}+\mathrm{SETH_n} = \sum_{dayhour}[\text{t-SET} - \text{t-SET}_\mathrm{d}]^{+} + \sum_{nighthour}[\text{t-SET} - \text{t-SET}_\mathrm{n}]^{+} \quad (5\text{-}3)$$

Where N is the duration (in days) of a heat event, $\mathrm{SETH_d}$ is the severity of the event during the daytime, $\mathrm{SETH_n}$ reflects the preceding nighttime severity, t-SET is the hourly SET value during the day or night time, t-SETd and t-SETn are the t-SET threshold values, respectively, during the day and night time. For both the outdoor heatwave and indoor overheating, the value of t-SETd is fixed at 30°C. The value of t-SETn for an outdoor heatwave event is 26°C, and t-SETn for an indoor overheating event is 30°C, when considering the neutral thermal level for occupants sleeping on a mattress. The "+" sign means only positive values are considered for analysis. A heat event is declared if the $\mathrm{SETH_d}$ value exceeds 4 °C·h for at least two successive days (Laouadi et al. 2020a).

With the above thermal-based index or temperature-based index, the duration, severity, and intensity of each heat event over the long term can be identified. Three extreme years (i.e., with the longest, the most severe, and the most intense heat events) were selected. It should be noted that the outcome from the selection process of three years might be the same year, or two years, or indeed, three different years.

5.2.2 Long-term climate data

Long term climate data, consisting of a continuous time series of historical data comprising hourly values of air temperature, relative humidity, atmospheric pressure, wind speed and direction, total cloud cover, solar radiation (global horizontal, direct normal, and diffuse horizontal), and snow-

cover was prepared for selected Canadian and US cities located in different North American climate zones. According to ASHRAE Standard 169-2013 (ASHRAE, 2013a), Canada and the US have eight temperature-based climate zones and three moisture regimes, the moisture regimes being classified as A, B, or C. From Canada, three cities were selected for analysis: Ottawa (Ontario), Montreal (Quebec) from climate zone 6A (Cold-Humid), and Toronto (Ontario) from zone 5A (Cool-Humid). Those selected from the USA, included the cities of: Baltimore (Maryland), Houston (Texas), and Phoenix (Arizona) representing climate zones: 4A (Mixed-Humid), 2A (Hot-Humid), and 3B (Hot-Dry), respectively.

The historical climate data for the Canadian cities were prepared for the period of 1986-2016 by collecting observations of historical climate from Environment and Climate Change Canada (ECCC, 2018) and filling in missing values from bias-corrected Climate Forecast System Reanalysis (CFSR) data (Saha et al. 2010) to prepare a complete time-series. A detailed description of the methodology used is described in (Gaur et al., 2019). For the US cities, the data was prepared for the period of 1991-2010. The hourly historical climate time series for air temperature, relative humidity, atmospheric pressure, wind speed and direction, total cloud cover variables were collected from the Climate Forecast System Reanalysis (CFSR) database (Saha et al. 2010). The hourly solar radiation data, including global, direct, and diffuse radiation, were taken from the National Solar Radiation Data Base (NSRDB, 2012).

Table 5-1 Archetype building model parameters for each city

City	Toronto Montreal, Ottawa		Baltimore		Houston Phoenix		Toronto Montreal, Ottawa	
Climate zone	Cool-Humid Cold-Humid		Mixed-Humid		Hot-Humid Hot-Dry		Cool-Humid Cold-Humid	
Building type	Single-detached house						Row house	
Orientation of windows	N-S-E-W		N-S-E-W		N-S-E-W		N-S (or E-W)	
Footprint area (m^2)	80		80		80		110	
Window Wall ratio (%)	16		16		16		24	
Construction	Old	Current	Old	Current	Old	Current	Old	Current
Exterior Wall Effective R (m^2 KW^{-1})	1.83	3.17	1.25	2.08	0.61	1.44	1.83	3.17
Basement Wall Effective R (m^2 KW^{-1})	0.1	1.26	0.1	1.26	0.1	1.26	0.1	1.26
Basement Floor Effective R (m^2 KW^{-1})	0.26	1.69	0.26	1.69	0.26	1.69	0.26	1.69
Attic insulation Effective R (m^2 KW^{-1})	3.6	8.2	1.43	7.76	1.2	6.2	3.6	8.2
Window U-Value (W m^{-2} K^{-1})	2.58	1.58	2.69	1.4	2.69	1.4	2.58	1.58
SHGC	0.7	0.67	0.5	0.31	0.5	0.31	0.7	0.67
Design Infiltration Rate (ACH@50Pa)	6.86	2.32	6.86	2.32	6.86	2.32	9.32	2.8

5.2.3 Building Data: Archetype building models and configurations

This study focuses on typical residential building construction as is prevalent in North America based on archetype house models. The reason for selecting residential buildings is that most of the historical heatwaves fatalities occurred in residential homes, as demonstrated by the 2018 heatwave that occurred in Montreal, Canada (Lamothe et al., 2019) and as well, that of the 2003 European heatwave (Vellei et al., 2017). Natural Resources Canada (NRCan) has generated archetype building models based on rating over 500,000 homes across Canada (Parekh et al., 2012). Therefore, the single-detached home and row house archetype buildings were used for this study. The house models were created using EnergyPlus software (DOE, 2020). Each home model has two above-ground floors, an attic space and a full basement. The first floor was assigned to

the living room, where occupants may spend most of their time during the daytime, and the second floor was the bedroom. Internal heat gains from occupancy, lights, and equipment were taken from the National Building Code of Canada (NRC, 2015) specifically: 3 people per home, lighting gains =5 W/m^2, and; equipment heat gains = 5 W/m^2. According to the International Energy Conservation Code, the single-detached archetype house model is also applied to USA locations, but considering local construction practice in accordance with the International Energy Conservation Code (IECC, 2018). The basement boundary wall and floor surface temperatures were pre-calculated by running the basement and slab pre-processor in EnergyPlus (DOE, 2020).

The building age affects building overheating conditions. A higher overheating risk is often found in new homes (French, 2008) and new apartment buildings Maivel et al. (2015) as compared to older buildings because of higher glazing surface areas, lower ventilation rates, reduced external shading, and to a lesser extent increased levels of thermal insulation in newer homes. In retrofitted buildings, strategies including improved airtightness, higher-level insulation, high-performance windows, and large south-facing windows that would increase overheating risk (Mavrogianni et al. 2013; Ibrahim and Pelsmakers, 2018; Gupta et al, 2019). Therefore, both older (1980s) and current construction practices were considered for the archetype buildings. The home construction characteristics for each city and climate zone are summarised in Table 5-1. The single-detached home has windows on each facade on the first and second floors, whereas the row house has windows on the south and north facades (N-S orientation) or east and west facades (E-W orientation).

Apart from the building construction age, building operation could also alter indoor conditions. As well, shading systems affect solar heat gains through windows and therefore the risk of overheating. Exterior shadings such as external shutters, awnings, and overhangs are found to

reduce the risk of overheating (Zinzi et al., 2017; Ruff et al., 2018). Strategies such as natural ventilation and night cooling are also typical methods to reduce indoor heat discomfort while avoiding, or minimizing, the need for mechanical cooling in buildings (Brotas and Nicol, 2016; Stazi et al., 2017). Although cooling systems are perhaps considered an efficient solution to resolve overheating problems in buildings, many countries have encouraged or mandated the adoption of passive cooling measures for existing and new buildings to permit complying with energy efficiency and carbon emission standards (ASHARE, 2013; Committee on Climate Change, 2019). As such, passive operation measures for the building models investigated in this study were considered. Furthermore, the rapid use of air-conditioning during heat events may have a major impact on summertime electricity demand and would increase the risk of HVAC failures or blackouts (Ostro et al., 2010). Given this possibility, operation measures such as intermittent cooling should also be considered in the building models studied.

Taking all of the information into consideration, seven (7) different building operation measures were applied to archetype homes that included both old and current construction practices, as shown in Table 5-2. The seven (7) selected measures, based on the above literature, were to include measures that influence indoor overheating conditions. The proposed method can be applied to other cases should there be interest in evaluating additional measures. In this study, three (3) primary passive measures were considered, including the use of interior blinds, exterior screen shadings, and natural ventilation (i.e. opening windows). Interior blinds were opened by setting the slats in a horizontal position (slat angle 90°) and closed by setting the slats' vertical position (slat angle 175°). Exterior screen shades were always set closed with a 5% openness factor. The above three (3) configurations were combined with natural ventilation. Natural ventilation was realized by opening windows by 25% when the indoor temperature exceeded both 26°C and the

outdoor temperature. The impact of intermittent cooling was also considered by operating a central air-conditioner (when windows are closed) to supply cool air to the living room and bedroom during the daytime from 11:00 am to 6:00 pm (M7 measure, applied to the single home model based on current construction practice). A relaxed setpoint temperature was fixed at 30.6°C (Laouadi et al., 2020a,b), which corresponded to a t-SET= 30°C (corresponds to a slightly warm comfort level) at a relative humidity of 50%.

Table 5-2 Building operation measures for abating indoor temperature

Measure	Description
M1	Interior blinds open (slat angle: 90°) + closed windows
M2	Interior blinds closed (slat angle:175°) + closed windows
M3	Interior blinds open + opened windows
M4	Interior blinds closed+ opened windows
M5	Exterior shading closed + closed windows
M6	Exterior shading closed + opened windows
M7	Interior blinds closed + closed windows + intermittent cooling

Building simulations were conducted using the weather and building data as was previously described. For Canadian locations, the simulations were conducted over 31 years (1986-2016); for USA locations, simulations were conducted for 20 years (1991-2010). In total, 5,661 simulations were conducted for the selected building models and locations. From the simulation results and POS analysis, a unique EHY can be selected for each city.

5.3. Results

5.3.1 Outdoor extreme years

Figure 5-2 shows the distribution of EHYs of the six cities forming part of this evaluation study based on thermal-based and temperature-based indices. The majority of the EHYs selected using

either of the two indices are different. The thermal-based EHYs are often above the Y=X line, indicating they often occur in a later year than the temperature-based extreme year. About 70% of the thermal-based extreme years range between 2000-2013, whereas 70% of the temperature-based years vary between 1998-2006. As such, the distribution of thermal-based extreme years shows a trend of increasing heatwave events in more recent years whereas the latter does not, suggesting that the thermal-based years seem more consistent with recent and actual heat events for these cities. For example, in Montreal, Canada, the most lethal heatwave occurred in 2010, causing 9.3 deaths per million population (Lamothe et al., 2019). This is consistent with the overall trend of climate change. Figure 5-2 also shows most of the cities have different years identified for these two different indices, whereas three cities have the same year identified from the thermal-based and temperature-based indices: Baltimore (Long heatwave year), Ottawa (Intense heatwave year), and Montreal (Intense heatwave year).

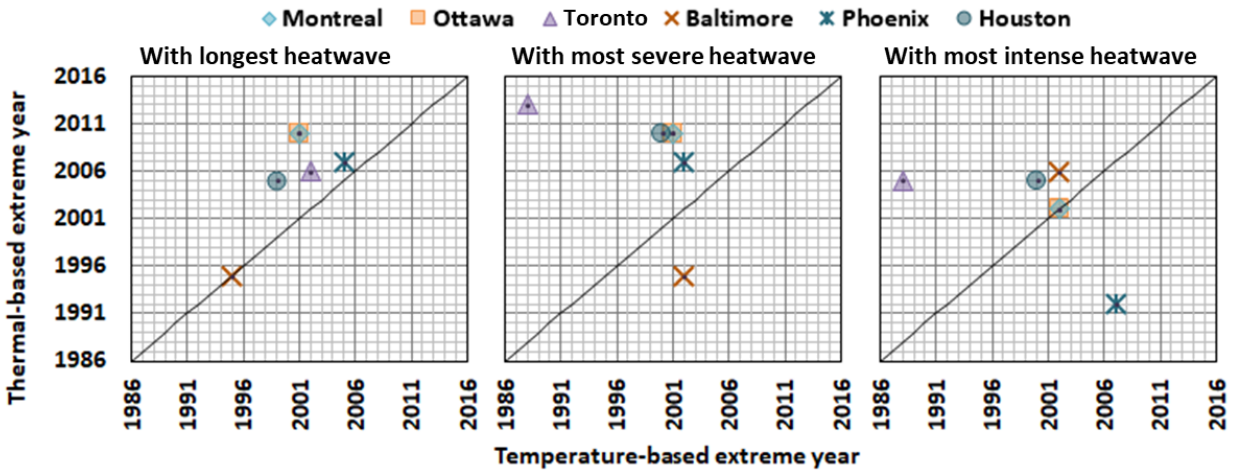

Figure 5-2 Different outdoor extreme years selected by thermal-based index and temperature-based index for different heatwave types.

Figure 5-3 provides a comparison of the magnitudes of three types of outdoor extreme years for each of the six city locations. The six cities are ranked from higher to lower latitude. As may be

apparent, the heatwaves become more severe as the latitude decreases. The difference in EHYs obtained from thermal and temperature-based indices can be understood by focusing on the cities of Phoenix and Houston. Phoenix is located in a hot-dry climate zone (2A), whereas Houston is situated in the hot-humid climate zone (3B); understandably, the humidity levels of the two cities are significantly different. With the thermal-based index, the duration, intensity, and severity of heatwaves in Phoenix are weaker than those experienced in Houston. In contrast, using the temperature-based index, Phoenix is subject to more acute heatwave events than Houston. This difference arises because the thermal-based index includes the effect of the higher humidity as is present in the hot-humid climate zone whereas the temperature-based index only considers the temperature.

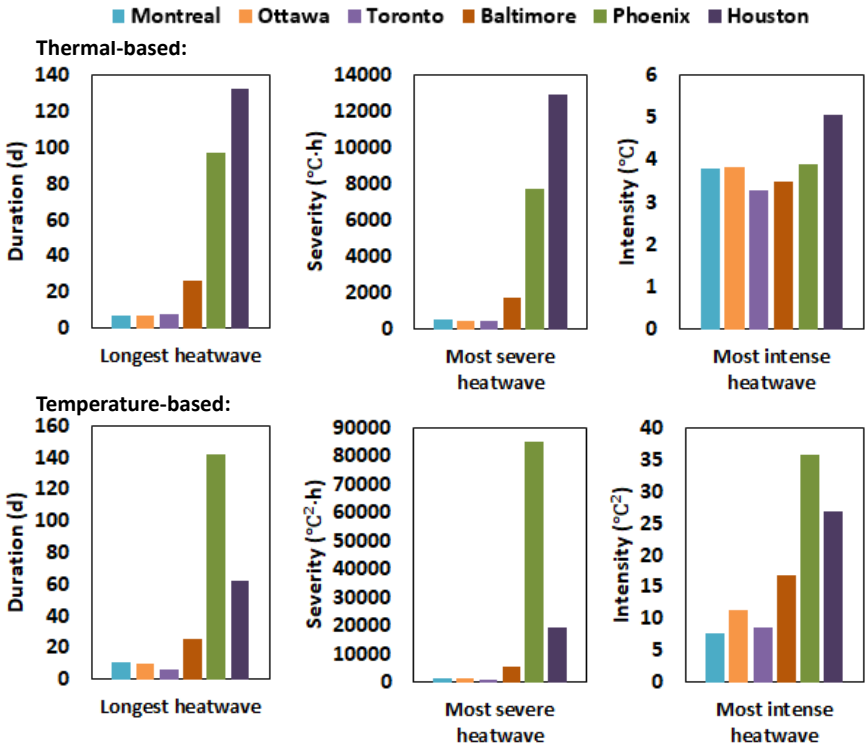

Figure 5-3 The duration, intensity, and severity of heatwave events in EHYs for each city

5.3.2 Indoor extreme years and POS calculation

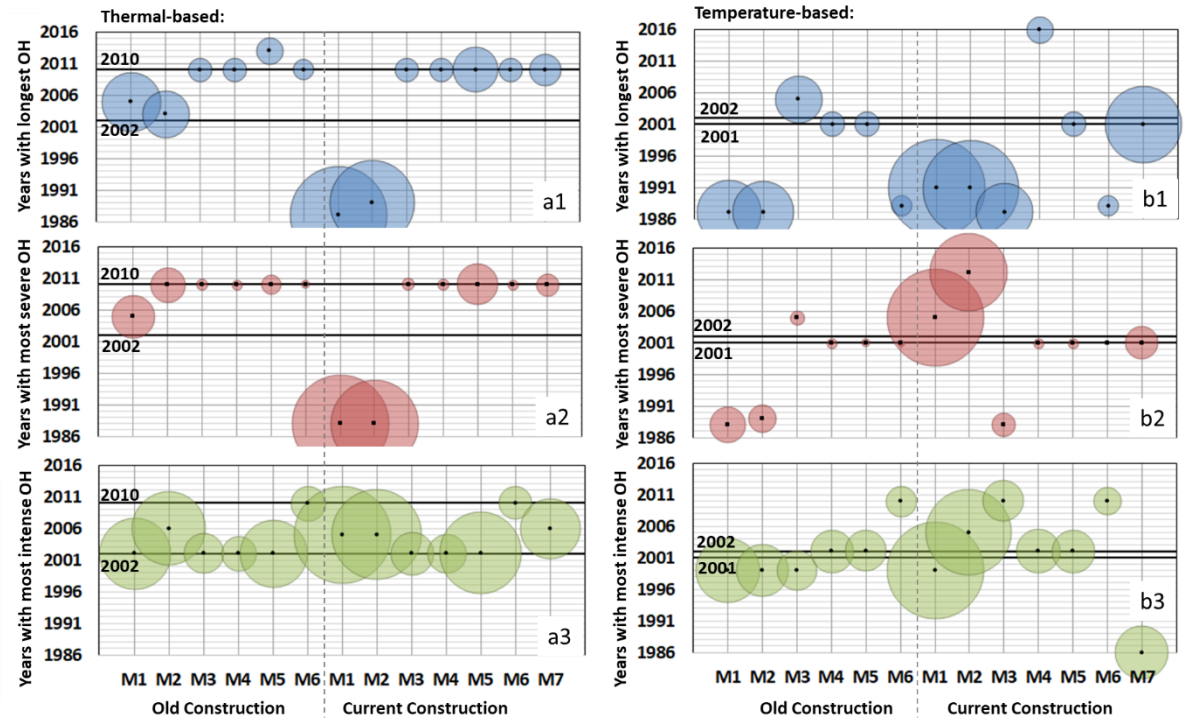

Figure 5-4 Indoor extreme years and overheating (OH) magnitude (relative) for single-detached home located in Ottawa (Ontario) and for various configurations Note: Black dots represent the indoor extreme year for each configuration; the bubble size relates to the duration (Blue), severity (Red), and intensity (Green) of indoor overheating, respectively; the solid lines in each subfigure correspond to outdoor extreme years

To illustrate the method to calculate POS, the results of indoor and outdoor extreme years for the single-detached home and row house (N-S) located in Ottawa, Canada, are presented and compared. The effects of different climate zones and building orientations will be analyzed in subsequent sections. Figure 5-4 shows the indoor extreme years (black dots) with the longest, most severe, and most intense indoor overheating (OH) for each building configuration in Ottawa and

the relative magnitude of indoor overheating. The outdoor extreme years (solid horizontal lines) are also shown to permit a comparison with the indoor extreme years.

Figure 5-4a shows the extreme years as determined from the use of the thermal-based index. As already mentioned in Section 5.3.1 (Figure 5-2), the thermal-based outdoor extreme years have been identified as 2010 (having the longest and most severe heatwave) and 2002 (with the most intense heatwave). For the majority of building measures, indoor extreme years (black dots) with the longest (Figure 5-4a1) and most severe (Figure 5-4a2) indoor overheating are located on the lines of the outdoor extreme year (2010), with the exception of M1 and M2 for older and current construction, and M5 for older buildings. For the majority of building measures, indoor extreme years experiencing the most intense (Figure 5-4a3) overheating are 2002, with the exception of M2 and M6 of older buildings, and M1, M2, M6, and M7 for buildings of the current construction practice. However, for M6, 2010 is identified as the indoor extreme year with the most intense overheating for older and current buildings. It is evident that having multiple selection criteria and different heatwave events complicated the analysis.

The use of POS is proposed as a means to permit synthesizing the data and thus simplifying the process of determining an EHY, as is shown in Table 5-3. The vote count for the occurrence of an outdoor extreme year given an indoor extreme year is 1 when the indoor and outdoor extreme years "synchronize" (i.e., when the dots align along with one of the solid lines). For example, for buildings of older construction and M1, the indoor extreme year for long duration events (Figure 5-a1) is 2005, which is different from 2010 and 2002 (the dot is not located on any of the solid lines), hence the vote is 0; for older construction and M3, the indoor extreme year for long duration events is 2010 (Figure 5-4a1), which is the same as the outdoor extreme year for long duration events; the vote is thus given as 1.

Table 5-3 Calculation example of POS of single house located in Ottawa, Canada (heat events based on thermal-based index)

Building age	Building operation measure	Vote of indoor extreme years presence in outdoor extreme years		
		Long Year	Severe Year	Intense Year
Old Construction	M1	0	0	1
	M2	0	1	0
	M3	1	1	1
	M4	1	1	1
	M5	0	1	1
	M6	1	1	1
Current Construction	M1	0	0	0
	M2	0	0	0
	M3	1	1	1
	M4	1	1	1
	M5	1	1	1
	M6	1	1	1
	M7	1	1	0
Sum of votes		8	10	9
Sum of building configurations		13	13	13
POS (c=1, m=13)		62% = 8/13	77% = 10/13	69% = 9/13
POS (c=3, m=13)		70% = (8 + 10 + 9)/(13 × 3)		

When comparing the POS value of each of the three types of extreme years (long duration / severe / intense), the POS of each type needs to be calculated (c=1). For example, considering the synchronization of outdoor and indoor extreme years for long duration events (Figure 5-4a1), the total votes is 8 (i.e. summation of votes in the first column of Table 5-3). The total number of building configurations, m, is 13 (M1-M6 for older construction and M1-M7 for current construction), so the POS value is 62% (8/13), which indicates there 62% of the cases for which the indoor heatwave of longest duration occurs during the outdoor extreme years (i.e. these EHYs are "synchronized"). The year having the most number of "synchronizations" for the duration of a heatwave is 2010. In other words, 2010 is the year having outdoor heatwave events with the longest duration and as well, indoor overheating events with the longest duration for most of the archetype

buildings located in Ottawa. Using this same procedure, the POS values for outdoor and indoor extreme severe years were calculated as 77% (2010 for Ottawa), and the POS value of outdoor and indoor extreme intense years was 69% (2002 for Ottawa).

When all heatwaves are considered regardless of their types (c=3), the total vote is 27 (8+10+9), and the total number of building configurations, m, is 13, producing a POS value of 70%. This means that 70% of the cases may experience both indoor and outdoor heatwaves for a single home in Ottawa. Measures M1, M2, M5, and M7 are all without natural ventilation and lack air and thermal exchange with the outdoors, hence this could be the reason why their indoor extreme years are not synchronized with the outdoor extreme years. In real buildings, the scenarios for measures M1 and M2 (i.e. closed windows + interior blinds open (M1) or closed (M2)) could not last long in summer because they would eventually lead to higher indoor temperatures. Figure 5-4b shows the temperature-based indoor and outdoor extreme years. Compared to thermal-based extreme years, temperature-based indoor extreme years are much less synchronized with outdoor EHYs (fewer black dots are located along the solid lines).

The bubble size in Figure 5-4 indicates the magnitudes (duration, severity, and intensity) of indoor overheating. No matter whether a thermal-based (Figure 5-4a) or temperature-based overheating index used (Figure 5-4b), duration and severity of indoor overheating of buildings having temperature abatement measures M1 and M2 are greater than other measures, which implies that the use of interior blinds has a limited effect on reducing indoor overheating risk. The intensity of indoor overheating for all abatement measures is relatively similar.

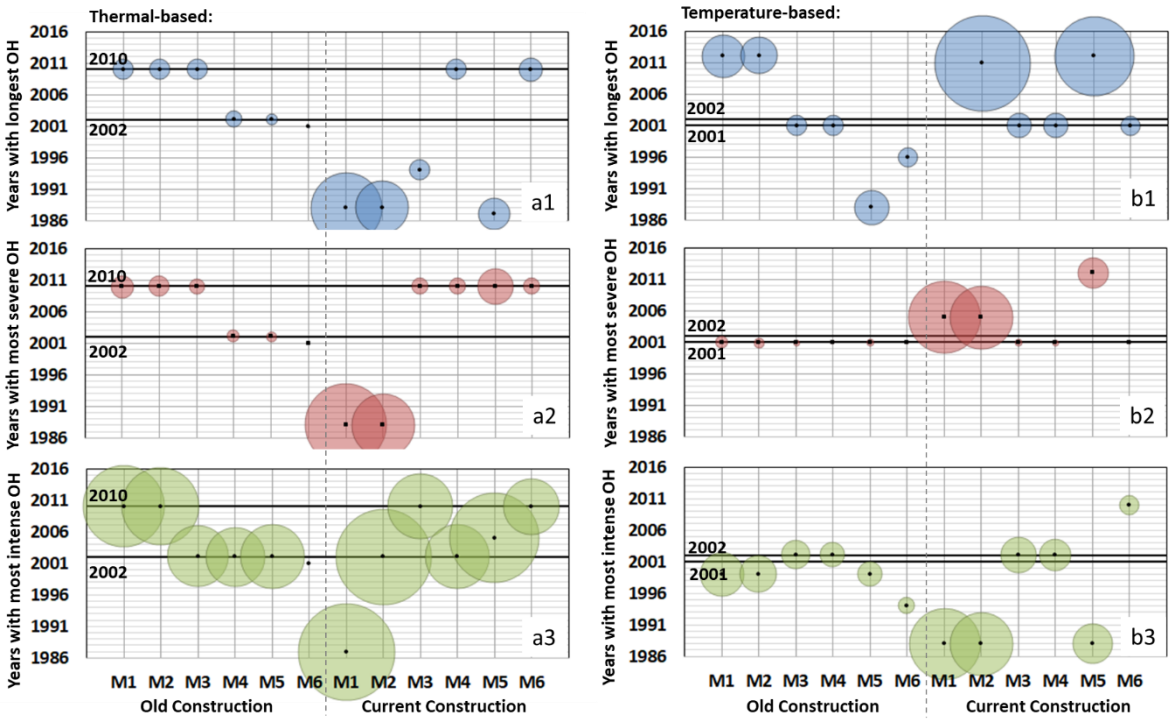

Figure 5-5 Indoor extreme years and overheating (OH) magnitude (relative) for row houses (N-S orientation) of various configurations located in Ottawa (Ontario). Note: Black dots represent indoor extreme year for each configuration; the size of bubbles indicates the duration (Blue), severity (Red), and intensity (Green), respectively, of indoor overheating; the two solid lines in each subfigure correspond to each of the outdoor extreme years.

Figure 5-5 shows the indoor extreme years (black dots) with the longest, most severe, and most intense overheating for row houses having windows located in the N-S orientation. The outdoor EHYs are also shown in the figure to permit comparing these to indoor extreme years. Similar to that obtained for the single-detached home, for the majority of building operation measures to abate indoor temperatures, thermal-based indoor extreme years are synchronized with the corresponding outdoor EHYs, whereas there is much less synchronization for the temperature-based selection. As for the magnitude of overheating, compared to the single home (Figure 5-4a1,

a2; b1,b2), the duration and severity of indoor overheating is lower for the row house (Figure 5-5a1,a2;b1,b2), which for row houses is due to the windows only being located in the N-S orientation (according to the original archetype building models created based on actual statistics), whereas for a single home, windows are oriented in all the four orientations. The thermal-based intensity of indoor overheating for a row house (Figure 5-5a3) is similar to that of a single home (Figure 5-4a3), whereas the temperature-based intensity of indoor overheating for the row house (Figure 5-5b3) is less than that of the single home (Figure 5-4b3), which indicates that the temperature-based index may underestimate the intensity of overheating risk.

5.3.3 EHY selections based on percentage of synchronization (POS)

In this section, the values of POS for the thermal-based index are compared to that of the temperature-based index taking into consideration the three types of heatwave events (i.e. long duration, severe, and intense) for different climate zones. A higher value of POS means it is more suitable to choose an index and to choose a heatwave type.

Figure 5-6 compares the POS value for the thermal-based and temperature-based indices. Figure 5-6a shows that the thermal-based POS is higher than the temperature-based POS for all three building types (i.e single home; row house-NS windows; row house-EW windows). Figure 5-6b shows the POS values for the single-detached home located in the five climate zones considered in this study. All cases indicate that the thermal-based POS value is higher than those of the temperature-based POS values. When comparing hot-dry and hot-humid climates, thermal-based POS values are much higher for hot-humid climates because the thermal-based index considers the effects of humidity.

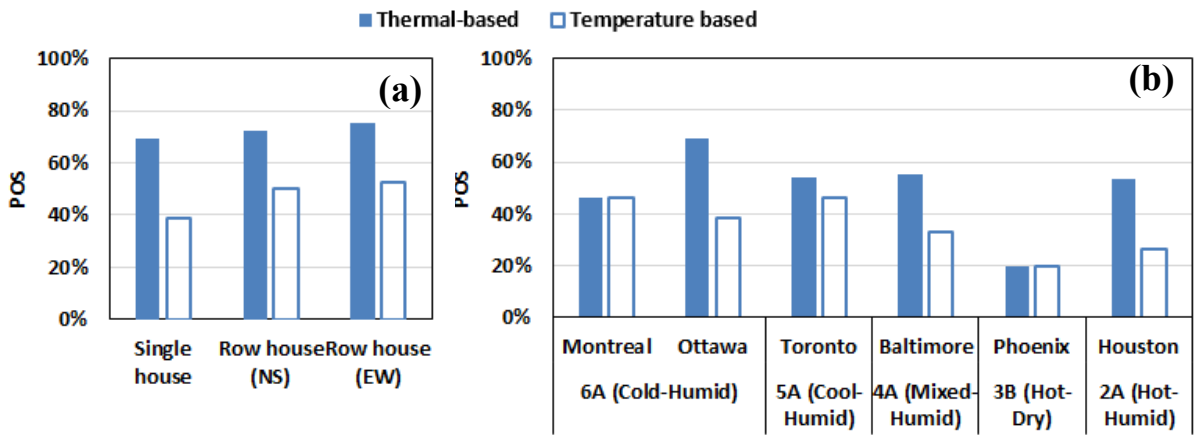

Figure 5-6 POS values with effect of thermal-based and temperature-based indices for (a) different building types (b) five climate zones.

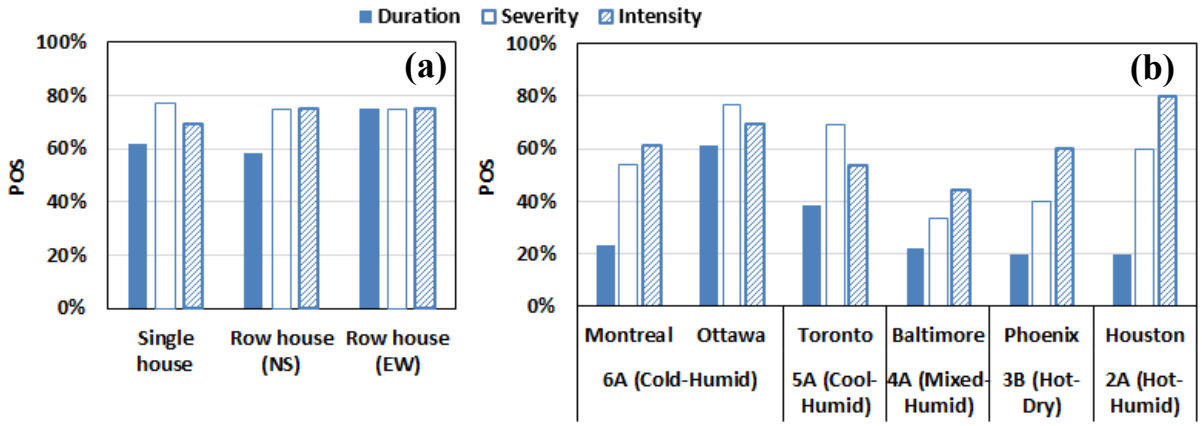

Figure 5-7 Thermal-based POS values in respect to three types of overheating events (duration/severity/intensity) for (a) different building types (b) five climate zones

In Figure 5-7 a comparison of the thermal-based POS values is shown for the three types of heatwave events (duration /severity/intensity). According to that shown in Figure 5-7a, severity-based and intensity-based POS values are similar for the three building types and higher than the duration-based POS value. The thermal capacity of the building envelops delays the occurrence of indoor overheating and mismatches the durations of outdoor and indoor extreme heat events. From Figure 5-7b, the severity-based and intensity-based POS values are higher than that of the duration-

based POS values for all climate zones. The highest severity-based POS value occurs in a cold-humid climate. The highest intensity-based POS values arise in the hot-humid climate, which indicates that it is better to select EHYs in cool or cold climate zones based on the heatwave type for which priority is given, in decreasing order of importance, to severity > intensity > duration. In contrast, in a mixed or hot climate, it is better to select EHYs based on the heatwave type for which the priority is given, as before in decreasing order of importance, to intensity > severity > duration. The severity and intensity of extreme heatwave events have been shown to cause health effects on humans, where severe exposure to heat (considering both time and magnitude) is likely to physiologically overwhelm body functions even without active awareness of the occupant under stress, such as during sleep (Anderson et al., 2013). People also tend to experience thermal discomfort due to short, hot periods because they have not had the opportunity to adapt their behavior or adjust their expectations (De Dear and Brager, 2002). In hot climate zones, the duration of heatwaves can extend from weeks to months, and as such, it is, therefore, important to evaluate heat-related health injuries over a short period.

Therefore, if a single extreme heatwave year needs to be determined as a reference, for the cool and cold climates it is recommended to choose the severe extreme year whereas for mixed or hot climates the intense extreme year should be chosen as reference, with either type of extreme heatwave year based on the thermal-based index. This conclusion has been reached based on the previous analysis of POS values reflecting the majority of the archetype buildings and occupant responses for a specific climate. Table 5-4 provides the unique EHY as a reference for each of the cities considered in this study.

Table 5-4 The unique EHY of each city.

City	Unique EHY	Extreme heatwave	
		Severity (°C·h)	Intensity (°C)
Ottawa	2010	436.5	2.6
Montreal	2010	521.7	3.2
Toronto	2013	431.9	3.0
Baltimore	2006	1088.1	3.5
Phoenix	1992	3924.4	3.9
Houston	2005	12418.1	5.1

5.3.4 Application – Building overheating evaluation by selected extreme years

To demonstrate the benefit of a single EHY identified, we evaluated building overheating conditions during heatwave events. According to the analysis given in Section 5.3.2, the overheating magnitude in a single-detached home is higher than that for a row house, so the former building type is evaluated in this section. Here, the thermal comfort metric SET is used to evaluate the indoor thermal comfort level: SET > 30°C indicates an uncomfortable and unacceptable hot condition, where occupants are likely to start sweating (Parsons, 2003). The temperature abatement operation measure M4 (closed interior blinds with open windows) is considered typical for cold climate locations, whereas measure M6 (closed exterior shades with open windows) is considered typical for hot climate locations. These selections are useful because the usage of window shadings is regionally dependent. For example, external shading devices in residential buildings are uncommon in temperate or cold climates such as those of Europe and other high latitude areas such as Canada, whilst windows in almost all dwellings have internal blinds or curtains (Mavrogianni et al., 2017).

Figures 5-8a-c show the indoor SET, air temperature, and relative humidity in a single-detached home of current construction practice and temperature abatement measure M4 during the most

severe thermal-based heatwave years that include: 2013 for Toronto, 2010 for Ottawa, and 2010 for Montreal. The simulations start at the same initial conditions but thereafter use different EHY data. The most severe heatwave in Toronto is longer in duration than in Ottawa and Montreal. During the heatwave, the daytime indoor SET is above 30℃ for four to six successive days, which leads to the heat stress of building occupants.

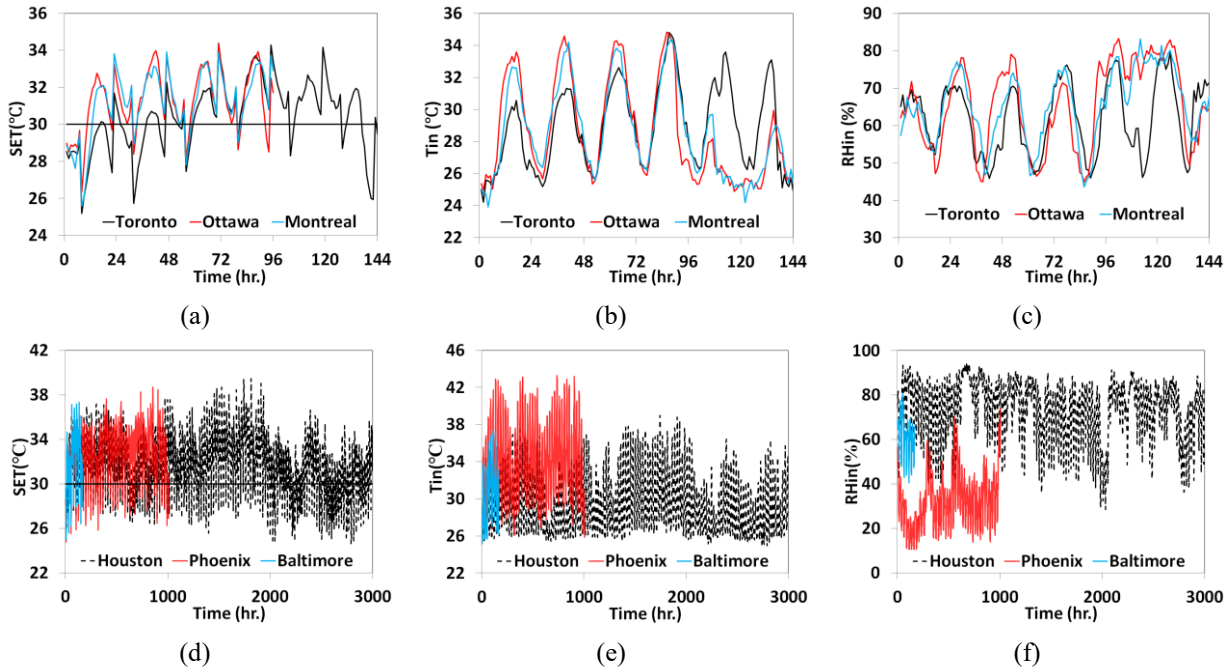

Figure 5-8 Indoor thermal conditions in single-detached home of current construction and using typical temperature abatement measure M4 during the most severe heatwaves in Toronto, Ottawa, and Montreal (a) (b) (c) and the most intense heatwaves in Houston, Phoenix, and Baltimore (d) (e) (f).

Figures 8d-f show the building indoor SET, air temperature, and relative humidity in the single-detached home of current construction and that includes temperature abatement measure M6 during the most intense thermal-based heatwave years that include: 2005 for Houston, 1992 for Phoenix, and 2006 for Baltimore. The intense heatwaves experienced in Baltimore, Phoenix, and Houston last 480h, 960h, and 3000h, respectively, amongst which the intense heatwave in Houston

covers the entire summer period. During the overlap period of heatwaves of these three cities, the building indoor SET is comparable and above 30℃ during successive days; this means the heat stress experienced by building occupants during these heatwave events is comparable. During the heatwave event in Houston, the building's indoor temperature is not the highest. Nonetheless, the indoor relative humidity is maintained at much higher levels than those found in the other cities, resulting in a continuously high level of building indoor SET and thus severe overheating.

5.4. Conclusions

In this study, a method has been proposed to quantify the degree of synchronization between outdoor heatwave events and building indoor overheating conditions based on the concept of POS (Percentage of Synchronization). A higher value of POS indicates a higher chance of building indoor overheating occurring based on outdoor heatwave events for the majority of archetype buildings and situations for specific climate zones. A higher value of POS also indicates that a selection method (temperature-based or thermal-based) or a heatwave type (i.e. longest duration, most severe, and most intense) could also result in a greater chance of overheating conditions arising in buildings. Should an extreme or worst scenario need to be evaluated, a selection method producing a higher value of POS is preferred since this is more significant when conducting building indoor overheating analysis using building simulations.

In summary, the conclusions are:

- In building overheating-centric studies, the EHYs should be selected according to the severity and intensity of heatwaves defined by the thermal-based index, especially for humid climates.

- The EHYs selected with thermal-based index result in higher POS than the temperature-based index for buildings located in cold to hot climate zones, especially in the climate zones with high humidity.
- The EHYs with the most intense and severe heatwaves lead to higher POS than the years with the longest heatwave, indicating the intensity and severity of heatwaves are more significant than the duration of heatwaves when selecting EHYs for building centric analysis.
- In cool or cold climates, the severe extreme year should be selected. In mixed or hot climates, the intense extreme year should be selected.
- The concept of POS (Percentage of Synchronization) can be applied to different types of buildings located in various climate zones to be used as a criterion to select the most significant EHYs for indoor overheating studies.

As previously mentioned, the POS-based EHYs are needed to permit evaluating archetype building responses to extreme heat events and as such, the selection could depend on building type and the temperature abatement operational measures used. Given these choices, different extreme years could be obtained. However, if a building archetype employing typical operational measures to abate indoor temperatures has been well defined, the proposed use of POS is entirely applicable. Since many reference building models (e.g. developed by DOE or NRCan) are developed based on the statistics of building stocks this is often the case. It may indeed be preferable that those developing reference models can apply this method to determine a unique EHY for each model type; this would benefit the building practitioner community, as the process needs to be undertaken but once for any given building type.

On the other hand, to further demonstrate its usefulness, the proposed method ought still to be applied to other building types, different building temperature abatement measures, and in different climate zones. The proposed method can be applied to selecting the unique extreme year, which might be time-consuming work. It is also possible to identify a unique EHY for most of the different building types or actual urban building stocks provided building information is available. This would help ensure that building-scale or urban-scale building overheating analysis can be simplified and consistent amongst all researchers.

As well, completing over 5000 building simulations to select a single weather file may be cumbersome. One alternative is to use the method of meta-models without then the need to run many building simulations. Also, the verified extreme years for the six cities of this study can be applied directly. The overall, contribution of this paper would is to propose an essential concept of synchronization between temperature-based and thermal-based indices for assessing extreme heat events and a new method using POS values, that can be applied to other cities around the globe, irrespective of their climate. In EHY selection for building overheating study, the thermal-based index is confirmed to be more suitable than the temperature-based index; the heatwave intensity and severity are more important than the duration.

Chapter 6 Quantifying Building and Zone Level Thermal Resilience against Summertime Heat Events

The contents of this chapter are published in "Lili Ji, Chang Shu, Abdelaziz Laouadi, Michael Lacasse and Liangzhu (Leon) Wang (2023), Quantifying improvement of building and zone level thermal resilience by cooling retrofits against summertime heat events, Building and Environment, https://doi.org/10.1016/j.buildenv.2022.109914". The contents are slightly modified.

Abstract

Quantifying building resilience to extreme weather conditions helps identify the capability of a building system to tolerate disturbances and recover from extreme events. The robustness of building retrofit strategies can also be evaluated through their contributions to building resilience. In this study, building thermal resilience to summertime heatwaves is defined based on the concept of resilience trapezoid. The Thermal Resilience Index (TRI) with several labeling classes (Class F to Class A+) is proposed to quantify the resilience levels with respect to the relative improvement from original indoor thermal conditions. In addition to evaluating the overall resilience of a building, the resilience of each thermal zone in the building can be quantified with the proposed TRI criteria. A quantification framework is proposed by using the Standard Effective Temperature (SET) index as the performance indicator, and the entire procedure is demonstrated with a long-term care building of five stories. Four retrofit measures and their combinations are implemented to improve the building resilience to heatwaves. The results show layered multiple strategies are necessary to improve both the overall resilience of the building and the resilience of its component thermal zones. The resilience of the building can achieve the level of Class B after the combined

strategies are applied, providing an improvement of 50%-70% in the degree of resilience. The proposed TRI index and spatial distribution analysis are useful in evaluating the overall and zonal resilience of a building.

6.1. Introduction

Global climate change has led to an increased occurrence of extreme weather events. Heatwaves have become one of the predominant extreme weather events with increasing frequency, intensity, and severity in recent years (Ji et al., 2022a; Mora et al., 2017). During a heatwave, it remains a question as to how a building could adapt, absorb, and alleviate the disruptive impacts of the extremely hot weather, shelter occupants against the environmental heat, and eventually recover its normal operational status after the event. The answer to the question directly leads to an important concept of 'resilience', which defines the capacity of a subject to anticipate, absorb, adapt to, and/or rapidly recover from a disruptive event (Cabinet Office, 2011). The primary features of 'resilience' include robustness, resourcefulness, rapid recovery, and adaptability (NIAC, 2010). The resilience concept has been widely applied to natural disasters such as hurricanes (Sun et al., 2020), floods (Vardoulakis et al., 2015), and earthquakes (Ayyub, 2014), whereas not many investigations have applied this concept to buildings under heatwave conditions (Attia et al., 2021). A building's resilience against heatwaves determines the thermal performance of the building from the perspective of thermal comfort and the heat stress experienced by building occupants. Therefore, this study focuses on the concept of 'building thermal resilience', which quantifies the capability of a building system to tolerate disturbances from extreme heat events and to be retrofitted to achieve a robust and fast recovering building system (Homaei and Hamdy, 2021).

A limited number of previous studies on building thermal resilience have been published, which can be grouped into two main categories. One category is based on metrics that do not have a direct connection to the resilience concept, such as overheating hours or comfort indices, and are noted to have a relatively vague definition of building thermal resilience. Lomas and Ji (Lomas and Ji, 2009), and Lomas and Giridharan (Lomas and Giridharan, 2012) assessed the resilience of naturally ventilated buildings to climate change with the overheating hours quantified with respect to the time when the air temperature within the building was above fixed and adaptive thresholds (CIBSE, 2017). Burman et al. (Burman et al., 2014) adopted a framework involving vulnerability, resilience, and adaptive capacity to assess the overheating and energy performance in non-domestic buildings. Based on the ASHRAE adaptive thermal comfort model (ASHRAE-55, 2017), Coley et al. (Coley et al., 2017) proposed a probabilistic adaptive comfort equation for the design of resilient buildings. In all these studies, the concept of resilience was mentioned, but a quantitative definition of resilience was not provided. In comparison, attempts were made to define building thermal resilience in some other studies. Attia et al. (Attia et al., 2021) reviewed the resilience studies at both urban and building scales and proposed the definition of resilient cooling against heatwaves or power outages involving vulnerability, resistance, robustness, and recoverability. However, no quantitative analysis was provided. Zhang et al. (Zhang et al., 2021) also reviewed different resilient cooling strategies and qualitatively assessed those strategies against four criteria for resilience, which included absorptive capacity, adaptive capacity, restorative capacity, and recovery speed. A recent work by Homaei and Hamdy (Homaei and Hamdy, 2021) proposed a framework and labeling metric for building thermal resilience with the main focus, however, on power outages during heating seasons. In summary, there is a lack of quantitative studies that have been completed on building thermal resilience during summertime

heatwaves. Considering the increasing occurrence of threats from extreme heat events, it is therefore imperative to define building thermal resilience during summertime heatwaves so that different mitigation strategies can be quantitatively evaluated. The outcomes from such work would be valuable to researchers to understand better building resilience during heatwaves and helpful to stakeholders to permit the selection of the appropriate mitigation strategies for their buildings and communities. Results from such studies would also help develop associated building codes and standards.

Through the process of defining and quantifying building thermal resilience, the following challenges and research questions need to be addressed:

1) Selection of the appropriate resilience profile

A resilience profile describes the transition stages that cover the entire resilient procedure of interruption, degradation, and recovery. Therefore, it is important to select a resilience profile that reflects the actual responses of building thermal resilience. The general resilience profiles include the resilience triangle (Bruneau et al., 2003) and resilience trapezoid (Panteli and Mancarella, 2017). Their difference is that the latter takes into account the post-threat degradation state when there are no effective actions to recover from the threats (Panteli et al., 2017; Panteli and Mancarella, 2017).

2) Determination of the quantitative resilience assessment metric

Defining an assessment metric is key to the quantification of resilience. Previous work on building resilience with respect to power outages, as completed by Homaei and Hamdy (Homaei and Hamdy, 2021), defined a metric of 'Weighted Unmet Thermal Performance (WUMTP)' based on two event phases (during and post-event), three hazard levels, and penalties that would accrue from

the different exposure times. Chang and Shinozuka (Chang and Shinozuka, 2004) measured the resilience of communities from earthquakes through a probabilistic metric of 'Resilience (R)' with the loss of performance and time to recovery. The probability was calculated numerically to quantify the uncertainty concerning resilience. Another probabilistic resilience metric Re was proposed by Ayyub et al. (Ayyub, 2014) to consider robustness, resourcefulness, and system aging. Henry et al. (Henry and Emmanuel Ramirez-Marquez, 2012) proposed a dynamic metric of resilience Я(t|ej) to define a time-dependent system resilience of a road network as the ratio of recovery and total loss. Their study was later expanded (Hosseini et al., 2016) to evaluate resilience from different perspectives using different indices.

In the current study, to measure building thermal resilience, it is important to take into account the entire resilient process during and after the occurrence of a heatwave instead of the resilience at selected points in time. As well, the focus in this study is on a deterministic resilience metric, not a probabilistic resilience metric, given that the former would be the first step, and the latter can be achieved by inferential simulations of future disruptive events.

3) Determination of the performance indicator of building thermal resilience

A performance indicator that represents the condition of a system's performance is needed for the resilience curve of the system. Typical heat-stress indices can be used as performance indicators. For example, Homaei and Hamdy (Homaei and Hamdy, 2021) used the operative temperature as the building performance indicator. However, the operative temperature did not consider indoor humidity and occupants' physiological response. There are direct, empirical, and rational heat-stress indices in the field of building thermal environment analysis (Holmes et al., 2016). Direct indices such as dry bulb temperature and wet bulb temperature can be measured and used to evaluate the heat stress conditions. Empirical indices are developed from field experiments and

generally expressed in terms of some environmental parameter, not a physiological parameter (Brake and Bates, 2002). Examples of empirical indices include the Effective Temperature (ET), Wet Bulb Globe Temperature (WBGT), and others. Rational indices include physiological parameters such as sweat rate, core temperature, or heart rate and parameters that are calculated based on physiological models (Ji et al., 2022b, 2021), such as Predicted Heat strain (PHS), Standard Effective Temperature (SET), and others. Summertime building thermal performance is not only related to the indoor temperature but also other environmental parameters as well as occupants' physiological responses (Ji et al., 2022a). Evidently, rational heat stress indices can comprehensively be used to evaluate indoor thermal conditions (air temperature, relative humidity, radiation, airspeed) and related human physiology when subjected to such conditions. Hence such an index is, therefore, the most suitable within a framework for assessing thermal performance of a building and should be considered for adoption as a performance indicator.

4) Whole building level versus zone level thermal resilience

Another important part of building thermal resilience that has been ignored in previous studies is the thermal resilience at the thermal zone level. It should be noted that an occupant might dwell in a few thermal zones in a building and is only affected by the resilience of these specific zones. If these specific zones have a reduced level of resilience, the occupant would continuously feel uncomfortable no matter how well the other zones perform or the overall building performs. Besides, the unbalance of zone level thermal resilience would lead to different rates of recovery from heatwaves, and this, in turn, would further affect an occupants' thermal comfort by temperature steps (Nagano et al., 2005). Therefore, an analysis of zone-level thermal resilience is necessary to help attain a uniformly comfortable indoor environment.

To summarise and address the above four research questions, it is evident that a building's thermal resilience, when subjected to summertime heatwaves, has not yet been clearly defined nor quantified. In this paper, a framework is proposed to measure building thermal resilience at both the whole building and thermal zone levels. Based on the thermal performance of the building during heatwaves, the building's thermal resilience profile is developed from which the thermal resilience index can be quantified. Thereafter, a case study is completed to demonstrate the evaluation framework. Researchers, building designers, and policymakers can use this evaluation framework to measure and label buildings from the perspective of thermal resilience. The trade-off between building thermal risk and energy consumption could also be evaluated using the quantitative tool developed in this study for assessing building thermal resilience.

6.2. Methodology

In this study, a building thermal resilience profile is proposed based on the concept of a resilience trapezoid, which describes the shapes of the performance profiles from the start of an interruption until the end of the event and the restoration of adequate thermal comfort. The heat-stress index SET is adopted as the building thermal performance indicator. A new Thermal Resilience Index (TRI) is proposed to quantify building thermal resilience and the improvements after applying mitigation strategies. The process of deriving the TRI is based on the study by Homaei and Hamdy (Homaei and Hamdy, 2021). In Table 6-1, the proposed method is compared to that of Homaei and Hamdy's (Homaei and Hamdy, 2021) method. A detailed explanation is presented in the following subsections.

Table 6-1 Comparison of the proposed method with a previous work

Components		Proposed method	**Homaei and Hamdy** (Homaei and Hamdy, 2021)
Definition (Section 6.2.1)	Performance indicator	Standard Effective Temperature (SET)	Operative Temperature (OT)
	Resilience profile	Resilience trapezoid	Resilience triangle
Quantification (Section 6.2.2)	Building level resilience	√	√
	Zone level resilience	√	X
Labeling (Section 6.2.2.3)	Resilience labeling	√	√
	Each labeled class connected to resilience improvement	√	X
Implementation (Section 6.2.3)	Application scenarios	Summertime heatwave	Winter power outage

6.2.1 Definition --- Building thermal resilience trapezoid

The resilience triangle is the foundation for an empirical resilience assessment (Panteli et al., 2017). It covers the transition from the interruption state to the recovery state (Chang and Shinozuka, 2004). However, the degradation state after the interruption and before the restoration is not considered (Panteli et al., 2017). In comparison, the resilience trapezoid, the solid black curve shown in Figure 6-1, is a more complete model that can capture the time and degree of system failure, the time the system stays in the extreme state, and the time required to recover to a normal state. The area of the trapezoid is often used as a quantitative metric to evaluate the resilience of the system and the efficiency of resilience enhancement strategies (Panteli et al., 2017).

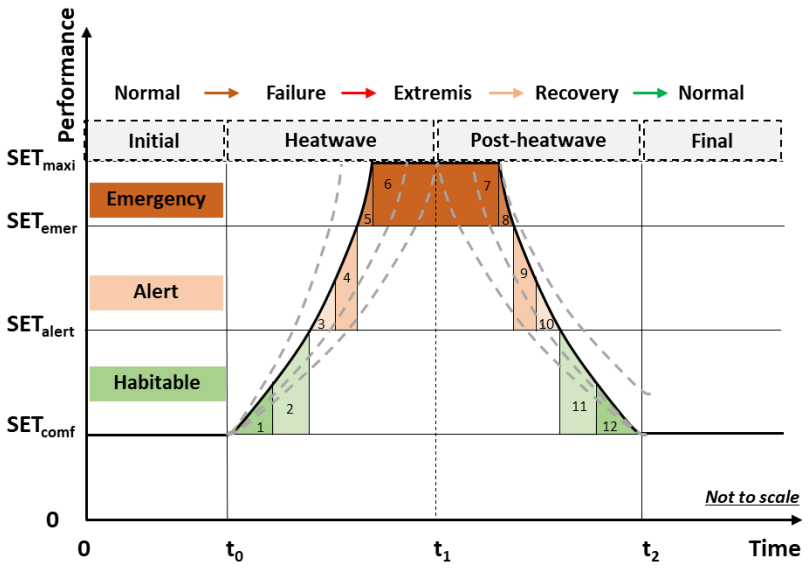

Figure 6-1 Building thermal resilience curve based on resilience trapezoid and 12 segments (#1~12) in the curve (dashed curves mean possible trends in real cases)

The resilience trapezoid model is used in this study to suit the characteristic variation in building thermal performance during heatwave events as observed from measurements in real buildings. Figure 6-2 shows the Standard Effective Temperature (SET) (black curve) in a building calculated based on a two-node bioheat model (Ji et al., 2021) by inputting measured indoor temperature and relative humidity from May to August (Shu et al., 2020) and the local outdoor air temperature (grey curve) measured from the roof of the building. With 28℃ (CIBSE, 2017) as the threshold temperature for indoor and outdoor heat events, the red and green shading highlights the time frames during which indoor overheating and outdoor heatwave events occur, respectively. It can be noticed that the indoor SET increases during the heatwave, showing that the tolerance to the heatwave for this building starts to decrease. The indoor SET increases to the maximum at the end of the heatwave, whereas it does not necessarily decrease soon after the peak occurs but normally stays at an extreme level for a certain period of time. Indoor overheating still persists after the

outdoor heatwave, which implies that there is a post-heatwave extreme state with respect to building thermal performance. Afterward, the indoor SET gradually recovers to the normal level (similar to pre-heatwave). It should be noted that when there are no effective actions to defend against the heatwave, a post-heatwave extreme state should be considered in the building thermal resilience curve, which is the reason that resilience trapezoids are used instead of resilience triangles.

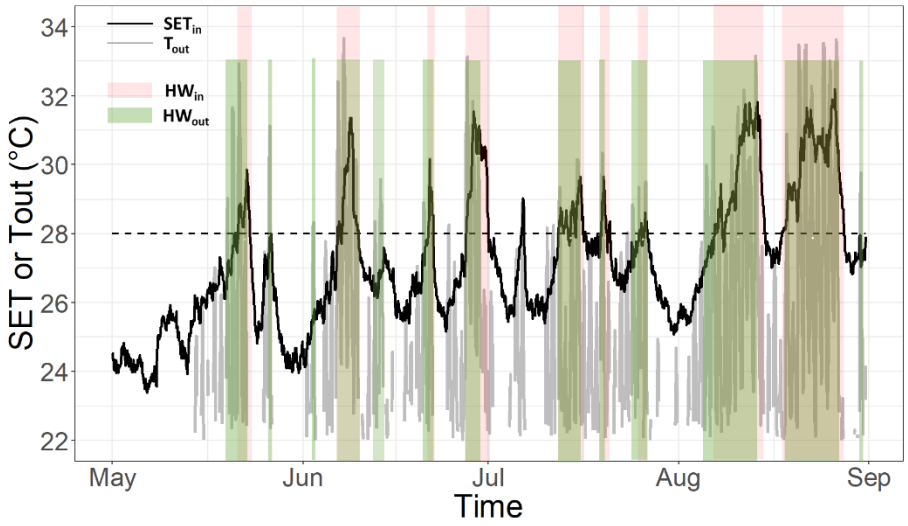

Figure 6-2 Summertime building thermal performance based on measured data

Based on the above observation, a conceptual curve for building thermal resilience is proposed in Figure 6-1. With SET as the performance indicator, the curve consists of two periods (i.e., the heatwave period (t_0~t_1) and post-heatwave period (t_1~t_2)), three thresholds (i.e., SETcomf, SETalert, and SETemer), and three hazard levels (i.e., habitable, alert, emergency). The SETmax is the maximum SET value for a heatwave event. The thresholds are related to the heat stress of the building occupants. As a rational heat-stress index, the relationship between SET and occupants' thermal sensation has already been explored in previous studies (Ji et al., 2022d). According to the ASHRAE 7-point predicted thermal sensation (PTS) scale for thermal sensation

(ASHRAE-55, 2017), a higher value of thermal sensation implies that an occupant feels more heat stress. Therefore, the thresholds SETcomf, SETalert, and SETemer can be determined based on the relationship of SET and the predicted thermal sensation (PTS) (Gao et al., 2015), as given by:

$$PTS = 0.25SET - 6.03, R^2 = 0.998 \quad (6\text{-}1)$$

Based on the ASHRAE 7-point scale (ASHRAE-55, 2017), when PTS = 0, the comfort level is neutral, and the SETcomf is calculated to be 24.12℃. The SETalert = 28.12℃ and SETemer = 32.12℃ are calculated when PTS = 1 and PTS =2 (ASHRAE-55, 2017), respectively. The three SET threshold values divide the resilience trapezoid into three hazard levels: the habitable level, heat alert level, and emergency level.

6.2.2 Quantification --- Building Thermal Resilience Index

a. Zone-level thermal resilience

The area of the trapezoid is often used as a quantitative metric to evaluate resilience (Panteli et al., 2017), and as suggested by Homaei and Hamdy (Homaei and Hamdy, 2021), the two periods, three thresholds, and three hazard levels divide the area into 12 segments. Figure 6-1 shows the 12 segments (S1-12) of the resilience curve across different phases (during and post heatwave) and hazard levels. The colored area of each segment, i, is defined as SETHi (℃·h), which is the integration of the area of SET above its hazard threshold over time. For each hazard level, the longer the performance stays at a given level, the more difficult the recovery will be, and as such, the first half of exposure time under each hazard level is regarded as ‘easy recovery exposure’, whereas the second half is referred to as a ‘difficult recovery exposure’. To reflect this effect on resilience, penalty coefficients are assigned to each of the segments (SETHi) based on logical assumptions (Homaei and Hamdy, 2021). These coefficient values for different exposure segments

are given in Table 6-2. The higher the penalty coefficient, the more difficult for the building to recover from exposure to heat. For example, the penalty value is higher during the heatwave ($W_{1,i=1-6}$ = 0.6) as compared to after the heatwave ($W_{1,i=7-12}$ = 0.4). The emergency level has the highest penalty value ($W_{2,i=5-8}$ = 0.7) amongst the three hazard levels (habitable level: $W_{2,i=1,2,11,12}$ = 0.1; alert level: $W_{2,i=3,4,9,10}$ = 0.2). The difference in penalty value for different stages of the resilience profile is reflected by $W_{3,i}$. For example, during the heatwave, in the habitable level, the penalty value for S1 is $W_{3,1}$ =2 and for S2 it is $W_{3,2}$=8, and so on. With these coefficient values, the weighted value for SETHi (WSETHi) of each segment is calculated as given in Equation 6-2.

$$WSETH_i = SETH_i W_{1,i} W_{2,i} W_{3,i} \quad (6\text{-}2)$$

Table 6-2 Penalty coefficients for the 12 segments (Homaei and Hamdy, 2021)

Segments S_i	**Coefficients**		
	$W_{1,i}$ (during or post-heatwave penalty)	$W_{2,i}$ (hazard level penalty)	$W_{3,i}$ (exposure time penalty)
S_1	0.6	0.1	2
S_2	0.6	0.1	8
S_3	0.6	0.2	10
S_4	0.6	0.2	20
S_5	0.6	0.7	20
S_6	0.6	0.7	40
S_7	0.4	0.7	40
S_8	0.4	0.7	20
S_9	0.4	0.2	20
S_{10}	0.4	0.2	10
S_{11}	0.4	0.1	8
S_{12}	0.4	0.1	2

In building performance simulations such as using EnergyPlus (DOE, 2020), the thermal zones are normally assumed to be one node in the simulation, with each having its individual resilience curve. So the resilience metric WSETHz (°C·h) for the thermal zone is the summation of the 12 segments of this zone, for which:

$$WSETH_z = \sum_{i=1}^{12} WSETH_i \quad (6\text{-}3)$$

where z indicates that it is the thermal zone WSETH, and i is the segment counter.

The zone level thermal resilience index TRIz is calculated from the ratio of the original zone value for $WSETH_{z,o}$ to the retrofitted zone value for $WSETH_{z,r}$:

$$TRI_z = WSETH_{z,o}/WSETH_{z,r} \quad (6\text{-}4).$$

As such, the TRIz of each zone in the original building is 1.0, and the TRIz of zones for retrofitted buildings represent their relative resilience level as compared to their own original condition. With the TRIz values of zones in retrofitted buildings, one can tell if the zone level resilience has been improved, no matter what the original situation.

b. Building-level thermal resilience

To quantify the thermal resilience of the whole building, WSETHb can be calculated by the weighted average of the zonal WSETH with the room areas for zones, as given by:

$$WSETH_b = \sum \frac{WSETH_{z,j} \times A_j}{\sum_1^N A_j} \quad (6\text{-}5)$$

where b indicates that the value of WSETH being calculated is for the overall building, and $WSETH_{z,j}$ is the WSETH value of each thermal zone, Aj is the floor area of each zone, j is the thermal zone counter, and N is the total number of thermal zones in the studied building.

To mitigate indoor overheating and enhance the building thermal resilience, retrofit strategies are often applied to buildings. Compared to the original building before the retrofit, it is necessary to know the improvement in resilience level that the retrofits bring to the building. An index that is the ratio of resilience performance of the original building to that of the retrofitted building is therefore defined as the building thermal resilience index (TRI), which is given by:

$$TRI = WSETH_{b,o}/WSETH_{b,r} \quad (6\text{-}6)$$

where $WSETH_{b,o}$ is the whole building WSETH of the original building, and $WSETH_{b,r}$ is the whole building WSETH of the retrofit building. After the retrofit, the indoor SET is expected to decrease, resulting in the reduction of WSETHb. A higher TRI value indicates that the building is more resilient to the extreme heat event; TRI < 1 means that the retrofit building is less resilient than the original baseline building; TRI = 1 means there is no improvement in resilience, and finally; TRI > 1 means the retrofitted building is more resilient than the original building.

c. Thermal resilience labeling

Similar to the resilience labeling used for energy systems (Rajagopalan and Leung Tony, 2012), building thermal resilience can be labeled into several classes (Homaei and Hamdy, 2021). By comparing the performance of an original building to that of a retrofit building, the building thermal resilience can be scaled from F to A+, where A+ represents the most resilient building, and F is the original building resilience level: a building having no retrofits. However, clear physical meaning for each class and the reason for the range division are needed. In this study, the range division, as summarized in Table 3, is based on improvement in resilience. When $WSETH_{b,r}$ of the retrofit building is 10% less than $WSETH_{b,o}$ of the original building, the TRI is calculated to be 1.1, the range 1.0-1.1 is therefore classified as Class E, representing 0-10% resilience improvement. For classes D to A+, the improvement on WSETH with an increment of 20% is applied to each class, and the corresponding ranges of TRI are calculated. This makes seven (7) labeling levels in total, which were adopted for the resiliency labeling of building energy performance (Pérez-Lombard et al., 2009). In this way, when $WSETH_{b,r}$ of the retrofit building is 30% less than $WSETH_{b,o}$ of the original building, the TRI is 1/(1-30%) = 1.4, so the range 1.1-1.4 is therefore classified as Class D, representing a resilience improvement of 10-30%. Similarly,

Classes from level C to level A+ represent resilience improvements, respectively, for ranges of: 30%-50%, 50%-70%, 70%-90%, and > 90%. With this labeling method, the higher class bands become broader, which reflects the growing difficulty to achieve a higher class of resilience. For example, the TRI needs to be increased more from Class C to Class B than from Class D to Class C. This labeling system can be applied to both building-level and zone-level resilience based on the value of TRIb and TRIz, respectively.

In this study, the goal of the building-level thermal resilience is set to be Class B (at least 50% of resilience improvement); the goal of zone-level thermal resilience is set to be 50% of thermal zones reach to Class B and the maximum difference of zone classes is less than one class (e.g. if the most resilient zone is Class B, the worst resilient zone should be at least Class C).

Table 6-3 Building thermal resilience labeling

Label	TRI	Resilience improvement
Class A^+	(10.0, +∞)	>90%
Class A	(3.3, 10.0]	70%-90%
Class B	(2.0, 3.3]	50%-70%
Class C	(1.4, 2.0]	30%-50%
Class D	(1.1,1.4]	10%-30%
Class E	(1.0, 1.1]	0-10%
Class F	(0, 1.0]	No improvement

6.2.3 Implementation --- Framework of building thermal resilience quantification

Based on the definition and quantification method given above, Figure 6-3 shows the framework used to quantify building thermal resilience. In the first step, a target heatwave event and the related climate data should be collected; this information would be input to conduct building simulations. To obtain the indoor thermal parameters (i.e., air temperature, relative humidity, and airspeed), the

original building and its retrofitted conditions should be simulated using a building performance simulation program, such as EnergyPlus (DOE, 2020). Then, the indoor thermal parameters are used as inputs to the SET model (Ji et al., 2021) to permit calculating the performance indicator SET. With the value of SET, the building thermal performance curve can then be determined. The building thermal performance curve can be abstracted based on the trapezoid resilience curve having 12 segments with respect to the two phases, three hazard levels, and exposure time at each level; the calculations can then be conducted. As such, in the third step, the zone level values for $WSETH_z$ and TRI_z can be calculated according to Equations 6-2 to 6-4, and the thermal resilience classes for each zone can be labeled given the values calculated for TRIz in accordance with that provided in Table 6-3. After which, the building level values for WSETHb and TRI_b can be calculated according to Equations 6-5 to 6-6, and the building thermal resilience classes can be labeled from the values of TRI_b calculated according to that given in Table 6-3. In the following sections, a case study is provided to illustrate this workflow.

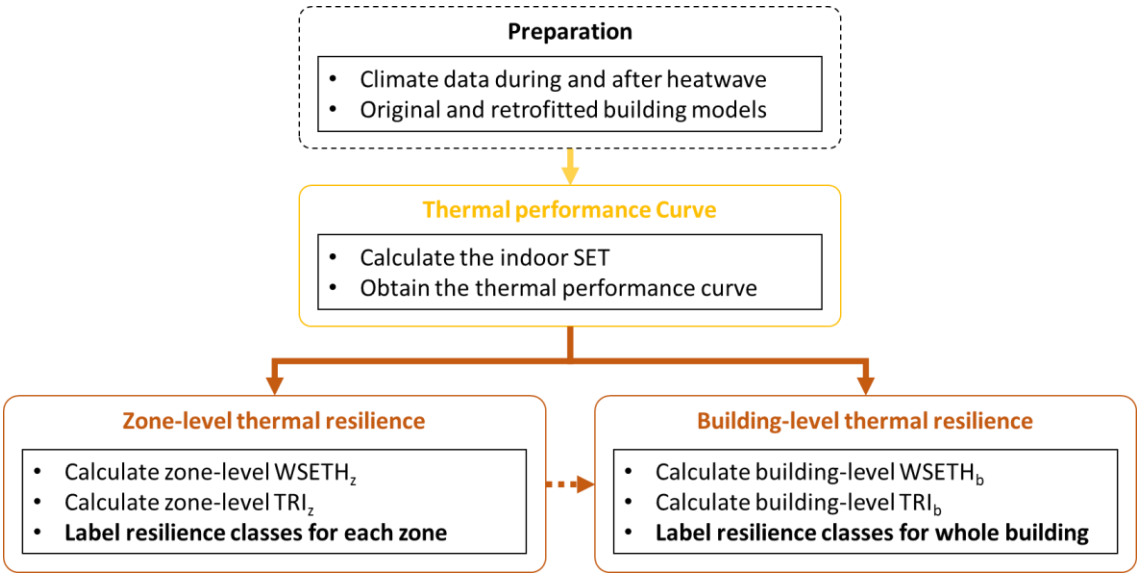

Figure 6-3 Framework of building thermal resilience quantification

6.3. Case study

6.3.1 Heatwave and climate data

From June 30 to July 05, 2018, a heatwave occurred in Montreal, Canada, and 66 heat-related deaths were reported because of this event (Lamothe et al., 2019). This heatwave event is used in this study as an example case to evaluate a building's thermal resilience. The weather data was collected from hourly measurements from a weather station located in the urban area of Montreal (Shu et al., 2022a). The air temperature, relative humidity, wind speed, wind direction, solar radiation, and precipitation were collected and converted to an EPW format for input to the Energyplus (DOE, 2020) building simulation model.

6.3.2 Building model and retrofit measures

The building model was developed for a long-term care building constructed in the 1980s with a footage area of 817m^2, which is one of the buildings in a monitoring campaign conducted in Montreal, Canada since the summer of 2020 (Leon et al., 2020). The indoor temperature and relative humidity (RH) in selected spaces on different floors and orientations were monitored continuously with a time interval of 15min. On-site weather stations were placed on the roofs of this building to gather local weather data, including air temperature, relative humidity, solar radiation, wind speed and direction, and precipitation. Those measured indoor and outdoor environment data were used to calibrate and validate the building model (Ji et al., 2022c). The detailed calibration procedure can be found in Appendices A.2.

The selected long-term care building is an L-shaped building facing the southerly direction and is composed of five floors above ground and one below-grade basement floor. All patient rooms and offices in this building are naturally ventilated. Figure 6-4(a) shows the map view of the building

and Figure 6-4(b) shows the 3-D model of the building as studied and developed in Design Builder®. Figures 6-4(c) and 6-4(d) are the thermal zone divisions of Floor 1 and the standard floors from Floors 2 to 5, respectively. A total of 80 thermal zones for naturally ventilated patient rooms, office rooms, and corridors were investigated to permit analyzing the zone-level and building-level thermal resilience.

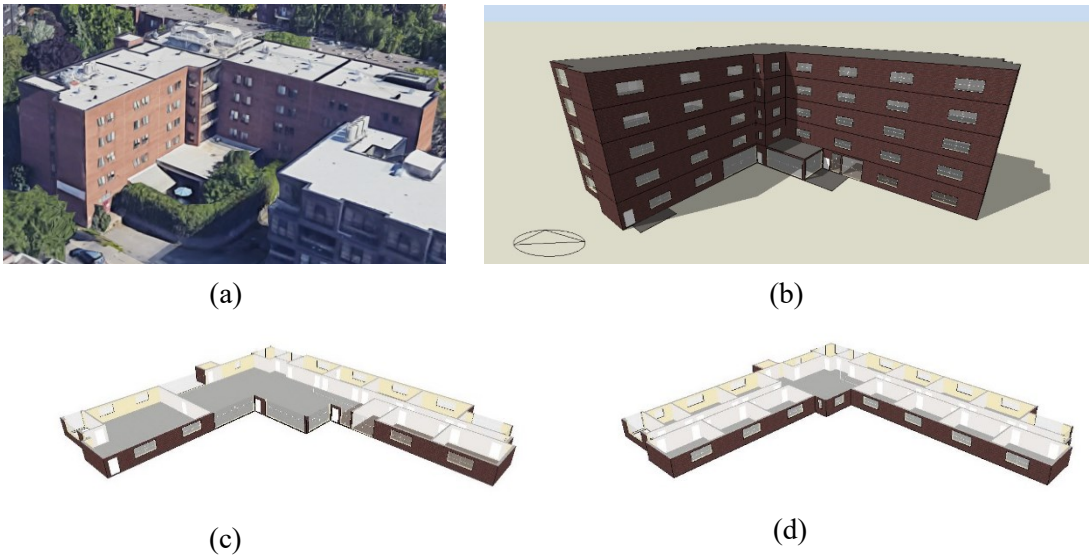

Figure 6-4 (a) Oblique aerial photo, (b)3-D model, (c) thermal zone division of Floor 1, and (d) thermal zone division of Floor 2~5 for a long-term care building located in Montreal, Canada

From a building survey, site visit, and architecture plan, the building parameters, operation schedules, and air conditioning information were collected (Wang and Shu, 2021). Some unknown parameters, including envelope thermal properties, internal heat gains, and natural ventilation rate, were calibrated through a Monte-Carlo method (Hoffman, 2014) based on the measured hourly indoor temperature (Ji et al., 2022c). Sensitivity analyses were conducted first to identify the most important parameters, and thereafter parametric simulations were conducted to determine the value of these unknown parameters. The calibrated values (Ji et al., 2022c) of the parameters are shown in Table 6-4.

Table 6-4 Calibrated parameter values

Category	Parameter	Unit	Value
Wall	Wall U-Value	W/m^2K	0.3
Roof	Roof U-Value	W/m^2K	0.25
Wall	Wall thermal mass	KJ/km^2	220
Roof	Roof thermal mass	KJ/km^2	335
Window	Window U-Value	W/m^2K	2.72
Window	Window SHGC	-	0.37
Interior blinds	Slat angle	Deg	59
	Solar reflectance		0.6
Equipment	Equipment power density	W/m^2	2.93
Lighting	Lighting power density	W/m^2	9.94
Air mass flow through cracks	Air mass flow coefficient at reference crack condition of walls and roof surfaces	kg/m·s	0.0025
		kg/m·s	0.0012
Natural ventilation control	Natural ventilation set point	℃	26
Interior room door opening factor	Width factor for door opening	%	47
Room window opening factor		%	10

In Figure 6-5, the measured and simulated data (average values of the three monitored rooms) are compared after applying the calibrated parameters during the calibration and validation periods. At the room level, the root mean square error (RMSE) of the calibration and validation range in value from 0.56℃ to1.09℃, which are both less than the requirement of 1.5℃ as suggested in previous studies (O' Donovan et al., 2019). The mean bias error (MBE) is within ± 1.2%, and the coefficient of variation of the RMSE (CvRMSE) is less than 3.65%, which is also within the standard requirement (±5% and 20%) as given in the literature (IPMVP, 2003). More details of the model development and calibration can be found in the authors' previous paper (Ji et al., 2022c).

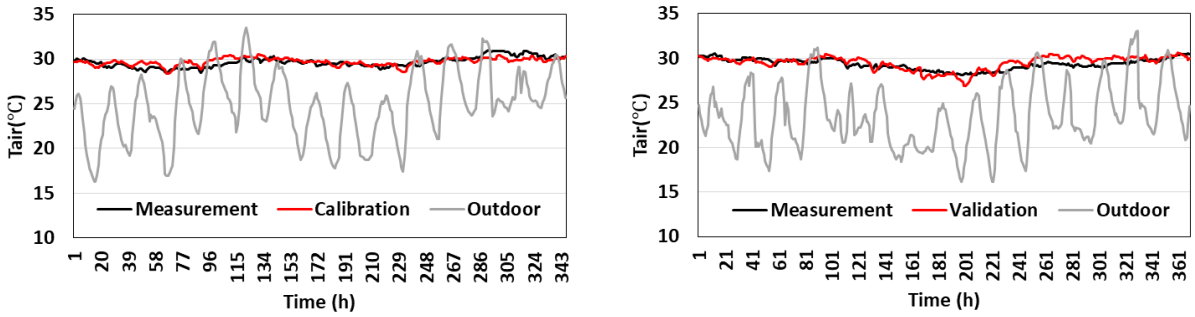

(a) (b)

Figure 6-5 Comparison of the measured and simulated data during (a) calibration period and (b) validation period

Table 6-5 Mitigation strategies of retrofit buildings and comparison with the original building

	Original building	**Retrofit building**
Shading	Interior blinds	Exterior shading (ES)
Natural ventilation	Window opening area 10%	Window opening area 50% (NV) Windows are open when the indoor temperature is higher than 26℃ and higher than the outdoor temperature (Laouadi et al., 2020b)
Roof	Regular roof	Green roof (GF) Height of plants 0.3 m; Leaf area index (LAI) 3; Leaf emissivity 0.9; Leaf reflectivity 0.2; Substrate thickness 0.1 m; Conductivity of dry soil 0.4 W/(m·K); Thermal absorption of soil 0.96 (Morakinyo et al., 2016)
Night ventilation (NiV)	No	Exhaust fans Operating time 9pm ~ 10am; Design pressure rise 420Pa; Fan total efficiency 0.6; Maximum air change rate $5h^{-1}$ (Guo et al., 2020)
Two strategies combination	/	ES+GF, ES+NiV, ES+NV, GF+NiV, GF+NV, NiV+NV
Three strategies combination	/	ES+GF+NiV, ES+GF+NV, ES+NiV+NV, GF+NiV+NV, ES+GF+NV
Four strategies combination	/	ES+GF+NiV+NV

Mitigation strategies were applied to the original calibrated building model, including replacing interior blinds with exterior shading (ES), increasing window opening area to enhance natural ventilation (NV), applying a green roof (GF), and applying night ventilation (NiV). Detailed descriptions of these four (4) building retrofit measures, and combinations of these measures with 2 to 4 strategy combinations, are listed in Table 6-5. The thermal resilience of the retrofit measures will be quantified using the proposed method.

6.4. Results

6.4.1 Thermal performance curve

Figure 6-6 shows the thermal performance curves of the original building and the retrofitted buildings. The buildings are named with respect to the strategies implemented for each of them. The effect of retrofits on the curves can be analyzed from three aspects: i) average reduction: lowering the black curve that reflects the average thermal performance of the whole building, ii) peak removal: lowering the highest curve that represents the most overheated zone, and iii) daily consistency: reducing fluctuation of curves that shows the difference between daytime and nighttime.

Amongst the four (4) individual retrofit strategies (GF, ES, NiV, NV), NV is the most efficient in average reduction by lowering the average curve to below SETemer threshold, and ES works well on peak removal by reducing the SET of the most overheated zone. NiV primarily affects the nighttime SET value but has a limited impact on daytime SET, which does not contribute to the daily consistency. GF has no significant influence on thermal conditions. Almost all the retrofit strategy combinations can improve the average thermal performance except for ES+GF and GF+NiV. However, without ES, the combinations of GF+NiV, GF+NV, NiV+NV, and

GF+NiV+NV cannot reduce the peak value of SET, which means they have a limited effect on the most overheated zone.

From the above qualitative analysis of the performance curves, no individual strategy can simultaneously improve the thermal performance of the whole-building average, the most overheated thermal zone, and the daily consistency, thus combined strategies are necessary. Furthermore, when analyzing building thermal resilience, not only should one focus on the overall mean curve, but the resilience of the thermal zones in the building should also be evaluated since these are related to the worst resilience case. A good retrofit strategy should be able to enhance the overall resilience as well as achieve the resilience uniformity of all thermal zones.

Due to the complexity of the effect of retrofits on building thermal performance, a single index is necessary to define the building resilience during and after the heatwave period, as well as the spatial distribution in thermal resilience of different thermal zones. With the single index value, one could simplify the analysis process for building overheating problems and resilience performance assessment. Otherwise, there is a need to compare different criteria and there is the possibility that each of these may yield different overheating results (Shu, 2021; Shu et al., 2022b). With the quantification method proposed in Section 6.2, the building thermal performance curve can be abstracted as a trapezoid resilience curve, and thereafter, the calculations for the thermal resilience index can be completed. The quantitative analysis for zone-level and building-level thermal resilience is presented in the following sections.

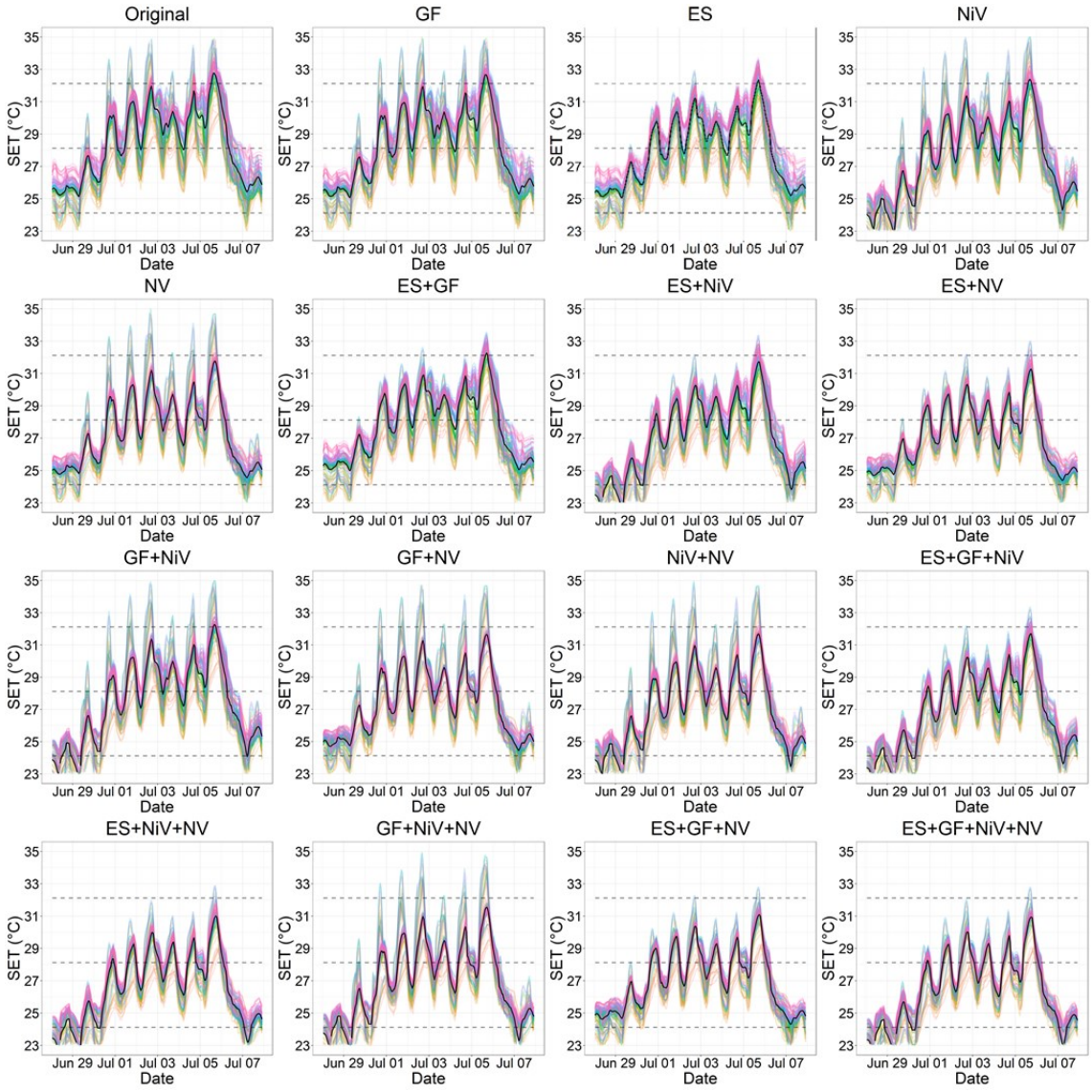

Figure 6-6 Thermal performance curves of the original building and retrofitted buildings (Note: The curves of different colors are the thermal performance curves of different thermal zones; the black curve is the averaged profile of all thermal zones)

6.4.2 Zone-level thermal resilience

As mentioned above, the focus ought to be made on the zone-level thermal resilience since it is more likely that occupants would be residing in the same zone or a few zones, and their thermal comfort is influenced to a greater extent by the resilience of a specific set of zones.

In Figure 6-7, the zone-level thermal resilience index (TRI_z) and labeled classes of the retrofitted buildings are shown. In this figure, for thermal zones located on different floors and facing different directions, the consequences of retrofit measures on the resilience levels are compared. It should be noted that the TRI_z of all zones in the original building is equal to 1.0 (Class F), and the TRI_z of each zone in the retrofitted buildings indicates the relative resilience improvement compared to the original condition.

For individual retrofit strategy (i.e., GF, ES, NiV, and NV), as in Figure 6-7, GF, NiV, and NV work better on upper floors (Floors 3~5) than on lower floors (Floors 1~2) to improve their zone resilience. They also improve more for zones facing north and east than zones facing south and east. ES has limited improvement for all the zones while working specifically well on Zone 1-7 (Floor 1, zone #7). Of note is that Zone 1-7 is facing south-west and has a smaller floor area than other zones and hence, more serious overheating problems in the original situation, whereby the ES retrofit measure decreases solar heat gains from the south-west in the afternoon and from this, the resilience level is improved. As such, individual strategies have different features with respect to improvements in resilience; more specifically, amongst these retrofit measures, NV is the most efficient, whereas the ES works well in the worst resilience zone. However, none of the individual strategies can achieve the zone-level resilience goal set in Section 2.2.3. NV makes 39% (<50%) of zones reach Class B and the deviation of labeling is two classes (Class D VS Class B, > one class).

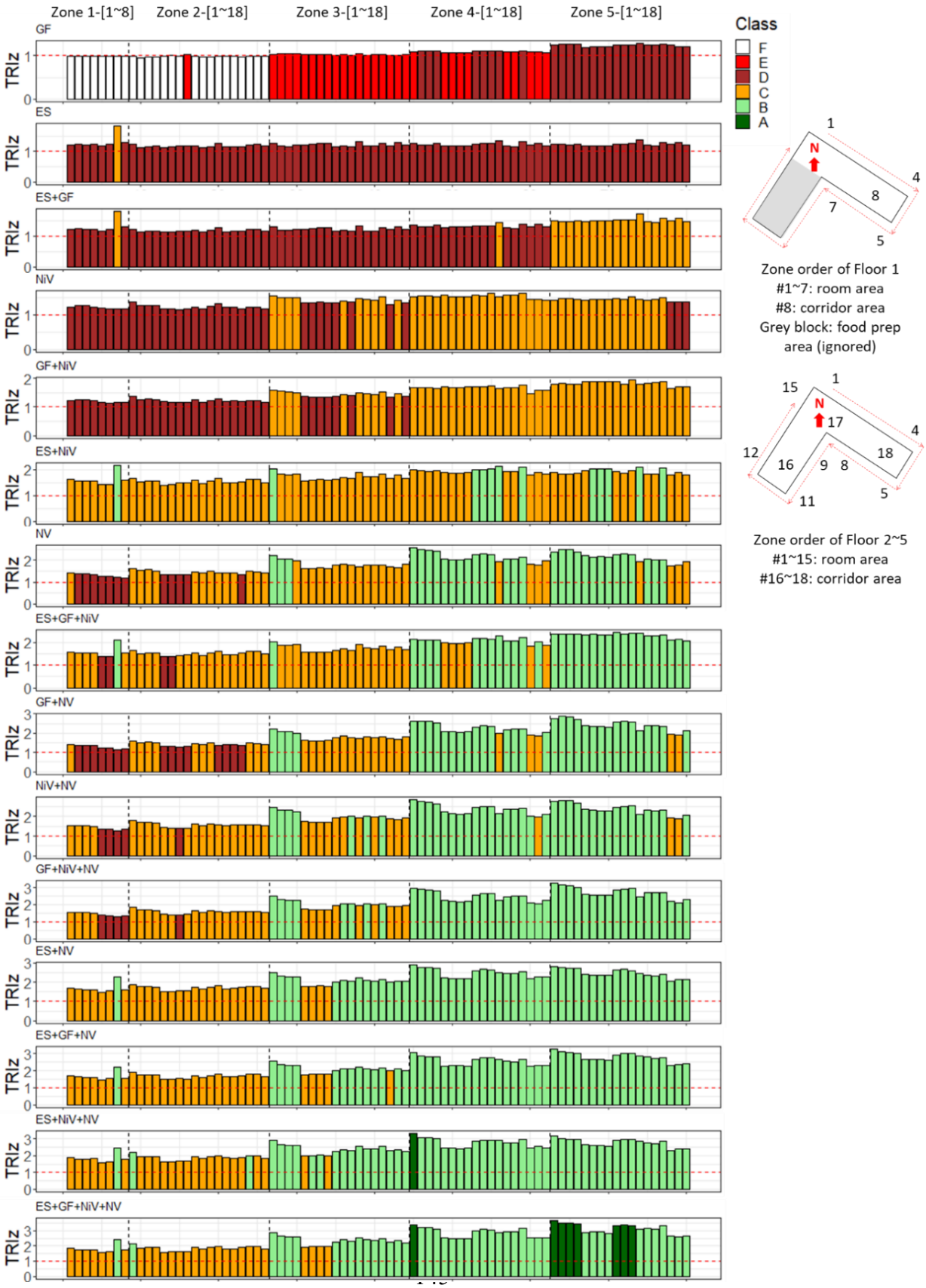
Zone 1-[1~8]
Zone 2-[1~18]
Zone 3-[1~18]
Zone 4-[1~18]
Zone 5-[1~18]
GF
ES
ES+GF
NiV
GF+NiV
ES+NiV
NV
ES+GF+NiV
GF+NV
NiV+NV
GF+NiV+NV
ES+NV
ES+GF+NV
ES+NiV+NV
ES+GF+NiV+NV
TRIz
Class
F
E
D
C
B
A
N
Zone order of Floor 1
#1~7: room area
#8: corridor area
Grey block: food prep area (ignored)
Zone order of Floor 2~5
#1~15: room area
#16~18: corridor area

Figure 6-7 Zone thermal resilience index (TRI_z) and labeled classes of the retrofitted buildings (Bars in different colors: TRI_z and resilience label of each thermal zone; Red horizontal dashed line: $TRI_z = 1$ (baseline); Black vertical dashed line: separator between floors)

Since individual retrofit measures have their own advantages and disadvantages, the combination of retrofit measures can take advantage of each measure. For example, the combination of ES+NV can achieve the zone-level resilience goal: 64% of zones reach Class B and the deviation of labeling is one class (Class C VS Class B). The combination of all four measures can improve 65% of zones to at least Class B. Zones on upper floors even reach Class A while most zones on lower floors stay at Class C, which actually does not contribute to the uniformity between zones. Therefore, when designing appropriate combinations of retrofit strategies, additional design efforts should be applied to improve the zone-level thermal resilience on lower floors, instead of simply increasing the layers of combination.

6.4.3 Building-level thermal resilience

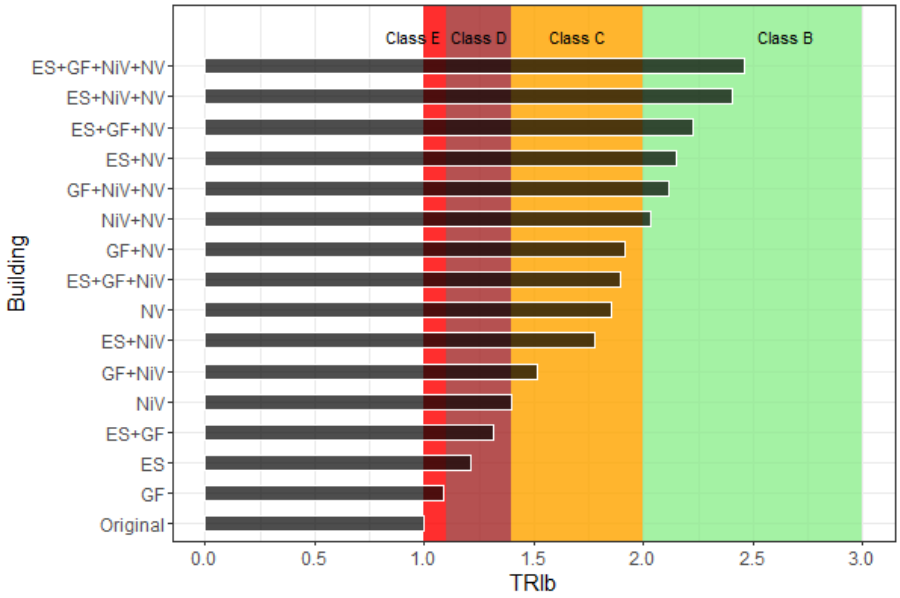

Figure 6-8 Building thermal resilience index (TRI_b) and labeled classes of the original building and retrofitted buildings

Figure 6-8 shows the TRI_b of the original building and different retrofitted buildings, including their overall building thermal resilience level. The buildings are designated by the types of measures implemented on them. For buildings with an individual retrofit strategy, none of them can reach the building-level thermal resilience goal of Class B, as set in Section 6.2.2.c. For buildings with combinations of two retrofit strategies, NiV+NV and ES+NV are labeled as Class B. Other buildings located in Class B have three or four strategy combinations.

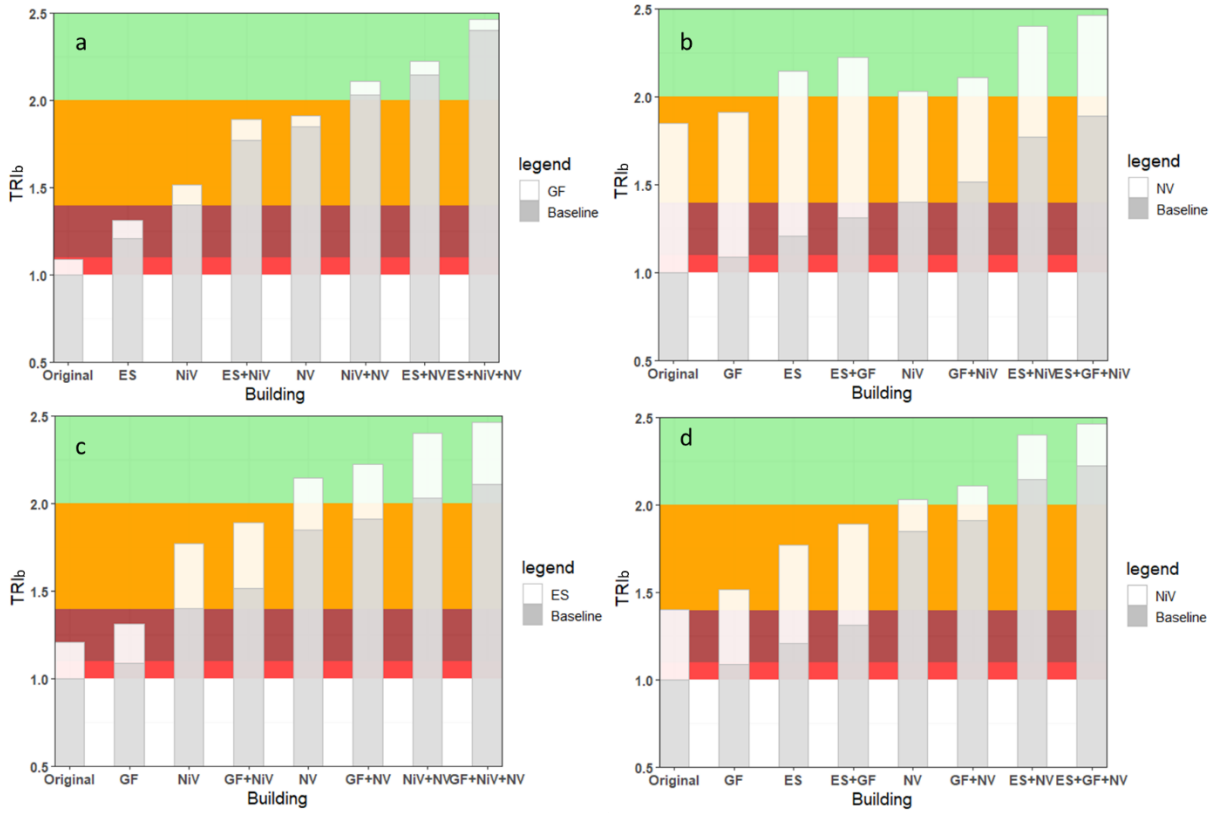

Figure 6-9 TRI_b increases by a single strategy applied on different baseline buildings: (a) Baseline buildings with GF; (b) Baseline buildings with NV; (c) Baseline buildings with ES; (d) Baseline buildings with NiV.

As well, with different baseline buildings, the efficiency of the same single strategy might vary. For example, as shown in Figure 6-9(b), using the building with ES as a baseline, adding NV can increase the TRI_b to the goal of Class B and the contribution of NV is 0.94, whereas, with NiV as a baseline, the TRI_b can also reach to Class B by adding NV but the contribution of NV is lower. It seems the selection of the best retrofit strategy also depends on the measures that have already been implemented in a building. Besides, the improvement of resilience level becomes more difficult with the baseline level becoming higher. As shown in Figure 6-9, when the baseline level is higher than Class C, the contribution by adding an individual strategy is less than when the

baseline level is lower. This means that more appropriate strategy and design are needed to make the building to Class A or A+.

6.5. Discussion

A new resilience parameter, the building Thermal Resilience Index (TRI) was proposed in this study, as well as an associated labeling system to quantify the level of building thermal resilience that also includes the distribution of thermal zone level resilience. Higher values for TRI_b imply that the building is more resilient to heatwaves and the zones are more balanced. Based on the resilience improvement, building thermal resilience can be labeled, which makes it easier to measure and visualize a resilience level. Apart from the building overall resilience index, the relative resilience of each zone compared to its original situation can also be calculated as the zone level thermal resilience index TRI_z. The analysis of zone-level resilience can help select more efficient retrofit measures according to their performance on zones of different floors and directions.

Another way to evaluate the zone level resilience is through the spatial distribution of their thermal resilience. Equation 6-3 indicates that the $WSETH_z$ is the absolute thermal resilience of each zone: the lower the value, the more resilient the zone. The distribution of $WSETH_z$ represents the resilience uniformity of all zones.

Figure 6-10 shows the frequency distribution of $WSETH_z$ for all thermal zones in each building. The left column indicates the building overall resilience class (from Class F to B), and each building is categorized in the corresponding class. From Class F to Class B, the mean and standard deviation (Std) of the spatial resilience distribution tend to be smaller. In the analysis in Section 6.4, among the individual strategies, NV is the most efficient and ES can improve the worst zone

resilience; among the combinations of two strategies, NiV+NV and ES+NV can reach the building-level goal of Class B, and ES+NV can as well reach the zone-level goal. The Std of NV, ES, NiV+NV, and ES+NV are therefore important to note. The Std of ES is 95.3, which is much higher than the Std of NV (24.7); the Std of NiV+NV and ES+NV are comparable, both close to 21.0. The Std of three or four strategies are lower but have limitations in the implementation in reality and retrofit expenses. Overall, ES+NV is the most recommended in this case study, which can realize both building-level and zone-level resilience goals, and leads to a good resilience uniformity of all zones.

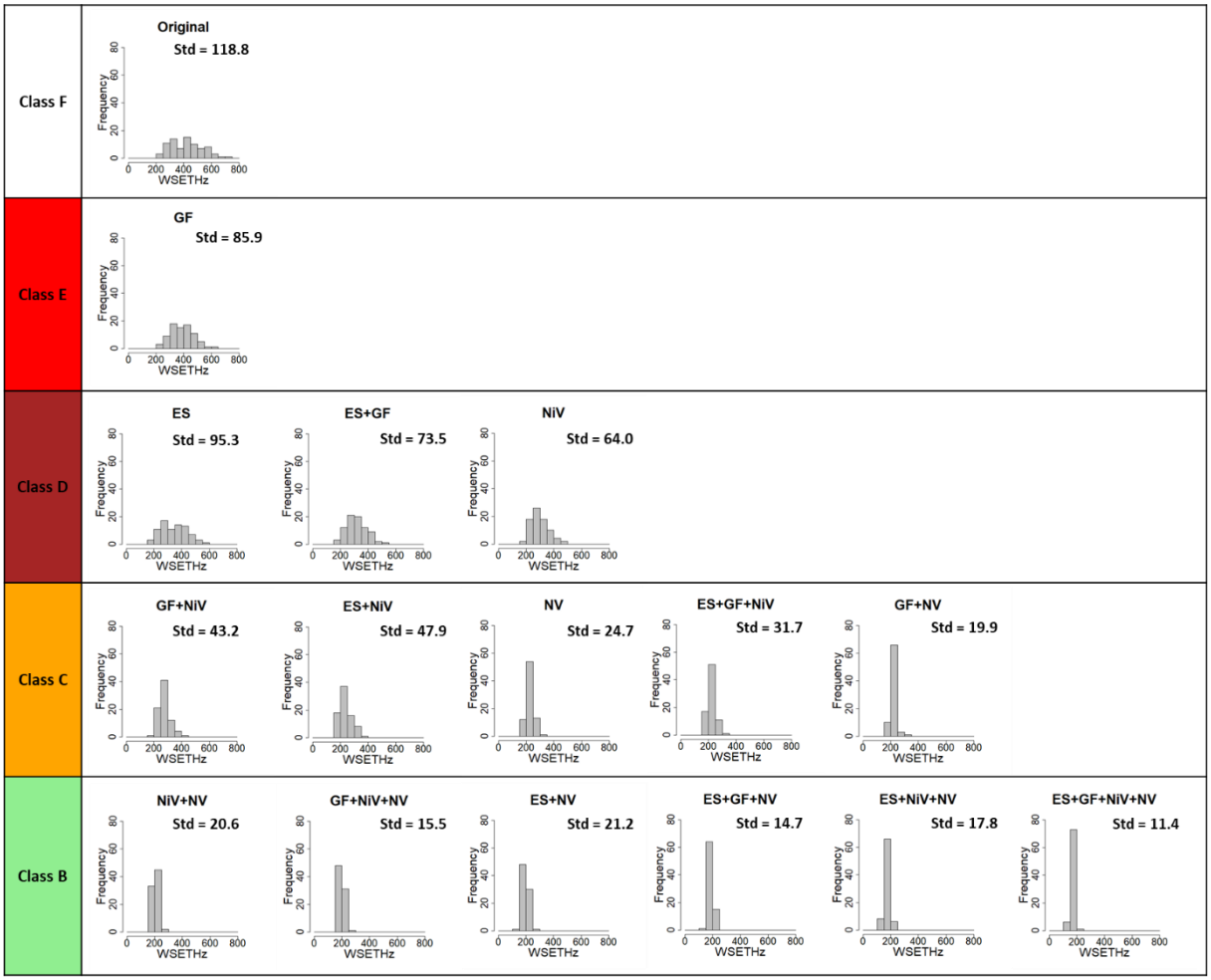

Figure 6-10 Distribution of $WSETH_z$ (Std: Standard deviation of $WSETH_z$ of all thermal zones, which indicates the variation of resilience among the zones in the studied building. Small Std values mean the zones in the building tend to have similar resilience evaluated by $WSETH_z$.)

This study emphasizes the analysis of thermal resilience from both building-level and zone-level. Thermal zones have different ability to recover from a heatwave, which causes some zones to remain uncomfortable hot for a longer period of time and this, in turn, leads to thermal risks to occupants living in these zones, especially for vulnerable people, such as those that are older, as well as children and sick people (Ji et al., 2022b). This is particularly true for large buildings, such as long-term care centers, senior homes, and hospitals. Some rooms could be most vulnerable, and

special retrofit measures should be implemented in the event that the whole building strategy cannot meet the worst zone requirement.

One of the limitations of this study is the lack of acceptance criteria for resilience, that is, the class for which the resilience level is deemed acceptable. In future studies, criteria can be explored and defined to indicate the meaning of different classes. For example, by considering the trade-off between the investment in retrofit strategies and the return on thermal resilience, one can optimize the building thermal resilience with the lowest cost in money and energy, from which the objective of attaining an acceptable level of resilience can be recommended.

In addition to the deterministic resilience index, probabilistic (Ayyub, 2014; Chang and Shinozuka, 2004) or dynamic indexes (Henry and Emmanuel Ramirez-Marquez, 2012) are also worth investigating. Building thermal properties are not constant; they are affected by material aging with the time of usage. A probabilistic index can take into account the uncertainty of the building performance with lifelong aging effects and from the influence of future weather conditions. The uncertainty in calculating thermal performance indicators, such as the uncertainty in the SET model, could also be considered in the probabilistic index. Besides, a building is a dynamic system. Its thermal performance might be changed by the occupant behaviors and building operations. A dynamic index can evaluate human adaptive behaviors during the heatwave and measure the real-time resilience level. These quantification methods will be explored in future studies.

The method proposed in this study is illustrated by building thermal resilience against heatwaves. A similar procedure may also be used in other scenarios, such as winter/summer power outages, community or city-scale thermal resilience, and so on.

6.6. Conclusions

In this study, building thermal resilience with respect to the occurrence of summertime heatwave events is defined and quantified. The quantitative resilience approach consisting of the resilience profile, the resilience metric, and the performance indicator was investigated. A framework for building thermal resilience quantification was proposed, which includes the following important factors:

- The conceptual building thermal resilience curve has the profile of a resilience trapezoid.
- A resilience parameter, the Thermal Resilience Index (TRI), can be calculated by determining the improvement in relative resilience from original conditions.
- The zone-level and building-level thermal resilience can be labeled based on the value of TRI_z and TRI_b, respectively, and each labeled class represents the percentage of improvement in resilience.
- The distribution in zone-level resilience can also be analyzed by the absolute thermal resilience of each zone $WSETH_z$. A smaller standard deviation of the distribution means the zone resilience is more homogenous.
- The Standard Effective Temperature (SET) can be used as a performance indicator to permit defining the building thermal performance curve.

The resilience framework is illustrated for a building before and after retrofits with respect to the occurrence of a heatwave event. The different retrofit strategies studied included exterior shading (ES), green roof (GF), natural ventilation (NV), and night ventilation (NiV). The results obtained from the case study were the following:

- Among the individual strategies, NV is the most efficient, whereas ES can improve the thermal resilience of the most overheated zone.
- The combination of ES+NV is the most recommended in this case, which can efficiently improve building-level resilience and more than 50% of zone-level thermal resilience to Class B, as well as reach a good resilience uniformity of zones.
- Most strategies and their combinations are more efficient on upper floors than on lower floors. Design efforts should therefore be applied to improve the thermal resilience on lower floors, instead of simply increasing the layers of combination.
- The efficiency of a retrofit strategy could be affected by the strategies that have already been implemented in the building. NV is more efficient in building with ES than NiV. The improvement in building resilience class becomes difficult when the baseline class is at Class C and above.

Chapter 7 Conclusions and Future Work

7.1. Conclusions

This research focused on evaluating human thermal response and building resilience to extreme heat events. Three essential aspects related to the indoor heat-stress situation were explored: occupants' vulnerability, outdoor extreme heat events and building thermal resilience. An existing Bioheat model was improved to better apply to hot exposure situations. The heat vulnerability of older people was investigated based on the improved Bioheat model and the age-related changes. The approaches of selecting extreme weather years (EHYs) were evaluated for indoor overheating-centric studies. The quantification method of building thermal resilience was explored and applied to real building cases for assessing the resilience enhancement efficiency of passive cooling strategies. Related research problems were solved about young and older people's physiological responses to hot exposure, indices and heatwave patterns considered in EHY selection, and resilient cooling strategy quantification. The conclusions were the following:

- The existing two-node bioheat model for average-aged people can be improved by additional temperature control signals and optimizing the values of the model constants to hot exposure. The recently published thermoregulatory models about sweating, skin blood flow, shivering, and sweat evaporation efficiency can be integrated into the two-node structure to inter-compare their efficiency in improving the prediction of physiological responses, including core temperature and mean skin temperature. After adjusting based on the age-related weakening changes in physiology and thermoregulatory activities for sweating, vasomotor, and shivering, the two-node bioheat model can be applied to predict older people's physiological responses.

- In building overheating-centric studies, the EHYs should be selected according to severity and intensity instead of the duration of heatwaves. The heatwaves should be defined by the thermal-based index instead of only air temperature. The EHYs selected with thermal-based index results in a higher percentage of synchronization (POS) of outdoor and indoor heat events than the temperature-based index for buildings located in the cold to hot climate zones, especially in the climate zones with high humidity. The EHYs with the most intense and severe heatwaves lead to higher POS than the years with the longest heatwave, indicating the intensity and severity of heatwaves are more significant than the duration of heatwaves when selecting EHYs for building centric analysis. In cool or cold climates, the severe extreme year should be chosen. In mixed or hot climates, the intense extreme year should be selected.
- The concept of POS can be applied to different types of buildings in various climate zones to be used as a criterion for selecting the most significant EHYs for indoor overheating studies. A representative historical EHY for each city of three cities in Canada and three in the US was chosen from long-term climate data.
- Based on the building thermal resilience quantification, among the four studied overheating retrofit strategies, including exterior shading (ES), green roof (GF), natural ventilation (NV), and night ventilation (NiV), NV is the most efficient, whereas ES can improve the thermal resilience of the most overheated zone. The combination of ES+NV is the most recommended, which can efficiently enhance building-level resilience and more than 50% of zone-level thermal resilience to Class B, as well as reach a good resilience uniformity of zones.

7.2. Contributions

This research developed models to quantify young and older adults' physiological responses to heat-stress conditions and building thermal resilience against extreme heat events, as well as the method to select extreme reference weather years for indoor overheating studies. These models and methods were validated and demonstrated with case studies and could be extensively used in studies related to protecting human health and enhancing building resilience to heat events. The models and methods include:

- A bioheat model for average-aged people with an improved thermoregulatory system in the two-node model was developed and validated using experimental data covering hot and cold exposure conditions. The thermoregulatory system was improved by including additional temperature control signals and optimizing the values of the model constants. The model constants were optimized based on the combined RMSE to predict the core and skin temperatures. Inter-comparison was conducted for the proposed thermoregulatory models together with recently published thermoregulatory models for sweating (six models), skin blood flow (three models), shivering (three models), and sweat evaporation efficiency (four models) in the two-node structure. The improved two-node model was proved to accurately predict core and skin temperatures under a wide range of hot and cold exposure conditions.
- A new bioheat model for older people was developed based on the two-node model for average-aged people, accounting for the age-related weakening changes in physiology and thermoregulatory activities for sweating, vasomotor, and shivering. Two types of age-related physiological changes were considered, including the weakening of

thermoregulatory activities and sensory delays in triggering thermoregulatory actions. Under steady hot and cold exposures, the proposed model predictions agreed well with the experiments: the maximum deviation was 0.30℃ in the core temperature and 0.60℃ in the mean skin temperature. The proposed model can also capture the relative difference in physiological responses between older and young people in hot to cold scenarios.

- A new method was proposed to select extreme hot years for building indoor overheating analysis. The extreme hot year (EHY) was determined by quantifying the degree of synchronization between outdoor heatwave events and building indoor overheating conditions based on the concept of Percentage of Synchronization (POS). A higher value of POS indicates a higher chance of building indoor overheating occurring based on outdoor heatwave events for many archetype buildings and situations for specific climate zones.
- A new quantification framework was proposed to evaluate the building and zone level thermal resilience to extreme heat events. The framework was based on the investigation of the resilience profile, the resilience metric, and the performance indicator. The conceptual building thermal resilience curve has the profile of a resilience trapezoid. A resilience parameter, the Thermal Resilience Index (TRI), can be calculated by determining the improvement in relative resilience from original conditions. The zone-level and building-level thermal resilience can be labelled based on the value of TRI_z and TRI_b, respectively. Each labelled class represents the percentage of improvement in resilience. The distribution in zone-level resilience can also be analyzed by the absolute thermal resilience of each zone $WSETH_z$. A smaller standard deviation of the distribution means

the zone resilience is more homogenous. The Standard Effective Temperature (SET) can be used as a performance indicator to define the building thermal performance curve.

7.3. Future work

The main contribution of this research is proposing validated models and methods to be used in the studies about climate-resilient buildings, from the three aspects of occupants' physiological responses, building thermal resilience and selection of extreme weather data from a long-term period.

The proposed models and methods can be extensively implemented on larger spatial and temporal scales. With projected future climate data, one can select the extreme reference weather and then thereby investigate the climate change impact on human health and building resilience, based on which to explore potential mitigations to avoid negative consequences due to global warming. Based on a similar concept, with weather data of different climate zones of the world, the quantification method can be applied and label the building thermal resilience in different climates, thus, providing a quantitative comparison of various climates and their impact on buildings.

The proposed method can quantitively evaluate the health risk reduction and resilience enhancement efficiency of climate mitigation strategies such as nature-based solutions (NBS), which have been regarded to have significant potential to mitigate the effects of heatwaves, reduce heat vulnerability and enhance the thermal resilience (Kabisch et al., 2016). The type and extent of NBS, as well as the spatial distribution of the NBS at the community scale, directly influence the local microclimate and in turn, the safety to humans to thermal effects due to extreme heat events. As buildings act as wind obstacles and anthropogenic heat is released into the environment, the interactions between outdoor microclimate and indoor thermal conditions can also be affected

by NBS configurations. The proposed tools can act as quantitative evaluations of human thermal risks and community-building thermal resilience levels with and without the protection of NBS strategies under the impact of urban heat islands and climate change. The use of labeling of the resilience level allows quantifying the performance of a given NBS configuration, thereby permitting a detailed design to be achieved.

Due to older people being more vulnerable than young people to heat or cold conditions, predicting older people's thermal sensations is also important for controlling the built environment and avoiding extreme heat/cold injuries. Previous studies mainly focused on predicting the thermal sensation of general population, and the data-driven methods are often not constrained by physiological responses. Integrated models can be studied to combine the proposed physiological model of older people and the data-driven methods. The surveyed data on older people's thermal sensations can be found in ASHRAE Global Thermal Comfort Database II (Földváry Ličina et al., 2018). The dataset has collected the environmental conditions, subjects' factors, and thermal sensation vote (TSV) survey results. With the environmental conditions (air temperature, mean radiant temperature, relative humidity, and airspeed) and subject factors (clothing insulation, height, and weight) as inputs, core and skin temperatures, water loss, and standard effective temperature (SET) can be calculated by the two-node model of older people. The above physiological parameters and building operation mode (natural-ventilated/air-conditioned), older people's gender, surveyed seasons, and climate zones can be used to train the data-driven model to predict older people's thermal resilience in various scenarios.

References

Ahmadalipour, A., Moradkhani, H., 2018. Escalating heat-stress mortality risk due to global warming in the Middle East and North Africa (MENA). Environ. Int. 117, 215–225. https://doi.org/10.1016/j.envint.2018.05.014

Ahmed, K., Hasu, T., Kurnitski, J., 2022. Actual energy performance and indoor climate in Finnish NZEB daycare and school buildings. J. Build. Eng. 56, 104759. https://doi.org/10.1016/j.jobe.2022.104759

Ahmed, T., Kumar, P., Mottet, L., 2021. Natural ventilation in warm climates: The challenges of thermal comfort, heatwave resilience and indoor air quality. Renew. Sustain. Energy Rev. 138, 110669. https://doi.org/10.1016/j.rser.2020.110669

Akbari Rad, S., Joshaghani, H.R., Khoshnia, M., Hosseini, S.M., 2016. Comparison of Serum Strontium and Antimony Levels in Patients with Esophageal Cancer and Healthy People. Med. Lab. J. 10. https://doi.org/10.18869/acadpub.mlj.10.4.9

Aliberti, A., Bottaccioli, L., Macii, E., Di Cataldo, S., Acquaviva, A., Patti, E., 2019. A non-linear autoregressive model for indoor air-temperature predictions in smart buildings. Electron. 8, 1–17. https://doi.org/10.3390/electronics8090979

Anderson, M., Carmichael, C., Murray, V., Dengel, A., Swainson, M., 2013. Defining indoor heat thresholds for health in the UK. Perspect. Public Health 133, 158–164. https://doi.org/10.1177/1757913912453411

Appenzeller, U., Meyer, C., Menz, G., Blaser, K., Crameri, R., 1999. IgE-Mediated reactions to autoantigens in allergic diseases. Int. Arch. Allergy Immunol. 118, 193–196. https://doi.org/10.1159/000024064

Arima, Y., Ooka, R., Kikumoto, H., 2017. Proposal of typical and design weather year for building energy simulation. Energy Build. 139, 517–524. https://doi.org/10.1016/j.enbuild.2017.01.056

ASHARE, 2013. Energy Standard for Buildings Except Low-Rise Residential Buildings 2013, 404–636.

ASHRAE-55, 2017. Thermal environmental conditions for human occupancy. ANSI/ASHRAE Stand. - 55 7, 6.

ASHRAE, 2013a. ANSI/ASHRAE standard 169-2013 climatic data for building design standards.

ASHRAE, 2013b. Handbook of Fundamentals. 2013. Atlanta, GA: American Society for Heating, Refrigerating and Air Conditioning Engineers.

ASHRAE, 2002. ASHRAE Guideline 14-2002: Measurement of Energy Demand and Savings; American Society of Heating.

ASHRAE Standards Committee, 2004. Addendum to Standard 90.1-2001. Energy Standardfor BuildingsExcept Low-RiseResidential Buildings 8400.

Attia, S., Levinson, R., Ndongo, E., Holzer, P., Berk Kazanci, O., Homaei, S., Zhang, C., Olesen, B.W., Qi, D., Hamdy, M., Heiselberg, P., 2021. Resilient cooling of buildings to protect against heat waves and power outages: Key concepts and definition. Energy Build. 239, 110869. https://doi.org/10.1016/j.enbuild.2021.110869

Ayyub, B.M., 2014. Systems resilience for multihazard environments: Definition, metrics, and valuation for decision making. Risk Anal. 34, 340–355. https://doi.org/10.1111/risa.12093

Baba, F.M., Ge, H., Zmeureanu, R., Wang, L. (Leon), 2022. Calibration of building model based on indoor temperature for overheating assessment using genetic algorithm: Methodology, evaluation criteria, and case study. Build. Environ. 207, 108518. https://doi.org/10.1016/j.buildenv.2021.108518

Balmain, B.N., Sabapathy, S., Louis, M., Morris, N.R., 2018. Aging and Thermoregulatory Control: The Clinical Implications of Exercising under Heat Stress in Older Individuals. Biomed Res. Int. 2018. https://doi.org/10.1155/2018/8306154

Benchekroun, M., Chergui, S., Ruggiero, F., Di Turi, S., 2019. Improving the indoor climate of the traditional Ottoman houses in the Medina of Algiers. IOP Conf. Ser. Mater. Sci. Eng. 609, 0–7. https://doi.org/10.1088/1757-899X/609/4/042073

Bilbao, J., Miguel, A., Jose A, F., 2003. Test Reference Year Generation and Evaluation Methods in the Continental Mediterranean Area. J. Appl. Meteorol. Climatol. 390–400. https://doi.org/10.1175/1520-0450(2004)043<0390:TRYGAE>2.0.CO;2

Blazejczyk, K., Epstein, Y., Jendritzky, G., Staiger, H., Tinz, B., 2012. Comparison of UTCI to selected thermal indices. Int. J. Biometeorol. 56, 515–535. https://doi.org/10.1007/s00484-011-0453-2

Brake, R., Bates, G., 2002. A valid method for comparing rational and empirical heat stress indices. Ann. Occup. Hyg. 46, 165–174. https://doi.org/10.1093/annhyg/mef030

Brotas, L., Nicol, F., 2016. Using Passive Strategies to prevent overheating and promote resilient buildings, in: Proceedings of: 32nd International Conference on Passive and Low Energy Architecture. Cities, Buildings, People: Towards Regenerative Environments. Los Angeles.

Bruneau, M., Chang, S.E., Eguchi, R.T., Lee, G.C., O'Rourke, T.D., Reinhorn, A.M., Shinozuka, M., Tierney, K., Wallace, W.A., von Winterfeldt, D., 2003. A Framework to Quantitatively Assess and Enhance the Seismic Resilience of Communities. Earthq. Spectra 19, 733–752. https://doi.org/10.1193/1.1623497

Bunker, A., Wildenhain, J., Vandenbergh, A., Henschke, N., Rocklöv, J., Hajat, S., Sauerborn, R., 2016. Effects of Air Temperature on Climate-Sensitive Mortality and Morbidity Outcomes in the Elderly; a Systematic Review and Meta-analysis of Epidemiological Evidence. EBioMedicine 6, 258–268. https://doi.org/10.1016/j.ebiom.2016.02.034

Buonomano, A., Montanaro, U., Palombo, A., Santini, S., 2015. Adaptive control for building thermo-hygrometric analysis: A novel dynamic simulation code for indoor spaces with multi-enclosed thermal zones. Energy Procedia 78, 2190–2195. https://doi.org/10.1016/j.egypro.2015.11.316

Burman, E., Kimpian, J., Mumovic, D., 2014. Reconciling Resilience and Sustainability in Overheating and Energy Performance Assessment of Non-Domestic Buildings, in: Proceedings of: The 2nd International Conference on Urban Sustainability and Resilience.

Bustinza, R., Lebel, G., Gosselin, P., Bélanger, D., Chebana, F., 2013. Health impacts of the July 2010 heat wave in Québec, Canada. BMC Public Health 13. https://doi.org/10.1186/1471-2458-13-56

Cabinet Office, 2011. Keeping the country running: natural hazards and infrastructure. Improv. UK's Abil. to absorb, respond to Recover from emergencies.

Candas, V., Libert, J.P., Vogt, J.J., 1979. Human skin wettedness efficiency of sweating. J. Appl. Physiol. 46, 522–28.

Chang, S.E., Shinozuka, M., 2004. Measuring improvements in the disaster resilience of communities. Earthq. Spectra 20, 739–755. https://doi.org/10.1193/1.1775796

Chien, L.C., Guo, Y., Zhang, K., 2016. Spatiotemporal analysis of heat and heat wave effects on elderly mortality in Texas, 2006-2011. Sci. Total Environ. 562, 845–851. https://doi.org/10.1016/j.scitotenv.2016.04.042

Christoph Nytsch-Geusen, Kushagra Mathur, Lucas Westermann, 2021. Development of a real-time test bed for indoor climate simulation in a VR environment using a digital twin. Proc. 14th Model. Conf. 2021, Linköping, Sweden, Sept. 20-24, 2021 181, 263–269. https://doi.org/10.3384/ecp21181263

CIBSE, 2017. Design methodology for the assessment of overheating risk in homes - CIBSE TM59. Chart. Inst. Build. Serv. Eng. https://doi.org/CIBSE TM59: 2017

CIBSE, 2014. Design Summer Years for London Design Summer Years for London. Tm49.

CIBSE, 2013. The limits of thermal comfort : avoiding overheating in European buildings-CIBSE TM52, The Chartered Institution of Building Services Engineers. https://doi.org/10.1017/CBO9781107415324.004

Cirrincione, L., Marvuglia, A., Scaccianoce, G., 2021. Assessing the effectiveness of green roofs in enhancing the energy and indoor comfort resilience of urban buildings to climate change: Methodology proposal and application. Build. Environ. 205, 108198. https://doi.org/10.1016/j.buildenv.2021.108198

Coccarelli, A., Hasan, H.M., Carson, J., Parthimos, D., Nithiarasu, P., 2018. Influence of ageing on human body blood flow and heat transfer: A detailed computational modelling study. Int. j. numer. method. biomed. eng. 34, 1–21. https://doi.org/10.1002/cnm.3120

Coley, D., Herrera, M., Fosas, D., Liu, C., Vellei, M., 2017. Probabilistic adaptive thermal comfort for resilient design. Build. Environ. 123, 109–118. https://doi.org/10.1016/j.buildenv.2017.06.050

Committee on Climate Change, 2019. Committee on Climate Change, UK housing: fit for the future?.

Crawley, D.B., Lawrie, L.K., 2015. Rethinking the tmy: Is the "typical" meteorological year best for building performance simulation? 14th Int. Conf. IBPSA - Build. Simul. 2015, BS 2015, Conf. Proc. 2655–2662.

De Dear, R.J., Brager, G.S., 2002. Thermal comfort in naturally ventilated buildings: Revisions to ASHRAE Standard 55. Energy Build. 34, 549–561. https://doi.org/10.1016/S0378-7788(02)00005-1

DeGroot, D.W., Kenney, W.L., 2007. Impaired defense of core temperature in aged humans during mild cold stress. Am. J. Physiol. - Regul. Integr. Comp. Physiol. 292, 103–108. https://doi.org/10.1152/ajpregu.00074.2006

Dodoo, A., 2020. Energy and indoor thermal comfort performance of a Swedish residential building under future climate change conditions. E3S Web Conf. 172, 1–8. https://doi.org/10.1051/e3sconf/202017202001

DOE, 2020. Energyplus. https://energyplus.net/

Doherty, T.J., Arens, E., 1988. Evaluation of the physiological bases of thermal comfort models. ASHRAE Trans. 94. https://escholarship.org/uc/item/6pq3r5pr

Dongmei, P., Mingyin, C., Shiming, D., Minglu, Q., 2012. A four-node thermoregulation model for predicting the thermal physiological responses of a sleeping person. Build. Environ. 52, 88–97. https://doi.org/10.1016/j.buildenv.2011.12.020

Dousset, B., Gourmelon, F., Laaidi, K., Zeghnoun, A., Giraudet, E., Bretin, P., Mauri, E., Vandentorren, S., 2011. Satellite monitoring of summer heat waves in the Paris metropolitan area. Int. J. Climatol. 31, 313–323.

Dufour, A., Candas, V., 2007. Ageing and thermal responses during passive heat exposure: Sweating and sensory aspects. Eur. J. Appl. Physiol. 100, 19–26. https://doi.org/10.1007/s00421-007-0396-9

Eady, A., Dreyer, B., Hey, B., Riemer, M., Wilson, A., 2020. Reducing the risks of extreme heat for seniors: Communicating risks and building resilience. Heal. Promot. Chronic Dis. Prev. Canada 40, 215–224. https://doi.org/10.24095/hpcdp.40.7/8.01

Eames, M.E., 2016. An update of the UK ' s design summer years : Probabilistic design summer years for enhanced overheating risk analysis in building design. https://doi.org/10.1177/0143624416631131

Egilson, M., 2022. Extreme heat and human mortality: A review of heat-related deaths in B.C. in

summer 2021. British Columbia. https://www2.gov.bc.ca/assets/gov

Elmadfa, I., Meyer, A.L., 2008. Body composition, changing physiological functions and nutrient requirements of the elderly. Ann. Nutr. Metab. 52, 2–5. https://doi.org/10.1159/000115339

Elsharkawy, H., Zahiri, S., 2020. The significance of occupancy profiles in determining post retrofit indoor thermal comfort, overheating risk and building energy performance. Build. Environ. 172, 106676. https://doi.org/10.1016/j.buildenv.2020.106676

Energy Systems Research Unit, 2020. ESP-r. https://www.esru.strath.ac.uk//applications/esp-r/

Enescu, D., 2019. Models and indicators to assess thermal sensation under steady-state and transient conditions. Energies 12. https://doi.org/10.3390/en12050841

Engineers, C.I. of B.S., n.d. CIBSE Guide J: Weather, solar and illuminance data. CIBSE, London.

Eriksson, L., Grozman, G., Grozman, P., Sahlin, P., Vorre, M.H., Ålenius, L., 2012. CFD-Free, Efficient, Micro Indoor Climate Prediction in Buildings. First Build. Simul. Optim. Conf. 149–156.

Escandón, R., Suárez, R., Alonso, A., Mauro, G.M., 2022. Is indoor overheating an upcoming risk in southern Spain social housing stocks? Predictive assessment under a climate change scenario. Build. Environ. 207. https://doi.org/10.1016/j.buildenv.2021.108482

Fabrizio, E., Monetti, V., 2015. Methodologies and advancements in the calibration of building energy models. Energies 8, 2548–2574. https://doi.org/10.3390/en8042548

FEMP, 2008. M&V Guidelines: Measurement and Verification for Federal Energy Projects Version 3.0.

Fiala, D., Havenith, G., Bröde, P., Kampmann, B., Jendritzky, G., 2012. UTCI-Fiala multi-node model of human heat transfer and temperature regulation. Int. J. Biometeorol. 56, 429–441. https://doi.org/10.1007/s00484-011-0424-7

Fiorito, F., Vurro, G., Carlucci, F., Campagna, L.M., De Fino, M., Carlucci, S., Fatiguso, F., 2022. Adaptation of Users to Future Climate Conditions in Naturally Ventilated Historic Buildings: Effects on Indoor Comfort. Energies 15. https://doi.org/10.3390/en15144984

Firląg, S., Murray, S., 2013. Impacts of airflows, internal heat and moisture gains on accuracy of modeling energy consumption and indoor parameters in passive building. Energy Build. 64, 372–383. https://doi.org/10.1016/j.enbuild.2013.04.024

Flores-Larsen, S., Bre, F., Hongn, M., 2022. A performance-based method to detect and characterize heatwaves for building resilience analysis. Renew. Sustain. Energy Rev. 167, 112795. https://doi.org/10.1016/j.rser.2022.112795

Flores-Larsen, S., Filippín, C., 2021. Energy efficiency, thermal resilience, and health during extreme heat events in low-income housing in Argentina. Energy Build. 231, 110576. https://doi.org/10.1016/j.enbuild.2020.110576

Földváry Ličina, V., Cheung, T., Zhang, H., de Dear, R., Parkinson, T., Arens, E., Chun, C., Schiavon, S., Luo, M., Brager, G., Li, P., Kaam, S., Adebamowo, M.A., Andamon, M.M., Babich, F., Bouden, C., Bukovianska, H., Candido, C., Cao, B., Carlucci, S., Cheong, D.K.W., Choi, J.H., Cook, M., Cropper, P., Deuble, M., Heidari, S., Indraganti, M., Jin, Q., Kim, H., Kim, J., Konis, K., Singh, M.K., Kwok, A., Lamberts, R., Loveday, D., Langevin, J., Manu, S., Moosmann, C., Nicol, F., Ooka, R., Oseland, N.A., Pagliano, L., Petráš, D., Rawal, R., Romero, R., Rijal, H.B., Sekhar, C., Schweiker, M., Tartarini, F., Tanabe, S. ichi, Tham, K.W., Teli, D., Toftum, J., Toledo, L., Tsuzuki, K., De Vecchi, R., Wagner, A., Wang, Z., Wallbaum, H., Webb, L., Yang, L., Zhu, Y., Zhai, Y., Zhang, Y., Zhou, X., 2018. Development of the ASHRAE Global Thermal Comfort Database II. Build. Environ. 142, 502–512. https://doi.org/10.1016/j.buildenv.2018.06.022

Frank, S.M., Raja, S.N., Bulcao, C., Goldstein, D.S., 2000. Age-related thermoregulatory differences during core cooling in humans. Am. J. Physiol. - Regul. Integr. Comp. Physiol. 279, 349–354. https://doi.org/10.1152/ajpregu.2000.279.1.r349

French, L., 2008. Design and construction features that cause new houses in New Zealand to overheat. Victoria University of Wellington. https://researcharchive.vuw.ac.nz/xmlui/bitstream/handle/10063/857/thesis.pdf?sequence=1

Gagge, A., Fobelets, A., Berglund, L., 1986. A standard predictive index of human response to the thermal environment. ASHRAE Trans. 92, 709–731. https://www.aivc.org/resource/standard-predictive-index-human-response-thermal-environment

Gagge, A., Stolwijk JAJ, Y, N., 1971. Effective temperature scale based on a simple model of human physiological regulatory response. ASHRAE Trans. http://hdl.handle.net/2115/37901

Ganguly, S., Ahmed, A., Wang, F., 2020. Optimised building energy and indoor microclimatic predictions using knowledge-based system identification in a historical art gallery. Neural Comput. Appl. 32, 3349–3366. https://doi.org/10.1007/s00521-019-04224-7

Gao, J., Wang, Y., Wargocki, P., 2015. Comparative analysis of modified PMV models and SET models to predict human thermal sensation in naturally ventilated buildings. Build. Environ. 92, 200–208. https://doi.org/10.1016/j.buildenv.2015.04.030

Gaur, A., Lacasse, M., Armstrong, M., 2019. Climate data to undertake hygrothermal and whole building simulations under projected climate change influences for 11 Canadian cities. Data 4. https://doi.org/10.3390/data4020072

Government of Canada, 2014. Action for Seniors report.

Greaney, J.L., Stanhewicz, A.E., Wolf, S.T., Kenney, W.L., 2020. Thermoregulatory reflex control of cutaneous vasodilation in healthy aging. Temperature 00, 1–12. https://doi.org/10.1080/23328940.2020.1832950

Guergova, S., Dufour, A., 2011. Thermal sensitivity in the elderly: A review. Ageing Res. Rev. 10, 80–92. https://doi.org/10.1016/j.arr.2010.04.009

Guo, R., Gao, Y., Zhuang, C., Heiselberg, P., Levinson, R., Zhao, X., Shi, D., 2020. Optimization of cool roof and night ventilation in office buildings: A case study in Xiamen, China. Renew. Energy 147, 2279–2294. https://doi.org/10.1016/j.renene.2019.10.032

Guo, S., Yan, D., Hong, T., Xiao, C., Cui, Y., 2019. A novel approach for selecting typical hot-year (THY) weather data. Appl. Energy 242, 1634–1648. https://doi.org/10.1016/j.apenergy.2019.03.065

Gupta, R., Gregg, M., Irving, R., 2019. Meta-analysis of summertime indoor temperatures in new-build , retrofitted , and existing UK dwellings Meta-analysis of summertime indoor temperatures in new-build , retrofitted , and existing UK dwellings. Sci. Technol. Built Environ. 0, 1–14. https://doi.org/10.1080/23744731.2019.1623585

Gustin, M., McLeod, R.S., Lomas, K.J., Petrou, G., Mavrogianni, A., 2020. A high-resolution indoor heat-health warning system for dwellings. Build. Environ. 168, 106519. https://doi.org/10.1016/j.buildenv.2019.106519

Hamdy, M., Carlucci, S., Hoes, P.J., Hensen, J.L.M., 2017. The impact of climate change on the overheating risk in dwellings—A Dutch case study. Build. Environ. 122, 307–323. https://doi.org/10.1016/j.buildenv.2017.06.031

Hatvani-Kovacs, G., Belusko, M., Skinner, N., Pockett, J., Boland, J., 2016. Heat stress risk and resilience in the urban environment. Sustain. Cities Soc. 26, 278–288. https://doi.org/10.1016/j.scs.2016.06.019

Havenith, G., 2001. Individualized model of human thermoregulation for the simulation of heat stress response. J. Appl. Physiol. 90, 1943–1954. https://doi.org/10.1152/jappl.2001.90.5.1943

Havenith, G., Fiala, D., 2016. Thermal indices and thermophysiological modeling for heat stress. Compr. Physiol. 6, 255–302. https://doi.org/10.1002/cphy.c140051

Henry, D., Emmanuel Ramirez-Marquez, J., 2012. Generic metrics and quantitative approaches for system resilience as a function of time. Reliab. Eng. Syst. Saf. 99, 114–122. https://doi.org/10.1016/j.ress.2011.09.002

Heracleous, C., Michael, A., Savvides, A., Hayles, C., 2021. Climate change resilience of school premises in Cyprus: An examination of retrofit approaches and their implications on thermal and energy performance. J. Build. Eng. 44, 103358. https://doi.org/10.1016/j.jobe.2021.103358

Herrera, M., Ramallo-González, A.P., Eames, M., Ferreira, A.A., Coley, D.A., 2018. Creating extreme weather time series through a quantile regression ensemble. Environ. Model. Softw. 110, 28–37. https://doi.org/10.1016/j.envsoft.2018.03.007

Hess, J.J., Sathish, L.M., Knowlton, K., Saha, S., Dutta, P., Ganguly, P., Tiwari, A., Jaiswal, A., Sheffield, P., Sarkar, J., Bhan, S.C., Begda, A., Shah, T., Solanki, B., Mavalankar, D., 2018. Building resilience to climate change: Pilot evaluation of the impact of India's first heat action

plan on all-cause mortality. J. Environ. Public Health 2018. https://doi.org/10.1155/2018/7973519

Hirata, A., Nomura, T., Laakso, I., 2015. Computational estimation of body temperature and sweating in the aged during passive heat exposure. Int. J. Therm. Sci. 89, 154–163. https://doi.org/10.1016/j.ijthermalsci.2014.11.001

Hoffman, 2014. The No-U-Turn Sampler: Adaptively Setting Path Lengths in Hamiltonian Monte Carlo. J. Mach. Learn. Res. 15, 1593–1623. https://doi.org/10.48550/arXiv.1111.4246

Holmes, S.H., Phillips, T., Wilson, A., 2016. Overheating and passive habitability: Indoor health and heat indices. Build. Res. Inf. 44, 1–19. https://doi.org/10.1080/09613218.2015.1033875

Holowatz, L.A., Kenney, W.L., 2010. Peripheral mechanisms of thermoregulatory control of skin blood flow in aged humans. J. Appl. Physiol. 109, 1538–1544. https://doi.org/10.1152/japplphysiol.00338.2010

Homaei, S., Hamdy, M., 2021. Thermal resilient buildings: How to be quantified? A novel benchmarking framework and labelling metric. Build. Environ. 201, 108022. https://doi.org/10.1016/j.buildenv.2021.108022

Honda, Y., Kondo, M., McGregor, G., Kim, H., Guo, Y.L., Hijioka, Y., Yoshikawa, M., Oka, K., Takano, S., Hales, S., Kovats, R.S., 2014. Heat-related mortality risk model for climate change impact projection. Environ. Health Prev. Med. 19, 56–63. https://doi.org/10.1007/s12199-013-0354-6

Hosseini, M., Javanroodi, K., Nik, V.M., 2022. High-resolution impact assessment of climate change on building energy performance considering extreme weather events and microclimate – Investigating variations in indoor thermal comfort and degree-days. Sustain. Cities Soc. 78, 103634. https://doi.org/10.1016/j.scs.2021.103634

Hosseini, S., Barker, K., Ramirez-Marquez, J.E., 2016. A review of definitions and measures of system resilience. Reliab. Eng. Syst. Saf. 145, 47–61. https://doi.org/10.1016/j.ress.2015.08.006

Huang, H., Kato, S., Hu, R., 2012. Optimum design for indoor humidity by coupling Genetic Algorithm with transient simulation based on Contribution Ratio of Indoor Humidity and Climate analysis. Energy Build. 47, 208–216. https://doi.org/10.1016/j.enbuild.2011.11.040

Ibrahim, A., Pelsmakers, S.L.J., 2018. Low-energy housing retrofit in North England : Overheating risks and possible mitigation strategies. https://doi.org/10.1177/0143624418754386

Iddon, C.R., Mills, T.C., Giridharan, R., Lomas, K.J., 2015. The influence of hospital ward design on resilience to heat waves: An exploration using distributed lag models. Energy Build. 86, 573–588. https://doi.org/10.1016/j.enbuild.2014.09.053

IECC, 2018. International Energy Conservation Code.

IJ, H., RR, P., HE, A., EC, B., 1978. Generation of a typical meteorological year, in: Analysis for Solar Heating and Cooling. San Diego. https://www.osti.gov/biblio/7013202

Inoue, Y., Nakao, M., Araki, T., Ueda, H., 1992. Thermoregulatory responses of young and older men to cold exposure. Eur. J. Appl. Physiol. Occup. Physiol. 65, 492–498. https://doi.org/10.1007/BF00602354

IPMVP, 2003. International Performance Measurement & Verification Protocol: Concepts and Option for Determining Energy Savings in New Construction. https://doi.org/https://www.nrel.gov/docs/fy02osti/31505.pdf

Irving, S., Ford, B., Etheridge, D., 2005. Natural ventilation in non-domestic buildings. CIBSE Appl. Man. AM10 70.

ISO 7933, 2017. Ergonomics of the thermal environment — Analytical determination and interpretation of heat stress using the predicted heat strain model.

Issahaku, P.A., Neysmith, S., 2013. Policy implications of population ageing in West Africa. Int. J. Sociol. Soc. Policy 33, 186–202. https://doi.org/10.1108/01443331311308230

Itani, M., Ghaddar, N., Ghali, K., Laouadi, A., 2020a. Development of heat stress charts for older people under indoor environmental conditions. Energy Build. 224, 110274. https://doi.org/10.1016/j.enbuild.2020.110274

Itani, M., Ghaddar, N., Ghali, K., Laouadi, A., 2020b. Bioheat modeling of elderly and young for prediction of physiological and thermal responses in heat-stressful conditions. J. Therm. Biol. 88, 102533. https://doi.org/10.1016/j.jtherbio.2020.102533

Jentsch, M.F., Eames, M.E., Levermore, G.J., 2015. Generating near-extreme Summer Reference Years for building performance simulation. https://doi.org/10.1177/0143624415587476

Ji, L., Laouadi, A., Shu, C., Gaur, A., Lacasse, M., Wang, L. (Leon), 2022a. Evaluating approaches of selecting extreme hot years for assessing building overheating conditions during heatwaves. Energy Build. 254, 111610. https://doi.org/10.1016/j.enbuild.2021.111610

Ji, L., Laouadi, A., Shu, C., Wang, L., Lacasse, M.A., 2021. Evaluation and improvement of the thermoregulatory system for the two-node bioheat model. Energy Build. 249, 111235. https://doi.org/10.1016/j.enbuild.2021.111235

Ji, L., Laouadi, A., Wang, L., Lacasse, M.A., 2022b. Development of a bioheat model for older people under hot and cold exposures. Build. Simul. 15, 1815–1829. https://doi.org/10.1007/s12273-022-0890-3

Ji, L., Shu, C., Hou, D., Laouadi, A., Leon, L., Lacasse, M., 2022c. Predicting indoor air temperatures by calibrating building thermal model with coupled airflow networks. 2022 CLIMA 2022 14th REHVA HVAC World Congr. 1–8. https://doi.org/10.34641/clima.2022.340

Ji, L., Shu, C., Laouadi, A., Wang, L. (Leon), Lacasse, M., 2022d. Predicting older people ’ s

thermal sensation by a new integrated driven model, in: IAQ 2020: Indoor Environmental Quality Performance Approaches Transitioning from IAQ to IEQ. ASHRAE, Athens, Greece.

Kabisch, N., Frantzeskaki, N., Pauleit, S., Naumann, S., Davis, M., Artmann, M., Haase, D., Knapp, S., Korn, H., Stadler, J., Zaunberger, K., Bonn, A., 2016. Nature-based solutions to climate change mitigation and adaptation in urban areas: Perspectives on indicators, knowledge gaps, barriers, and opportunities for action. Ecol. Soc. 21. https://doi.org/10.5751/ES-08373-210239

Karaki, W., Ghaddar, N., Ghali, K., Kuklane, K., Holmér, I., Vanggaard, L., 2013. Human thermal response with improved AVA modeling of the digits. Int. J. Therm. Sci. 67, 41–52. https://doi.org/10.1016/j.ijthermalsci.2012.12.010

Katal, A., Mortezazadeh, M., Wang, L. (Leon), 2019. Modeling building resilience against extreme weather by integrated CityFFD and CityBEM simulations. Appl. Energy 250, 1402–1417. https://doi.org/10.1016/j.apenergy.2019.04.192

Katić, K., Li, R., Zeiler, W., 2016. Thermophysiological models and their applications: A review. Build. Environ. 106, 286–300. https://doi.org/10.1016/j.buildenv.2016.06.031

Kenney, W.L., 2012. Physiological response to the thermal environment, in: Stellman, J. (Ed.), International Labour Organization's Encyclopaedia of Occupational Health and Safety. https://www.iloencyclopaedia.org/part-vi-16255/heat-and-cold/item/

Kenney, W.L., Munce, T.A., 2003. Physiology of Aging Invited Review: Aging and human temperature regulation. Pandolf KB. Exp Aging Res Ageing Res Rev Exp Aging Res 17, 41–76.

Kenny, G.P., Flouris, A.D., Yagouti, A., Notley, S.R., 2019. Towards establishing evidence-based guidelines on maximum indoor temperatures during hot weather in temperate continental climates. Temperature 6, 11–36. https://doi.org/10.1080/23328940.2018.1456257

Kenny, G.P., Notley, S.R., Gagnon, D., 2017. Direct calorimetry: a brief historical review of its use in the study of human metabolism and thermoregulation. Eur. J. Appl. Physiol. 117, 1765–1785. https://doi.org/10.1007/s00421-017-3670-5

Kim, Y. ook, Lee, W., Kim, H., Cho, Y., 2020. Social isolation and vulnerability to heatwave-related mortality in the urban elderly population: A time-series multi-community study in Korea. Environ. Int. 142, 105868. https://doi.org/10.1016/j.envint.2020.105868

Kistelegdi, I., Baranyai, B., 2013. Dynamic Simulations Supported Indoor Climate and Energy Building Modeling. Int. J. Eng. Technol. 181–186. https://doi.org/10.7763/ijet.2013.v5.537

Klein, S.A., Beckman, W.A., Mitchell, J.W., Duffie, J.A., Duffie, N.A., Freeman, T.L., Mitchell, J.C., Braun, J.E., Evans, B.L., Kummer, J.P., 2004. TRNSYS 16–A TRaNsient system simulation program, user manual. Sol. Energy Lab. Madison Univ. Wisconsin-Madison.

Kownacki, K.L., Gao, C., Kuklane, K., Wierzbicka, A., 2019. Heat stress in indoor environments

of scandinavian urban areas: A literature review. Int. J. Environ. Res. Public Health 16, 1–18. https://doi.org/10.3390/ijerph16040560

Kramer, R., van Schijndel, J., Schellen, H., 2013. Inverse modeling of simplified hygrothermal building models to predict and characterize indoor climates. Build. Environ. 68, 87–99. https://doi.org/10.1016/j.buildenv.2013.06.001

Kubota, H., Kuwabara, K., Hamada, Y., 2014. The development and initial validation of a virtual dripping sweat rate and a clothing wetness ratio for use in predictive heat strain models. Int. J. Biometeorol. 58, 1339–1353. https://doi.org/10.1007/s00484-013-0736-x

Künzel, H.M., Holm, A., Zirkelbach, D., Karagiozis, A.N., 2005. Simulation of indoor temperature and humidity conditions including hygrothermal interactions with the building envelope. Sol. Energy 78, 554–561. https://doi.org/10.1016/j.solener.2004.03.002

Lamothe, F., Roy, M., Racine-Hamel, S.-É., 2019. Enquête épidémiologique - Vague de chaleur à l'été 2018 à Montréal. https://santemontreal.qc.ca/fileadmin/user_upload/Uploads/tx_asssmpublications/pdf/publications/

Langner, M., Scherber, K., Endlicher, W.R., 2013. Indoor heat stress: An assessment of human bioclimate using the UTCI in different buildings in Berlin. Erde 144, 260–273. https://doi.org/10.12854/erde-144-18

Laouadi, A., Bartko, M., Lacasse, M.A., 2020a. A New Methodology of Evaluation of Overheating in Buildings. Energy Build. 226, 110360. https://doi.org/10.1016/j.enbuild.2020.110360

Laouadi, A., Gaur, A., Lacasse, M.A., Bartko, M., Armstrong, M., 2020b. Development of reference summer weather years for analysis of overheating risk in buildings. J. Build. Perform. Simul. 0, 1–19. https://doi.org/10.1080/19401493.2020.1727954

Lee, W.V., Shaman, J., 2017. Heat-coping strategies and bedroom thermal satisfaction in New York City. Sci. Total Environ. 574, 1217–1231. https://doi.org/10.1016/j.scitotenv.2016.07.006

Lei, M., van Hooff, T., Blocken, B., Pereira Roders, A., 2022. The predicted effect of climate change on indoor overheating of heritage apartments in two different Chinese climate zones. Indoor Built Environ. 31, 1986–2006. https://doi.org/10.1177/1420326x221085861

Leon, L., Shu, C., Ge, H., Zmeureanu, R., Lacasse, M., Leroyer, S., 2020. Assessment of summertime overheating conditions in vulnerable buildings in Montréal. 2nd Int. Conf. New Horizons Green Civ. Eng. (NHICE-02), Victoria, BC, Canada, April 29 – May 01, 2020 2–5.

Levermore, G.J., Parkinson, J.B., 2006. Analyses and algorithms for new test reference years and design summer years for the UK. Build. Serv. Eng. Res. Technol. 27, 311–325. https://doi.org/10.1177/0143624406071037

Li, B., Yang, Y., Yao, R., Liu, H., Li, Y., 2017. A simplified thermoregulation model of the human body in warm conditions. Appl. Ergon. 59, 387–400. https://doi.org/10.1016/j.apergo.2016.09.010

Li, H., Yang, Y., Lv, K., Liu, J., Yang, L., 2020. Compare several methods of select typical meteorological year for building energy simulation in China. Energy 209, 118465. https://doi.org/10.1016/j.energy.2020.118465

Liang, C., Zheng, G., Zhu, N., Tian, Z., Lu, S., Chen, Y., 2011. A new environmental heat stress index for indoor hot and humid environments based on Cox regression. Build. Environ. 46, 2472–2479. https://doi.org/10.1016/j.buildenv.2011.06.013

Lim, H., Zhai, Z.J., 2017. Comprehensive evaluation of the influence of meta-models on Bayesian calibration. Energy Build. 155, 66–75. https://doi.org/10.1016/j.enbuild.2017.09.009

Liotta, G., Inzerilli, M.C., Palombi, L., Madaro, O., Orlando, S., Scarcella, P., Betti, D., Marazzi, M.C., 2018. Social interventions to prevent heat-related mortality in the older adult in Rome, Italy: A quasi-experimental study. Int. J. Environ. Res. Public Health 15, 1–13. https://doi.org/10.3390/ijerph15040715

Liu, C., Kershaw, T., Eames, M.E., Coley, D.A., 2016. Future probabilistic hot summer years for overheating risk assessments. Build. Environ. 105, 56–68. https://doi.org/10.1016/j.buildenv.2016.05.028

Liu, C., Kershaw, T., Fosas, D., Ramallo Gonzalez, A.P., Natarajan, S., Coley, D.A., 2017. High resolution mapping of overheating and mortality risk. Build. Environ. 122, 1–14. https://doi.org/10.1016/j.buildenv.2017.05.028

Liu, S., Kwok, Y.T., Lau, K., Ng, E., 2021. Applicability of different extreme weather datasets for assessing indoor overheating risks of residential buildings in a subtropical high-density city. Build. Environ. 194, 107711. https://doi.org/10.1016/j.buildenv.2021.107711

Lomas, K.J., Giridharan, R., 2012. Thermal comfort standards, measured internal temperatures and thermal resilience to climate change of free-running buildings: A case-study of hospital wards. Build. Environ. 55, 57–72. https://doi.org/10.1016/j.buildenv.2011.12.006

Lomas, K.J., Ji, Y., 2009. Resilience of naturally ventilated buildings to climate change: Advanced natural ventilation and hospital wards. Energy Build. 41, 629–653. https://doi.org/10.1016/j.enbuild.2009.01.001

Lomas, K.J., Porritt, S.M., 2017. Overheating in buildings: lessons from research. Build. Res. Inf. 45, 1–18. https://doi.org/10.1080/09613218.2017.1256136

López-García, E., Lizana, J., Serrano-Jiménez, A., Díaz-López, C., Ángela Barrios-Padura, 2022. Monitoring and analytics to measure heat resilience of buildings and support retrofitting by passive cooling. J. Build. Eng. 57. https://doi.org/10.1016/j.jobe.2022.104985

Loughnan, M., Carroll, M., Tapper, N.J., 2015. The relationship between housing and heat wave

resilience in older people. Int. J. Biometeorol. 59, 1291–1298. https://doi.org/10.1007/s00484-014-0939-9

Lundgren-Kownacki, K., Martínez, N., Johansson, B., Psikuta, A., Annaheim, S., Kuklane, K., 2017. Human responses in heat – comparison of the Predicted Heat Strain and the Fiala multi-node model for a case of intermittent work. J. Therm. Biol. 70, 45–52. https://doi.org/10.1016/j.jtherbio.2017.05.006

Ma, T., Xiong, J., Lian, Z., 2017. A human thermoregulation model for the Chinese elderly. J. Therm. Biol. 70, 2–14. https://doi.org/10.1016/j.jtherbio.2017.08.002

Machard, A., Inard, C., Alessandrini, J.-M., Pelé, C., Ribéron, J., 2020. A Methodology for Assembling Future Weather Files including Heatwaves for Building Thermal Simulations from Regional Climate Models Multi-years Datasets. Submitt. to Energies 1–34.

Macintyre, H.L., Heaviside, C., Taylor, J., Picetti, R., Symonds, P., Cai, X.M., Vardoulakis, S., 2018. Assessing urban population vulnerability and environmental risks across an urban area during heatwaves – Implications for health protection. Sci. Total Environ. 610–611, 678–690. https://doi.org/10.1016/j.scitotenv.2017.08.062

Maivel, M., Kurnitski, J., Kalamees, T., 2015. Field survey of overheating problems in Estonian apartment buildings. Archit. Sci. Rev. 58, 1–10. https://doi.org/10.1080/00038628.2014.970610

Martínez-Ibernón, A., Aparicio-Fernández, C., Royo-Pastor, R., Vivancos, J.L., 2016. Temperature and humidity transient simulation and validation in a measured house without a HVAC system. Energy Build. 131, 54–62. https://doi.org/10.1016/j.enbuild.2016.08.079

Martínez-Mariño, S., Eguía-Oller, P., Granada-Álvarez, E., Erkoreka-González, A., 2021. Simulation and validation of indoor temperatures and relative humidity in multi-zone buildings under occupancy conditions using multi-objective calibration. Build. Environ. 200. https://doi.org/10.1016/j.buildenv.2021.107973

Mavrogianni, A., Pathan, A., Oikonomou, E., Biddulph, P., Symonds, P., Davies, M., 2017. Inhabitant actions and summer overheating risk in London dwellings. Build. Res. Inf. 45, 119–142. https://doi.org/10.1080/09613218.2016.1208431

Mavrogianni, A., Taylor, J., Oikonomou, E., Raslan, R., 2013. The unintended consequences of energy efficient retrofit on indoor air pollution, condensation & overheating risk in a typical Georgian mid-terrace house. Futur. Build 2013. https://www.researchgate.net/publication/

Mba, C.J., 2010. Population ageing in Ghana: Research gaps and the way forward. J. Aging Res. 2010. https://doi.org/10.4061/2010/672157

Mba, L., Meukam, P., Kemajou, A., 2016. Application of artificial neural network for predicting hourly indoor air temperature and relative humidity in modern building in humid region. Energy Build. 121, 32–42. https://doi.org/10.1016/j.enbuild.2016.03.046

Meade, R.D., Akerman, A.P., Notley, S.R., McGinn, R., Poirier, P., Gosselin, P., Kenny, G.P., 2020. Physiological factors characterizing heat-vulnerable older adults: A narrative review. Environ. Int. 144, 105909. https://doi.org/10.1016/j.envint.2020.105909

Mitchell, D., Heaviside, C., Vardoulakis, S., Huntingford, C., Masato, G., P Guillod, B., Frumhoff, P., Bowery, A., Wallom, D., Allen, M., 2016. Attributing human mortality during extreme heat waves to anthropogenic climate change. Environ. Res. Lett. 11. https://doi.org/10.1088/1748-9326/11/7/074006

Mohaibesh, D., Monna, S., Qadi, H., Sokkar, R., 2021. Towards climate resilient residential buildings: Learning from traditional typologies. J. Phys. Conf. Ser. 2042. https://doi.org/10.1088/1742-6596/2042/1/012146

Mora, C., Dousset, B., Caldwell, I.R., Powell, F.E., Geronimo, R.C., Bielecki, C.R., Counsell, C.W.W., Dietrich, B.S., Johnston, E.T., Louis, L. V., Lucas, M.P., Mckenzie, M.M., Shea, A.G., Tseng, H., Giambelluca, T.W., Leon, L.R., Hawkins, E., Trauernicht, C., 2017. Global risk of deadly heat. Nat. Clim. Chang. 7, 501–506. https://doi.org/10.1038/nclimate3322

Morakinyo, T.E., Dahanayake, K.W.D.K.C., Adegun, O.B., Balogun, A.A., 2016. Modelling the effect of tree-shading on summer indoor and outdoor thermal condition of two similar buildings in a Nigerian university. Energy Build. 130, 721–732. https://doi.org/10.1016/j.enbuild.2016.08.087

Murphy, S., 2017. The construction of a modified Typical Meteorological Year for photovoltaic modeling in India. Renew. Energy 111, 447–454. https://doi.org/10.1016/j.renene.2017.04.033

Nagano, K., Takaki, A., Hirakawa, M., Tochihara, Y., 2005. Effects of ambient temperature steps on thermal comfort requirements. Int. J. Biometeorol. 50, 33–39. https://doi.org/10.1007/s00484-005-0265-3

Nastos, P.T., Matzarakis, A., 2012. The effect of air temperature and human thermal indices on mortality in Athens, Greece. Theor. Appl. Climatol. 108, 591–599. https://doi.org/10.1007/s00704-011-0555-0

NIAC, 2010. A Framework for Establishing Critical Infrastructure Resilience Goals: Final Report and Recommendations. Final Rep. Recomm. by Counc. 1–73.

Nicol, F., Bahadur Rijal, H., Imagawa, H., Thapa, R., 2020. The range and shape of thermal comfort and resilience. Energy Build. 224, 110277. https://doi.org/10.1016/j.enbuild.2020.110277

Nik, V.M., 2016. Making energy simulation easier for future climate – Synthesizing typical and extreme weather data sets out of regional climate models (RCMs). Appl. Energy 177, 204–226. https://doi.org/10.1016/j.apenergy.2016.05.107

Notley, S.R., D'Souza, A.W., Meade, R.D., Richards, B.J., Kenny, G.P., 2020. Whole-body heat exchange in women during constant- and variable-intensity work in the heat. Eur. J. Appl.

Physiol. 120, 2665–2675. https://doi.org/10.1007/s00421-020-04486-3

Novieto, D.T., 2013. Adapting a human thermoregulation model for predicting the thermal response of older persons. De Montfort University. https://dora.dmu.ac.uk/bitstream/handle/2086/9489/1.%20DNovieto_PhDThesis.pdf?sequence=1

NRC, 2017. National Energy Code of Canada for Buildings. Can. Comm. Build. Fire Codes. https://nrc.canada.ca/en/certifications-evaluations-standards/codes-canada/codes-canada-publications/national-energy-code-canada-buildings-2017

NRC, 2015. National Building Code of Canada 2015. https://nrc.canada.ca/en/certifications-evaluations-standards/codes-canada/codes-canada-publications/national-building-code-canada-2015

NSRDB, 2012. National Solar Radiation Data Base. URL https://nsrdb.nrel.gov/

O' Donovan, A., O' Sullivan, P.D., Murphy, M.D., 2019. Predicting air temperatures in a naturally ventilated nearly zero energy building: Calibration, validation, analysis and approaches. Appl. Energy 250, 991–1010. https://doi.org/10.1016/j.apenergy.2019.04.082

Ooka, R., Minami, Y., Sakoi, T., Tsuzuki, K., Rijal, H.B., 2010. Improvement of sweating model in 2-Node Model and its application to thermal safety for hot environments. Build. Environ. 45, 1565–1573. https://doi.org/10.1016/j.buildenv.2009.12.012

Ostro, B., Rauch, S., Green, R., Malig, B., Basu, R., 2010. Original Contribution The Effects of Temperature and Use of Air Conditioning on Hospitalizations 172, 1053–1061. https://doi.org/10.1093/aje/kwq231

Ozaki, M., Sessler, D.I., Matsukawa, T., Ozaki, K., Atarashi, K., Negishi, C., Suzuki, H., 1997. The Threshold for Thermoregulatory Nitrous Oxide/Bevoflurane Anesthesia the Elderly. Int. Anesth. Reseach Soc. 97. https://doi.org/10.1097/00000539-199705000-00014

Paliouras, P., Matzaflaras, N., Peuhkuri, R.H., Kolarik, J., 2015. Using measured indoor environment parameters for calibration of building simulation model - A passive house case study. Energy Procedia 78, 1227–1232. https://doi.org/10.1016/j.egypro.2015.11.209

Panteli, M., Mancarella, P., 2017. Modeling and evaluating the resilience of critical electrical power infrastructure to extreme weather events. IEEE Syst. J. 11, 1733–1742. https://doi.org/10.1109/JSYST.2015.2389272

Panteli, M., Mancarella, P., Trakas, D.N., Kyriakides, E., Hatziargyriou, N.D., 2017. Metrics and Quantification of Operational and Infrastructure Resilience in Power Systems. IEEE Trans. Power Syst. 32, 4732–4742. https://doi.org/10.1109/TPWRS.2017.2664141

Parekh, A., 2012. Representative Housing Thermal Archetypes for Energy Analysis Models. Ottawa.

Peng, R.D., Bobb, J.F., Tebaldi, C., McDaniel, L., Bell, M.L., Dominici, F., 2011. Toward a

quantitative estimate of future heat wave mortality under global climate change. Environ. Health Perspect. 119, 701–706. https://doi.org/10.1289/ehp.1002430

Pérez-Lombard, L., Ortiz, J., González, R., Maestre, I.R., 2009. A review of benchmarking, rating and labelling concepts within the framework of building energy certification schemes. Energy Build. 41, 272–278. https://doi.org/10.1016/j.enbuild.2008.10.004

Pfafferott, J., Rißmann, S., Sühring, M., Kanani-Sühring, F., Maronga, B., 2021. Building indoor model in PALM-4U: Indoor climate, energy demand, and the interaction between buildings and the urban microclimate. Geosci. Model Dev. 14, 3511–3519. https://doi.org/10.5194/gmd-14-3511-2021

Pioppi, B., Pigliautile, I., Piselli, C., Pisello, A.L., 2020. Cultural heritage microclimate change: Human-centric approach to experimentally investigate intra-urban overheating and numerically assess foreseen future scenarios impact. Sci. Total Environ. 703, 134448. https://doi.org/10.1016/j.scitotenv.2019.134448

Rahif, R., Norouziasas, A., Elnagar, E., Doutreloup, S., Pourkiaei, S.M., Amaripadath, D., Romain, A.C., Fettweis, X., Attia, S., 2022. Impact of climate change on nearly zero-energy dwelling in temperate climate: Time-integrated discomfort, HVAC energy performance, and GHG emissions. Build. Environ. 223. https://doi.org/10.1016/j.buildenv.2022.109397

Rajagopalan, P., Leung Tony, C.Y., 2012. Progress on building energy labelling techniques. Adv. Build. Energy Res. 6, 61–80. https://doi.org/10.1080/17512549.2012.672002

RDH, 2017. Deep Building Enclosure Energy Retrofit Study, Multi-Unit Residential Building Deep Energy Retrofit Study- Enclosure Retrofit. https://www.rdh.com/wp-content/uploads/2019/07/Deep-Building-Enclosure-Energy-Retrofit-Study.pdf

Rida, M., Ghaddar, N., Ghali, K., Hoballah, J., 2014. Elderly bioheat modeling: changes in physiology, thermoregulation, and blood flow circulation. Int. J. Biometeorol. 58, 1825–1843. https://doi.org/10.1007/s00484-013-0785-1

Rida, M., Kelly, N., 2017. Toward better estimation of HVAC Loads: Integrating a detailed human thermal model into building simulation. Energy Procedia 122, 1147–1152. https://doi.org/10.1016/j.egypro.2017.07.455

Rohdin, P., Molin, A., Moshfegh, B., 2014. Experiences from nine passive houses in Sweden - Indoor thermal environment and energy use. Build. Environ. 71, 176–185. https://doi.org/10.1016/j.buildenv.2013.09.017

Ruff, M., Kirmse, S., Kahnt, A., 2018. Self-regulating Solar Shading System for the Building Envelope Based on Thermal Shape Memory Effect, in: ACTUATOR 2018: 16th International Conference on New Actuators. pp. 25–27. https://doi.org/https://ieeexplore.ieee.org/document/8470872

Ryzhov, A., Ouerdane, H., Gryazina, E., Bischi, A., Turitsyn, K., 2019. Model predictive control of indoor microclimate: Existing building stock comfort improvement. Energy Convers.

Manag. 179, 219–228. https://doi.org/10.1016/j.enconman.2018.10.046

Saha, 2010. NCEPClimate Forecast System Reanalysis (CFSR) Selected Hourly Time-Series Products, January 1979 to December 2010. Research Data Archive at the National Center for Atmospheric Research, Com- putational and Information Systems Laboratory [WWW Document]. https://doi.org/https://rda.ucar.edu/datasets/ds093.1/

Sana, S., Abolfazl Hayati, Salmanzadeh, M., 2021. Optimization of Window-to-Wall Ratio for Buildings Located in Different Climates: An IDA-Indoor Climate and Energy Simulation Study. Energies 14. https://doi.org/10.3390/ en14071974

Schellen, L., van Marken Lichtenbelt, W.D., Loomans, M.G.L.C., Toftum, J., de Wit, M.H., 2010. Differences between young adults and elderly in thermal comfort, productivity, and thermal physiology in response to a moderate temperature drift and a steady-state condition. Indoor Air 20, 273–283. https://doi.org/10.1111/j.1600-0668.2010.00657.x

Schünemann, C., Schiela, D., Ortlepp, R., 2021. How window ventilation behaviour affects the heat resilience in multi-residential buildings. Build. Environ. 202, 107987. https://doi.org/10.1016/j.buildenv.2021.107987

Schünemann, C., Son, S., Ortlepp, R., 2022. Heat resilience of apartment buildings in Korea and Germany: comparison of building design and climate. Int. J. Energy Environ. Eng. 13, 889–909. https://doi.org/10.1007/s40095-022-00476-7

Sessler, D.I., 2008. Temperature monitoring and perioperative thermoregulation. Anesthesiology 109, 318–338. https://doi.org/10.1097/ALN.0b013e31817f6d76

Shaposhnikov, D., Revich, B., Bellander, T., Bedada, G.B., Bottai, M., Kharkova, T., Kvasha, E., Lezina, E., Lind, T., Semutnikova, E., Pershagen, G., 2014. Mortality related to air pollution with the Moscow heat wave and wildfire of 2010. Epidemiology 25, 359–364. https://doi.org/10.1097/EDE.0000000000000090

Shi, D., Song, J., Du, R., Chan, P.W., 2021. Dual challenges of heat wave and protective facemask-induced thermal stress in Hong Kong. Build. Environ. 206, 108317. https://doi.org/10.1016/j.buildenv.2021.108317

Shindell, D., Zhang, Y., Scott, M., Ru, M., Stark, K., Ebi, K.L., 2020. The Effects of Heat Exposure on Human Mortality Throughout the United States. GeoHealth 4. https://doi.org/10.1029/2019GH000234

Shu, C., 2021. Assessment of the Effects of Extreme Heat Events on Buildings. Concordia University. https://spectrum.library.concordia.ca/id/eprint/990006/

Shu, C., Gaur, A., Wang, L. (Leon), Bartko, M., Laouadi, A., Ji, L., Lacasse, M., 2022a. Added value of convection permitting climate modelling in urban overheating assessments. Build. Environ. 207, 108415. https://doi.org/10.1016/j.buildenv.2021.108415

Shu, C., Ji, L., Wang, L., Bai, X., Lacasse, M., Ge, H., Zmeureanu, R., Wang, L. (Leon), 2020.

Field Survey on Indoor Overheating in School and Hospital Buildings in Montréal. 2nd Int. Conf. New Horizons Green Civ. Eng. (NHICE-02), Victoria, BC, Canada, April 29 – May 01, 2020 2–5.

Shu, C., Xie, Z., Ji, L., Baril, D., Wang, L., Bai, X., Yang, S., Zmeureanu, R., Lacasse, M., Laouadi, A., Gaur, A., 2022b. Comparing Multiple Overheating Assessment Metrics Using Measured Data, in: 5th International Conference on Building Energy and Environment (COBEE 2022). Montreal, Canada.

Silvero, F., Lops, C., Montelpare, S., Rodrigues, F., 2019. Impact assessment of climate change on buildings in Paraguay—Overheating risk under different future climate scenarios. Build. Simul. 12, 943–960. https://doi.org/10.1007/s12273-019-0532-6

SMITH, E., C., 1993. A Transient, Three-Dimensional Model of the Human Thermal System. KSU, Diss.

Soebarto, V., Zhang, H., Schiavon, S., 2019. A thermal comfort environmental chamber study of older and younger people. Build. Environ. 155, 1–14. https://doi.org/10.1016/j.buildenv.2019.03.032

Sözer, H., Aldin, S.S., 2019. Predicting the indoor thermal data for heating season based on short-term measurements to calibrate the simulation set-points. Energy Build. 202. https://doi.org/10.1016/j.enbuild.2019.109422

Stapleton, J.M., Larose, J., Simpson, C., Flouris, A.D., Sigal, R.J., Kenny, G.P., 2014. Do older adults experience greater thermal strain during heat waves? Appl. Physiol. Nutr. Metab. 39, 292–298. https://doi.org/10.1139/apnm-2013-0317

Stazi, F., Tomassoni, E., Di, C., 2017. Super-insulated wooden envelopes in Mediterranean climate : Summer overheating , thermal comfort optimization , environmental impact on an Italian case study. Energy Build. 138, 716–732. https://doi.org/10.1016/j.enbuild.2016.12.042

Sun, K., Specian, M., Hong, T., 2020. Nexus of thermal resilience and energy efficiency in buildings: A case study of a nursing home. Build. Environ. 177, 106842. https://doi.org/10.1016/j.buildenv.2020.106842

Sun, K., Zhang, W., Zeng, Z., Levinson, R., Wei, M., Hong, T., 2021. Passive cooling designs to improve heat resilience of homes in underserved and vulnerable communities. Energy Build. 252, 111383. https://doi.org/10.1016/j.enbuild.2021.111383

Takada, S., Kobayashi, H., Matsushita, T., 2009. Thermal model of human body fitted with individual characteristics of body temperature regulation. Build. Environ. 44, 463–470. https://doi.org/10.1016/j.buildenv.2008.04.007

Takada, S., Matsumoto, S., Matsushita, T., 2013. Prediction of whole-body thermal sensation in the non-steady state based on skin temperature. Build. Environ. 68, 123–133. https://doi.org/10.1016/j.buildenv.2013.06.004

Takada, S., Sakiyama, T., Matsushita, T., 2011. Validity of the two-node model for predicting steady-state skin temperature. Build. Environ. 46, 597–604. https://doi.org/10.1016/j.buildenv.2010.09.008

Tariku, F., Kumaran, K., Fazio, P., 2010. Integrated analysis of whole building heat, air and moisture transfer. Int. J. Heat Mass Transf. 53, 3111–3120. https://doi.org/10.1016/j.ijheatmasstransfer.2010.03.016

Tartarini, F., Schiavon, S., Cheung, T., Hoyt, T., 2020. CBE Thermal Comfort Tool: Online tool for thermal comfort calculations and visualizations. SoftwareX 12, 100563. https://doi.org/10.1016/j.softx.2020.100563

Taylor, J., Wilkinson, P., Davies, M., Armstrong, B., Chalabi, Z., Mavrogianni, A., Symonds, P., Oikonomou, E., Bohnenstengel, S.I., 2015. Mapping the effects of urban heat island, housing, and age on excess heat-related mortality in London. Urban Clim. 14, 517–528. https://doi.org/10.1016/j.uclim.2015.08.001

Tejedor, B., Casals, M., Gangolells, M., Macarulla, M., Forcada, N., 2020. Human comfort modelling for elderly people by infrared thermography: Evaluating the thermoregulation system responses in an indoor environment during winter. Build. Environ. 186, 107354. https://doi.org/10.1016/j.buildenv.2020.107354

Teyton, A., Tremblay, M., Tardif, I., Lemieux, M.A., Nour, K., Benmarhnia, T., 2022. A Longitudinal Study on the Impact of Indoor Temperature on Heat-Related Symptoms in Older Adults Living in Non–Air-Conditioned Households. Environ. Health Perspect. 130, 1–8. https://doi.org/10.1289/EHP10291

Thermal Energy System Specialists, 2019. TRNSYS.

Tikuisis, P., Giesbrecht, G.G., 1999. Prediction of shivering heat production from core and mean skin temperatures. Eur. J. Appl. Physiol. Occup. Physiol. 79, 221–229. https://doi.org/10.1007/s004210050499

Tsoka, S., 2015. Optimizing indoor climate conditions in a sports building located in Continental Europe. Energy Procedia 78, 2802–2807. https://doi.org/10.1016/j.egypro.2015.11.630

Tsuzuki, K., Iwata, T., 2002. Thermal comfort and thermoregulation for elderly people taking light exercise. Proc. indoor air 647–652.

Tsuzuki, K., Ohfuku, T., 2002. Thermal sensation and thermoregulation in elderly compared to young people in Japanese winter season. Proc. Indoor Air 659–664.

Ţurcanu, F.E., Popovici, C.G., Verdes, M., Ciocan, V., Hudişteanu, S.V., 2020. Indoor climate modelling and economic analysis regarding the energetic rehabilitation of a church. Energies 13. https://doi.org/10.3390/en13112815

Unnikrishnan, G., Hatwar, R., Hornby, S., Laxminarayan, S., Gulati, T., Belval, L.N., Giersch, G.E.W., Kazman, J.B., Casa, D.J., Reifman, J., 2021. A 3-D virtual human thermoregulatory

model to predict whole-body and organ-specific heat-stress responses. Eur. J. Appl. Physiol. 121, 2543–2562. https://doi.org/10.1007/s00421-021-04698-1

van Loenhout, J.A.F., le Grand, A., Duijm, F., Greven, F., Vink, N.M., Hoek, G., Zuurbier, M., 2016. The effect of high indoor temperatures on self-perceived health of elderly persons. Environ. Res. 146, 27–34. https://doi.org/10.1016/j.envres.2015.12.012

van Steen, Y., Ntarladima, A.M., Grobbee, R., Karssenberg, D., Vaartjes, I., 2019. Sex differences in mortality after heat waves: are elderly women at higher risk? Int. Arch. Occup. Environ. Health 92, 37–48. https://doi.org/10.1007/s00420-018-1360-1

Vanggaard, L., Kalev, K., Juhani, S., Ingvar, H., 2011. Response patterns in finger and central body skin temperatures under mild whole body cooling, in: 14th International Conference on Environmental Ergonomics, Nafplio, Greece. pp. 124–127.

Vardoulakis, S., Dimitroulopoulou, C., Thornes, J., Lai, K.M., Taylor, J., Myers, I., Heaviside, C., Mavrogianni, A., Shrubsole, C., Chalabi, Z., Davies, M., Wilkinson, P., 2015. Impact of climate change on the domestic indoor environment and associated health risks in the UK. Environ. Int. 85, 299–313. https://doi.org/10.1016/j.envint.2015.09.010

Varquez, A.C.G., Darmanto, N.S., Honda, Y., Ihara, T., Kanda, M., 2020. Future increase in elderly heat-related mortality of a rapidly growing Asian megacity. Sci. Rep. 10, 1–9. https://doi.org/10.1038/s41598-020-66288-z

Vellei, M., Ramallo-González, A.P., Coley, D., Lee, J., Gabe-Thomas, E., Lovett, T., Natarajan, S., 2017. Overheating in vulnerable and non-vulnerable households. Build. Res. Inf. 45, 102–118. https://doi.org/10.1080/09613218.2016.1222190

Vicedo-Cabrera, A.M., Scovronick, N., Sera, F., Royé, D., Schneider, R., Tobias, A., Astrom, C., Guo, Y., Honda, Y., Hondula, D.M., Abrutzky, R., Tong, S., Coelho, M. de S.Z.S., Saldiva, P.H.N., Lavigne, E., Correa, P.M., Ortega, N.V., Kan, H., Osorio, S., Kyselý, J., Urban, A., Orru, H., Indermitte, E., Jaakkola, J.J.K., Ryti, N., Pascal, M., Schneider, A., Katsouyanni, K., Samoli, E., Mayvaneh, F., Entezari, A., Goodman, P., Zeka, A., Michelozzi, P., de'Donato, F., Hashizume, M., Alahmad, B., Diaz, M.H., Valencia, C.D.L.C., Overcenco, A., Houthuijs, D., Ameling, C., Rao, S., Di Ruscio, F., Carrasco-Escobar, G., Seposo, X., Silva, S., Madureira, J., Holobaca, I.H., Fratianni, S., Acquaotta, F., Kim, H., Lee, W., Iniguez, C., Forsberg, B., Ragettli, M.S., Guo, Y.L.L., Chen, B.Y., Li, S., Armstrong, B., Aleman, A., Zanobetti, A., Schwartz, J., Dang, T.N., Dung, D. V., Gillett, N., Haines, A., Mengel, M., Huber, V., Gasparrini, A., 2021. The burden of heat-related mortality attributable to recent human-induced climate change. Nat. Clim. Chang. 11, 492–500. https://doi.org/10.1038/s41558-021-01058-x

Vidhyashankar, R., Vinze, R., Nagarathinam, S., Natrajan, V.K., 2022. Modelling spatial variations in thermal comfort in indoor open-plan spaces using a whole-building simulation tool. J. Build. Eng. 46, 103727. https://doi.org/10.1016/j.jobe.2021.103727

Wang, L. (Leon), Shu, C., 2021. Chapter 2: Assessment of the Effect of Urban Heat Island on Buildings., in: Enteria, N., Santamouris, M., Eicker, U. (Eds.), Urban Heat Island (UHI)

Mitigation. Advances in 21st Century Human Settlements. Spinger, Singapore.

Wang, S., 2020. Spatial patterns and social-economic influential factors of population aging: A global assessment from 1990 to 2010. Soc. Sci. Med. 253, 112963. https://doi.org/10.1016/j.socscimed.2020.112963

Wang, Z., Wang, J., He, Y., Liu, Y., Lin, B., Hong, T., 2020a. Dimension analysis of subjective thermal comfort metrics based on ASHRAE Global Thermal Comfort Database using machine learning. J. Build. Eng. 29, 101120. https://doi.org/10.1016/j.jobe.2019.101120

Wang, Z., Yu, H., Jiao, Y., Wei, Q., Chu, X., 2018. A field study of thermal sensation and neutrality in free-running aged-care homes in Shanghai. Energy Build. 158, 1523–1532. https://doi.org/10.1016/j.enbuild.2017.11.050

Wang, Z., Zhang, H., He, Y., Luo, M., Li, Z., Hong, T., Lin, B., 2020b. Revisiting individual and group differences in thermal comfort based on ASHRAE database. Energy Build. 219. https://doi.org/10.1016/j.enbuild.2020.110017

Watkins, R., Levermore, G.J., Parkinson, J.B., 2013. The design reference year - A new approach to testing a building in more extreme weather using UKCP09 projections. Build. Serv. Eng. Res. Technol. 34, 165–176. https://doi.org/10.1177/0143624411431170

Whitman, S., Good, G., Donoghue, E.R., 1997. Mortality in Chicago attributed to the July 1995 heat wave Public Health Biefs Mortality in Chicago Attributed to the July 1995 Heat Wave. Am. J. Public Health 87, 1515–1518.

WMO, 2017. Guidelines on the calculation of climate normals. https://library.wmo.int/index.php?lvl=notice_display&id=20130#.Y8ri0XbMK5c

Xiong, J., Ma, T., Lian, Z., de Dear, R., 2019. Perceptual and physiological responses of elderly subjects to moderate temperatures. Build. Environ. 156, 117–122. https://doi.org/10.1016/j.buildenv.2019.04.012

Yang, S., Wan, M.P., Chen, W., Ng, B.F., Zhai, D., 2019. An adaptive robust model predictive control for indoor climate optimization and uncertainties handling in buildings. Build. Environ. 163, 106326. https://doi.org/10.1016/j.buildenv.2019.106326

Yang, Y., Yao, R., Li, B., Liu, H., Jiang, L., 2015. A method of evaluating the accuracy of human body thermoregulation models. Build. Environ. 87, 1–9. https://doi.org/10.1016/j.buildenv.2015.01.013

Yaqubi, O., Rodler, A., Guernouti, S., Musy, M., 2022. Creation and application of future typical weather files in the evaluation of indoor overheating in free-floating buildings. Build. Environ. 216, 109059. https://doi.org/10.1016/j.buildenv.2022.109059

Yuan, J., Huang, P., Chai, J., 2022. Development of a calibrated typical meteorological year weather file in system design of zero-energy building for performance improvements. Energy 259, 125031. https://doi.org/10.1016/j.energy.2022.125031

Zeng, Z., Zhang, W., Sun, K., Wei, M., Hong, T., 2022. Investigation of pre-cooling as a recommended measure to improve residential buildings' thermal resilience during heat waves. Build. Environ. 210, 108694. https://doi.org/10.1016/j.buildenv.2021.108694

Zhang, C., Kazanci, O.B., Levinson, R., Heiselberg, P., Olesen, B.W., Chiesa, G., Sodagar, B., Ai, Z., Selkowitz, S., Zinzi, M., Mahdavi, A., Teufl, H., Kolokotroni, M., Salvati, A., Bozonnet, E., Chtioui, F., Salagnac, P., Rahif, R., Attia, S., Lemort, V., Elnagar, E., Breesch, H., Sengupta, A., Wang, L.L., Qi, D., Stern, P., Yoon, N., Bogatu, D.I., Rupp, R.F., Arghand, T., Javed, S., Akander, J., Hayati, A., Cehlin, M., Sayadi, S., Forghani, S., Zhang, H., Arens, E., Zhang, G., 2021. Resilient cooling strategies – A critical review and qualitative assessment. Energy Build. 251, 111312. https://doi.org/10.1016/j.enbuild.2021.111312

Zhang, S., Lin, Z., 2021. Predicted Mean Vote with skin wettedness from standard effective temperature model. Build. Environ. 187, 107412. https://doi.org/10.1016/j.buildenv.2020.107412

Zhang, S., Lin, Z., 2020. Standard effective temperature based adaptive-rational thermal comfort model. Appl. Energy 264, 114723. https://doi.org/10.1016/j.apenergy.2020.114723

Zhang, W., Hiyama, K., Kato, S., Ishida, Y., 2013. Building energy simulation considering spatial temperature distribution for nonuniform indoor environment. Build. Environ. 63, 89–96. https://doi.org/10.1016/j.buildenv.2013.02.007

Zhao, Q., Lian, Z., Lai, D., 2020. Thermal Comfort models and their developments: A review. Energy Built Environ. https://doi.org/10.1016/j.enbenv.2020.05.007

Zhao, W., Mustakallio, P., Lestinen, S., Kilpeläinen, S., Jokisalo, J., Kosonen, R., 2022. Numerical and Experimental Study on the Indoor Climate in a Classroom with Mixing and Displacement Air Distribution Methods. Buildings 12, 1314. https://doi.org/10.3390/buildings12091314

Zinzi, M., Pagliaro, F., Agnoli, S., Bisegna, F., Iatauro, D., 2017. ScienceDirect ScienceDirect Assessing the overheating risks in Italian existing school buildings renovated with nZEB targets a heat demand-outdoor Assessing the feasibility of using the. Energy Procedia 142, 2517–2524. https://doi.org/10.1016/j.egypro.2017.12.192

Appendices

A.1. Calculation of Standard Effective Temperature (SET) based on the developed Bioheat models

Referring to ASHARE 55 (2017), SET is defined as the temperature of an imaginary environment at 50% RH, <0.1 m/s (20 fpm) average airspeed V_a, and $T_r = T_a$, in which the total heat loss from the skin of an imaginary occupant with an activity level of 1.0 met and a clothing level of 0.6 clo is the same as that from a person in the actual environment with actual clothing and activity level. SET can be calculated with Newton's iterative solution, as shown in Figure A.1-1.

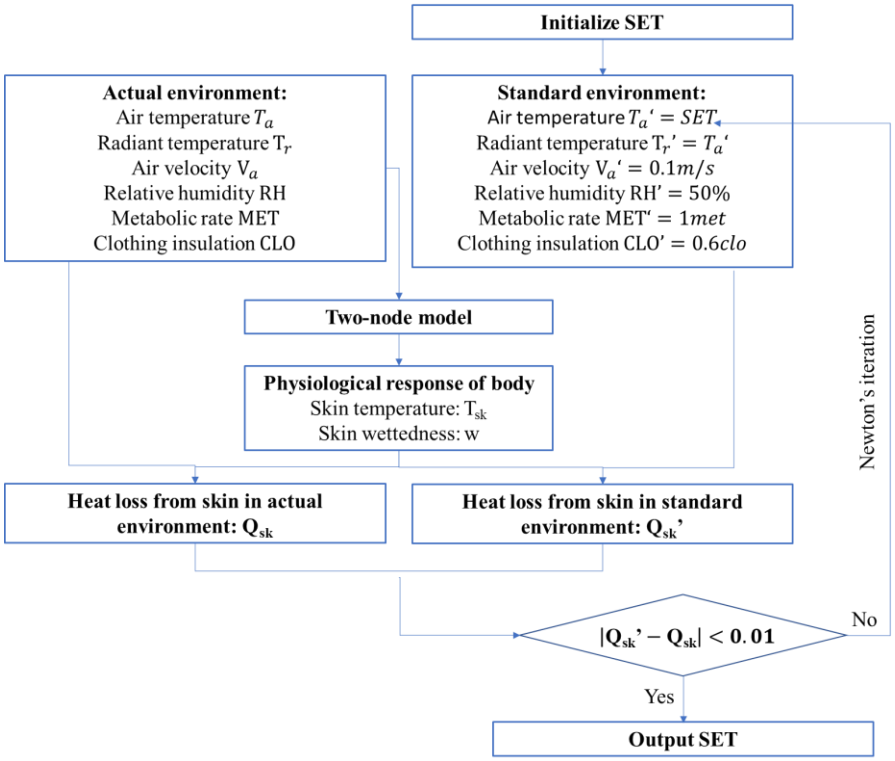

Figure A.1-1 Calculation of SET (Zhang and Lin, 2020)

A.2. Building modeling and calibration based on measured data

Building models that can accurately predict hourly indoor air temperatures in free-running situations are key to understanding overheating conditions and the resilience of passive cooling strategies under a changing climate. To accurately predict indoor temperatures, it is necessary to properly model pressure-driven infiltration and natural ventilation. This can be achieved by coupling a building thermal model to an airflow network model. The development of coupled building thermal and airflow network models is described in this section to calibrate building models using field measurements of indoor air temperature.

Figure A.2-1 shows the procedure of building modelling and calibration. Through building survey, site visit and architecture plan, building parameters, operation schedules, and HVAC systems information are collected. Airflow network (AFN) is applied to the building models. There are unknown parameters to be calibrated based on the measured indoor hourly temperature. The subsections below will introduce the procedure in detail with three measured and modelled buildings.

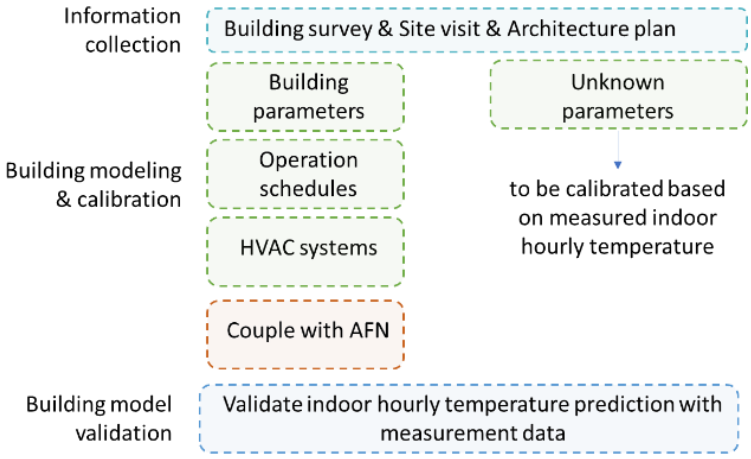

Figure A.2-1 Procedure of building modeling and calibration

A building measurement campaign was conducted to monitor the indoor and outdoor thermal conditions of different types of buildings in Montreal, Canada (Shu et al., 2020). The indoor temperature and relative humidity (RH) in selected spaces on different floors and orientations of 13 buildings (three primary schools, three hospitals and four residential buildings) were monitored continuously over the summer seasons from 2020 to 2021. On-site weather stations were placed on the roofs of buildings to gather local weather data, including air temperature, relative humidity, solar radiation, wind speed and direction, and precipitation. With the monitored indoor and outdoor conditions, the overheating issues of these buildings can be assessed during the monitored period. However, with climate change, the overheating conditions in future climate projections need to be predicted and possible mitigation strategies need to be investigated using calibrated building models.

Among the monitored buildings, three buildings including a long-term care building (LTCB), a primary school (PS), and a multi-unit social housing (SH) are modelled in Design Builder™ and exported for use in an EnergyPlus simulation package. The monitored LTCB is an L-shaped building facing the northwest direction and is composed of five floors above the ground and below-grade basement floor. The total length and width of the building are 44m and 42m, respectively. The size of a typical private patient room in the building is 5.4m x 3.6m. The building was constructed in 1980 with exterior walls made of concrete and solid brick veneer cladding. There were no central cooling systems in the building. As for the mechanical ventilation system, five lounge spaces used a central system to provide fresh air.

The PS building is a 3+1 story building originally built in 1930. The building was partially retrofitted six times including the extension in 1955, adding boiler room in 2008, masonry in 2009,

plumbing in 2014, and new roof in 2015, sanitary blocks and foundations in 2019. The building can accommodate 396 students and 24 teaching staff. The total length and width of the building are 53m and 46m, respectively. The size of a typical private classroom in the building is 9.4m x 8.1m. The building was constructed with exterior walls made of concrete panels and solid brick veneer claddings. There were no cooling systems or mechanical ventilation system in the buildings. The classrooms were cooled by natural ventilation by opening windows and portable fans (in some classrooms). The SH building is a three-story building built in 2008 and mainly occupied by older people. The total length and width of the building are 105m and 18.5m, respectively. The size of a typical unit in the building is 9.2m x 8.2m. The building is composed of 54 suites (dwelling units) with one bedroom. Each unit was occupied by one or two people. There were no cooling and mechanical ventilation system in the dwelling units. An activity room on the first floor is cooled by a rooftop unit. Indoor sensors were installed in selected rooms in the above buildings to monitor the air temperature and relative humidity. In each building, all the sensors were installed in the same locations in each room, about 1.7-meter height near the corner. Outdoor weather stations were installed on the roof of the buildings to monitor the air temperature, relative humidity, wind speed, and solar radiation. The monitored data were collected during the summer 2020.

According to the information collected through building surveys, site visits and onsite measurement, the original building models were developed. The 3D models of the three buildings are shown in Figure A.2-2.

(a) (b) (c)

Figure A.2-2 3-D view of the as-simulated building models

The unknown building parameter values were calculated through building model calibration using the monitored temperature data. The ranges of the unknown parameter values were taken from related published literature and the national building code of Canada. Table A.2-1 summarizes the ranges of the unknown building parameters for building calibration of the LTCB. Unknown parameters and ranges of the primary school and social housing are also analyzed in a similar way, the tables of which are not listed here due to the page's limitation.

Table A.2-1 Unknown parameters and ranges of the Long-term care building

Building Parameter		Range	Unit	References
Wall	U-Value	0.25-0.62	W/m^2K	RDH (2017)
	Thermal mass	150-350	W/m^2K	
Roof	U-Value	0.15-0.39	KJ/km^2	
	Thermal mass	150-350	KJ/km^2	
Window	U-Value	2.38-3.31	W/m^2K	Double glazing with aluminum frame
	SHGC	0.3-0.7	/	
Shading	Slat angle	5-175	Deg	Blind shading parameter
	Solar reflectance	0.4-0.9	/	
Internal heat gain	Lighting power density	6.6-11.3	W/m^2	NECB2017
	Equipment power density	2.5-10	W/m^2	NECB2017
Infiltration	Air mass flow coefficient at reference crack condition	Walls: 0-0.0040 Roof: 0-0.0045	kg/s	RDH (2017)
Natural ventilation	Natural ventilation temperature set point	22-26	℃	Comfort range
	Window opening factor	0-0.1	/	Site visit
	Room door opening factor	0-1	/	
	Exterior doors opening factor	0.025		

The airflow network models are applied to the building models. The buildings are treated as a collection of nodes representing thermal zones in the building and flow elements representing

cracks, doors, ducts, and other flow paths between the zones. Conservation of mass flows between the zones generates simultaneous nonlinear equations, which can be solved to determine the resultant flow through the building. Using an airflow network model to predict ventilation rates in a building allows the inclusion of external weather data in the calculation. The natural variability of the ventilation drivers such as wind speed and direction and thermal effects can be incorporated into the calculation, providing more realistic ventilation predictions than using a fixed ventilation rate based on open window area alone. The airflow through each leakage component is assumed to follow the leakage relationship of a crack flow, which is characterized by the air mass flow coefficient (C) and exponent (n) as in Equation A.2-1.

$$\dot{m}_a = \dot{V}_a \times A \times \rho = C \cdot \Delta P^n \quad \text{(A.2-1)}$$

Where $\dot{m}_a$ is the maximum mass flow rate of each surface (kg/s), $\dot{V}_a$ is the maximum volume flow rate per area ($m^3/s/m^2$), A is the component surface area (m^2), ρ is air density (kg/m^3), ΔP pressure differential across the leakage component (Pa), n is the leakage exponent coefficient, defaulted to 0.65.

In the pre-modelling stage, the design infiltration rate for good airtightness of 0.4 ACH (NRC, 2017) for the whole building is set, and the DesignBuilder software automatically creates the leakage data of each exterior and interior surface. However, the infiltration rate is dynamic, affected by wind pressure and surface leakage characteristics. For old buildings (1980), the maximum leakage rate for the entire similar buildings was found to be 0.72 CFM/SF@75Pa = 3.66L/s/m2@75Pa, according to RDH (2017) (RDH, 2017). For retrofit or new buildings, referring to ASHARE 90.1 (ASHRAE Standards Committee, 2004), ABAA and NECB (NRC, 2017), the

maximum air leakage for the entire building built after 2005 is 2.0L/s·m2@75Pa. Therefore, to make the leakage data closer to the actual situation, calculations of the maximum air mass flow coefficient for the exterior surfaces of the monitored rooms, assuming a uniform distribution over exterior building surfaces, are shown in Table A.2-2.

Table A.2-2 Calculated air leakage data of the monitored natural ventilated rooms (using the Long-term care building as an example)

Surface	Air leakage limit @75Pa ($L/s/m^2$)	Area (m2)	Air density (Reference condition) (kg/L)	n	C (max)
Roof	3.66	20.297	0.0012	0.7	0.0043
Wall_North	3.66	13.095	0.0012	0.7	0.0028
Wall_West	3.66	2.987	0.0012	0.7	0.00063
Wall_South	3.66	18.893	0.0012	0.7	0.0040

In the airflow model, the exterior windows are opened when the indoor temperature is higher than the outdoor temperature and a given set point temperature (the natural ventilation setpoint temperature will be calibrated based on the monitored data). The thermal and ventilation conditions in the zones are affected by the window and door operations (the opening area percentage will be calibrated based on the monitored data), infiltration through the crack of roofs, walls, and partitions, as well as the air released through exhaust fans. The airflow path through the large horizontal openings is applied to the vertical stairway and elevator thermal zones. The building calibration process is composed of five steps: parametric simulation with all variables, the first-round calibration, sensitivity analysis, parametric simulation with the most important four variables, second round calibration, as shown in Figure A.2-3.

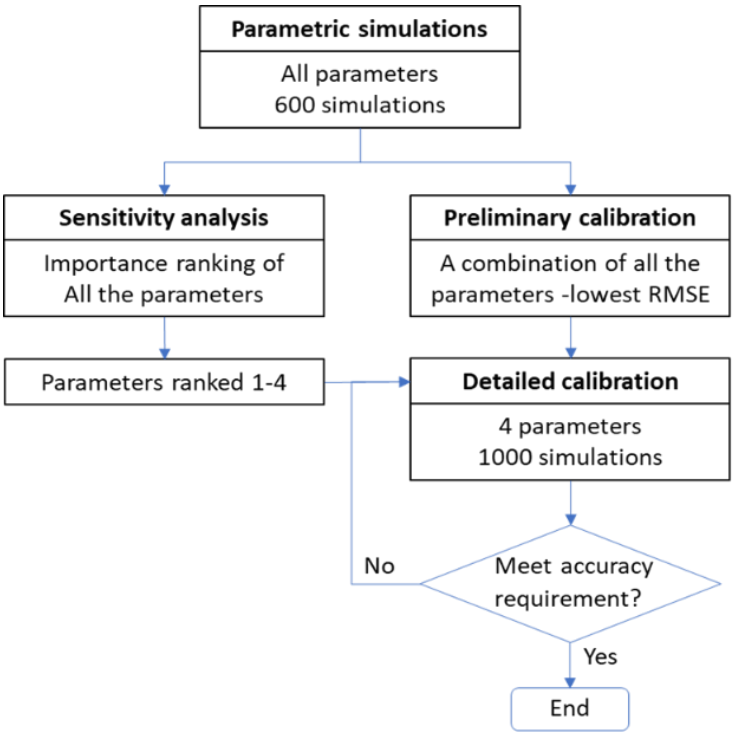

Figure A.2-3 Building calibration procedure

In the first step, the unknown model parameters with their practical ranges are defined. The Hamiltonian Monte-Carlo (HMC) sampling method is used for 600 random samplings within each parameter range. HMC is a random sampling algorithm applicable when the model parameters are continuous rather than discrete and able to suppress random walk behavior through a clever auxiliary variable scheme that transforms the problem of sampling from a target distribution into the problem of simulating Hamiltonian dynamics (Hoffman, 2014). So 600 combinations of all the defined parameters are obtained, and then 600 parametric simulations are performed. The parametric simulations are realized with an R package named “eplusr”, which enables to use EnergyPlus directly in the R language. The input-output dataset can be used to do sensitivity analysis to identify the most important parameters of the building thermal model, as explained in the next paragraphs. The input-output dataset can also be used to do the first-round calibration of

all the defined parameters. In this round calibration, the simulated indoor air temperatures are compared with measurements, and the RMSE is calculated. The parameter combination corresponding to the minimum RMSE is adopted for the building model. In the second step, the most important four parameters (obtained from the sensitivity analysis) are further calibrated. HMC is again used for 1000 random samplings within each parameter range, resulting in 1000 combinations of all the defined parameters, and then 1000 parametric simulations are performed. The simulated indoor air temperature is compared with measurements, and the RMSEs are calculated. The parameter combination corresponding to the minimum RMSE is adopted for the building model. The calibration process stops when the RMSE reaches its low-level value of below 1.5℃. This low-level value is taken from the study of (O' Donovan et al., 2019) about the error of predicting air temperatures in a naturally ventilated building. After calibration, validation is then done with the other set of measured data during the different periods for the calibration stage. All the above steps are realized and automated using a script developed in the R programing language.

Typically, there are six steps for implementing sensitivity analysis in building performance analysis: determine input variations; create building energy models; run energy models; collect simulation results; run sensitivity analysis; presentation of sensitivity analysis results. The first four steps have been finished after the first round of parametric simulation. So that the input-output dataset from the first-round parametric simulations is collected to feed the sensitivity analysis to identify the most important parameters. Three different approaches are utilized to offer robust analysis results: SRC, t-value, and random forest variable importance. High SRC means more important of the variable. The t-value is the statistic used to test whether the coefficient of the corresponding variable is zero. The higher the absolute value of t, the more important is the

corresponding variable. The conditional variable importance from the random forest applies to correlated inputs. If there is a large variation of the outputs unexplained (i.e., non-linear effects in the model), the conditional variable importance from the random forest can be used. The three approaches are integrated into one index called Sensitivity Value Index (SVI) (Lim and Zhai, 2017) to avoid the potential inconsistency.

After calibration, the building models are validated with measured indoor temperature data (over different periods of time). For the LTCB, the monitored data were collected from July 14, 2020 to August 13, 2020. Therefore, the data from July 14 to July 28 were selected for model calibration so that all the parameters to be calibrated have significant effects on indoor temperature, and the data from July 29 to August 13 were selected for model validation. For the PS, the monitored data were collected from August 04, 2020 to September 30, 2020. Therefore, the data from August 26 to September 13 (school occupied) were used for the calibration and the data from September 14 to 30 were used for validation. For the SH, the monitored data were collected from May 01 to 26, 2021. However, from May 01 to 13, the outdoor temperature was from 5℃ to 20℃ and the simulated indoor temperature was lower than 22℃, which made natural ventilation not activated. Therefore, the data from May 14 to 20 were used for the calibration and the data from May 21-26 were used for the validation.

Table A.2-3(a) shows the evaluation criteria (RMSE) of the calibration and validation results for each room and their spatial averages in LTCB. At a room level, the RMSE of the calibration and validation are from 0.56℃ to1.09℃, which are less than the 1.5℃ requirement (O'Donovan et al. 2019). The MBE is within ±1.2% and the CvRMSE is less than 3.65%. At a building level (calculated by averaging the data of the three rooms), the validation results show that the RMSE

is 0.54℃, the MBE is 0.58% and the CvRMSE is 1.85%. Table A.2-3(b) shows the evaluation criteria results of PS. At room level, the RMSE of the calibration and validation are from 0.63℃ to 0.78℃. The MBE is within ±1.39% and the CvRMSE is less than 3.19%. At the building level (calculated by average data of the two rooms), validation results show that the RMSE is 0.67℃, the MBE is -0.12% and the CvRMSE is 2.78%. Table A.2-3(c) shows the evaluation criteria results of SH. At room level, the RMSE of the calibration and validation are from 0.56℃ to1.50℃. The MBE is within ±4.9% and the CvRMSE is less than 5.28. In building level (calculated by average data of the four rooms), validation results show that the RMSE is 0.71℃, the MBE is 0.47% and the CvRMSE is 2.55%. The positive MBE value means the simulated data are in general slightly higher than the measured data. The negative MBE value means the simulated data are in general slightly lower than the measured data.

Table A.2-3 Error metrics for the predictions of the hourly indoor air temperatures of monitored rooms in (a) LTCB (b) PS and (c) SH

(a)

Error metrics	Room 1		Room 2		Room 3		Room Average	
	Cal.	Val.	Cal.	Val.	Cal.	Val.	Cal.	Val.
RMSE (°C)	0.56	0.66	0.57	0.55	1.09	1.08	0.46	0.54
MBE (%)	0.25	0.90	-0.70	0.57	1.182	0.285	0.244	0.58
CvRMSE (%)	1.93	2.31	1.89	2.02	3.63	3.61	1.54	1.85

(b)

Error metrics	Room 1		Room 2		Room Average	
	Cal.	Val.	Cal.	Val.	Cal.	Val.
RMSE (°C)	0.73	0.7	0.63	0.78	0.63	0.67
MBE (%)	-0.82	1.17	-0.90	-1.39	-0.86	-0.12
CvRMSE (%)	2.57	3.12	2.22	3.19	2.21	2.78

(c)

Error metrics	Bedroom 1		Living room 1		Bedroom 2		Living room 2		Room average	
	Cal	Val	Cal	Val	Cal	Val	Cal	Val	Cal	Val
RMSE (°C)	0.63	1.05	0.56	0.91	1.49	0.77	1.21	1.50	0.59	0.71
MBE (%)	1.19	1.08	1.25	0.52	-4.90	-0.67	-3.72	0.99	-1.65	0.47
CvRMSE (%)	2.44	3.86	2.16	3.33	5.28	2.71	4.35	5.51	2.18	2.55

Figure A.2-4 compares the measured and simulated indoor temperature (average values of the three monitored rooms of LTCB) after applying the calibrated parameter values during the calibration and validation periods. To analyse whether the simulated data can capture the peak indoor temperatures, the distribution of the measured and simulated hourly temperatures during the validation period are shown in Figure A.2-5. During the validation period, there are 11 hours when the measured temperature is above 30.4℃ (the last bin in Figure A.2-5 (a)), and 8 hours when the simulated temperature is above 30.4℃ (the last bin in Figure A.2-5(b)). Therefore, the simulated data can capture 73% of the peak temperatures. Comparing the three bins of 29.8℃ to 30.4℃, the simulations overestimate the hours between 29.8℃ to 30.4℃ by 85 hours, but underestimate the temperature in the bins of 28.4℃ to 29.4℃ by 87 hours. This deviation might be because of occupant behavior in adjusting window and door openings under different weather conditions to control nature ventilation, whereas in the simulation the opening factors of windows and doors are kept constant during the simulation period.

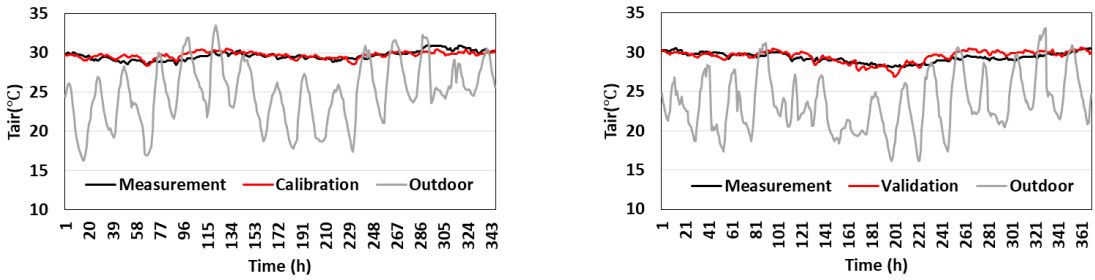

(a) (b)

Figure A.2-5 Comparison of the measured and simulated data (room averages of LTCB) during (a) calibration period and (b) validation period

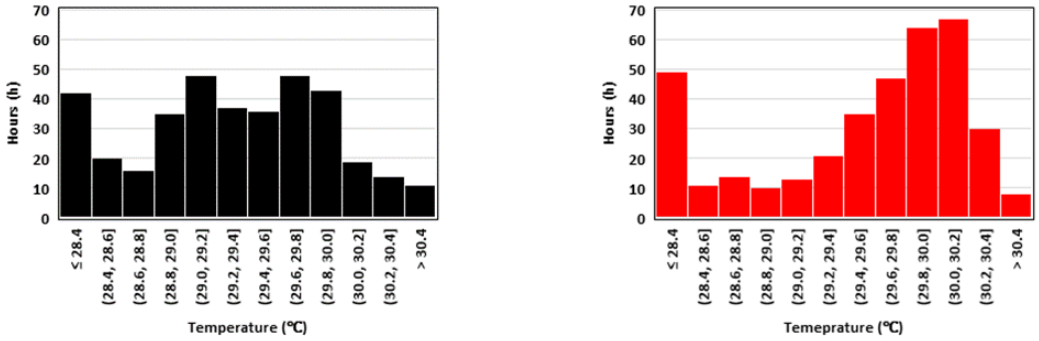

(a) (b)

Figure A.2-6 Distribution of average room data of LTCB during the validation period: (a) measured and (b) simulated temperatures

Figure A.2-6 shows a comparison between the measured and simulated data (average data of the two rooms in PS) after applying the calibrated parameter values, and the distribution of the measured and simulated hourly temperatures during the validation period is shown in Figure A.2-7. There are 26 hours when the measured temperature is above 31.2℃, and 42 hours when the simulated temperature is above 31.2℃. Therefore, the simulated data can capture 100% of the peak temperatures with a slight overestimation. The hours of the measured and simulated temperature above 28℃ are as well comparable: 514 hours versus 522 hours, respectively.

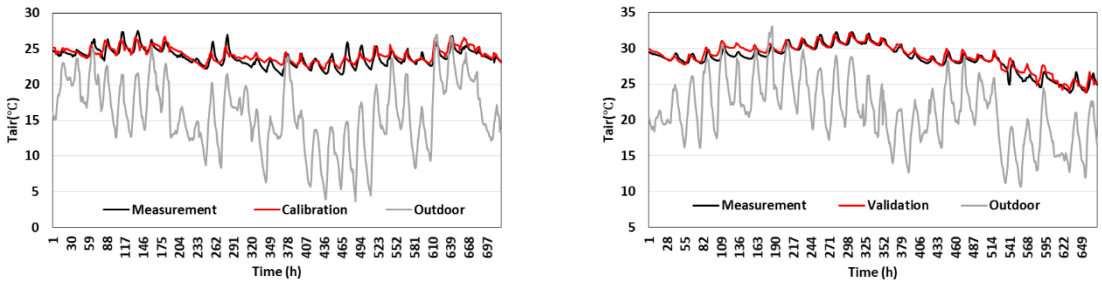

(a) (b)

Figure A.2-7 Comparison of the measured and simulated data (room averages of PS) during (a) calibration period and (b) validation period

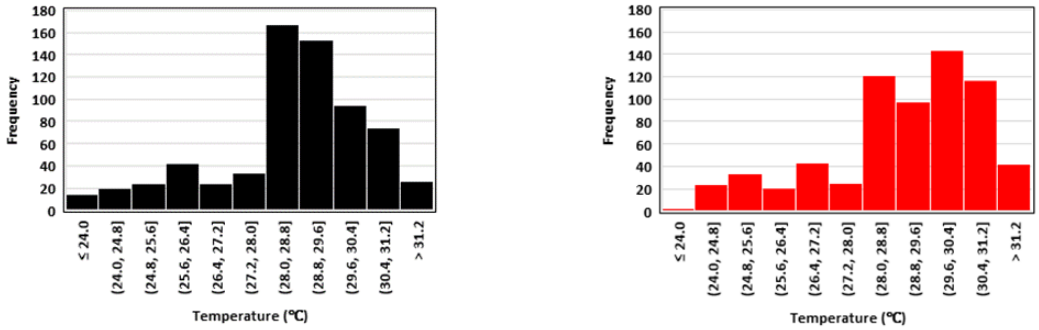

(a) (b)

Figure A.2-8 Distribution of average room data of PS during the validation period: (a) measured and (b) simulated temperatures

Figure A.2-8 shows the comparison of the measured and simulated data (average data of the four rooms in SH) after applying the calibrated parameters. The distribution of the measured and simulated hourly temperatures during the validation period is shown in Figure A.2-9. There are 10 hours when the measured temperature is above 30.0℃, and 8 hours when the simulated temperature is above 30.0℃. Therefore, the simulated data can capture 80% of the peak temperatures. The hours of the measured and simulated temperatures above 29℃ are comparable: 36 hours versus 41 hours, respectively.

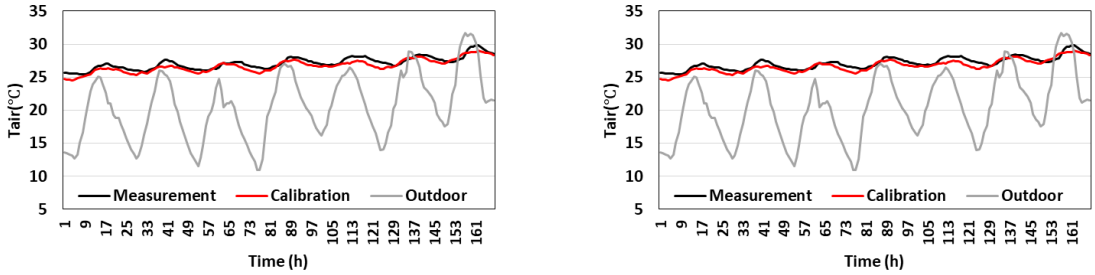

(a) (b)

Figure A.2-8 Comparison of the measured and simulated data (room averages of SH) during (a) calibration period and (b) validation period

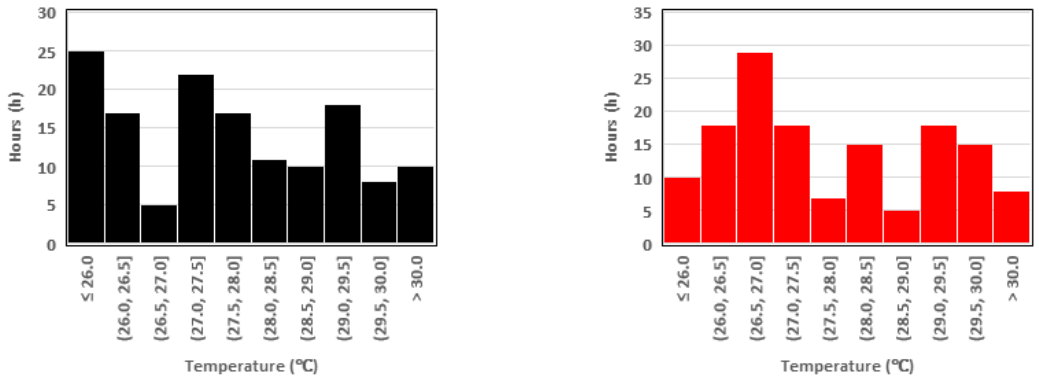

(a) (b)

Figure A.2-9 Distribution of average room data of SH during the validation period: (a) measured and (b) simulated temperatures

The calibrated values of the unknown parameters of the LTCB model are shown in Table A.2-5.

Table A.2-5 Calibrated parameter values of LTCB

Object	Parameter	Unit	Final value
Wall	Wall U-Value	W/m^2K	**0.3**
Roof	Roof U-Value	W/m^2K	**0.25**
Wall	Wall thermal mass	KJ/km^2	**220**
Roof	roof thermal mass	KJ/km^2	**335**
Window	Window U-Value	W/m^2K	**2.72**
Window	Window SHGC	-	**0.37**
Interior blinds	Slat angle	Deg	**59**
	Solar reflectance		**0.6**
Equipment	Equipment power density	W/m^2	**2.93**
Lighting	Lighting power density	W/m^2	**9.94**
Air mass flow through cracks	Air mass flow coefficient at reference crack condition of walls and roof surfaces	kg/m·s	**0.0025**
		kg/m·s	**0.0012**
Natural ventilation control	Natural ventilation set point	℃	**26**
Interior room door opening factor	Width factor for door opening	%	**47**
Room window opening factor		%	**10**